



National Library
of Canada

Acquisitions and
Bibliographic Services Branch

395 Wellington Street
Ottawa, Ontario
K1A 0N4

Bibliothèque nationale
du Canada

Direction des acquisitions et
des services bibliographiques

395, rue Wellington
Ottawa (Ontario)
K1A 0N4

Your file - Votre référence

Our file - Notre référence

NOTICE

The quality of this microform is heavily dependent upon the quality of the original thesis submitted for microfilming. Every effort has been made to ensure the highest quality of reproduction possible.

If pages are missing, contact the university which granted the degree.

Some pages may have indistinct print especially if the original pages were typed with a poor typewriter ribbon or if the university sent us an inferior photocopy.

Reproduction in full or in part of this microform is governed by the Canadian Copyright Act, R.S.C. 1970, c. C-30, and subsequent amendments.

AVIS

La qualité de cette microforme dépend grandement de la qualité de la thèse soumise au microfilmage. Nous avons tout fait pour assurer une qualité supérieure de reproduction.

S'il manque des pages, veuillez communiquer avec l'université qui a conféré le grade.

La qualité d'impression de certaines pages peut laisser à désirer, surtout si les pages originales ont été dactylographiées à l'aide d'un ruban usé ou si l'université nous a fait parvenir une photocopie de qualité inférieure.

La reproduction, même partielle, de cette microforme est soumise à la Loi canadienne sur le droit d'auteur, SRC 1970, c. C-30, et ses amendements subséquents.

**COMBINED CONVECTIVE AND INFRARED DRYING OF A
CAPILLARY POROUS BODY**

by

JEAN-MICHEL PARROUFFE

**A Thesis Submitted to the Faculty of Graduate Studies
and Research in Partial Fulfilment of the
Requirements for the Degree of
Doctor of Philosophy**

**Department of Chemical Engineering
McGill University
Montreal**

©

June 1992



National Library
of Canada

Acquisitions and
Bibliographic Services Branch

395 Wellington Street
Ottawa, Ontario
K1A 0N4

Bibliothèque nationale
du Canada

Direction des acquisitions et
des services bibliographiques

395, rue Wellington
Ottawa (Ontario)
K1A 0N4

Vous êtes votre référence

Vous êtes votre référence

The author has granted an irrevocable non-exclusive licence allowing the National Library of Canada to reproduce, loan, distribute or sell copies of his/her thesis by any means and in any form or format, making this thesis available to interested persons.

L'auteur a accordé une licence irrévocable et non exclusive permettant à la Bibliothèque nationale du Canada de reproduire, prêter, distribuer ou vendre des copies de sa thèse de quelque manière et sous quelque forme que ce soit pour mettre des exemplaires de cette thèse à la disposition des personnes intéressées.

The author retains ownership of the copyright in his/her thesis. Neither the thesis nor substantial extracts from it may be printed or otherwise reproduced without his/her permission.

L'auteur conserve la propriété du droit d'auteur qui protège sa thèse. Ni la thèse ni des extraits substantiels de celle-ci ne doivent être imprimés ou autrement reproduits sans son autorisation.

ISBN 0-315-80269-3

Canada

ABSTRACT

This research has resulted in the design and development of an experimental facility to study the combined convective infrared (I.R.) drying process of a capillary porous material (glass beads) in high temperature flow conditions.

The necessity to decrease the heat transfer coefficient for the effect of high mass transfer flux (when convection is combined with I.R. heating) has been demonstrated. Further, the analogy between the transfer of heat and mass expressed in terms of average heat and mass transfer coefficient ratios has been verified to apply when the surface is not contaminated. Experiments have also showned that there is a link between the evaporation temperature and crust formation at the evaporating surface. Moreover, an increase in the heat transfer coefficient was observed when the surface reaches the boiling point and is higher than that of the flowing air. Lastly, it was observed that the critical moisture content is independent of the convective drying parameters, sample thickness and the overall incident heat flux.

A drying front model is also presented and tested with the experimental results in convection drying and for the combined process. The drying time, the bottom temperature evolution, the surface temperature evolution up to the critical point and the overall shape of the drying rate curve were well reproduced by the model. Simulations have also showned that the effect of the diffusion mass flux on the heat and mass transfer coefficients leads to a decrease of the evaporation rate by a maximum of 8 % for both the purely convective and combined processes.

RÉSUMÉ

Cette recherche a permis la conception et le développement d'un montage expérimental afin d'étudier le séchage mixte infra-rouge et convection haute température d'un matériau poreux capillaire (billes de verre).

La nécessité de diminuer le coefficient de transfert de chaleur à cause de l'effet d'un transfert de masse élevé (lors du séchage mixte) a été démontrée. De plus, Il a été vérifié que la similitude entre les transferts de chaleur et de masse exprimée en terme de rapport de coefficients de transferts moyens s'applique lorsque la surface du matériau n'est pas contaminée. Les résultats expérimentaux ont aussi montré qu'un lien existait entre la température d'évaporation et la formation d'une croûte à la surface. Une augmentation du coefficient de transfert de chaleur à été observée lorsque la température de surface atteint le point d'ébullition et est supérieure à la température de l'écoulement. Enfin, il a été observé que la teneur en eau critique est indépendante des paramètres de séchage convectif, de l'épaisseur et du flux de chaleur radiatif incident.

Un modèle à front a été présenté et testé avec les résultats expérimentaux en séchage convectif et mixte. Les temps de séchage, l'évolution de la température au fond de l'échantillon, l'évolution de la température à la surface jusqu'à la teneur en eau critique ainsi que la forme générale de la courbe de vitesse de séchage ont été assez bien reproduits. Les simulations ont aussi montré que l'effet sur les coefficients de transfert de chaleur et de masse du flux de diffusion à la surface conduisent à une décroissance maximale de la vitesse de séchage de 8 % pour les séchages convectif et mixte.

ACKNOWLEDGEMENTS

I would like to express my sincere appreciation and gratitude to my thesis advisors, Dr. A. S. Mirjundar and Dr. M Dostie (LTEE) for their invaluable guidance, constructive advice as well as continuous encouragement. Their patience, scientific rigor, skill and willingness to devote long hours of their time to my questions have been greatly appreciated.

A special word of thank to Marlène Tremblay for formatting this thesis, to LTEE technicians and machine shops staff as well as Alain Poulin, Martin Bédard and Gaétan St. Louis for their help in constructing the equipment

The financial support of this work by Hydro-Québec through its research laboratories IREQ and LTEE is gratefully acknowledged.

Last, but not least, I would like to thank Karine for her love, patience understanding and continuous moral support.

TABLE OF CONTENTS

	Page
ABSTRACT.....	i
RÉSUMÉ.....	ii
ACKNOWLEDGEMENTS.....	iii
TABLE OF CONTENTS.....	iv
LIST OF FIGURES	ix
LIST OF TABLES	xix
NOMENCLATURE	xxii
CHAPTER I - INTRODUCTION	1
1.1 Background.....	1
1.2 Objectives of the present study	3
1.3 Outline of the thesis.....	4
CHAPTER II - LITERATURE REVIEW.....	5
2.1 Prior experimental studies on I.R. drying.....	5
2.2 Modelling of drying.....	12
CHAPTER III - EXPERIMENTAL APPARATUS AND PROCEDURES.....	17
3.1 Introduction	17
3.2 Experimental apparatus	17
3.2.1 Oven test section	18
3.2.2 Container for test samples.....	25

3.2.3 Consolidated glass bead test sample preparation	27
3.2.4 Wetting apparatus and procedure.....	32
3.2.5 Sample holder	34
3.3 Operating parameters.....	36
3.4 Data acquisition and treatment	36
3.4.1 Data recording: hardware and procedure	36
3.4.2 Drying experiments.....	38
3.4.3 Smoothing of drying curve.....	39
3.4.4 Determination of the critical moisture content.....	42
3.5 Experimental reproducibility.....	44
3.6 Experimental uncertainty.....	47
CHAPTER IV - CONVECTIVE DRYING EXPERIMENTS	49
4.1 Introduction	49
4.2 Convective heat transfer coefficients in convection drying.....	49
4.3 Test of the analogy between the heat and mass transfer in convection drying.....	56
4.3.1 Comparison with theoretical and previous experimental results	64
4.3.2 Sensitivity study.....	66
4.4 Critical moisture content in convective drying.....	71
4.5 Conclusions.....	75
CHAPTER V - COMBINED CONVECTIVE AND INFRARED DRYING EXPERIMENTS	77
5.1 Introduction	77
5.2 Overall incident radiative heat flux.....	77
5.2.1 Overall incident radiative heat flux in free convection-I.R. evaporation experiments	79

5.2.2 Incident I.R. source and test section wall radiative heat fluxes in free convection-I.R. evaporation experiments.....	87
5.3 Test sample surface absorptivity under I.R. heat flux.....	93
5.4 Convective heat transfer coefficients in combined convection- I.R. drying.....	97
5.4.1 Overall incident radiative heat flux in combined convection-I.R. drying experiments.....	97
5.4.2 Convective heat transfer coefficients.....	108
5.4.3 Discussion of results.....	110
5.5 Test of the analogy between the heat and mass transfer in combined convection-I.R. drying.....	126
5.6 Critical moisture content in combined convective and radiative drying.....	137
5.7 Conclusions.....	144

CHAPTER VI - COMBINED CONVECTIVE AND INFRARED DRYING

MODELLING.....	146
6.1 Introduction.....	146
6.2 Hypotheses.....	149
6.3 Mass conservation equations.....	151
6.4 Energy conservation equation.....	155
6.5 Drying front parameters for simulations.....	161
6.6 Convective drying simulations.....	163
6.6.1 Experimental drying curve: correction for geometrical effects.....	165
6.6.2 The surface temperature measurement bias in convective drying.....	169
6.6.3 The drying front position correction effect in convective drying.....	173
6.6.4 The transfer coefficient corrections and the drying front model results in convective drying.....	176

6.6.5 Comparison between the convective drying runs and the drying front model.....	182
6.7 Combined convective and I.R. drying simulations.....	187
6.7.1 The surface temperature measurement bias in the combined convective-I.R. drying process	187
6.7.2 The drying front position correction effect in the combined convective-I.R. drying process	190
6.7.3 The transfer coefficients correction and the drying front model results in the combined convective-I.R. drying process.....	195
6.7.4 Comparison between experimental combined convective- I.R. drying data and the drying front model predictions	198
6.8 Conclusions.....	207
 CHAPTER VII - CONCLUSIONS.....	209
7.1 Summary.....	209
7.2 Contributions to knowledge.....	211
7.3 Recommendations for future work.....	212
 REFERENCES.....	213
 APPENDIX 1: THE EXPERIMENTAL SET-UP ACCESSORIES OR EQUIPMENTS	226
 APPENDIX 2: THE SPATIAL LOCATION OF THE MEASURING POINTS WITH RESPECT TO Oxyz.....	227
 APPENDIX 3: MEASUREMENT DEVICES AND/OR SENSORS	228

APPENDIX 4: THE THERMOPHYSICAL PROPERTIES OF WATER, WATER VAPOR, AIR AND THE GLASS BEADS	229
APPENDIX 5: THE RADIATIVE HEAT EXCHANGE IN THE TEST SECTION: THE HYPOTHESES, SURFACES, SYSTEM OF EQUATIONS AND SOLUTION.....	233
APPENDIX 6: EMISSIVITY MEASUREMENT	238
APPENDIX 7: HEAT TRANSFER COEFFICIENT CORRELATION.....	244
APPENDIX 8: EVALUATION OF THE HEAT TRANSFER LOSS OR GAIN DURING THE FREE CONVECTION-I.R. WATER EVAPORATION EXPERIMENTS.....	247
APPENDIX 9: EVALUATION OF THE MAXIMAL FRACTION OF THE EMITTED I.R. HEAT FLUX ABSORBED BY THE AIR LAYER BETWEEN THE SOURCE AND THE SAMPLE	257
APPENDIX 10: CORRECTION TO THE EXPERIMENTAL DRYING CURVE OF A TRUNCATED CONE TO OBTAIN THE CORRESPONDING DRYING CURVE FOR A CYLINDER.....	253
APPENDIX 11: THE HEAT AND MASS TRANSFER ANALOGY	257

LIST OF FIGURES

<u>Figure</u>	<u>Caption</u>	<u>Page</u>
3.1	Oven schematic.....	19
3.2	Photograph of the oven and the test section.....	20
3.3a	Test section: bottom view.....	21
3.3b	Test section: cross sectional view.....	21
3.3c	Test section: top view	22
3.4a	Container mold: top view.....	26
3.4b	Container mold: cross sectional view.....	26
3.5	Photograph of a random glass beads sample.....	28
3.6	Photograph of beads from a sintered sample.....	28
3.7	Schematic of the wetting apparatus.....	33
3.8	The sample and sample holder: cross sectional view	35
3.9	Schematic of the data acquisition system	37
3.10a	The typical drying rate curve N_v vs. X	40
3.10b	The typical m vs. t curve.....	40

3.11	The determination of X_c on the T_s vs. X curve	43
4.1a	A typical transfer coefficient ratio distribution at $T_\infty^* = 80^\circ\text{C}$	68
4.1b	A typical transfer coefficient ratio distribution at $T_\infty^* = 130^\circ\text{C}$	68
4.2	A typical transfer coefficient ratio distribution at $T_\infty^* = 180^\circ\text{C}$	69
4.3	The critical point curve from the convective drying results	74
5.1	A typical q_{is} vs. t curve from the heat flux meter after insertion in the blackbody cavity opening	78
5.2a	Temperature evolution within the water layer during an evaporation experiment (T_w vs. t for 2 heating elements on)	81
5.2b	Temperature evolution within the water layer during an evaporation experiment (T_w vs. t for 8 heating elements on)	81
5.3a	The overall incident radiative heat flux from evaporation experiments (q_{is} vs. t for 2 and 4 heating elements on)	85
5.3b	The overall incident radiative heat flux from evaporation experiments (q_{is} vs. t for 6 and 8 heating elements on)	85
5.4a	Correlation of the overall incident radiative heat flux (q_{is} vs. t for 2 and 4 heating elements on)	86
5.4b	Correlation of the overall incident radiative heat flux (q_{is} vs. t for 6 and 8 heating elements on)	86

5.5a	The sample surface temperature as a function of the overall incident heat flux from free convection-I.R. drying runs (T_s° vs. q_{is}°).....	96
5.5b	The sample surface temperature as a function of the overall incident heat flux from forced convection I.R. drying runs (T_s° vs. q_{is}°).....	96
5.6a	Characteristic power input curves from the combined convective and I.R. drying runs (P_i vs. t for 2 heating elements on).....	98
5.6b	Characteristic power input curves from the combined convective and I.R. drying runs (P_i vs. t for 8 heating elements on).....	98
5.7a	A typical scaled-up fraction of characteristic power input curves from the combined convective and I.R. drying runs (P_i vs. t for 2 heating elements on).....	99
5.7b	A typical scaled-up fraction of characteristic power input curves from the combined convective and I.R. drying runs (P_i vs. t for 8 heating elements on).....	99
5.8a	The radiative heat transfer rate within the test section as a function of the convective heat transfer coefficient (Q_R° vs. h_{cc}°).....	105
5.8b	The convective heat transfer rate within the test section as a function of the convective heat transfer coefficient (Q_c° vs. h_{cc}°).....	105
5.9a	The convective heat transfer rate within the test section as a function of the power input for 2 heating elements (Q_c° vs. P_i°).....	106

5.9b	The convective heat transfer rate within the test section as a function of the power input for 8 heating elements (\dot{Q}_c vs. \dot{P}_i).....	106
5.10a	Photograph of sample No. X after completion of the experimental schedule: overall view of the surface	115
5.10b	Photograph of sample No. XII after completion of the experimental schedule: overall view of the surface	115
5.11a	Photograph of sample No. X after completion of the experimental schedule: a typical fraction of the surface magnified (X40).....	116
5.11b	Photograph of sample No. XII after completion of the experimental schedule: a typical fraction of the surface magnified (X40).....	116
5.12a	The drying rate as a function of the overall incident heat flux from free convection-I.R. drying runs (N_v vs. q_{is})	119
5.12b	The drying rate as a function of the overall incident heat flux from forced convection I.R. drying runs (N_v vs. q_{is})	119
5.13a	The heat transfer coefficient correction factor as a function of the overall incident heat flux from forced convection I.R. drying runs (θ_h vs. q_{is})	122
5.13b	The mass transfer coefficient correction factor as a function of the overall incident heat flux from forced convection I.R. drying runs (θ_K vs. q_{is})	122
5.14a	Hanna's correction factor as a function of the overall incident heat flux from forced convection I.R. drying runs (H_c vs. q_{is})	130

5.14b	The ratio of experimental mass transfer coefficients from I.R. drying to unaffected mass transfer coefficient from convective drying as a function of the predicted mass transfer coefficient ratio (θ_{Ke} vs. θ_{Kp}).....	130
5.15a	A frequency distribution for $\left(\frac{Nu}{Sh_p} \frac{Sc}{Pr}\right)^*$ from the combined convective and I.R. drying runs.....	132
5.15b	A frequency distribution for $\left(\frac{Nu_{BL}}{Sh_{pBL}} \frac{Sc}{Pr}\right)^*$ from the combined convective and I.R. drying runs.....	132
5.16a	A frequency distribution for $\left(\frac{Nu}{Sh_y} \frac{Sc}{Pr}\right)^*$ from the combined convective and I.R. drying runs.....	133
5.16b	A frequency distribution for $\left(\frac{Nu_{BL}}{Sh_{yBL}} \frac{Sc}{Pr}\right)^*$ from the combined convective and I.R. drying runs.....	133
5.17	The critical point curve from the convective and combined convective-I.R. drying runs	141
5.18	The critical saturation from convective, I.R. and combined convective -I.R. drying runs from various studies.....	142
6.1a	The funicular and pendular drying regimes.....	150

6.1b	The elementary control volume.....	150
6.1c	The control volume grid.....	150
6.2a	The drying curve for run no. co4.....	166
6.2b	The drying rate curve for run no. co4.....	166
6.3	The surface and bottom temperatures for run no. co4.....	167
6.4	The isotherms within the dried sample close to the surface thermocouple for run no. co9.....	171
6.5	The 5.5 mm sample: cross sectional view.....	174
6.6a	The drying curve for run no. co7: test of the drying front position correction.....	177
6.6b	The surface and bottom temperatures for run no. co7: test of the drying front position correction.....	177
6.7a	The drying rate curve for run no. co7: test of the drying front position correction.....	178
6.7b	The drying rate curve for run no. re6: test of the drying front position correction.....	178
6.8a	The drying curve for run no. re6: test of the drying front position correction.....	179
6.8b	The surface and bottom temperatures for run no. re6: test of the drying front position correction.....	179

6.9a	The drying curve for run no. co11: test of the transfer coefficient correction procedure (B.L.T.)	180
6.9b	The surface and bottom temperatures for run no. co11: test of the transfer coefficient correction procedure (B.L.T.)	180
6.10a	The drying rate curve for run no. co11: test of the transfer coefficient correction procedure (B.L.T.).....	181
6.10b	The drying rate curve for run no. re18.....	181
6.11a	The drying curve for run no. re18.....	183
6.11b	The surface and bottom temperatures for run no. re18.....	183
6.12a	The drying curve for run no. co8.....	184
6.12b	The surface and bottom temperatures for run no. co8.....	184
6.13a	The drying rate curve for run no. co8.....	185
6.13b	The drying rate curve for run no. re21	185
6.14a	The drying curve for run no. re21	186
6.14b	The surface and bottom temperatures for run no. re21.....	186
6.15	An evaluation of the experimental surface temperature measurement bias for the combined convective and I.R. drying runs.....	189

6.16a	The drying curve for run no. ir1: test of the drying front position correction.....	192
6.16b	The surface and bottom temperatures for run no. ir1: test of the drying front position correction	192
6.17a	The drying rate curve for run no. ir1: test of the drying front position correction.....	193
6.17b	The drying rate curve for run no. ir4: test of the drying front position correction.....	193
6.18a	The drying curve for run no. ir4: test of the drying front position correction.....	194
6.18b	The surface and bottom temperatures for run no. ir4: test of the drying front position correction	194
6.19a	The drying curve for run no. ir15: test of the transfer coefficient correction procedure (B.L.T.)	196
6.19b	The surface and bottom temperatures for run no. ir15: test of the transfer coefficient correction procedure (B.L.T.)	196
6.20a	The drying rate curve for run no. ir15: test of the transfer coefficient correction procedure (B.L.T.)	197
6.20b	The drying rate curve for run no. ir12	197
6.21a	The drying curve for run no.ir12	199
6.21b	The surface and bottom temperatures for run no. ir12.....	199

6.22a	The drying curve for run no. ir2.....	200
6.22b	The surface and bottom temperatures for run no. ir2.....	200
6.23a	The drying rate curve for run no. ir2.....	201
6.23b	The drying rate curve for run no. i85h.....	201
6.24a	The drying curve for run no. i85h.....	202
6.24b	The surface and bottom temperatures for run no. i85h.....	202
6.25a	The drying curve for run no. i38h: The transition to the boiling point temperature at low radiative heat flux ($q_{is}^* = 7920 \text{ W/m}^2$).....	203
6.25b	The surface and bottom temperatures for run no. i38h: The transition to the boiling point temperature at low radiative heat flux ($q_{is}^* = 7920 \text{ W/m}^2$).....	203
6.26a	The drying rate curve for run no. i38h: The transition to the boiling point temperature at low radiative heat flux ($q_{is}^* = 7920 \text{ W/m}^2$).....	204
6.26b	The drying rate curve for run no. i76h: The transition to the boiling point temperature at high radiative heat flux ($q_{is}^* = 22020 \text{ W/m}^2$)	204
6.27a	The drying curve for run no. i76h: The transition to the boiling point temperature at high radiative heat flux ($q_{is}^* = 22020 \text{ W/m}^2$)	205

6.27b	The surface and bottom temperatures for run no. i76h: The transition to the boiling point temperature at high radiative heat flux ($q_{is}^* = 22020 \text{ W/m}^2$).....	205
A5.1a	Test section: bottom view.....	234
A5.1b	Test section: cross sectional view.....	234
A5.1c	Test section: top view	235
A6.1	The emissivity measurement set-up.....	239
A6.2a	The emissivity of the test section walls: E_t	241
A6.2b	The emissivity of the stainless steel shield: E_{sc}	241
A6.3	The emissivity of the glass beads sample: E_g	243
A7.1	The Nu vs. Re curve: experiments and correlation (A7.2).....	246
A8.1	The heat transfer rates on the vessel side	248

LIST OF TABLES

<u>Table</u>	<u>Title</u>	<u>Page</u>
3.1	Glass beads bed characteristics	31
3.2	Summary of the reproducibility study: N_v^* , t_o , t_c and X_c	45
3.3	Maximum experimental uncertainty for dependent and independent variables	48
4.1	Heat transfer coefficients from the convective drying runs.....	54
4.2a	The transfer coefficient ratios from the convective drying runs.....	62
4.2b	The transfer coefficient ratios from the convective drying runs.....	63
4.3	Sensitivity study of the transfer coefficient ratios from the convective drying runs	70
4.4	Critical moisture content in convection drying.....	72
5.1a	The incident I.R. source and test section walls radiative heat fluxes estimated from the evaporation runs.....	89
5.1b	The incident I.R. source and test section walls radiative heat fluxes estimated from the evaporation runs.....	90
5.2	Evaluation of the sample equivalent hemispherical total emissivity under I.R. heat flux	95

5.3a	The incident I.R. source and test section radiative wall heat fluxes from combined convective and I.R. drying runs.....	103
5.3b	The incident I.R. source and test section radiative wall heat fluxes from combined convective and I.R. drying runs.....	104
5.4a	Heat transfer coefficients from the combined convective and I.R. drying runs.....	111
5.4b	Heat transfer coefficients from the combined convective and I.R. drying runs.....	112
5.5	Comparison of $(K_{yBL})_{varp}$ and h_{cBL} after (combined convective-I.R. drying runs) and before (convective runs): the effect of crust formation on sample No. XII and XIII from convective drying runs	114
5.6	Test on the prediction of the heat transfer coefficient with the boundary layer theory from the combined convective and I.R. drying runs.....	123
5.7	The transfer coefficient ratios from the combined convective and I.R. drying runs (raw data).....	128
5.8	The transfer coefficient ratios from the combined convective and I.R. drying runs (T_s corrected).....	129
5.9	The transfer coefficient ratios from the combined convective and I.R. drying runs and the correction procedures.....	134
5.10a	Critical moisture content from the combined convective and I.R. drying runs.....	139

5.10b	Critical moisture content from the combined convective and I.R. drying runs.....	140
6.1	Measured and simulated surface temperatures for convective drying: evaluation of the experimental bias at the end of drying	172
6.2	Measured and simulated drying times, bottom and surface temperatures at the end of drying with and without drying front correction for convective drying.....	175
6.3	Measured and simulated drying times and bottom temperatures at the end of drying with and without drying front correction for combined convective and I.R. drying.....	191

NOMENCLATURE

<u>Symbol</u>	<u>Meaning</u>	<u>Unit</u>
a_f	External surface of the control volume	m^2
a_{ki}	Interface area between k and i phase	m^2
A_{CO_2}	Mean total absorptivity of CO_2	-
A_g	Mean total absorptivity of the gas layer	-
A_{H_2O}	Mean total absorptivity of H_2O	-
A_s	Sample surface area	m^2
A_t	Overall test section area	m^2
A_w	Pyrex dish evaporation area	m^2
b	Sample height	m
B_h	Energy flux ratio	-
B_K	Driving force used at high mass flux and molar flux ratio	-
c_g	Total molar concentration of the gaseous mixture	mol/m^3
cor	Parameter equal to 1 when the drying front correction is applied (otherwise 0)	-
c_{pa}	Air specific heat	J/kgK
c_{pb}	Glass beads or Pyrex specific heat	J/kgK
c_{pg}	Gaseous mixture specific heat	J/kgK
c_{pv}	Water vapor specific heat	J/kgK
c_{pw}	Water specific heat	J/kgK
d	Particle diameter	m
D	Sample diameter	m
D_{va}	Binary diffusivity of vapor in air	m^2/s
D_ϵ	Effective diffusion coefficient of vapor in the porous matrix	m^2/s
e	distance separating the bottom and upper plate	m
E_a	Total hemispherical emissivity of the aluminium foil	-
E_{cy}	Total hemispherical emissivity of the cylindrical radiative screen	-
E_{CO_2}	Emissivity of carbon dioxide	-
E_{H_2O}	Emissivity of water vapor	-
E_{np}	Total hemispherical emissivity of the 3M Nextel black paint	-
E_s	Total hemispherical emissivity of the sample surface	-
E_{sc}	Total hemispherical emissivity of the planar radiative screen	-

E_t	Total hemispherical emissivity of the test section wall	-
E_w	Total hemispherical emissivity of water	-
E_4	Equivalent total hemispherical emissivity of surface 4 (the I.R. source aperture)	-
f	Diffusion resistance factor	-
F_{ij}	Shape factor	-
h	Overall heat transfer coefficient	W/m ² K
h_c	Forced or free convection heat transfer coefficient	W/m ² K
h_{cBL}	Heat transfer coefficient corrected with the Boundary Layer theory	W/m ² K
h_{cc}	Forced convection heat transfer coefficient predicted from the experimentally obtained correlation for low mass flux (Appendix 7)	W/m ² K
h_{cp}	Forced convection heat transfer coefficient predicted from h_{cc} and the boundary layer theory (B.L.T.)	W/m ² K
h_k	k phase enthalpy	J/kg
h_v	Vapor enthalpy	J/kg
H_c	Hanna's correction factor	-
\bar{J}	Flux term	W/m ²
k	Apparent thermal conductivity of wet bed	W/mK
k_a	Thermal conductivity of dry air	W/mK
k_d	Thermal conductivity of dry glass beads bed	W/mK
k_{dif}	Thermal conductivity due to the transfer of latent heat by vapor movement under the influence of a temperature gradient	W/mK
k_{dw}	Thermal conductivity of the solid and liquid phase	W/mK
k_g	Thermal conductivity of the gaseous phase	W/mK
k_v	Thermal conductivity of vapor	W/mK
k_T	Trymer 9501 thermal conductivity	W/mK
K_y	Mass transfer coefficient based on mole fraction	mol/m ² s
K_{yBL}	Mass transfer coefficient based on mole fraction corrected with the B.L. theory	mol/m ² s
K_p	Mass transfer coefficient based on density	m/s
K_{pBL}	Mass transfer coefficient based on density corrected with the Boundary Layer theory	m/s
Le	Lewis number, Sc/Pr	-
L_e	Mean beam length	m

L_j	Distance on the sample or sample holder	m
m	Sample and sample holder mass	kg
m_b	Glass beads bed or pyrex dish mass	kg
m_i	i^{th} recorded mass value	kg
$m_{k,i}$	k phase mass flux at the control volume boundary	kg/m ² s
m_w	Total amount of water within the sample or pyrex dish at time t	kg
M	Average molecular weight of water	kg/mol
M_w	Molecular weight of water	kg/mol
n	Number of phases or degree of freedom	-
N	Total number of recorded data m	-
Nu	Nusselt number	-
N_v	Drying rate	kg/m ² s
p_{CO_2}	Partial pressure of CO ₂	N/m ²
p_{H_2O}	Partial pressure of H ₂ O	N/m ²
p_v	Partial vapor pressure	N/m ²
P_i	Power input	W
Pr	Prandtl number,	-
P_∞	Test section pressure	N/m ²
q_{ab}	Net absorbed heat flux on the surface in combined convective and I.R. drying	W/m ²
q_{ac}	Accumulation heat flux	W/m ²
q_c	Convective heat flux	W/m ²
q_{is}	Overall incident radiative heat flux on the sample surface	W/m ²
q_{its}	Incident heat flux from test section wall on the sample or water	W/m ²
\bar{q}_k	Conduction heat flux for the k phase	W/m ²
q_{sir}	Incident heat flux from I.R. source on the sample or water	W/m ²
q_{ts}	Net radiative flux between the test section walls and the sample	W/m ²
Q	Rate of heat transfer at the sample surface	W
Q_{ac}	Rate of heat accumulation inside the sample	W
Q_C	Rate of convective heat transfer from surface 2 and 3	W
Q_j	Rate of heat input to surface j or output of surface j	W
Q_R	Rate of radiative heat transfer from surface 2 and 3	W
Q_v	Rate of energy transport by the water vapor at the sample surface	W
r	Correlation coefficient	-

r_i	Radius	m
r_v	Reproducibility parameter	-
R	Perfect gas constant	J/molK
R_c	Convective resistance coefficient	m/s
R_{D1}	Surface diffusion resistance coefficient	m ² s/kg
R_{D2}	Diffusion resistance coefficient through the dried layer	m ² s/kg
Re	Reynolds number	-
S	Average or local bed saturation	-
Sc	Schmidt number	-
S_c	Average bed saturation at critical point	-
Sh	Sherwood number	-
S_m	Smoothing spline function	kg
S_s	Surface saturation	-
S_{ir}	Irreducible saturation	-
t	Student's t test variable	-
t	Time	s
t_c	Critical time	s
t_{av}	Time in the middle of the P.C.D.R.P.	s
t_o	Overall drying time	s
t_1	Time at the start of the P.C.D.R.P.	s
t_2	Time at the end of the P.C.D.R.P.	s
T_{amb}	Ambiant or room temperature	K
T_b	Sample bottom temperature	K
T_d	Air dew point temperature	K
T_f	Drying front temperature	K
T_h	Heat flux transducer temperature	K
T_{pi}	Test section bottom plate temperatures	K
T_s	Sample surface temperature	K
T_{sir}	Heating elements temperature	K
T_t	Average test section wall temperature	K
T_{ti}	Local test section wall temperatures	K
T_w	Water or evaporation temperature	K
T_{win}	Initial water temperature for evaporation experiments	K
T_2	Average temperature of surface 2 (defined in Appendix 5)	K
T_3	Average temperature of surface 3 (defined in Appendix 5)	K

T_4	Equivalent radiative temperature of surface 4 (defined in Appendix 5)	K
T_∞	Test section airflow temperature	K
$T_{\infty i}$	Local test section airflow temperatures	K
v	Overall volume of the control volume	m^3
v_∞	Test section air velocity	m/s
V_{cy}	Equivalent cylinder bed volume	m^3
\bar{V}_{ki}	ki interface velocity	m/s
\bar{V}_f	Control volume speed	m/s
V_i	Parameter to be tested for reproducibility	-
V_t	Overall sample volume	m^3
V_v	Volume fraction of water vapor	m^3/m^3
y_{vs}	Water vapor mole fraction at the sample surface	-
y_{vf}	Water vapor mole fraction at the front	-
$y_{v\infty}$	Water vapor mole fraction within the test section flow	-
x_{cv}	Control volume boundary position with respect to the surface	m
x'_f	Corrected drying front position	kg/kg
x_f	Drying front position from the surface	kg/kg
X	Moisture content (dry basis)	kg/kg
X_c	Critical moisture content (dry basis)	kg/kg
X_{cs}	Critical moisture content at the surface (dry basis)	kg/kg
X_{in}	Initial moisture content (dry basis)	kg/kg
X_w	Uniform moisture content in the wet zone(dry basis)	kg/kg

Greek Symbols

α	Angle	$^\circ$
α_k	Volume fraction of the k phase	m^3/m^3
β_k	Part of the surface a_f occupied by k phase at the i^{th} boundary	m^2/m^2
δ_{kj}	Kronecker delta	-
δx	Width of the control volume	m
Δh_i	Heat transfer coefficient difference	W/m^2K
ΔH_v	Heat of evaporation of water	J/kg
Δt	Time step	s
ΔT_i	Temperature difference	K
Δx_i	Control volume node spacing or distance	m

$\Delta\rho$	Density difference	kg/m ³
ε	Glass beads bed porosity	m ³ /m ³
θ_h	Correction factor for the heat transfer coefficient	-
θ_K	Correction factor for the mass transfer coefficient	-
κ	Permeability	m ²
λ_{\max}	Wavelength at which the emissive power is maximum for a given temperature	m
μ_a	Dynamic viscosity of air	kg/ms
μ_g	Dynamic viscosity of the gaseous mixture	kg/ms
μ_v	Dynamic viscosity of vapor	kg/ms
ρ_b	Bulk glass density	kg/m ³
ρ_d	Glass beads bed density	kg/m ³
ρ_g	Gaseous mixture density	kg/m ³
ρ_{vs}	Water vapor density at the sample surface	kg/m ³
$\rho_{v\infty}$	Water vapor density within the test section flow	kg/m ³
φ_k	Volumic source in the k phase of Ψ_k	Ψ_k/m^3s
ϕ_h	Rate factor for the heat transfer coefficient	W/m ² K ⁴
ϕ_K	Rate factor for the mass transfer coefficient	W/m ² K ⁴
σ	Stefan-Boltzman constant	W/m ² K ⁴
σ_m	Smoothing parameter	-
ω_i	Weight of the data	g
ω_v	Water vapor mass fraction	-
Ψ_k	k phase function	-

Subscripts

a	Air
ac	Accumulation
amb	Ambiant
av	Average
b	Beads, bottom or glass
BL	Corrected with the Boundary Layer Theory
c	Critical or convection
cy	Cylinder
co	Cone

d	Dew point or dry
e	Experiment
f	Final, film or at front location
g	Air-vapor mixture
h	Heat transfer coefficient
i	thermocouple location; input
in	Initial condition
ir	Irreducible
is	Incident on the sample surface
its	Incident on the sample surface from the test section walls
k	k phase
K	Mass transfer coefficient
m	Mass; smoothing
np	3M Nextel paint characteristic
o	Overall
p	Evaluated at constant pressure; plate or predicted
v	Vapor
s	Surface
sc	Screen
sir	From or characteristic of the infrared source
t	Test section
ts	Exchanged between test section and the sample
varp	Quantity evaluated taking into account variation in density
w	Water, evaporation or wet zone
y	Mole fraction driving force
1	Relative to surface 1
2	Relative to surface 2 or surface average
2D	Evaluated with Flux2D
3	Relative to surface 3 or volume average
4	Relative to surface 4
ρ	Concentration driving force
∞	Test section flow parameter

Superscripts

1	Evaluated at $t+\Delta t$
---	---------------------------

0	Evaluated at t
•	Average during the Pseudo Constant Drying Rate Period (P.C.D.R.P.)
'	Corrected front position
—	Vector
=	Tensor

CHAPTER I - INTRODUCTION

1.1 BACKGROUND

Conventional convective drying processes being energy intensive and relatively slow, other techniques are being more intensively studied to minimize or offset these limitations. One may cite the following methods for drying of web-like or panel shaped materials:

- a) Impingement drying;
- b) Through drying (for permeable materials);
- c) Superheated steam drying;
- d) Radio-frequency drying;
- e) Infrared (I.R.) drying.

Among these, the use of I.R. heating has significant advantages for industrial drying applications (Orfeuil, 1987):

- a) Direct transfer of heat to the product;
- b) Low thermal inertia of the I.R. heat source;
- c) High heat flux intensity (up to 60 kW/m^2);
- d) Choice of the emitter wavelength to match the product absorption characteristics;
- e) Accurate local application of the heat flux only where needed;
- f) Heating homogeneity due to radiation penetration (small thickness);
- g) Ease of combination with other heating modes (convection, conduction).

With electrical I.R. heat sources, these qualities translate into practical applications with the following advantages:

- a) Improved productivity;
- b) Reduction in overall furnace dimension;
- c) Improvement in product quality;
- d) Low investment cost;
- e) Flexible and fast process control;
- f) Energy efficient process;
- g) Simpler fabrication;
- h) Minimum maintenance requirements;
- i) No contamination of the product or pollution by heat source.

The following examples of I.R. heating applications in dehydration or partial drying have been presented by Orfeuil (1987):

- a) Paper, cardboard and textiles;
- b) Insulating boards, acoustic panels and gypsum board;
- c) Ceramics;
- d) Casting moulds and cores;
- e) Water paints and inks;
- f) Tobacco leaves;
- g) Plastic grains;
- h) Pharmaceutical products;
- i) Fish and vegetable products.

Despite their numerous applications, the design of a combined convective-I.R. drying oven still relies largely on experiments very often obtained with free convection-I.R. heating (no forced flow present) or with a full scale oven (Dostie et al., 1988). Such procedures do not allow one to account fully for the effect of coupling convection to I.R. heating or to study the specificity of this process. Thus there is need for the development of reliable procedures and

experimental facilities that will produce data of sufficient accuracy to obtain the necessary information (drying curves and temperature evolution) of the combined radiation/convection process at high gas temperatures and radiative heat fluxes.

To date the use of drying models (Puiggali, 1987; Bories, 1988) has been mainly confined to evaluate the effects of key heat (accumulation, convection, conduction) and mass transfer (capillarity, diffusion, gravity, sorption, convection) phenomena in relation to the material type (non-hygroscopic capillary porous materials, hygroscopic capillary porous materials, colloidal medium) and heating modes (convection, conduction, radiation or volumetric heating). Drying models have typically been attempted for a limited number of drying conditions. Most drying models necessitate a detailed knowledge of transport properties as well as intensive use of computer time. The following quotation from Franzen et al. (1987) underscores the limitations of the present drying models and model testing:

"The present theoretical development is ahead of the experimental testing of theories". "No model has been proven to be generally applicable. Ideally, a model should have a broad range of applications".

A model recently developed by Dostie (1991) is believed to be applicable over a wide range of drying conditions but remains to be tested extensively.

1.2 OBJECTIVES OF THE PRESENT STUDY

The objectives of this study were:

- a) To build a reliable experimental facility to study the high temperature combined convective-I.R. drying process;
- b) To evaluate the effect of I.R. heating on the convective heat and mass transfer coefficients;

- c) To determine the influence of combined convective and I.R. drying parameters on the critical moisture content of a model material;
- d) To test the applicability of a drying front model for the case of convective as well as combined convective-I.R. drying of a capillary porous medium (soda lime glass beads; 90-105 μm diameter range).

1.3 OUTLINE OF THE THESIS

Chapter II reviews works that have appeared in the published literature on experimental I.R. drying pointing out key results already obtained. Comments on one of the most widely accepted drying model and a summary of the arguments which favored the choice of a drying front model are also presented.

Chapter III describes the experimental apparatus designed and built, the procedures followed to carry out the experimental phase as well as testing of the reproducibility and uncertainty in the experimental results obtained.

Chapter IV presents an analysis of the convective drying experiments with respect to the heat and mass transfer analogy as expressed by the values taken by heat and mass transfer coefficient ratios, the high mass transfer rate effect on the transfer coefficients and the critical moisture content.

Chapter V presents a discussion of the combined convective-I.R. drying experiments with respect to the heat and mass transfer analogy, the high mass transfer rates effect on the transfer coefficients and the critical moisture content.

Chapter VI gives a brief description of the model used to simulate the I.R. drying process. The drying front model and the numerical solution technique are presented in detail. Finally, model predictions are compared with experimental drying data and discussed.

Chapter VII, includes the key conclusions of this work, contributions to prior knowledge and recommendations for future work.

CHAPTER II - LITERATURE REVIEW

2.1 PRIOR EXPERIMENTAL STUDIES ON I.R. DRYING

Yagi et al. (1957) presented one of the most extensive experimental study of combined convective-I.R. (infrared lamps) drying of capillary porous and colloidal media (river and standard sand, iron beads, wood powder and porcelain clay, $d = 9-740 \mu\text{m}$, $b = 7-61 \text{ mm}$, $T_{\infty}^* \sim 8-33 \text{ }^{\circ}\text{C}$, $v_{\infty}^* \sim 1.1-1.3 \text{ m/s}$, $q_{iS}^* = 5110-10450 \text{ W/m}^2$). Here d is the particle diameter, b the bed thickness, T_{∞}^* the flow temperature, v_{∞}^* the flow velocity and q_{iS}^* the overall incident radiative heat flux.

The following conclusions can be drawn from their research:

- a) The critical moisture content X_c (kg/kg dry basis) is constant (thus independent of drying parameters) as long as $d > 100 \mu\text{m}$. When $d < 100 \mu\text{m}$, X_c increases as d decreases (Figure 5.18). X_c is independent of q_{iS}^* ;
- b) The drying rate N_v^* during the constant drying rate period appears, on the average, to decrease with a decrease in d which might be linked to variation in emissivity (Shimizu et al., 1990). A significant constant drying rate period was reported ($q_{iS}^* = 10450 \text{ W/m}^2$); however, as d is decreased the constant drying rate period shortens. N_v^* increased as q_{iS}^* increased;
- c) The average evaporation temperature during the constant rate period T_w^* increases as q_{iS}^* is increased and is virtually independent of the material thickness. For the porcelain clay sample (colloidal medium), T_w^* was found to equal the boiling point temperature;
- d) The temperature evolution with time shows that the surface temperature (T_s) level-off rapidly after the beginning of I.R application and increases slowly up to the critical moisture content when it rises suddenly. Then, it is observed that the temperature reached, at a specific depth, just before the arrival of the front increases with depth up to a point (located between 10 mm and 20 mm) where it does not

change with increasing penetration of the front within the material; at this point the temperature distribution within the wet zone stays quite uniform while it varies almost linearly in the dried zone. The temperature gradients within the material prior to the drying front penetration are quite significant and diminish as X approaches X_c ;

- e) The stabilized (for depth higher than 10 to 20 mm) drying front temperature T_f increases as q_{is} is increased.

The book by Ginzburg (1969) summarized the early Russian works in the field of I.R. drying and baking of mainly food products. Numerous data on the radiative properties (reflectivity, absorptivity and transmissivity) of various products are presented as well as I.R. (infrared lamp, tubular quartz radiators, resistance elements, ceramic heaters) drying data such as:

- a) Steady and transient temperature distributions for dough-bread, macaroni dough, wheat grain layers, sunflower seeds (thick layers), rape and onions seeds, sesame kernel, tea, orange, lemon, meat and fish;
- b) I.R. drying curves for malt, wheat grain layers, sunflower seeds (thick layers), rape and onion seeds, sesame kernels, apples, carrots, green beans, turnips, green peas, cabbage, potatoes, macaroni, calcium tartrate, meat and fish;
- c) Drying rate curves for sand, macaroni dough, malt, sunflower seeds (thick layers) and bread;
- d) Moisture content distributions under I.R. drying for sand and clay.

These data give a qualitatively good picture of the process but are, in most cases, only weakly supported by accurate specification of all experimental conditions and procedures. Furthermore, no extensive and detailed data are provided to study the interaction between convection and I.R. heating as applied to the drying process.

Interested in the internal transfer phenomena that occur during the drying process, Min and Emmons (1972) presented results from free convection-I.R. (quartz infrared lamp) drying experiments (alumina powder, $b = 54$ mm, $T_{amb} = 20$ °C, $q_{is}^* = 6270$ W/m²) where the temperature, moisture and pressure distribution measurements have shown that:

- a) The temperature vs. time curves essentially confirm the observations that were made by Yagi et al. (1957);
- b) The moisture measurements made from an evaluation of a.c. conductance between two electrodes inserted in the test material show that the front arrival creates (a) a sharp drop in conductance coinciding with the break in the corresponding temperature vs. time curve (b) the moisture density increases due to condensation (evaporation-condensation phenomenon) prior to the arrival of the front;
- c) The pressure peak location corresponds to the front location and its maximal recorded intensity was 70 Pa above atmospheric.

Seki et al. (1977) provided data on free convection-I.R. (infrared lamp) drying of thick beds (glass beads, $d = 360-1500$ μ m, $b = 100$ mm, $T_{\infty}^* = T_{amb}$, $q_{is}^* = 760-8820$ W/m²). They observed that:

- a) For $q_{is}^* \geq 4640$ W/m², T_f reaches the boiling point and stays there up to the end of drying. For $q_{is}^* < 4640$ W/m², T_f increases with increase in the drying front progression;
- b) For $d = 360$ μ m, a constant drying rate period exists during which T_s increases slowly. However as q_{is}^* is increased, the constant drying rate period duration shortens and the rate of drift of T_s as a function of time during the constant drying rate period increases. For $d = 970$ μ m, no constant drying rate period can be observed whatever the value of q_{is}^* ;

- c) X_c always increases with increase in q_{is}^* (constant d , Figure 5.18) but its sensitivity to q_{is}^* is higher for small d ($d = 360 \mu\text{m}$). X_c values are much higher than corresponding values for thinner beds;
- d) The saturation distribution curves ($d = 360 \mu\text{m}$), evaluated by slicing the bed at the critical point, displays a rather steep transition between the lower part of the bed ($S \sim 1$) and the upper part of the bed (surface saturation ~ 0.1) for $q_{is}^* \geq 4640 \text{ W/m}^2$. Moisture distributions of bed constituted of different diameter glass beads ($d = 360, 970$ or $1500 \mu\text{m}$) show that, for the same q_{is}^* (8820 W/m^2) capillary forces drain more water from the lower bed zone toward the surface as smaller particles are used (at the critical point). Thus, steeper moisture content transitions are found as d is increased. Beyond the critical point, the evolution with time of the moisture content distribution evolution with time shows a smoother transition between the front ($S_f = 0$) and bottom bed saturations ($d = 360 \mu\text{m}$, $q_{is}^* = 760\text{-}8820 \text{ W/m}^2$).

Nishimura et al. (1983) provided data on the forced convection-I.R. (infrared lamp) drying of thin layers (PVA aqueous solution, $b = 100\text{-}400 \mu\text{m}$, $T_\infty^* = 20 \text{ }^\circ\text{C}$, $v_\infty^* \sim 2.5 \text{ m/s}$, absolute humidity = $0.011 \text{ kg H}_2\text{O/kg air}$, $q_{is}^* = 4.65 \text{ kW/m}^2$). Parameters varied were the initial water content and initial layer thickness b_{in} . Their experiments showed that:

- a) An increase of b_{in} increases the level of T_w^* and diminishes the drying rate. An increase of the initial water content lowers T_w^* slightly. T_w^* has a tendency to fall slightly at the end of the surface evaporation controlling period;
- b) The final dried film temperature increases with increase of the dried film thickness (which increases as the initial water content is decreased or the initial thickness increased);
- c) During the surface evaporation controlling period, the drying rate decreases with decrease in water content and the drying rate curves do not display any constant drying rate period. The maximal drying

rate increases as b_{in} increases while it is not affected by variations in initial water content;

- d) The critical water content increases with a decrease in the initial water content.

Hasatani et al. (1983) studied the forced convection-I.R. (infrared lamp; radiation temperature $T_{sir} \sim 2177$ °C) drying of thick layers of wet silica sand, a slurry of activated sludge and a water suspension of graphite particles ($d = 5$ μm , $b = 20$ mm, $T_{\infty}^* = 30\text{-}80$ °C, $v_{\infty}^* \sim 1.1$ m/s, absolute humidity = 0.006-0.012 kg H₂O/kg air, $q_{is}^* = 290\text{-}1400$ W/m²). Parameters varied were the suspension concentration (kg/m³), the material and q_{is}^* :

- a) A constant drying rate period was reported to exist for all three materials in the range of q_{is}^* studied;
- b) For the graphite suspension, during the constant rate period, the concentration (0.0 to 3.44 kg/m³) had no effect on the drying rate. During the preheating period, the drying rate is slightly decreased as the concentration is decreased;
- c) For the silica sand layer, the drying rate during the constant drying rate period goes up nonlinearly as q_{is}^* and T_{∞}^* increase.

With the same experimental equipment, Hasatani et al. (1988) compared various materials (Yallourn coal, silica sand and A2-brick) with same d dried under similar conditions ($d = 320$ μm , $b = 20$ mm, $T_{\infty}^* = 27\text{-}72$ °C, $v_{\infty}^* \sim 0.5$ m/s, absolute humidity = 0.005-0.007 kg H₂O/kg air, $q_{is}^* = 0\text{-}1080$ W/m²):

- a) The drying rate during the falling rate period is almost unchanged (as compared to the one observed with convection) by the addition of radiation ($q_{is}^* = 662$ W/m²) for silica sand and brick. However, it is enhanced for the case of coal;
- b) Temperature distributions were similar to the ones presented by Yagi et al. (1957) except for the fact that no temperature gradients were

reported for the case of a silica sand layer during the preheating and constant drying rate period ($q_{is}^* = 662 \text{ W/m}^2$).

Dostie et al. (1988) presented drying curves and drying times for convective and combined convective-I.R. drying (ceramic panel with corrugated heating strips; $T_{sir} = 815 \text{ }^\circ\text{C}$) of sheathing panels made of wood products and acoustic tiles containing mineral materials and cellulose. The experiments were carried out in a pilot dryer where air flow was either perpendicular or parallel to the panel ($b = 12.7\text{-}15.9 \text{ mm}$, $T_\infty^* = 160\text{-}180 \text{ }^\circ\text{C}$, $q_{is}^* = 14.0\text{-}16.1 \text{ kW/m}^2$). The key results of their experiments are:

- a) The drying time can be reduced by a factor two with intermittent I.R. heating as compared to convective heating alone. Infrared drying times are 25 % less than the best drying time achieved by convection only in the pilot oven;
- b) The use of intermittent I.R. heating allows control of the product surface temperature. This is in agreement with the many experimental results presented by Ginzburg (1969).

Shimizu et al. (1990) studied the effects of q_{is}^* from far infrared (FIR; $\sim 2 \leq \lambda \leq 12 \text{ } \mu\text{m}$; mullite cylinder) and near infrared radiative heaters (NIR; $\sim 1.5 \leq \lambda \leq 5 \text{ } \mu\text{m}$; quartz cylinder) as well as the effects of the dry material surface emissivity (E_s) and d on N_v^* and T_w^* in the constant drying rate period of free convection-I.R. drying (alumina, silver and stainless steel powders, $d = 38\text{-}250 \text{ } \mu\text{m}$, $b = 14.5 \text{ mm}$, $T_\infty^* \sim 8\text{-}33 \text{ }^\circ\text{C}$, $v_\infty^* \sim 1.1\text{-}1.3 \text{ m/s}$, $q_{is}^* = 1070\text{-}5890 \text{ W/m}^2$). They found that:

- a) N_v^* increases linearly with q_{is}^* (FIR);
- b) N_v^* increases when E_s increases (FIR); this increase is higher at higher q_{is}^* . However, the N_v^* increase is not proportional to the E_s increase probably as a result of the water being at the surface level. T_w^* behaves similar to N_v^* ;

- c) N_v^* increases with particle size (in agreement with results of Yagi et al.(1957)) and this increase is higher at high q_{is}^* (FIR);
- d) For beds of alumina and silver particle, it was observed that N_v^* is higher, for same q_{is}^* , when radiation comes from an FIR heater rather than from an NIR heater as a result of a lower absorptivity for the wavelength range of the NIR heater.

Recently, Navarri (1990, 1991) summarized preliminary results on the forced convection-I.R. drying of a capillary porous medium. The results (Navarri, 1990) concern the case of a quarry sand layer dried with an FIR ($T_{sir} \sim 827$ °C) heater ($d = 250-400$ μm , $b = 7$ mm, $T_{\infty}^* \sim 30-90$ °C, $v_{\infty}^* \sim 2.2$ m/s, $q_{is}^* = 10640$ W/m²). Three results were reported for T_{∞}^* equal to 30 °C, 50 °C and 90 °C from which it can be observed that:

- a) The critical moisture content X_c (range $\sim 0.047-0.059$) is almost independent of (variations in the order of ± 20 % corresponds probably to the reproducibility of such a measurement) T_{∞}^* variations;
- b) The constant drying rate period (on the drying rate curve) shortens as T_{∞}^* is increased; however, strictly speaking, no "plateau" was observed; as expected N_v^* increases as T_{∞}^* is increased;
- c) T_w^* (range $\sim 65-68$ °C) is not significantly affected by increase in T_{∞}^* .

Other results (Navarri, 1991) were obtained with sea sand dried using convection and an NIR ($T_{sir} \sim 1927$ °C) heater ($d = 200-250$ μm , $b = 5$ mm, $T_{\infty}^* \sim 20-28$ °C, $v_{\infty}^* \sim 2.1-6.0$ m/s, relative humidity = 30 to 50 %, $q_{is}^* = 10.0-18.5$ kW/m²). Seven results were reported in terms of the drying rate curves which show that:

- a) The critical moisture content X_c (range $\sim 0.036-0.050$) is almost constant as q_{is}^* is increased ($q_{is}^* = 10.0, 13.0, 15.0$ and

18.5 kW/m²) and is close to a value of 0.04 reported for convective drying at low temperature ($T_{\infty}^* \sim 30$ °C);

- b) The constant drying rate period (on the drying rate curve) seems to shorten as q_{is}^* is increased; the "plateau" is more pronounced as compared to the one from previous results with higher T_{∞}^* (Navarri, 1990). As expected N_v^* increases almost proportionally with q_{is}^* ;
- c) T_w^* increases as q_{is}^* is increased and is the highest when free convection is used;
- d) The analogy between the transfer of heat and mass expressed in terms of the convective heat and mass transfer coefficients ratios (Bird et al., 1960) has been partially validated since the convective heat transfer coefficient was assumed to be correctly evaluated from a correlation developed for convective conditions for which there is no evaporation or incident radiative heat flux. Furthermore, the film theory was implicitly assumed to be applicable to account for the high mass transfer rate effect on the mass transfer coefficient for the case of combined convective-I.R. drying.

In summary, prior experimental results clearly show that:

- a) No detailed drying data have been presented at the high temperature levels characteristic of many industrial processes (Dostie et al., 1988);
- b) The behavior of the convective heat and mass transfer coefficients during combined high temperature convective-I.R. drying has not been studied in depth.

2.2 MODELLING OF DRYING

Key references pertinent to modelling of drying have recently been discussed extensively by Chen (1986), Chiang (1987), Franzen et al. (1987), Moyne (1987), Perré (1987) and Bories (1988), to name a few. Furthermore, additional information can be found in the books by Krischer (1956), Luikov (1966) and

Keey (1972, 1978). So a brief review of only the most significant theoretical developments is given here.

Historically, the drying models can be grouped according to the internal moisture transport phenomena, viz.

- a) Liquid movement due to capillary forces;
- b) Vapor diffusion due to a partial pressure gradient (molecular diffusion) or a thermal gradient;
- c) Vapor effusion (Knudsen flow);
- d) Sorbed vapor diffusion;
- e) Liquid or vapor flow induced by a total pressure gradient;
- f) Liquid movement due to gravity.

Earlier attempts to model the drying process assumed a single dominant mechanism for moisture transfer following traditional chemical engineering approach to modelling by confining attention only to the rate-controlling (or the slowest) process when several processes occur concurrently.

The first theory put forward to explain experimental drying rates and moisture distributions was the liquid diffusion theory (Lewis, 1921; Sherwood, 1929) where the influence of heat transfer was neglected. The main mechanism of moisture transfer was postulated to be liquid water diffusion through the porous skeleton. Fick's law was used to write the moisture transfer equation, either with a constant diffusion coefficient or with a variable coefficient as a function of the moisture content. The liquid diffusion theory was applied with some success to the cases of wood in the hygroscopic regime and clay (Sherwood and Comings, 1933).

In the thirties questions (Comings and Sherwood, 1934; Sherwood, 1937) were raised about the validity of the liquid diffusion theory. It was pointed out that unrealistic moisture distribution was predicted for materials such as sand (Ceaglske and Hougen, 1937). On the other hand, the capillary flow theory,

developed following major contributions by soil scientists (e.g. Buckingham, 1907; Gardner; 1920) provided a significant improvement in predicting adequately these distributions during the constant drying rate period (Ceaglske and Hougen, 1937).

None of these theories is fully satisfactory for all materials (Perré, 1987). It was then necessary to account for additional moisture transfer mechanisms and the coupling with heat transfer within the material. Significant contributions to this development were made by Philip and De Vries (1957), Krischer (1963) and Luikov (1966). The porous medium being assumed equivalent to a continuum and in local thermodynamic equilibrium, the energy and mass conservation equations presented contains gradients of key driving forces: volumetric moisture content and temperature. Luikov (1966) added to these two equations the gaseous phase conservation equation which incorporates the contribution of the total pressure gradient (also included in the mass conservation equations).

The resulting system of 3 coupled non-linear differential equations was solved numerically (finite differences or finite elements) by many researchers and their results were found in qualitative agreement with earlier experimental observations (Harmathy, 1969; Berger and Pei, 1973; Huang, 1979, Eckert and Faghri, 1980; Dinulescu and Eckert, 1980). Meanwhile, the original set of equations was rationally founded by Whitaker (1977) using an approach in which the macroscopic balance equations are obtained by averaging, balance and transfer microscopic equations, over a representative volume (Bories, 1988). Detailed reviews of this most widely accepted model today have been presented by Perré (1987), Bories (1988), Illic and Turner (1989), Rogers and Kaviany (1991) and Kaviany (1991). It accounts, in its most general form, for all important moisture transport mechanisms already mentioned.

It is mainly since the beginning of the eighties that a systematic quantitative comparison between this model prediction and experimental results has been undertaken. In general, relatively good quantitative agreement has been found under several drying conditions e.g. convective or conduction drying of:

- a) Sand and sandstone (Crausse, 1983; Wei, 1984; Hadley; 1986);
- b) Concrete (Dayan and Glueckler, 1982; Moyne, 1987);
- c) Wood (Schajer et al., 1984; Plumb et al., 1985; Michel et al., 1987);
- d) Porous ceramic (Schajer et al., 1984);
- e) Tobacco sheet (Kobari et al., 1985);
- f) Wool bobbin, brick and corn kernel (Chen, 1986).

Despite these successful applications, major drawbacks still preclude wide engineering use of such a model. Indeed, too many internal transport heat and mass transfer coefficient have to be independently evaluated (Crausse, 1983) and in most cases the computing time to obtain a solution to the linearized system of equations is still significantly high (Rogers and Kaviany, 1991).

For many materials internal temperatures alone can be used as an accurate index for their potential damage (Ginzburg, 1969; Dostie et al., 1988). Hence, from a practical point of view, it is often of interest to predict the effect on the drying curve and the temperature evolution of combined convective-I.R. drying parameters such as:

- a) The external flow temperature, humidity and velocity, and;
- b) The incident overall radiative heat flux.

A model with a minimum number of parameters characterizing the internal heat and mass transfer would possibly allow the use of the information obtained from a limited drying experimental study in order to calibrate some of these parameters (Dostie, 1991). It is not in the objectives of this study to measure the moisture content and pressure distributions within the material thus it will not be quantitatively possible to test the prediction of these distributions as influenced by the process parameters (b , T_{∞}^* , v_{∞}^* , T_d^* , q_{is}^*).

The following well known experimental observations favor the use of a drying front model to perform the above mentioned goals:

- a) The drying rate during the constant drying rate period is close to the drying rate observable for free liquid surface evaporation and depends mainly on the external drying conditions (Keey, 1972). Thus the drying rate prediction during that period should be relatively easy to realize knowing the surface heat and mass transfer coefficients, the surface emissivity, the overall incident radiative heat flux and the thermal transport characteristics of the material;
- b) As the critical moisture content sensitivity to drying process parameters changes appears to be low, it should constitute an adequate determination of the falling rate period starting point;
- c) Numerous experimental determinations (Ceaglske and Hougen, 1937; Nissan et al., 1959; Peck et al., 1977, Chiang 1987) of moisture distributions have demonstrated beyond doubt the existence of a drying receding front within various materials (sand, wool, brick, apple) during most of the falling rate period. Furthermore, it has often been observed that a significant temperature rise occurs simultaneously as the drying front location coincides with the position of the thermocouple; the "sharpness" of the moisture transition between the dried and wet zone is, in general, higher for a capillary non-hygroscopic porous medium;
- d) The drying front recession seems to be the key factor for the drying rate fall and results in dominant heat and mass transfer resistances between the internal evaporating zone and the external flow.

The drying front model (Dostie, 1991) presented in chapter VII represents an extended version of one of the simplified models (receding plane model) discussed by Keey (1978). Chapter VII examines the drying models that have been previously used to simulate the free (no forced flow present) or forced convection-I.R. drying process.

CHAPTER III - EXPERIMENTAL APPARATUS AND PROCEDURES

3.1 INTRODUCTION

This chapter describes the experimental set-up (oven, test section, glass beads samples and sample holder), the operating parameters, the data acquisition procedure as well as experimental reproducibility and uncertainty in measured data.

3.2 EXPERIMENTAL APPARATUS

The experimental apparatus designed and built for this research was proven to produce reliable data and allow control of the following primary variables:

- a) Air temperature T_{∞} , velocity v_{∞} , pressure P_{∞} and air dew point temperature T_d ;
- b) Infrared heat source temperature T_{sir} , power input P_i .

The air dew point temperature could be stabilized close to ambient values (through air renewal) during an experiment but it was not controlled to a pre-selected value (range: -10.6 °C to +17.9 °C). The following variables were also recorded in each experiment:

- c) Mass m (sample and sample holder) and internal temperatures (surface T_s and bottom T_b);
- d) Test section wall temperatures T_{fi} ($i = 1,6$);
- e) Test section air temperatures $T_{\infty i}$ ($i = 1,5$);
- f) Test section bottom plate temperatures T_{pi} ($i = 1,4$).

3.2.1 OVEN TEST SECTION

A convective batch oven (Figure 3.1) was modified to include a thermally insulated test section, a bottom cavity as well as an I.R. heat source located in the upper cavity. A front door (see photograph in Figure 3.2) facilitated access to these various parts as well as the sample positioning at the beginning of each experiment. A detailed summary of the experimental accessories and assembly, their relevant technical and geometrical specifications as well as equipment manufacturers is given in Appendix 1.

The oven (Figure 3.1) consisted of a heating section with resistive elements, a squirrel cage fan driven by a D C motor and ducts of rectangular cross section. Figure 3.3 (a,b,c) is a scaled down drawing of the test section showing the spatial locations of all the measuring points¹. The test section was made of steel walls (610 X 500 X 100 mm) covered with a low emissivity ($E_t = 0.28$) aluminized silicone paint (FEROX -1203). A removable front panel (610 X 100 mm) was made for easy access to instrumentation and for visual inspection when introducing test samples. At the entrance of the test section a pressure equalization chamber (55 X 500 X 100 mm) followed by an assembly of perforated grids and meshes (flow mixer) reduced the inlet flow turbulence scale and improved the velocity profile uniformity. A top wall aperture (160 X 143 mm) located downstream allowed I.R. radiation to reach the sample. This aperture could be closed using a polished ($E_{sc} = 0.13$) stainless steel plate (1.6 mm thick) translating on guiding rails by means of a pneumatic cylinder. A second polished stainless steel radiative screen (0.4 mm thick), separated by a 5 mm gap from the first, was screwed onto it. Both plates were convectively cooled by the flow. As the cross-sectional area of the radiative screens were much lower than 5 % of the test section cross-sectional area, no correction for flow restriction was applied to v_∞ (Smolsky and Sergeev, 1962).

¹ The exact location (mm) in the test section of the measuring points with respect to Oxyz (Figure 3.3) can be found in Appendix 2

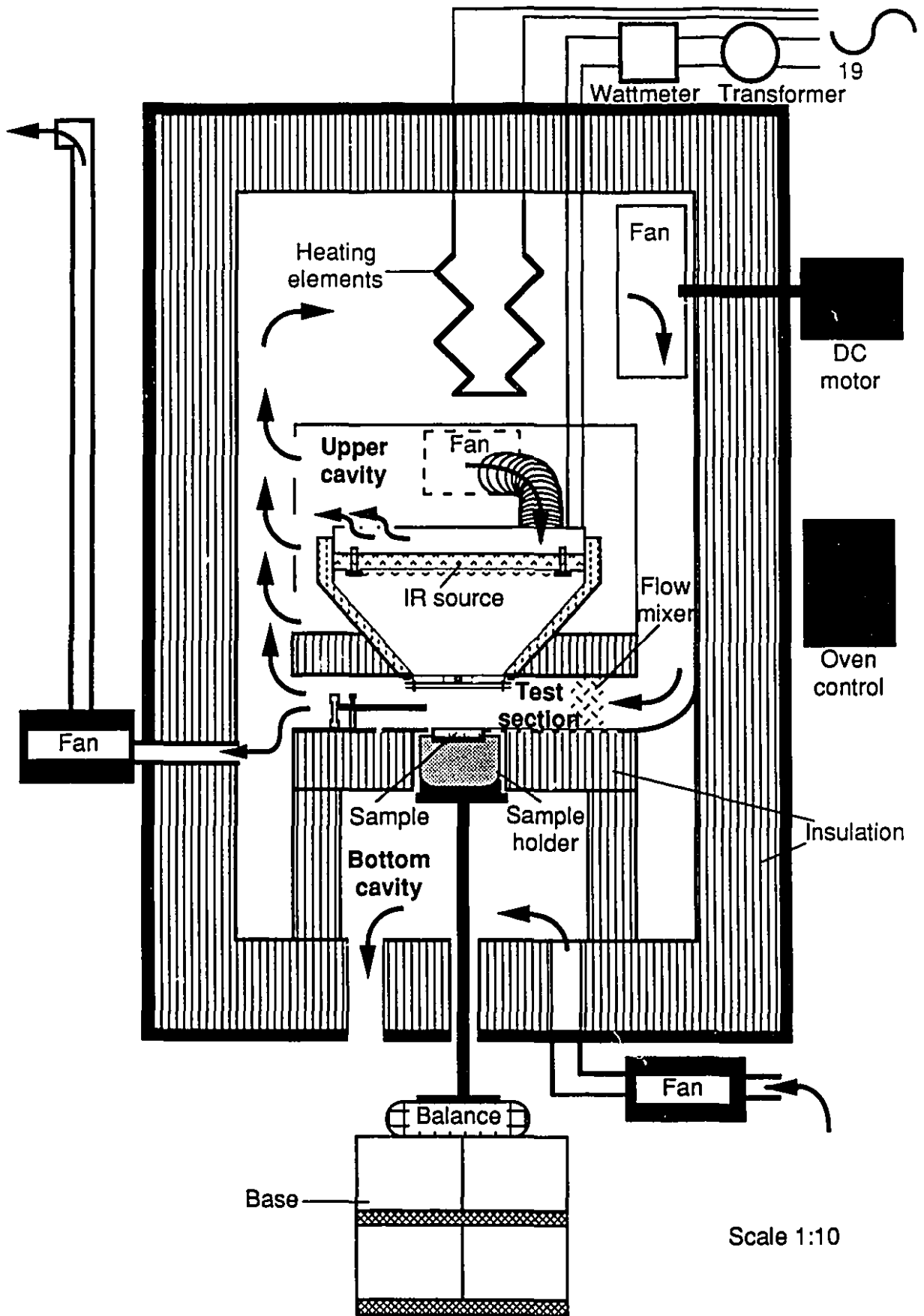


Figure 3.1 Oven schematic

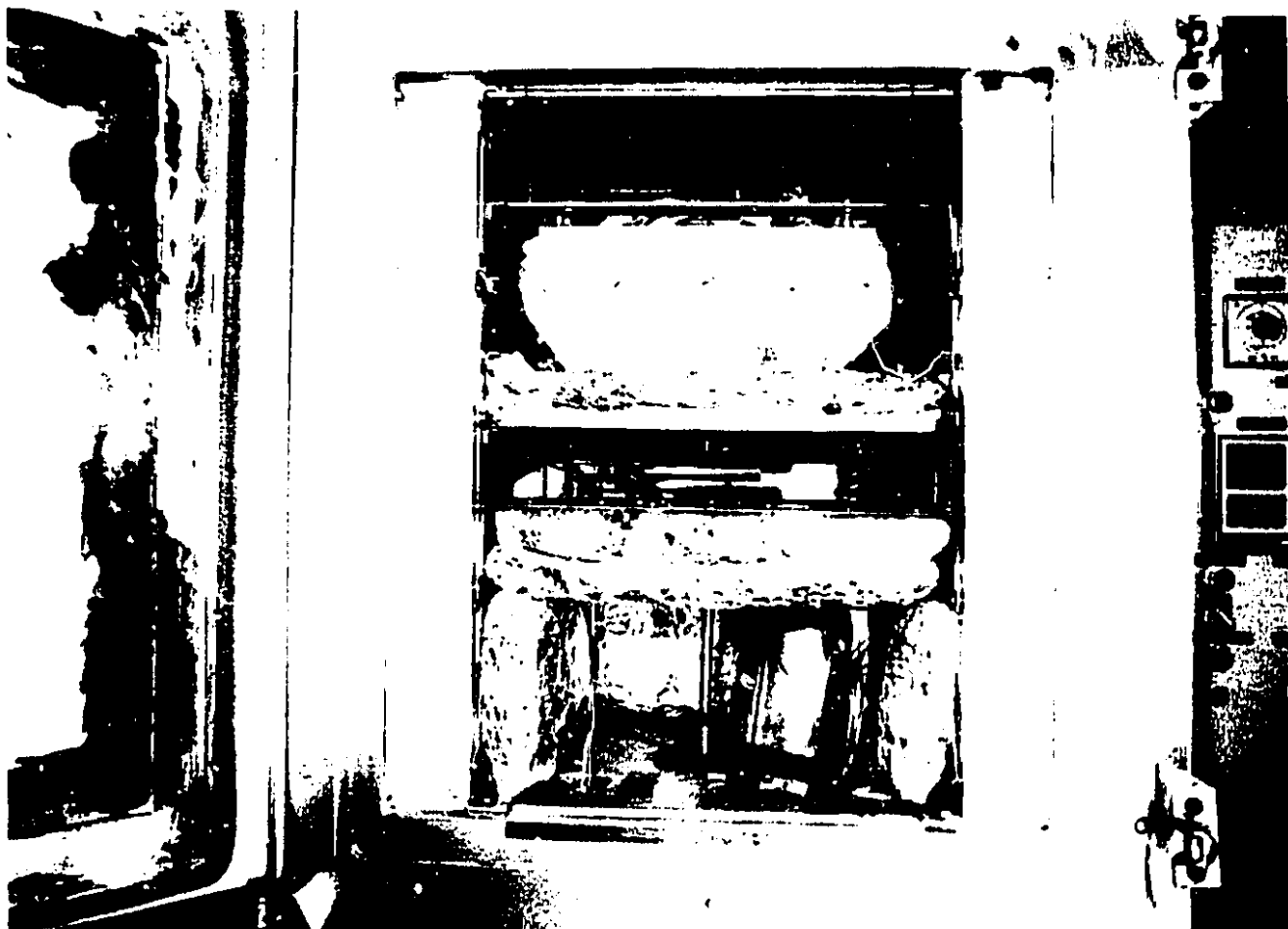


Figure 3.2 Photograph of the oven and the test section

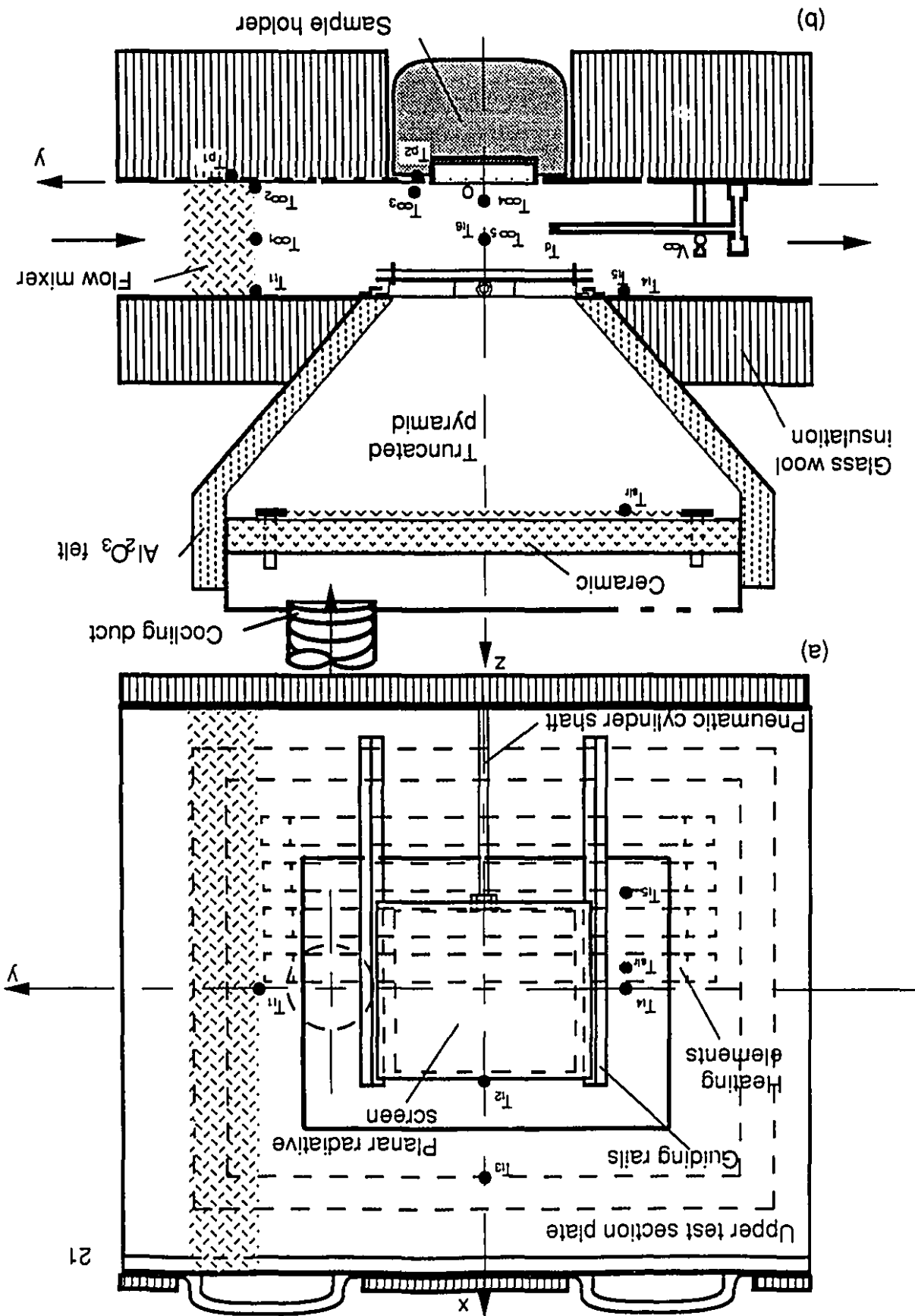
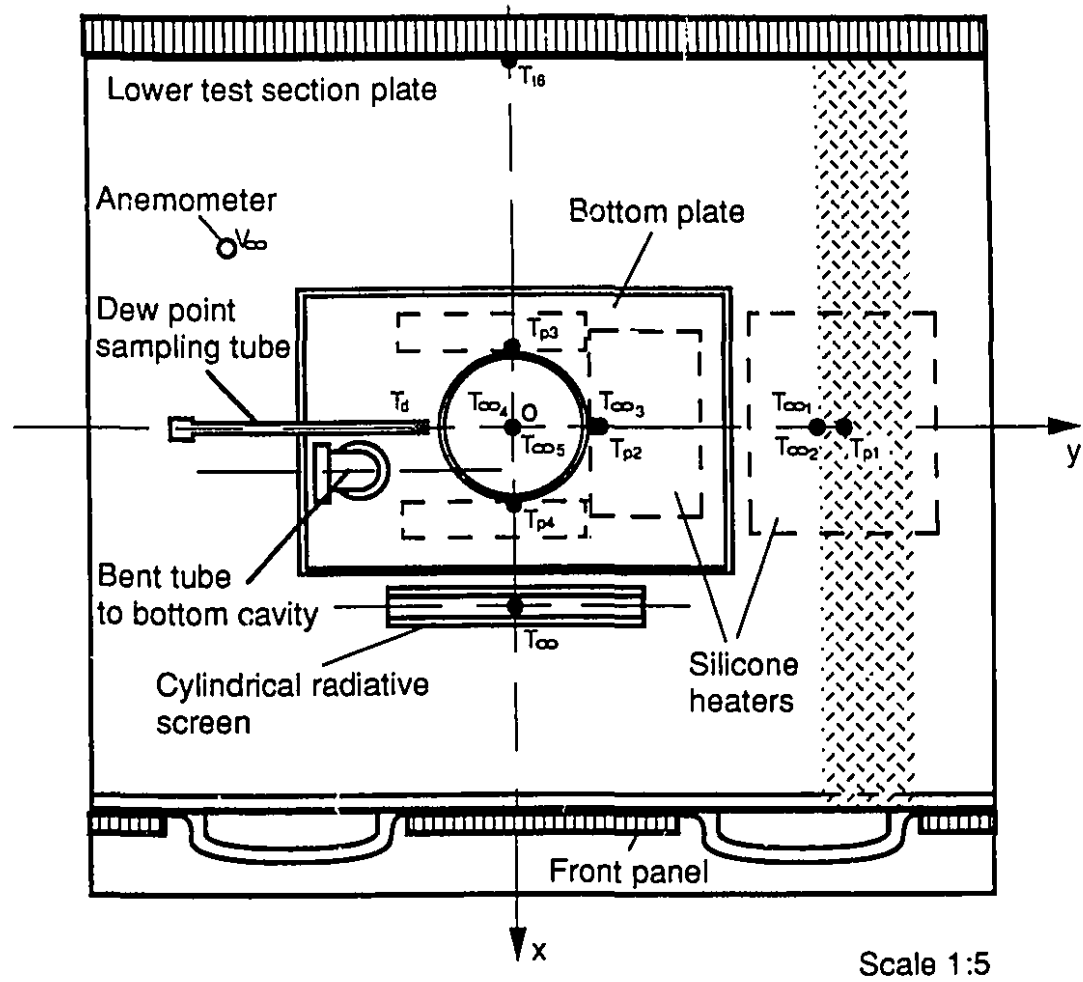


Figure 3.3a Test section: bottom view
 b Test section: cross sectional view



(c)

Figure 3.3c Test section: top view

The I.R. source was made of 8 low thermal inertia mesh heating elements. These corrugated resistive elements could be connected two at a time to give four levels of I.R. heat fluxes at the same reference temperature ($T_{sir} = 850\text{ }^{\circ}\text{C}$). This temperature was measured with a thermocouple spot-welded to one of the central heating elements and was controlled using a manual variable transformer; a wattmeter recorded the I.R. source power input (P_i). A detailed summary of the instrumentation and sensors used as well as their manufacturers and technical specifications is given in Appendix 3. The heating elements were stapled onto a low heat capacity ceramic (Armstrong, Ceramaguard) inserted in a metallic frame. The frame was fixed on the largest base of a truncated pyramid made of polished stainless steel plates (type 304). After insertion of an asbestos lining (4 mm thick), the pyramid's smallest base was screwed to a plate that was cut on the test section upper plate. The external insulation of the pyramid was made of an Al_2O_3 moldable felt (Cotronics Corp, No. 372).

A plate was cut and drilled (95.3 mm ϕ) on the test section bottom wall to receive the sample. On the back of this plate a set of three uniform flux silicone heaters were bonded (with a fine layer of silicone rubber epoxy) close to the hole so as to act as a guard against conductive heat losses to the bottom cavity. Both sides of the plate were covered with a low emissivity aluminium foil (final assembled thickness ~ 1.6 mm). Upstream of the plate an additional silicone heater decreased the first set load. For heater (bottom plate) temperature control and record, 3 thermocouples (T_{pi} ($i = 2,4$)) were located in grooves machined in the plate. A similarly positioned thermocouple (T_{p1}) was used to measure the upstream heater temperature. Temperature control to $1\text{ }^{\circ}\text{C}$ of the two sets of heaters was accomplished with two temperature controllers using the temperatures (T_{p1}, T_{p2}) from the largest heaters (Figure 3.3).

Thermocouples located on the upper wall and one side (T_{ti} ($i = 1,6$)) of the test section recorded the wall temperatures. They were screwed on after being soldered on to a brass ring. The same type of bare bead thermocouples were used to measure temperatures close to the flow mixer exit ($T_{\infty i}$ ($i = 1,2$)).

A solid state controller allowed adjustment of the flow velocity through control of the variable speed D.C. motor. An anemometer (self-heated platinum resistance temperature detector type) was used to measure the flow velocity (v_{∞}). A thermocouple located at middle test section height and protected from I.R. radiation (source or walls) by two polished stainless steel concentric tubes 145 mm long, 15 mm and 25.4 mm inside diameters (0.5 mm tube thickness) respectively, recorded the air temperature (T_{∞}). Its value could be adjusted to within 1 °C using the oven controller. The dimensions and surface characteristics of the cylindrical radiative ($E_{cy} \sim 0.13$) screens were defined according to a study by Pépin (1989) which demonstrated that with such shields, it was possible to get the air temperature with a temperature differential ($\Delta T = |T_{read} - T_{real}|$) lower than 3 °C although the external environment could radiate like a blackbody at 1000 K. In the present design we should expect much lower ΔT because only half side of the external cylinder sees a fraction of the radiating surface at 1123 K. Three additional air temperatures ($T_{\infty i}$ ($i = 3,5$)) were measured with stainless steel sheathed thermocouples located close to the sample surface (Figure 3.3) to verify that the incident flow was at T_{∞} .

A squirrel cage fan blew air in the back of the bottom cavity. The instrumentation was protected from direct air impingement with a stainless steel plate diffusing air on the cavity side. Two supplementary apertures were drilled close to the front door on the bottom cavity for air exhaust and wiring. An additional opening was machined in line with the lower test section hole, allowing an extensible rod to go through the bottom of the oven. It was used to measure the mass (m) of the sample holder and sample with a balance located directly under the oven. In order to protect it against mechanical shock and vibrations, the balance was placed on a two layer assembly; each layer was made of concrete blocks and a sheet of high density polyurethane foam. A 19 mm \varnothing bent tube connected the test section and the bottom cavity to equalize pressures thus avoiding airflow between the sample and the sample hole.

A variable speed squirrel cage fan supplied air to the back of the I.R. heat source to cool its electrical connections. Air from the test section was evacuated with a fan connected to a ventilation duct. A constant humidity flow was obtained with control on the air renewal rate through use of a shutter on the fan inlet. The air

dew point temperature (T_d) was measured with a condensation dew point hygrometer (Appendix 3) sampling the airflow downstream of the sample. Since preliminary experiments demonstrated that the pressure differential (pressure differential meter, Appendix 3) between the test section and the environment was lower than 0.03 mm Hg for the range of temperatures and velocities investigated, the static test section pressure (P_∞) was measured with a mercury barometer (0.1 mm Hg resolution) located outside the test section.

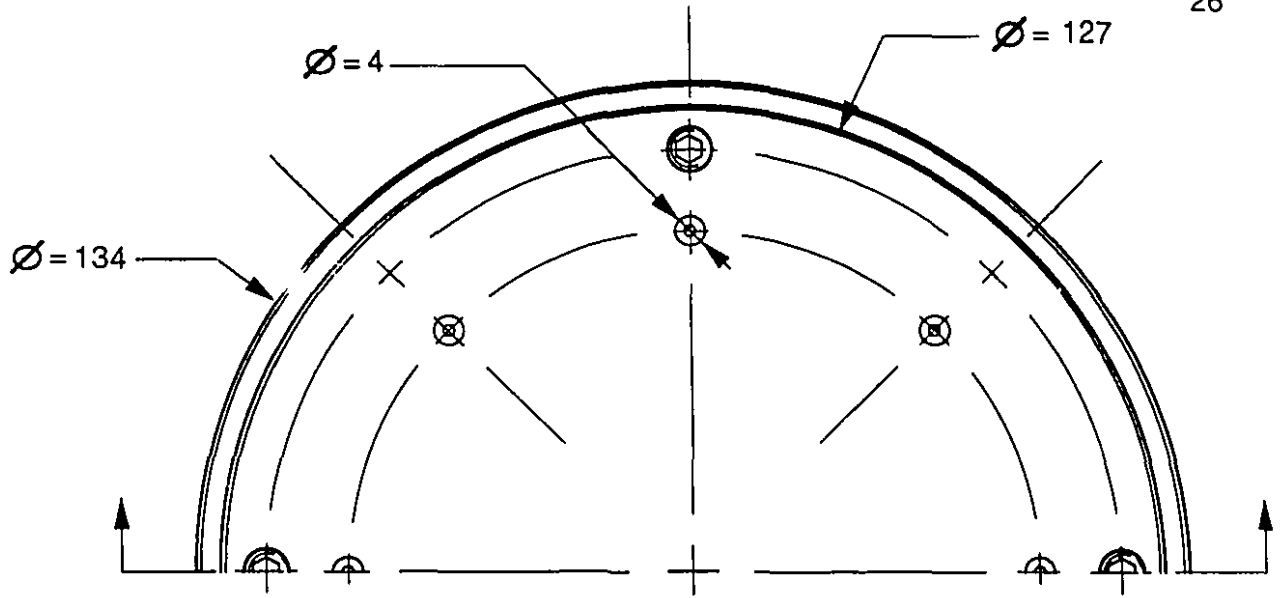
3.2.2 CONTAINER FOR TEST SAMPLES

In order to reduce as much as possible potential two-dimensional heat transfer effects on the sample, a low thermal conductivity (0.14 W/mK) $\text{Al}_2\text{O}_3\text{-SiO}_2$ ceramic (Cotronics Corp., Rescor 740) was chosen as the material for the sample containers. The design of the necessary stainless steel mold was dictated by three conflicting considerations:

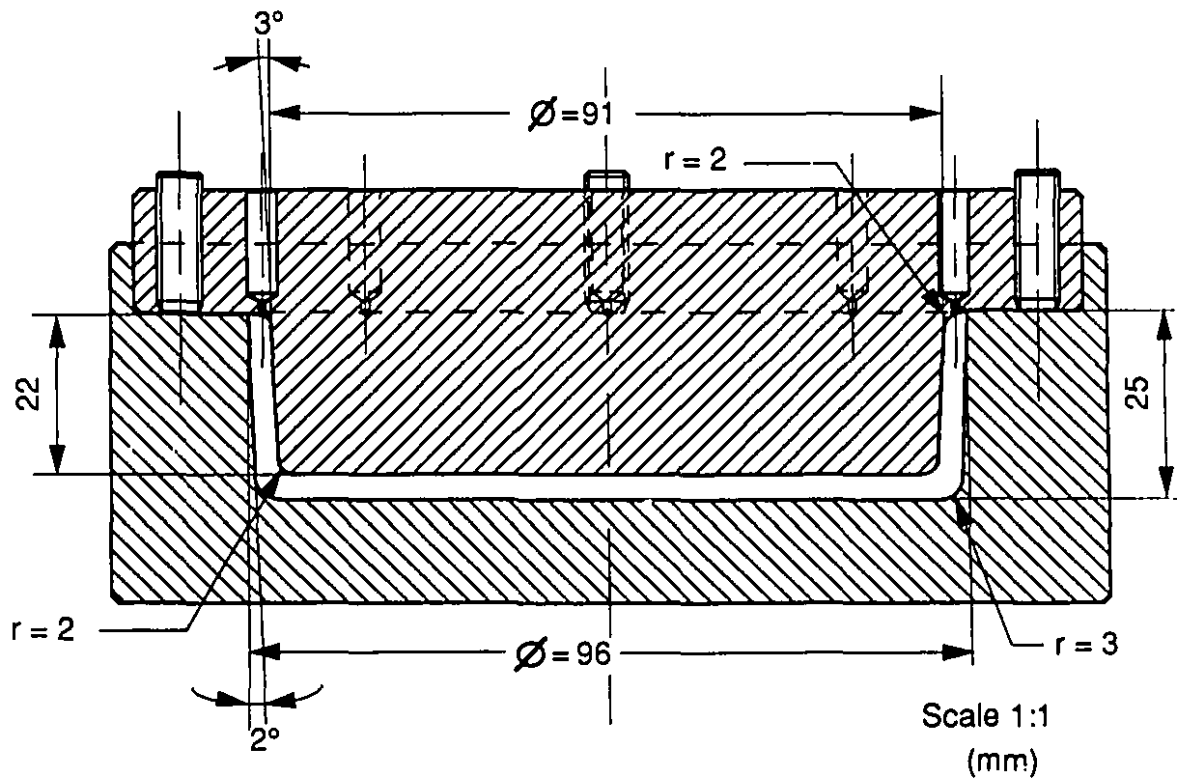
- a) The thickness of the container rim had to be the thinnest possible to decrease the convective and radiative heat transfer coming from the test section and the I R. heat source;
- b) The internal geometry had to approximate as closely as feasible a cylinder to avoid geometrical influence on the drying front progression;
- c) The insulation (wall) thickness had to be sufficient to minimize heat losses to surroundings.

Figure 3.4 gives the final design which was found to meet the above criteria adequately.

The following is a detailed description of the molding procedure employed to form the ceramic container. The ceramic was mixed to proper consistency according to the manufacturer's advice. The mixture was then poured in the bottom mold previously covered with a fine layer of a mold release lubricant (Cotronics Corp., 101MR). It was submitted to vertical vibration in order to



(a)



(b)

Figure 3.4a Container mold: top view

b Container mold: cross sectional view

eliminate air bubbles. The top mold was carefully inserted into the bottom mold and the assembly was put on a hydraulic press where a force of 10 tons was applied for 4 hours. The container was left within the mold to agglomerate overnight. After removal of the excess ceramic within the vents, 4 pressure screws were tightened slowly and alternatively to detach the top mold. Finally, insertion of the bottom mold in a convective oven at 110 °C for 2 minutes promoted a slight shrinkage of the consolidated container which can then be easily removed from the mold.

Various sample thicknesses (5 to 20 mm) were obtained by partially filling the container with the wet ceramic before drying (one day at room temperature and one night at 110 °C). Once dried, firing the container at 950 °C for 1 hour improved the container strength and the resulting shrinkage provided the final container diameter.

The final waterproofing step is detailed in the next section since it is linked to sample preparation.

3.2.3 CONSOLIDATED GLASS BEAD TEST SAMPLE PREPARATION

Sieves (U.S.A. series equivalent No. 80, 100, 120, 140, 170) were used to screen manually small quantities (100 ml) of spherical shape soda lime glass beads (AG 140/270) with a sphericity 1 according to the manufacturer (Potters Industries Inc.). This was carried twice to keep only beads in the 90-105 μm diameter range. Following a procedure put forward by Wong et al. (1984) to obtain "clean" glass beads, the beads were washed with a hydrochloric acid solution (0.22 g/ml) and carefully rinsed several times with deionized water. After drying, they were screened once more. A photograph (Figure 3.5) of a random sample of the glass beads shows the narrow diameter range achieved. The glass bead dimensions (average $d = 0.099 \text{ mm } \bar{\sigma}$; 0.003 standard deviation) were inspected with a dial calliper of 0.001 mm resolution.

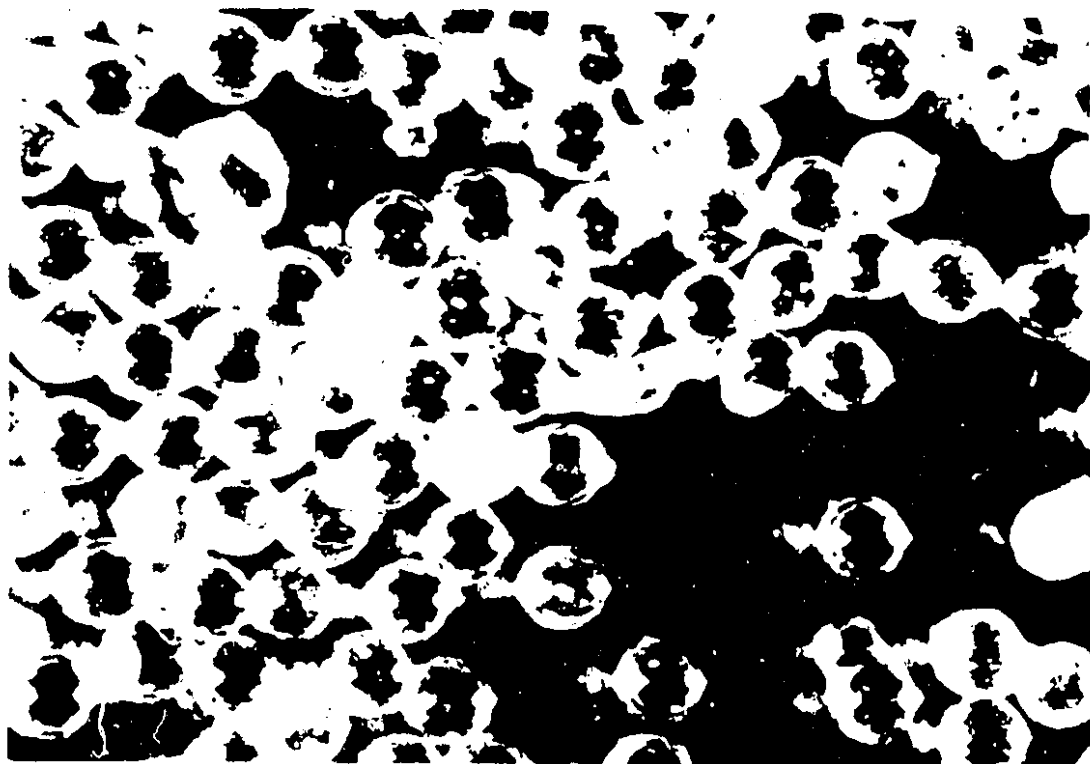


Figure 3.5 Photograph of a random glass beads sample

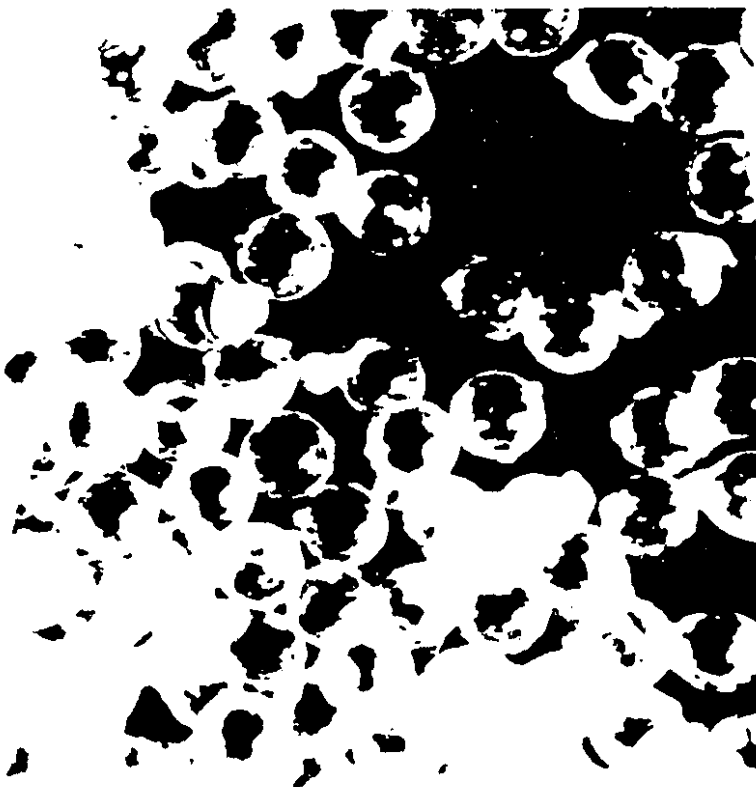


Figure 3.6 Photograph of beads from a sintered sample

The ceramic containers were sanded with a fine grade abrasive paper in order to obtain a precise sample height (b). It was then filled with glass beads, covered with a rigid circular plate (95 mm \varnothing) and centered on top of a vertically levelled vibrating apparatus (Ray Foster Dental Equipment). This shaking process has been used often to produce dense packings without creating large scale heterogeneities (Guyon et al., 1987). Before starting the vibrations at 60 Hz, a 1 kilogram weight was placed on the top plate. During compaction (30 minutes) small amounts of glass particles were added to keep the surface level.

Consolidation of the glass beads was achieved in a high temperature oven fitted with spiral heaters on two sides. The container filled with glass beads (on a plate) was located centrally on a metallic tripod in the oven cavity. As suggested by van Brakel and Heertjes (1974) to avoid differential shrinkage, it was shielded against direct radiation from heaters with a stainless steel bowl (120 mm \varnothing and 80 mm height). The consolidation cycle consisted of 6 hours of ramp heating to 650 °C (Van Brakel and Heertjes (1974), Charlaix et al. (1987), Guyon et al. (1987), Hulin et al. (1987)), followed by a two hour soak and final cooling to room temperature following oven shut-off. This specific sintering methodology was followed because visual observations of beads from the sintered sample with a microscope (Figure 3.6) showed that the beads retained their identity (Guyon et al. (1987)) after this procedure. This is critical if only minor perturbation of the transport properties is acceptable. Furthermore, it appeared that the slab had acceptable mechanical strength which is essential to obtain reproducible results in multiple drying experiments.

A calliper of 0.05 mm resolution was used to measure the slab thickness and diameter. The measurements were taken twice on four opposite locations around the bed diameter. The final reported results were averaged values.

A balance (0.01 g resolution) was used to evaluate the bone-dry and wetted weight of the test slab. A measurement of the immersed slab weight (together with the Archimedean principle) allowed us to compute the slab porosity according to ASTM standard test method (C20-87). For each slab, three measurements of each weight were taken and averaged. The glass density (ρ_b) on the average was 2497 kg/m³ (in agreement with the value for bulk glass) with

a measurement dispersion of $\pm 0.23\%$. A summary of the final bed characteristics is given in Table 3.1. Here b and D are the bed thickness and diameter respectively, ϵ is the bed porosity, ρ_d the dry density of the bed, V_t the bed overall volume and V_{cy} the equivalent cylinder bed volume (as discussed in section 6.6.1). The porosity range (0.368-0.383) of the samples is well within the applicable limiting porosity ranges established experimentally for random packing of equal spheres: close, 0.359-0.375; poured, 0.375-0.391 (Haughey and Beveridge, 1969). Although the shaking process used was described by van Brakel and Heertjes (1974) to produce inhomogeneities ($\sim 2\%$) in porosity distribution with height for thick beds (70 mm), an observation of the reported porosity distributions allows us to expect better results because only a fraction of this total porosity variation can occur across a thickness under 20 mm.

After the completion of the above measurements, both the test slab and container bottom plate were carefully machined to produce a groove for the location of two 0.5 mm outside diameter stainless steel sheathed thermocouples. The bottom of the slab was drilled along the axis to insert the surface thermocouple.

All thermocouples used to measure sample temperatures T_s or T_b and flow temperatures $T_{\infty i}$ have been previously calibrated (to $\pm 0.5\text{ }^\circ\text{C}$) in a stirred liquid bath according to ASTM standard test method E220.

The small clearance between the slab side and the container internal diameter (result of the sintering process) as well as the radial porosity variation at the wall (Rydgway and Tarbuck (1966)) were eliminated through use of a technique suggested by van Brakel and Heertjes (1974). First, five layers of a high temperature ($480\text{ }^\circ\text{C}$) silicone moisture sealer (Cotronics Corp., Duralco 1529) were necessary to waterproof the container and fill partially the clearance. Each of these layers was individually dried sequentially for two hours at room temperature, $121\text{ }^\circ\text{C}$ and $177\text{ }^\circ\text{C}$. Then, the slab and thermocouples were glued to the container with a high temperature ($400\text{ }^\circ\text{C}$) resistant epoxy (Theramic engineering Inc., No. 550). The mass of the absorbed water by the sample slab and the final sample were compared for each sample; it was ascertained that for all samples the former is greater than the latter by less than 0.1 g.

TABLE 3.1

GLASS BEAD BED CHARACTERISTICS

Sample No.	b (mm)	D (mm)	ϵ	ρ_d (kg/m ³)	V_t (cm ³)	V_{cy} (cm ³)
VI	20.0	89.4	0.372	1567	118.84	125.54
IX	5.5	89.0	0.383	1537	31.02	34.22
X	10.3	89.4	0.373	1565	60.22	64.66
XI	10.3	88.7	0.382	1544	60.22	63.65
XII	19.9	88.8	0.368	1580	117.56	123.24
XIII	20.0	89.0	0.370	1575	118.55	124.42

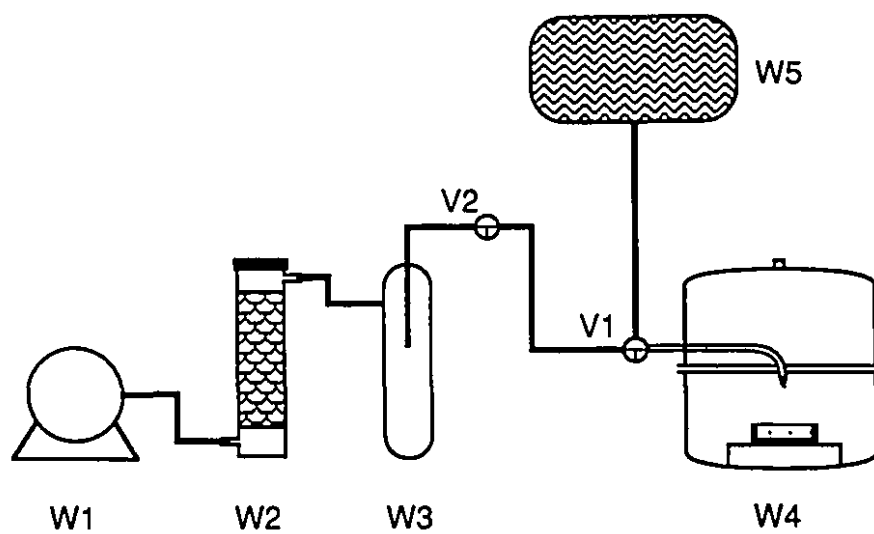
The last step was to cement a low emissivity aluminium foil on the rim of the container to decrease the absorbed radiative heat transfer coming from the cavity and I.R. source. Note that throughout this thesis the terms "consolidated glass bead sample" and "sample" are used interchangeably.

3.2.4 WETTING APPARATUS AND PROCEDURE

The schematic in Figure 3.7 gives an overview of the wetting apparatus. A high vacuum pump (W1, Sargent Welch model 1405) was connected through tygon tubing to a vacuum bell. A water trap protected the pump from liquid water intrusion. A shield against water vapour was insured by a desiccant drying column (Hammond Drierite Comp.). The bell was linked to a water deionized bag with a manual valve (V1) which performed water admission or vacuum connection. Another valve (V2) provided the means for isolating the network from atmospheric pressure. A similar apparatus was also used by Shibata et al. (1990). The following describes the sample wetting procedure in a stepwise manner:

- a) Introduce the sample fitted with thermocouples on a tray into the vacuum bell and close valve V2 (V1 is open);
- b) Energize the vacuum pump W1 to reach 10 mm Hg pressure;
- c) Slowly close V1 to admit water until the sample surface is covered with a thin water layer; then open V1;
- d) Wait 1/2 hour at 10 mm Hg pressure; then slowly open V2.

The same consolidated glass bead slab was wet according to this technique and to the much more time-consuming boiling technique put forward in the ASTM standard test method C20-87; it was found (within experimental uncertainty on mass measurement), that the amount of absorbed water were the same in both cases. Wong et al. (1984) and Guyon et al.(1987) advocated the use of the vacuum method to fill (or wet) a consolidated glass bead slab when the porosity had to be measured as described in section 3.2.3. It is inferred in the present



- W1: High vacuum pump
W2: Desiccant drying column
W3: Water trap
W4: Vacuum bell
W5: Water (deionized) bag

Figure 3.7 Schematic of the wetting apparatus

study, as Wong et al. (1984) did, that the small spread in the measured grain density (here $2497 \text{ kg/m}^3 \pm 0.23 \%$), suggest that there is essentially no occluded volumes in the samples (less than 0.5 % if they exist), i.e., the pore space is completely connected and can be fully saturated by the water.

3.2.5 SAMPLE HOLDER

While in many drying studies the whole sample is immersed within the flow of heated air giving rise to one dimensional drying through symmetric boundary conditions and use of a large sample, mounting the sample flush with the wall calls for careful experimental treatment as noted earlier by Crausse (1983), Prat (1986a), Moyne (1987), Perrin and Foures (1991). As a result, preliminary experiments were carried out and established that the final sample (Figure 3.8) was still significantly sensitive to two-dimensional heat transfer effects. Hence, thermocouples were inserted within the initial sample holder ("passive" insulation) to evaluate the magnitude of the conductive heat transfer through the bottom and side walls of the sample; for $T_\infty \sim 180 \text{ }^\circ\text{C}$, temperatures higher than $100 \text{ }^\circ\text{C}$ were recorded within the insulation located below the sample while T_s and T_b were still in the $45\text{-}55 \text{ }^\circ\text{C}$ range. Heat was coming from the upper side of the sample holder. Despite attempts to use different types of insulating materials (glasswool, ceramic board, polyurethane foam) the "passive" insulation concept failed to appreciably lower this transfer.

To minimize the conductive heat loss contribution, an "active" insulation (Figure 3.8) was devised consisting of a stainless steel bowl (A) fitted with a layer (B) of low thermal conductivity (0.02 W/mK) polyisocyanurate cellular plastic (Dow Chemical Corp., Trymer 9501). Inside a second "active" shield was a cylindrical aluminium fin (C) connected to two sealed container (D) acting as heat sinks. A tubular Trymer piece (E) insulated the internal diameter surface of the fin. This tube was held in place with an aluminium ring fin (F) glued on the cylindrical fin extremity. A Trymer plate (G) insulated the sample bottom. A clearance of about 1 mm existed between the sample sides and the ring fin to avoid excessive heat transfer. The top of the sample holder was insulated with a ceramic board (H) protected from radiative heat transfer by an aluminium foil (I).

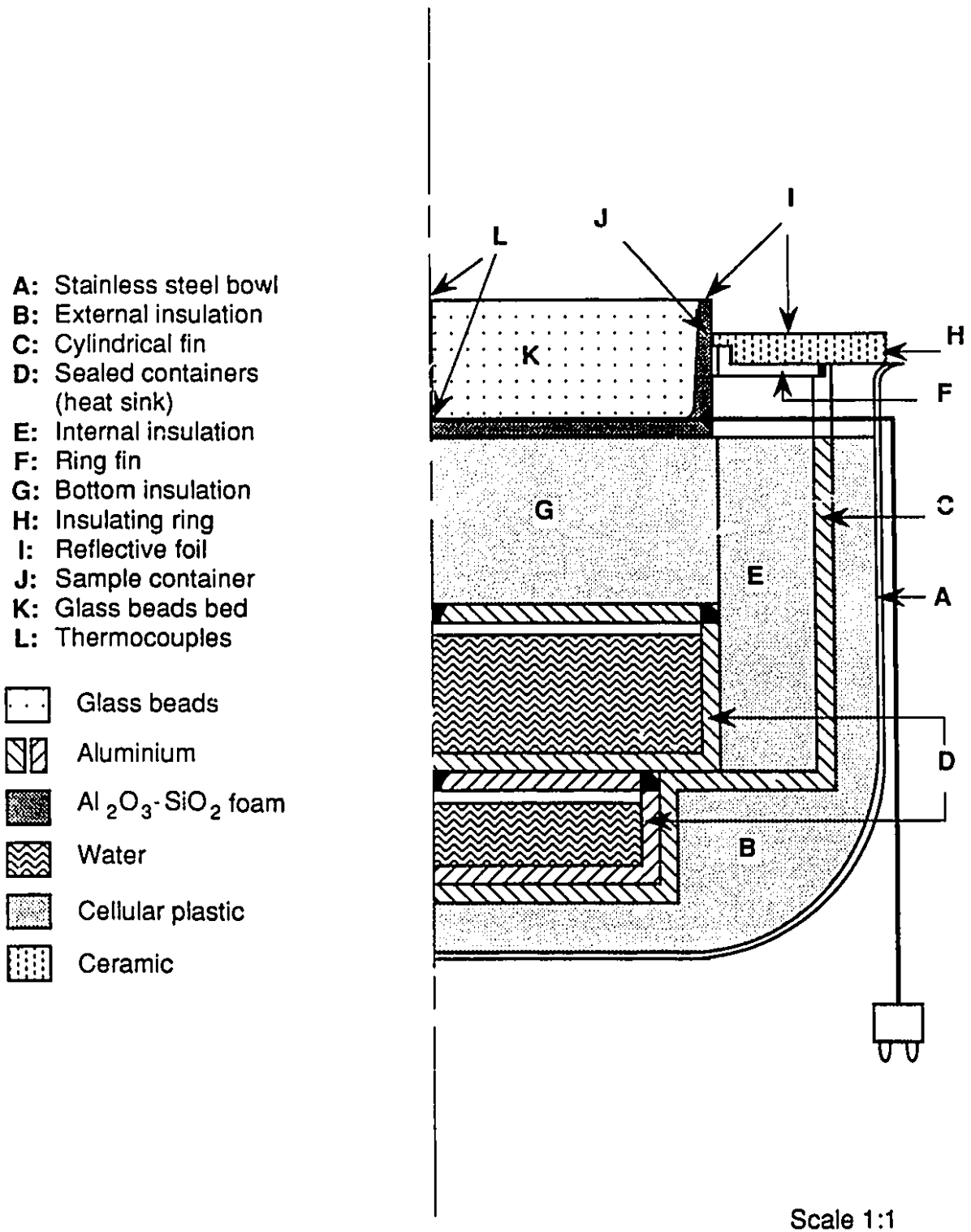


Figure 3.8 The sample and sample holder: cross sectional view

The sample holder and the containers were put in a freezer at $-25\text{ }^{\circ}\text{C}$ for two hours in order to accumulate enough thermal inertia for the whole duration of the experiment. As the length of the experiment shortened (in case of I.R. drying), only the largest heat sink was used. At the start of an experiment, the wetted sample was placed on top of the holder with the ceramic board around it. After insertion in the oven, heat coming from all directions was conducted down the cylindrical fin to the ice in the container. One dimensional drying conditions were maintained during the drying experiments as a result of thawing of ice and/or water heating taking place in the sealed containers (see section 3.5 for a quantitative evaluation).

3.3 OPERATING PARAMETERS

The scope of this research was limited to the following operating parameters:

- | | |
|--------------------------------------------------|------------------------------------------------------|
| a) Air temperature: T_{∞} | 80 - 180 $^{\circ}\text{C}$ |
| b) Flow velocity (in test section): v_{∞} | 2.1 - 6.2 m/s |
| c) Air dew point temperature: T_d | - 10.6 $^{\circ}\text{C}$ - +17.9 $^{\circ}\text{C}$ |
| d) Sample thickness: b | 5 - 20 mm |
| e) Incident heat flux: $q_{i,s}$ | 6.8 - 22.0 kW/m^2 |
| | on the sample surface |

3.4 DATA ACQUISITION AND TREATMENT

3.4.1 DATA RECORDING: HARDWARE AND PROCEDURE

Data acquisition was realized through a 3852 Hewlett-Packard data logger connected to a 360 Hewlett-Packard central unit where all data were stored. They could be transferred to a SUN 3/60 microcomputer for data analysis. Other hardware elements and links for data recording and experiment control are represented in Figure 3.9 which is self explanatory.

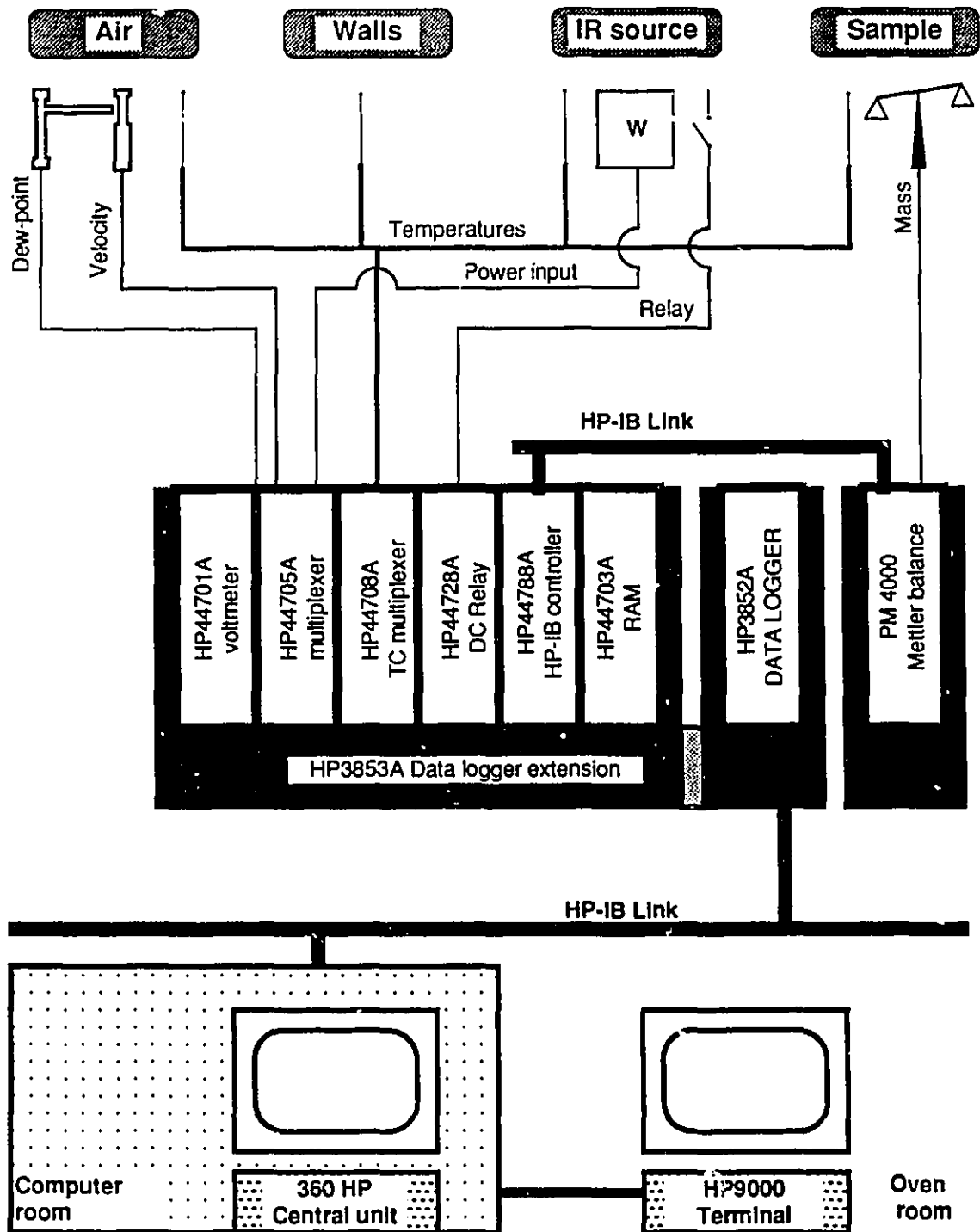


Figure 3.9 Schematic of the data acquisition system

A basic software called "CIR" was developed for the 360 unit by INTEK Inc. (Montreal, Canada) for managing all the operations related to graphic display, variable selection, recording times, file management and control of the relay for the sliding plate.

All measuring points were read at various rates depending upon their variation with time so that file sizes could be kept minimal while important surface temperature changes due to intermittent I.R. heating (I.H.) could still be tracked with acceptable accuracy. Measuring points to be recorded at the same time were grouped as follows:

Set no. 1: T_{∞} , v_{∞} , P_{∞} , T_d , T_{ij} ($i=1,6$), $T_{\infty i}$ ($i=1,5$) and T_{pi} ($i = 1,4$)

Set no. 2: m

Set no. 3: T_s and T_b

The time interval between the data readings was varied according to the total expected drying time to give the best sampling feasible. The mass was recorded separately because a maximum of about 290 data points could be treated with the smoothing technique discussed in section 3.4.3.

3.4.2 DRYING EXPERIMENTS

A typical drying experiment started with obtaining a bone dry sample placed in a convection oven at 110 °C for 1 hour. The sample was then cooled to room temperature in a desiccant-filled bell, weighed and wetted according to the wetting procedure described in section 3.2.4. While this was done, the oven flow parameters (T_{∞} , v_{∞}) were stabilized to their specific set-point values. For the I.R. drying experiments, the source was also heated a few minutes before initiating data recording (aperture plate closed). The wetted sample was weighed and assembled in the sample holder, then the oven front door was opened to connect the thermocouples and to adjust the sample in the test section cavity. The oven door was closed, data recording started and the aperture plate opened in case of I.R. drying. The variable transformer was manually controlled in order to obtain a constant T_{sir} (850 °C) of the I.R. source during the experiments.

3.4.3 SMOOTHING OF DRYING CURVE

As illustrated in Figure 3.10a, the typical drying rate curve (derived from raw data in Figure 3.10b) is "noisy" for experiments with forced convection alone. Similar curves (N_v vs. X) representative of I.R. drying results with free convection (no forced flow present) are presented in Figure 3.10a and b. From a comparison of these two types of curves it can be inferred that the observed "noise" is uncorrelated to signal recording but that this is a consequence of the combined influence of the balance-sample length together with the aerodynamic friction on the sample top surface and the sample holder sides. A secondary contribution to this "noise" was probably due to mechanical vibration of the oven transmitted to the balance base.

The m vs. t curve (forced convection) in Figure 3.10b was "smoothed" so that a computation of the first order derivative of the fitted function could give a continuous representation of the drying rate curve. An adequate method to smooth the drying curve was to use an algorithm specifically designed by Reinsch (1967) to produce a C^2 cubic spline approximation to noisy data. The smoothing spline S_m is the unique C^2 function which minimizes:

$$\int_0^{t_0} S_m'(t)^2 dt \quad (3.1)$$

subject to the constraint:

$$\sum_{i=1}^N \left| \frac{S_m(t_i) - m_i}{\omega_i} \right|^2 \leq \sigma_m \quad (3.2)$$

where ω_i is the weight of each data point (i) and σ_m the smoothing parameter. According to Reinsch (1967), ω_i should be an estimate of the standard deviation of m . An average value for ω_i (0.19) was calculated from the values used in the smoothing of all the experimental results: the standard deviation was 0.05.

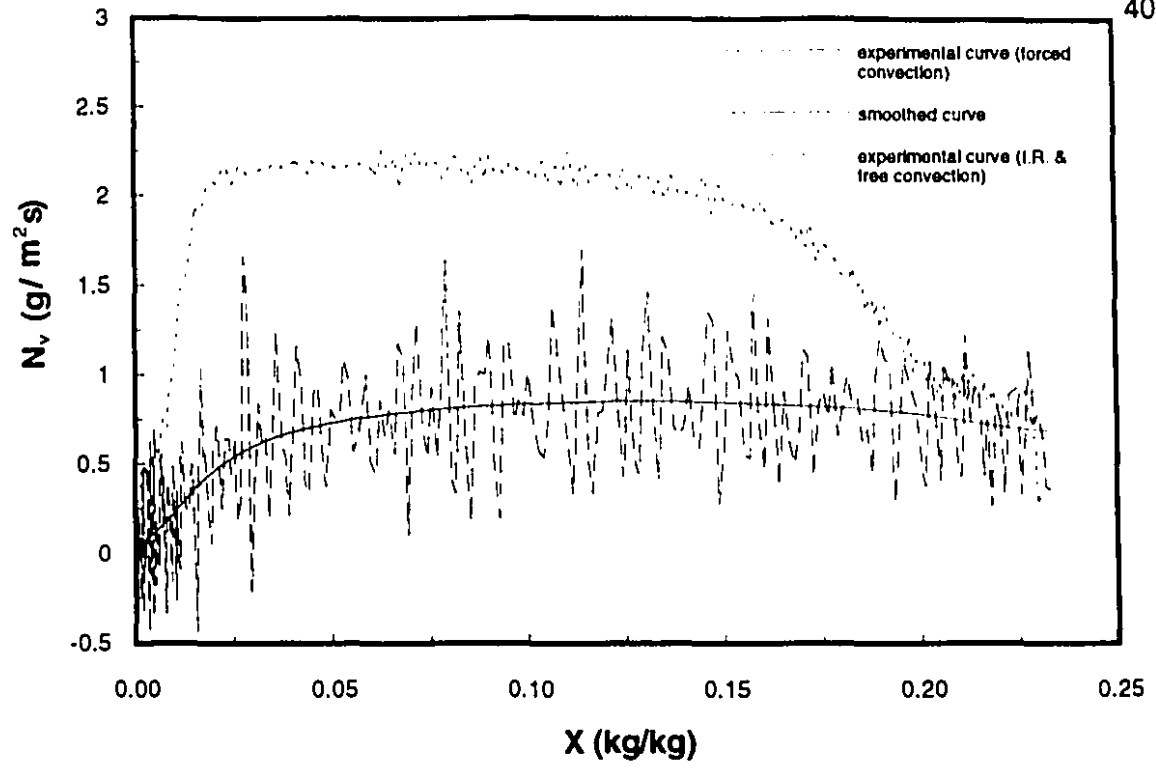


Figure 3.10a The typical drying rate curve N_v vs. X

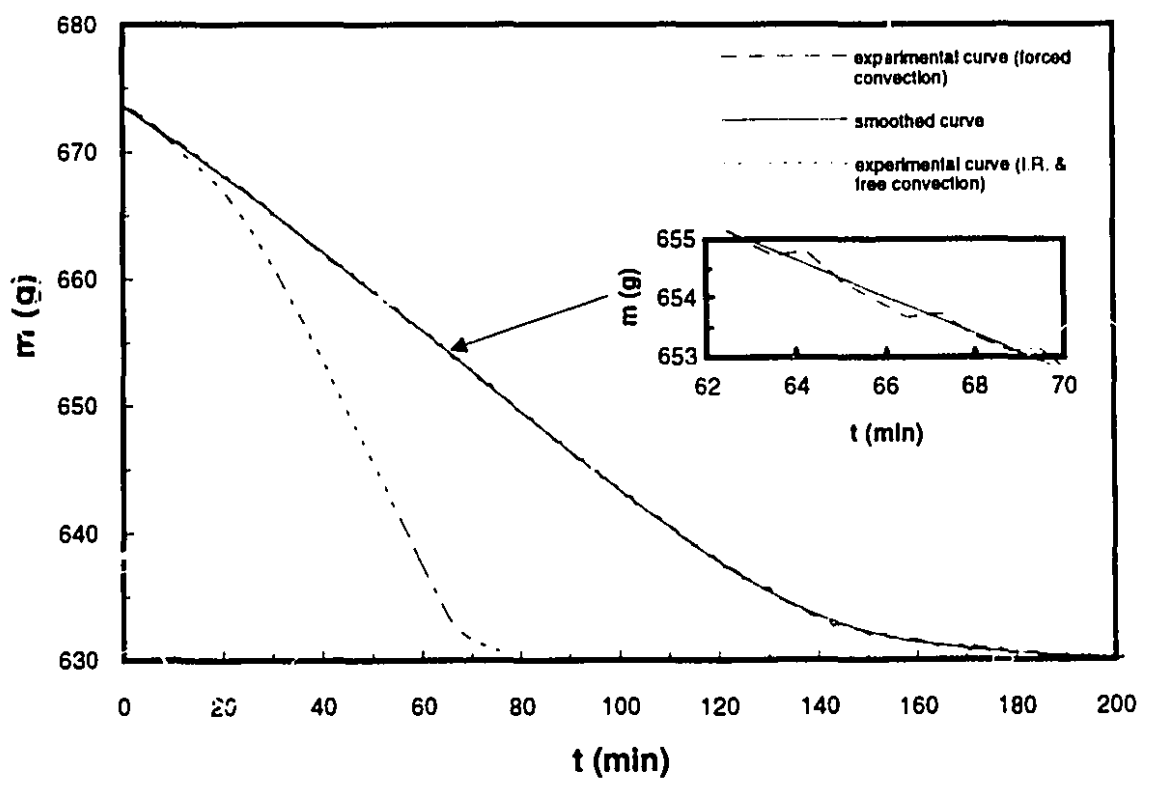


Figure 3.10b The typical m vs. t curve

σ_m was selected within the suggested interval by Reinsch (1967) viz.

$$N - \sqrt{N} \leq \sigma_m \leq N + \sqrt{N} \quad (3.3)$$

After trial an error on the smoothing of about 10 drying curves, a good value for σ_m was found to equal N , the total number of recorded data from the start of an experiment to the time when a bone dry sample state is reached. The sample was considered to have reached this state when the rate of change of the bottom temperature increased suddenly. The cubic spline approximation ($\omega_1 = 0.13$, $\sigma_m = 270$) is superimposed on the raw m vs t curve in Figure 3.10b providing a typical representation of the closeness between both results. The correlation coefficient r (Holman 1984) in this case is 0.9999 while the average correlation coefficient computed for all curves obtained in this study had an average value of 0.9994 with a standard deviation of only 0.0003. Figure 3.10a shows the drying rate curve for the raw and cubic spline approximation. Similarly shaped drying rate curves for experimental convective drying of glass beads bed have already been reported by van Brakel (1980), Cunningham and Kelly (1980), and Moyne (1987) and for free convection-I.R. drying of thick glass beads bed by Seki et al. (1977).

A 1 % percent relative standard deviation (McCormick and Roach, 1987) of the N_v value was chosen as a criterion to select the portion of the smoothed drying rate curve necessary for the computation of the average mass flux (N_v^*). It appeared from all the experimental results that this region of the drying rate curve was characterized by relatively small internal temperature variations usually associated with the so called "pseudo constant drying rate period" (P.C.D.R.P.; van Brakel, 1980). N_v^* was used in the energy and mass balances discussed in chapter IV and V to compute the convective heat transfer coefficient h_c^* , the mass transfer coefficient K_p^* (or K_y^*) and the sample total hemispherical emissivity E_s^* . * means that these quantities are average values representative of conditions prevailing during the P.C.D.R.P.. Note that throughout this thesis the terms "average mass flux computed during the P.C.D.R.P." and "average mass flux" are used interchangeably.

3.4.4 DETERMINATION OF THE CRITICAL MOISTURE CONTENT

Since there is no sharp discontinuity in rate observable on the drying rate curve (Figure 3.10a), it was found to be in most cases very difficult to determine graphically the critical moisture content X_c (averaged value across b) as defined in the classical theory of drying (Keey, 1972). According to Keey (1972), for a non-hygroscopic capillary porous material the critical point should occur when the moisture content at the exposed surface is zero. However, experimental determination of the moisture distribution, with various techniques: gravimetric method (Ceaglske and Hougen, 1937; Corben and Newitt, 1955); gamma ray absorption (Cunringham and Kelly, 1980, Van Brakel, 1980) and nuclear magnetic resonance imaging (Maneval et al., 1991), have shown beyond doubt that the surface moisture content (defined as an average value on a unit surface area) is not zero at the occurrence of the critical moisture content: (first critical moisture content). On the other hand, a rapid increase in surface temperature can be experimentally associated (Ceaglske and Hougen, 1937) with a surface saturation S_s reaching the irreducible saturation S_{ir} which correspond to the start of the pendular state at the bed surface (second critical moisture content). The concept of a critical moisture content based on $S_s = S_{ir}$ at the surface has been tested successfully by Schadler and Kast (1987) to determine, without previous drying experiment, the magnitude of X_c . Their experimental results confirm that the surface temperature increase rapidly at this point. Endo et al. (1977) as well as Chen and Pei (1989) pointed out (from experimental results in convective drying) that the "knee point" on the drying rate curve was always close to a deflection on the surface temperature curve from which the surface temperature begin to increase. Thus, in this study the critical moisture content was determined graphically on the T_s vs. X curve as show in Figure 3.11. The critical moisture content obtained by such procedure is likely to represent the average moisture content at which a drying front is appearing at the material surface (Chiang, 1987; Rogers and Kaviany, 1991).

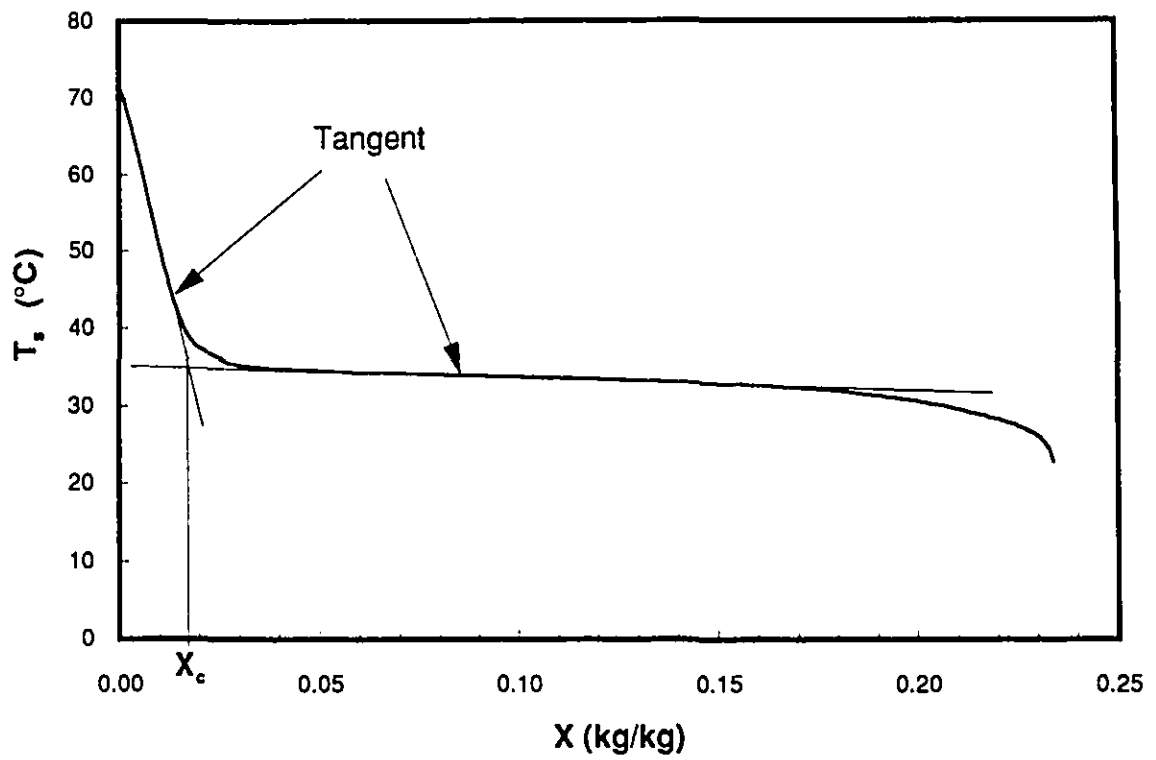


Figure 3.11 The determination of X_c on the T_s vs. X curve

3.5 EXPERIMENTAL REPRODUCIBILITY

The same set of experimental parameters ($T_{\infty}^* \sim 180$ °C, $v_{\infty}^* \sim 6$ m/s) suspected to generate the strongest two dimensional effects was chosen as representative of the experiments. A preparatory study was undertaken to quantify the experimental reproducibility, to verify if drying of the samples was actually one-dimensional, to check possible differences ensuing from the use of different samples with same or different thicknesses, and the impact of the thermocouples on the mass measurement.

According to Table 3.2, the variables studied were N_v^* , t_o the overall drying time, the critical time t_c and X_c . The reproducibility intervals presented here constitute conservative estimates because T_d^* was not the same for all experiments. The reproducibility level of a variable V was evaluated through computation of r_v defined by (Hasan, 1988):

$$r_v = \left| \frac{100 \cdot \text{Max}(V_1 - V_2)}{V^*} \right| \quad (3.4)$$

Where V^* is the average value computed from results of a set of replicate experiments with one or more samples. Taking into account the maximum ΔV (ΔN_v^* , Δt_o) observed, the N_v^* and t_o measurements with the same sample are reproducible within ± 7 % (column ten, Table 3.2) and ± 5 % (column twelve, Table 3.2) respectively. The X_c measurement was found reproducible within ± 19 % (column sixteen, Table 3.2). Although t_c values are reproducible within ± 12 % (column fourteen, Table 3.2), the reproducibility level of X_c can be explained with the fact that as X goes to zero, small errors (± 0.4 g) on the mass determination increases the relative uncertainty in the X determination. Yagi et al. (1957) presented X_c values in combined convective and I.R. drying with a reproducibility level of ± 26 % and ± 7 % for N_v^* . From Schadler and Kast (1989) experimental data in convective drying at very low velocity ($v_{\infty}^* \sim 0.25$ m/s) the reproducibility level of X_c can be evaluated to be ± 13 %.

TABLE 3.2

SUMMARY OF THE REPRODUCIBILITY STUDY: N_v , t_o , t_c and X_c

Run	Sa.	b	T_∞	v_∞	P_∞	T_d	T_s	N_v	N_{var} r_{Nv}	t_o	t_{oav} r_{t_o}	t_c	t_{cav} r_{t_c}	X_c	X_{cav} r_{X_c}	N_{var} r_{Nv}	
Nb.	Nb.	(mm)	(°C)	(m/s)	(kPa)	(°C)	(°C)	(kg/m ² s)	(kg/m ² s) (%)	(s)	(s) (%)	(s)	(s) (%)	(kg/kg)	(kg/kg) (%)	(kg/m ² s) (%)	
re12	IX	5.5	180.6	5.9	100.25	6.6	44.6	2.20e-03	2.21e-03	1320	1328	912	901	2.08e-02	2.24e-02	Sa. No. IX, XII, XIII	
re21	IX	5.5	180.1	6.2	98.15	4.6	46.1	2.23e-03	1	1335	1	890	2	2.41e-02	14		
re7	X	10.3	180.3	6.0	101.06	3.1	45.3	2.14e-03	2.07e-03	2520		1718		2.62e-02	2.21e-03		
re14	X	10.3	180.3	6.1	99.91	7.5	47.0	2.03e-03		2490	2473	1718	1714	2.49e-02			2.52e-02
re25	X	10.3	179.8	6.2	98.15	4.4	48.3	2.11e-03		2420	4	1664	5	2.56e-02		8	
re27	X	10.3	179.8	6.3	98.17	3.4	50.0	1.99e-03		2460		1756		2.43e-02			
re10	XI	10.3	180.3	6.1	100.87	3.8	46.2	2.35e-03	2.36e-03	2310		1604		2.40e-02	2.36e-02	Sa. No. IX, X, VI, XII, XIII	
re16	XI	10.3	180.3	6.1	99.78	7.1	45.7	2.35e-03		2340	2368	1557	1634	2.59e-02			19
re24	XI	10.3	179.8	6.3	98.15	4.7	48.4	2.36e-03		2440	5	1619	12	2.14e-02			
re26	XI	10.3	179.9	6.3	98.15	4.0	47.0	2.39e-03		2380		1756		2.33e-02			
re1	VI	20.0	180.3	6.1	101.82	4.5	Nd	2.23e-03	2.15e-03	4620		nd	nd	nd	nd	2.15e-03	
re3	VI	20.0	180.2	6.1	101.67	6.0	Nd	2.08e-03		4680	4635	nd	nd	nd	nd		12
re4	VI	20.0	180.3	6.1	101.52	5.8	Nd	2.16e-03		7	4620	1	nd	nd	nd	nd	Sa. No. VI, XII, XIII
re5	VI	20.0	180.3	6.1	101.46	6.7	Nd	2.13e-03		4620		nd	nd	nd	nd		
re6	XII	19.9	180.3	6.1	101.11	2.2	46.6	2.25e-03	2.23e-03	4631	4705	3020	3040	2.41e-02	2.59e-02	2.18e-03	
re13	XII	19.9	180.4	6.1	100.13	7.8	45.6	2.21e-03		4779	3	3060	1	2.78e-02	15		
re9	XII	20.0	180.2	6.2	100.90	3.4	46.6	2.24e-03		4995	4995	2899	2967	3.30e-02	3.21e-02		8
re15	XII	20.0	180.3	6.2	99.78	8.3	49.5	2.17e-03	3	4995	0	3034	5	3.11e-02	6		

nd: Not determined

Two remarks must be made when comparing results from samples No. IX, XII and XIII (last column, Table 3.2). First, the N_v^* values for sample No. IX, XII and XIII are approximately equal (within $\pm 4\%$) although samples No. XII and XIII are 4 times thicker than No. IX. Second, it should be noted that for most of the convective and all I.R. drying results presented in chapter VI, T_b is always lower than T_s despite the relatively high thickness-to-diameter ratio (1/5) of the 20 mm samples. These results strongly suggest that, at a macroscopic level, one-dimensional drying conditions prevail within the samples. Further, the average N_v^* value for the 10 mm samples is within $\pm 6\%$ of the average values obtained for the 5 and 20 mm samples. This does not contradict the conclusion about the one-dimensionality of the drying process but does exemplify the magnitude of the sample to sample N_v^* reproducibility which was within $\pm 12\%$ (last column, Table 3.2) for all samples except XI. The systematic higher flux observed for sample No. XI could not be explained simply and stresses the fact that drying data might be affected by a "sample bias" (van Brakel, 1980).

A comparison of N_v^* values found within $\pm 8\%$ for samples No. VI (without thermocouples), XII and XIII (last column, Table 3.2) confirms the validity of the values obtained for sample No. XII and XIII. It also shows that the thermocouples do not change N_v^* significantly because the observed differences are of the same order as N_v^* reproducibility for the same sample ($\pm 7\%$).

Average values of T_∞^* and v_∞^* between experiments were found to be reproducible within $\pm 0.7\text{ K}$ and $\pm 0.3\text{ m/s}$ respectively.

The I.R. heat flux uniformity was inspected on the sample surface at five locations (center, 25 mm from center and 45° , 135° , 225° , 315° orientation from v_∞ direction) using a water-cooled heat flux transducer, 12 mm \varnothing for the measurement area, model 64-2-18-K from Medtherm Corporation. The oven was not heated during these experiments in order to lower the convective contribution to the recorded heat flux; the air temperature ranged from 30°C (2 elements) to 60°C (8 elements). The measurements at the center were carried out 3 times, for 3 velocities and 4 heat fluxes (2 to 8 elements) so that the reproducibility of the measurement technique could be assessed. The maximum reproducibility

intervals of the I.R. heat flux for a given transducer location and v_{∞}^* (3 measurements), were found to be $\pm 1\%$, $\pm 2\%$, $\pm 4\%$ and $\pm 7\%$ for 2, 4, 6 and 8 elements respectively. For the same v_{∞} , heat fluxes recorded at the five positions were within $\pm 5\%$, $\pm 9\%$, $\pm 7\%$ and $\pm 13\%$ for 2, 4, 6 and 8 elements respectively. As a result it is conservatively estimated that the heat flux non-uniformity on the sample surface was always within $\pm 7\%$.

3.6 EXPERIMENTAL UNCERTAINTY

Moffat (1988) has recently summarized a single-sample uncertainty analysis, based on the root-sum-square method (Kline and McClintock (1953)) to describe the uncertainties in experimental results. This procedure, the experimental results and the instrument accuracy ratings obtained from technical specifications (Appendix 3) were used to calculate the maximum experimental uncertainties for the important independent and dependent variables tabulated in Table 3.3. In this thesis, the reported value is the best estimate for the result, and, with 95 % confidence, the true value is believed to lie within $\pm X$ of that value.

The uncertainties on T_{∞} , v_{∞} , T_d , T_{sir} and T_{pi} were calculated through observation of their behavior (variable error contributions) during the P.C.D.R.P. of all experiments. T_{ij} results are given for the convective runs (CO.) and combined convection and I.R. runs (CO.+I.R.). A discussion about the consequences of T_{ij} variation (nonuniformity) upon the computation of h_c^* and q_{is}^* can be found in chapter IV and V. The calibration of the thermocouples used to measure T_s and T_b gives us an uncertainty of about ± 0.5 K. However, perturbations generated by possible thermocouple localization errors and local variation of the porosity linked to the dry and wet patches surface phenomena or hole drilling, increase the uncertainty of the measurement. Furthermore, in case of I.R. heating there is always the possibility of I.R. penetration below the surface level. Thus, the uncertainty reported for T_s and T_b in Table 3.3 should constitute a conservative estimate. Reported values for h_c^* , K_p^* were computed taking into account all these uncertainties. The maximal uncertainty on the transfer coefficient ratios evaluated in chapter IV is $\pm 19\%$ based on results from Table 3.3.

TABLE 3.3

MAXIMUM EXPERIMENTAL UNCERTAINTY
FOR DEPENDENT AND INDEPENDENT VARIABLES

<u>Variables</u>	<u>Maximum Experimental Uncertainty</u>
Particle diameter, d	± 0.002 mm
Sample diameter, D	± 0.5 mm
Sample thickness, b	± 0.2 mm
Porosity, ϵ	± 0.001
Air temperatures, T_{∞} and $T_{\infty i}$ ($i=3,5$)	± 1.0 K
Airflow velocity, v_{∞}	± 0.27 m/s
Pressure, P_{∞}	± 25 N/m ²
Airflow dew-point temperature, T_d	± 0.5 K
I.R. source temperature, T_{sir}	± 5 K
I.R. incident heat flux, q_{is}	$\pm 4\%$
Sample temperature, T_s	± 1 K (CO.) ± 2 K (CO.+ I.R.)
Sample temperature, T_b	± 1 K (CO.)
Bottom plate temperature T_{pj} ($i=1,4$)	± 1 K
Wall temperatures, T_{ti} ($i=1,6$)	± 2 K (CO.) ± 8 K (CO. + I.R.)
Convective heat transfer coefficient, h_c^*	$\pm 7\%$ (CO.)
Convective mass transfer coefficient, K_p^*	$\pm 6\%$ (CO.)
Sample initial moisture content, X_{in}	$\pm 4\%$

CHAPTER IV - CONVECTIVE DRYING EXPERIMENTS

4.1 INTRODUCTION

The objectives of the convective drying experiments are the following:

- a) To verify if the heat and mass transfer analogy (Bird et al., 1960) is applicable to the case of drying a partially saturated surface within the parameter ranges investigated;
- b) To determine the critical moisture content ;
- c) To generate drying data for comparison with I.R. drying results and simulations with the drying front model.

4.2 CONVECTIVE HEAT TRANSFER COEFFICIENTS IN CONVECTION DRYING

The heat and mass transfer coefficients are evaluated from the measured temperatures and the drying rate curve. However, the following assumptions were necessary to evaluate all terms in the energy balance equation applicable to the sample:

- a) The heat and mass transfer coefficients are averaged over the sample evaporation surface and during the pseudo constant drying rate period (P.C.D.R.P) defined by the time interval $[t_1, t_2]$;
- b) The side and bottom surfaces of the sample are assumed to be adiabatic. The water and glass bead specific heat are constant;
- c) Temperature gradients within the sample are negligible during the P.C.D.R.P.. The surface temperature T_s is considered to be representative of the sample temperature.

The most significant physical phenomena contributing to local variations (on the surface) of the heat and mass transfer coefficients are the development of the thermal and concentration boundary layers from the leading edge of the sample (Kays and Crawford, 1980; Basilico and Martin, 1984; Prat, 1986 b; Moynes, 1987; Perrin and Darroles, 1988). The average transfer coefficient approach was preferred as a result of experimental difficulties associated with local measurements of the drying rate N_v as well as T_s and the surface moisture content X_s (Prat, 1991). In section 3.5, it was verified that the drying was essentially one-dimensional, at least on a macroscopic level, thus providing a justification for the second assumption. The third assumption is reasonable for two reasons. First, the temperature difference between the surface and the bottom computed during the P.C.D.R.P. for all convective results was always less than 6 °C. Second, the error generated by such approximation is felt mainly in the sensible heat term in the energy balance equation which represents at most 5 % of the heat of evaporation (Chiang, 1987).

The energy balance for the sample can be written:

$$Q - Q_v = Q_{ac} \quad (4.1)$$

where Q is the rate of heat transfer from the drying air stream to the surface of the sample, W; Q_v is the rate of energy transport by the water vapor, W; Q_{ac} is the rate of heat accumulation inside the sample, W. Q may be expressed as:

$$Q = hA_s(T_\infty - T_s) \quad (4.2)$$

where h is the overall (convective-radiative) heat transfer coefficient, W/m²K; A_s the sample surface area, m² and T_∞ the air temperature, K. Q_v may be expressed as:

$$Q_v = -\frac{dm_w}{dt} h_v \quad (4.3)$$

where the first term of the right-hand side is the instantaneous evaporation rate, kg/s; h_v the vapor enthalpy, J/kg. A detailed summary of all the physical properties of the air, water (vapor or liquid) and the glass beads is given in Appendix 4. The rate of heat accumulation is:

$$Q_{ac} = \frac{d((m_w c_{pw} + m_b c_{pb}) T_s)}{dt} \quad (4.4)$$

where m_w and m_b (Table 3.1) are the water and glass bead mass respectively, kg; c_{pw} and c_{pb} are the water and glass specific heat respectively, J/kgK. After some algebraic manipulation and integration over the time interval $[t_1, t_2]$, the final expression for the average overall heat transfer coefficient h^* during the P.C.D.R.P. is:

$$h^* = \frac{1}{(t_2 - t_1)} \left[\int_{t_1}^{t_2} \left(-\frac{1}{A_s} \left(\frac{dm_w}{dt} \right) \Delta H_v \right) dt + \int_{t_1}^{t_2} \left(\frac{(m_w c_{pw} + m_b c_{pb})}{A_s} \frac{dT_s}{dt} \right) dt \right] / (T_{-}^* - T_s^*) \quad (4.5)$$

Here the first term is the heat of evaporation which can be approximated by multiplying the average mass flux (N_v^*) and the average heat of evaporation of water (ΔH_v^*) calculated at the average surface temperature (T_s^*) during the P.C.D.R.P.. Superscript * indicates that this quantity was averaged from the recorded data during the P.C.D.R.P.. The second term was evaluated using the trapezoid rule for numerical integration and is referred to as an average accumulation heat flux q_{ac}^* , W/m².

The average convective heat transfer coefficient h_c^* (h^* decreases as a result of radiation effect from the test section walls) was derived from a modified form of equation 4.5 viz.

$$h_c^* = \frac{1}{(t_2 - t_1)} \left[\int_{t_1}^{t_2} \left(-\frac{1}{A_s} \left(\frac{dm_w}{dt} \right) \Delta H_v \right) dt + \int_{t_1}^{t_2} \left(\frac{(m_w c_{pw} + m_b c_{pb})}{A_s} \left(\frac{dT_s}{dt} \right) \right) dt - \int_{t_1}^{t_2} q_{rs} dt \right] / (T_{-}^* - T_s^*) \quad (4.6)$$

where q_{ts} is the net radiative heat flux exchanged between the test section walls and the sample. Since the measured T_s and T_{ij} values are almost constant during the P.C.D.R.P., q_{ts} may be replaced by its average value q_{ts}^* computed from the theory of radiation exchange in an enclosure of diffuse-gray surfaces (Siegel and Howell, 1981) and average temperatures (test section surfaces and sample surface). So as to attenuate the effects of potential wall temperature and emissivity non-uniformity and in agreement with the discussion presented in section 5.3, 4 surfaces (sample (1), 2, 3 and planar radiative screen (4)) were chosen to represent the enclosure. Throughout this research the word emissivity refers to the total hemispherical emissivity unless otherwise stated. Appendix 5 summarizes the hypotheses, geometrical location and identification of the surfaces, the shape factors, the equations as well as the solution technique.

The theory of radiation exchange in an enclosure of diffuse-gray surfaces was applied for four reasons:

- a) Siegel and Howell (1981) have presented measured data for the hemispherical normal spectral reflectivity of an aluminized silicone paint. Within the range 1-25 μm , it was almost independent of wavelength. Thus the test section walls can be considered to be gray;
- b) Schonhorst and Viskanta (1968) tested the appropriateness of the various analytical techniques to compute the radiant exchange between diffuse, specular and diffuse-specular surfaces. They found that regardless of the presence of specular surfaces, the diffuse surface analysis agreed best with experimental results. Siegel and Howell (1981) emphasized that within enclosures, the directional effects due to the presence of specular surfaces may be small because of the many reflections taking place between the surfaces;
- c) The surface area of possibly specular surfaces (stainless steel plate and aluminium foil) are small as compared to the aluminized painted area (ratio $8.5 \cdot 10^{-2}$ and $3.8 \cdot 10^{-2}$ respectively);

- d) The spectral distribution of the infrared radiation within the test section is relatively concentrated in the long wavelength infrared range ($6.4 \mu\text{m} < \lambda_{\text{max}} < 9.3 \mu\text{m}$) because the temperatures of the various surfaces within the cavity do not differ significantly from each other (40-180 °C maximum range).

The test section surface emissivity E_t (0.28), the planar radiative screen emissivity E_{sc} (0.13) and the sample surface emissivity E_s (0.95) were measured using an infrared pyrometer as described in Appendix 3, according to the procedure presented in Appendix 6.

The method of solution of the linear system of 4 equations with 4 unknowns (Q_j ; Appendix 5) was reliable since q_{ts}^* was equal to 0 when all surfaces temperature were taken to be identical. Furthermore, q_{ts}^* was also derived through use of the well known result for two gray surfaces which see each other and nothing else (Holman, 1981):

$$q_{ts}^* = \frac{\sigma(T_t^{*4} - T_s^{*4})}{\frac{1}{E_s} + \frac{A_s}{A_t} \left(\frac{1}{E_t} - 1 \right)} \quad (4.7)$$

where A_t is the overall test section area (including the radiative screen area), σ the Stefan-Boltzman constant and T_t^* is the average test section wall temperature taken equal to T_∞^* . A comparison of q_{ts}^* determined with each procedure generated differences lower than 2.8 % (based on average q_{ts}^*) in all cases. These differences can be explained by the increase in accuracy (Siegel and Howell, 1981) which result from increasing the number of areas describing the enclosure. Since the present differences are already low, one can expect to gain very little through use of additional surfaces.

The experimental parameters (run name, sample number, b , T_∞^* , v_∞^* , P_∞^* , T_d^*) characterizing each convective run as well as T_s^* , T_2^* , T_3^* , N_v^* , q_{ac}^* , q_{ts}^* , h^* , h_c^* and S are reported in Table 4.1.

TABLE 4.1

HEAT TRANSFER COEFFICIENTS FROM THE CONVECTIVE DRYING RUNS

Run	Sa.	b	T_{∞}	v_{∞}	P_{∞}	T_d	T_s	T_2	T_3	N_v	q_{ac}	$q_{ac}\%$	q_{ts}	$q_{ts}\%$	h	h_c	S
No.	No.	(mm)	(°C)	(m/s)	(kPa)	(°C)	(°C)	(°C)	(°C)	(kg/m ² s)	(W/m ²)	(%)	(W/m ²)	(%)	(W/m ² K)	(W/m ² K)	(.)
co2	X	10.3	79.9	2.0	99.37	3.0	30.6	77	73	0.55e-03	10	0.7	330	24.9	27.1	20.4	0.68-0.28
re18	XI	19.9	79.8	2.0	99.43	2.4	30.6	77	73	0.58e-03	30	1.9	330	23.6	29.0	22.2	0.82-0.39
co15	IX	5.5	80.2	4.5	99.53	3.0	29.3	79	76	0.83e-03	20	0.9	350	17.4	40.0	33.1	0.64-0.36
co4	X	10.3	80.5	4.5	99.46	5.2	32.9	79	77	0.79e-03	20	0.8	340	17.7	40.3	33.3	0.61-0.27
co3	XI	19.9	80.6	4.5	99.46	5.2	33.2	79	77	0.85e-03	40	1.8	340	16.3	44.0	36.9	0.73-0.39
co7	X	10.3	130.6	2.2	99.59	3.9	40.5	124	114	0.97e-03	20	0.9	760	32.6	26.1	17.7	0.61-0.28
co6	XI	19.9	130.7	2.2	99.49	3.4	43.0	124	113	0.96e-03	40	1.6	740	32.1	26.8	18.3	0.68-0.26
co9	IX	5.5	130.4	5.0	99.54	1.5	39.8	127	121	1.42e-03	60	1.7	810	23.6	38.4	29.5	0.66-0.35
co12	X	10.3	130.5	4.9	99.63	-1.8	42.2	127	121	1.35e-03	60	1.7	800	24.6	37.3	28.3	0.60-0.27
co8	XI	19.9	130.4	5.0	99.58	1.6	43.3	127	121	1.32e-03	100	3.0	800	24.9	37.4	28.4	0.71-0.31
co11	X	10.3	180.5	2.6	98.79	2.1	48.6	169	153	1.50e-03	50	1.4	1370	38.2	27.5	17.2	0.50-0.24
co10	XI	19.9	180.6	2.6	99.30	1.2	51.8	169	153	1.47e-03	70	1.9	1350	38.7	27.6	17.1	0.52-0.22
re12	IX	5.5	180.5	5.9	100.25	6.6	44.6	173	163	2.20e-03	80	1.5	1480	28.2	39.3	28.4	0.62-0.34
re21	IX	5.5	180.0	6.2	98.15	4.6	46.1	173	163	2.23e-03	80	1.6	1470	27.6	40.4	29.4	0.63-0.37
re7	X	10.3	180.3	6.0	101.06	3.1	45.3	174	164	2.14e-03	100	2.0	1490	29.1	38.7	27.6	0.53-0.42
re14	X	10.3	180.3	6.1	99.91	7.5	47.0	174	164	2.03e-03	120	2.4	1480	30.5	37.3	26.1	0.60-0.29
re25	X	10.3	179.8	6.3	98.15	4.4	48.3	174	164	2.11e-03	130	2.6	1470	29.1	39.3	28.2	0.60-0.32
re27	X	10.3	179.8	6.3	98.17	3.4	50.0	174	165	1.99e-03	120	2.5	1460	30.7	37.4	26.2	0.63-0.24
re10	XI	10.3	180.3	6.1	100.87	3.8	46.2	174	164	2.35e-03	110	2.0	1490	26.5	42.7	31.6	0.59-0.35
re16	XI	10.3	180.3	6.1	99.78	7.1	45.7	174	164	2.35e-03	80	1.5	1490	26.5	42.5	31.4	0.51-0.27
re24	XI	10.3	179.8	6.3	98.15	4.7	48.4	174	164	2.36e-03	100	1.7	1470	26.1	43.6	32.4	0.46-0.24
re26	XI	10.3	179.9	6.3	98.15	4.0	47.0	174	164	2.39e-03	140	2.4	1480	25.8	44.0	32.9	0.69-0.25
re6	XI	19.9	180.4	6.1	101.11	2.2	46.6	174	165	2.25e-03	210	3.9	1480	27.5	41.7	30.7	0.64-0.37
re13	XI	19.9	180.3	6.1	100.13	7.8	45.6	174	165	2.21e-03	180	3.4	1500	28.3	40.5	29.4	0.64-0.36
re9	XII	20.0	180.3	6.2	100.90	3.4	46.6	174	165	2.24e-03	220	4.0	1490	27.8	41.7	30.5	0.75-0.32
re15	XII	20.0	180.3	6.2	99.78	8.3	49.5	174	165	2.17e-03	220	4.3	1470	28.5	41.2	30.0	0.69-0.32

T_2^* and T_3^* were computed by averaging the recorded temperature from the thermocouples located on their surfaces (T_{11}^* , T_{13}^* , T_{15}^* : 2; T_{12}^* , T_{14}^* , T_{15}^* : 3). The radiative screen temperature was taken equal to T_∞^* . Values reported in the S column represent the average bed saturation at the start (t_1) and end (t_2) of the P.C.D.R.P.. In Table 4.1, q_{ac}^* % and q_{ts}^* % express in percent the ratio of q_{ac}^* and q_{ts}^* to the heat of evaporation ($N_V^* \Delta H_V^*$).

It can be observed that q_{ac}^* % ranges from 0.7 % (80 °C, 10.3 mm) to 4.3 % (180 °C, 20.0 mm). It increases as T_∞^* and v_∞^* increases. q_{ac}^* % is almost the same for 5.5 and 10.3 mm samples while it is about 1.5 to 3 times higher for a 20 mm than for a 10.3 mm sample.

For the same v_∞^* and T_∞^* , all computed q_{ts}^* differ by less than 5 %. This is a consequence of the good reproducibility of all the recorded surface temperature values (T_∞^* , T_s^* , T_2^* and T_3^* in Table 4.1). However, at the same T_∞^* , q_{ts}^* increases on the average by 3 % (80 °C), 6 % (130 °C) and 8 % (180 °C) when the velocity is approximately doubled. These small variations are easy to explain as the wall temperatures increase with v_∞^* through the increased rate of convective heat transfer to the walls which are not perfectly adiabatic. q_{ts}^* % ranges between 16 % to 39 % and is a relatively strong function of velocity since it decreases on the average by 34 % (80 °C), 28 % (130 °C) and 31 % (180 °C) when the velocity is doubled. A velocity rise, increases the magnitude of the convective heat transfer and thus decreases the relative contribution of radiation. These results undoubtedly show that the radiative heat flux from the walls contributes significantly to the mass flux in a small scale apparatus where the ratio (A_s/A_t) is very small ($\sim 9.1 \cdot 10^{-3}$). q_{ts}^* % was also identified to range from 30 % at $v_\infty^* = 18.6$ m/s to 50 % at $v_\infty^* = 6.2$ m/s by Basilico and Martin (1984) in an experimental study of superheated steam drying of wood at high temperature ($T_\infty^* = 150-190$ °C, $v_\infty^* = 6-19$ m/s).

Chiang (1987) presented experimental h^* values in the range (14.6-35.8 W/m²K) from drying experiments in a square duct (20 mm x 20 mm) with T_∞^* in the interval [75-85 °C], similar v_∞^* (1.4-5.6 m/s) and a small surface size sample (49X20 mm). In Table 4.1, a comparable h^* range may be found (26.1-44.0 W/m²K) for $T_\infty^* = 80$ °C. Though A_s/A_t are approximately the same in both

studies, at ($T_{\infty}^* \sim 85 \text{ }^{\circ}\text{C}$, $v_{\infty}^* \sim 4.6 \text{ m/s}$), h^* was $35.8 \text{ W/m}^2\text{K}$ in Chiang 's study while here it is found to be between 40.0 and $44.0 \text{ W/m}^2\text{K}$. This can be explained by the fact that the test section flow, in the present study, is not fully developed at the sample location which results in higher local h values (Kays and Crawford, 1980). Furthermore, the turbulence intensity is likely to be higher due to the presence of the flow mixer. The usual behavior of h^* increasing with increase in v_{∞}^* can be observed in Table 4.1 (column sixteen).

h_c^* (column seventeen, Table 4.1) is lower by 17.5 % to 46.9 % as compared to h^* . The actual experimental range of h_c^* ($17.1\text{-}36.9 \text{ W/m}^2\text{K}$) is well within the range ($11.6\text{-}116.0 \text{ W/m}^2\text{K}$), taken as representative by Bird et al. (1960), for forced convection of gases. However, it is on the low side of this range because the flow velocities in this work are low and the flow direction is parallel to the surface.

4.3 TEST OF THE ANALOGY BETWEEN THE HEAT AND MASS TRANSFER IN CONVECTION DRYING

The concept of analogy between momentum, heat and mass transfer was first put forward by Chilton and Colburn (1934). Since then, theoretical considerations as well as most experimental studies have confirmed this concept. However, questions have been raised recently (Pilitsis, 1986; Prat, 1986b; Perrin and Darolles, 1988; Rogers and Kaviany, 1990; Prat, 1991) about the applicability of such a concept to the case of prediction of the effective or average transfer coefficients in drying when the surface is not fully wetted. It is also becoming common to find drying studies (Plumb et al., 1985; Kaviany and Mittal, 1987; Chen and Pei, 1989) where the heat and mass transfer coefficients are taken to vary as a function of the surface moisture content. Since only limited experimental data have been presented to substantiate these conclusions in the drying literature, it is of interest to test the analogy based on a significant number of experimental determination of the average (over the surface area and during the P.C.D.R.P.) heat and mass transfer coefficients over a wide operating range.

In most cases convective drying can be considered to be a low mass flux process; thus two average mass transfer coefficients were computed from the experimental results. One is the classical mass transfer coefficient K_p^* (m/s) defined in the following way from the mass flux N_v^* :

$$N_v^* = K_p^*(\rho_{vs}^* - \rho_{v\infty}^*) \quad (4.8)$$

where ρ_{vs}^* and $\rho_{v\infty}^*$ are the water vapor density at the sample surface and within the test section flow respectively, kg/m^3 . ρ_{vs}^* was computed from T_s^* through use of the saturation pressure (Appendix 5) and perfect gas law and $\rho_{v\infty}^*$ from T_d^* . The usual definition (Nienow et al., 1969; Bird et al., 1960) of the mass transfer coefficient K_y^* ($\text{mol/m}^2\text{s}$) at high mass flux is:

$$N_v^* = K_y^* M_w \left(\frac{y_{vs}^* - y_{v\infty}^*}{1 - y_{vs}^*} \right) \quad (4.9)$$

where y_{vs}^* and $y_{v\infty}^*$ are the water vapor mole fraction at the sample surface and within the test section flow respectively and M_w is the molecular weight of water, kg/mol . In equation 4.9 the driving force (written B_K later on) expresses the ratio of the molar flux by bulk flow to the flux by molecular transport at the interface (Bird et al., 1960) upon the assumption of diffusion through a stagnant film (the molar flux of air is 0 at the interface). Both mass transfer coefficients (K_p^* , K_y^*) were used to calculate the following transfer coefficient ratios (Bird et al., 1960; Incropera and De Witt, 1985):

$$\left(\frac{Nu}{Sh_p} \frac{Sc}{Pr} \right)^* = \frac{h_c^*}{K_p^*(\rho_g c_{pg})_i} \quad (4.10)$$

$$\left(\frac{Nu}{Sh_y} \frac{Sc}{Pr} \right)^* = \frac{h_c^*(c_g)_i}{K_y^*(\rho_g c_{pg})_i} \quad (4.11)$$

where Nu^* is the Nusselt number (evaluated with h_c^*), Sh^* the Sherwood number (evaluated with K_p^* or K_y^*), ρ_g the gaseous mixture density, kg/m^3 ; c_{pg} the specific heat of the gaseous mixture at constant pressure, J/kgK ; c_g is the total molar concentration, mol/m^3 . The f subscript means that the quantity is evaluated at the mean film temperature and composition. Sc^* is the Schmidt number defined as:

$$Sc^* = \left(\frac{\mu_g}{\rho_g D_{va}} \right)_f \quad (4.12)$$

where μ_g (kg/ms) is the dynamic viscosity of the gaseous mixture and D_{va} (m^2/s) the binary diffusivity of vapor in air. Pr^* is the Prandtl number written as:

$$Pr^* = \left(\frac{\mu_g c_{pg}}{k_g} \right)_f \quad (4.13)$$

where k_g is the thermal conductivity of the gaseous mixture, (W/mK).

It was also decided to test the usual mass transfer correction procedures (boundary layer theory, film theory, penetration theory), summarized by Bird et al. (1960), using K_p^* and K_y^* . The corrected (with the boundary layer theory) mass transfer coefficient, K_{pBL}^* and K_{yBL}^* were defined by:

$$K_{pBL}^* = \frac{K_p^*}{\theta_K} \quad (4.14)$$

$$K_{yBL}^* = \frac{K_y^*}{\theta_K} \quad (4.15)$$

where the correction factor for the mass transfer coefficient θ_K was conveniently correlated (polynomial regression) as a function of B_K and the correction procedures from curves presented by Bird et al. (1960):

Boundary layer theory:

if $0.1 < (1 + B_K) < 10.0$

$$\ln(\theta_K) = 9.9944 \cdot 10^{-3} - 0.7738 \cdot \ln(1+B_K) - 5.5954 \cdot 10^{-2} \cdot (\ln(1+B_K))^2 \quad (4.16)$$

Film theory:

if $0.1 < (1 + B_K) < 10.0$

$$\ln(\theta_K) = -1.7146 \cdot 10^{-3} - 0.50775 \cdot \ln(1+B_K) - 4.0239 \cdot 10^{-2} \cdot (\ln(1+B_K))^2 \quad (4.17)$$

Penetration theory:

if $0.1 < (1 + B_K) < 10.0$

$$\ln(\theta_K) = 4.3753 \cdot 10^{-3} - 0.64831 \cdot \ln(1+B_K) - 3.4881 \cdot 10^{-2} \cdot (\ln(1+B_K))^2 \quad (4.18)$$

The corresponding correlation coefficients r were 1.00 and 59 points were used for each of the correlations. Although, it is not strictly correct to apply any of the correction procedures to K_p^* , this attempt was made to verify if, from an engineering point of view, we can still obtain a good prediction of the effect of high mass transfer rate on K_p . Equations 4.14 and 4.15 may include an additional correction factor because the theories put forward to account for high mass transfer rate effect assumed constant physical properties. It is possible to correct the mass transfer coefficient unaffected by the evaporating rate for the effect of density variation between the evaporating surface and the external flow. For gases, no correction for variation of viscosity or diffusivity is necessary because these quantities are relatively insensitive to concentration (Nienow, 1967). Hanna (1962) has put forward an approximate method which relies on the following correction factor:

$$H_c = \frac{(K_{BL}^*)_{varp}}{(K_{BL}^*)_{constp}} = \frac{\ln\left(\frac{M_s^*}{M_\infty^*}\right)}{\left(\frac{M_s^*}{M_\infty^*} - 1\right)} \quad (4.19)$$

Here, $(K_{BL}^*)_{constp}$ is either K_{pBL}^* or K_{yBL}^* already defined. M^* is the gas mixture average molecular weight (mol/m³) evaluated at the surface (_s) or for the flow conditions (_∞). H_c is Hanna's correction factor. Mendelson and Yerazunis (1965) and Loughlin et al. (1985) tested successfully the appropriateness of this relation to account for the effects of density variations (evaporation at the stagnant point of a cylinder, liquid droplet evaporation). A similar correction for the heat transfer coefficient which take into account the effect of density variation could not be found in the literature.

The heat transfer coefficient h_c^* was also corrected to yield h_{cBL}^* (the heat transfer coefficient when no mass transfer is present):

$$h_{cBL}^* = \frac{h_c^*}{\theta_h} \quad (4.20)$$

where the correction factor for the heat transfer coefficient θ_h was correlated as a function of the correction procedure (the correlation is the same as the one for θ_K) and B_h , which is the ratio of energy flux by bulk flow to the flux by molecular transport at the interface, may be written:

$$B_h = \frac{N_v^*(c_{pv})_s}{h_c^*} \quad (4.21)$$

where c_{pv} is the vapor specific heat (J/kgK). Again the ratios already defined in equations 4.10 and 4.11 were computed with h_{cBL}^* , $(K_{pBL}^*)_{varp}$ and $(K_{yBL}^*)_{varp}$:

$$\left(\frac{Nu_{BL}}{Sh_{pBL}} \frac{Sc}{Pr}\right)^* = \frac{h_{cBL}^*}{(K_{pBL}^*)_{varp} (\rho_g c_{pg})_t} \quad (4.22)$$

$$\left(\frac{Nu_{BL}}{Sh_{yBL}} \frac{Sc}{Pr} \right)^* = \frac{h_{cBL}^* (c_g)_f}{(K_{yBL})_{var\rho}^* (\rho_g c_{pg})_f} \quad (4.23)$$

The experimental parameters (run name, sample number, b , T_∞^* , v_∞^* , P_∞^* , T_d^*) characterizing each convective run as well as h_c^* , h_{cBL}^* , θ_h , θ_K , H_c , K_p^* , 4.10, $(K_{pBL})_{var\rho}^*$, 4.22, K_y^* , 4.11, $(K_{yBL})_{var\rho}^*$, 4.23 and $(Sc/Pr)_f^{*(2/3)}$ are reported in Tables 4.2a and b.

The magnitude of the correction applied to the heat transfer coefficient h_c^* to get h_{cBL}^* is characterized by the correction factor θ_h (Table 4.2a) almost constant for a specific temperature i.e. the average θ_h are 0.97 ± 0.01 (80 °C), 0.94 ± 0.01 (130 °C) and 0.91 ± 0.01 (180 °C). These results are comparable to correction factors in the order of 0.97 to 0.93 ($T_\infty^* = 150-190$ °C, $v_\infty^* = 6.2-18.6$ m/s) presented by Basilico and Martin (1984). θ_h does not appear to depend significantly on v_∞^* .

For the mass transfer coefficient K_p^* and K_y^* , the correction is slightly lower because the correction factors are greater; the average θ_K (Table 4.2a) are 0.98 ± 0.01 (80 °C), 0.95 ± 0.01 (130 °C) and 0.93 ± 0.01 (180 °C). Again, θ_K is not a function of v_∞^* .

H_c (Table 4.2a) was found to be in the range 1.01 (80 °C) to 1.03 (180 °C); It increase slightly with $(T_\infty^* - T_s^*)$ and is not a function of v_∞^* or T_d^* . Thus the increase of the mass transfer coefficient as a result of density variation is low in the case of convective drying over the operating range investigated.

The means of the right-hand side of equations 4.10, 4.11, 4.22 and 4.23 computed from all experimental results reported in Tables 4.2 are 1.01, 0.93, 1.01 and 0.93 respectively, while their standard deviation are 0.12, 0.13, 0.11 and 0.12 respectively (last row, Table 4.2a and b). The order of magnitude of the scatter quantified by these results is not unusual when the heat and mass transfer coefficients are determined simultaneously (Heertjes and Ringens, 1956; Obot and Trabold, 1992).

TABLE 4.2a

THE TRANSFER COEFFICIENT RATIOS FROM THE CONVECTIVE DRYING RUNS

Run No.	Sa. No.	b	T _∞ *	v _∞ *	P _∞ *	T _d *	h _c *	h _{cBL} *	θ _h	θ _K	H _c	K _p *	$\left(\frac{Nu Pr}{Sh_p Sc}\right)^*$	(K _{pBL}) _{varp}	$\left(\frac{Nu_{BL} Pr}{Sh_{pBL} Sc}\right)^*$	
(.)	(.)	(mm)	(°C)	(m/s)	(kPa)	(°C)	(W/m ² K)	(W/m ² K)	(4.16)		(4.19)	(m/s)	(4.10)	(m/s)	(4.22)	
co2	X	10.3	79.9	2.0	99.37	3.0	20.4	21.0	0.97	0.98	1.01	2.05e-02	0.93	2.10e-02	0.94	
re18	XII	19.9	79.8	2.0	99.43	2.4	22.2	22.8	0.97	0.98	1.01	2.14e-02	0.97	2.20e-02	0.97	
co15	X	5.5	80.2	4.5	99.53	3.0	33.1	34.0	0.97	0.98	1.01	3.39e-02	0.91	3.47e-02	0.91	
co4	X	10.3	80.5	4.5	99.46	5.2	33.3	34.1	0.98	0.98	1.01	2.62e-02	1.19	2.70e-02	1.18	
co3	XII	19.9	80.6	4.5	99.46	5.2	36.9	37.8	0.98	0.98	1.01	2.78e-02	1.25	2.87e-02	1.24	
co7	X	10.3	130.6	2.2	99.59	3.9	17.7	18.9	0.94	0.96	1.01	2.02e-02	0.89	2.14e-02	0.89	
co6	XII	19.9	130.7	2.2	99.49	3.4	18.3	19.5	0.94	0.95	1.02	1.75e-02	1.07	1.87e-02	1.06	
co9	X	5.5	130.4	5.0	99.54	1.5	29.5	31.3	0.94	0.96	1.01	3.03e-02	0.99	3.21e-02	0.99	
co12	X	10.3	130.5	4.9	99.63	-1.8	28.3	29.9	0.94	0.95	1.02	2.49e-02	1.15	2.67e-02	1.14	
co8	XII	19.9	130.4	5.0	99.58	1.6	28.4	30.0	0.95	0.95	1.02	2.34e-02	1.23	2.51e-02	1.21	
co11	X	10.3	180.5	2.6	98.79	2.1	17.2	19.1	0.90	0.92	1.02	2.03e-02	0.93	2.24e-02	0.94	
co10	XII	19.9	180.6	2.6	99.30	1.2	17.1	19.0	0.90	0.91	1.03	1.69e-02	1.11	1.91e-02	1.09	
re12	X	5.5	180.5	5.9	100.25	6.6	28.4	31.2	0.91	0.94	1.02	3.70e-02	0.83	3.99e-02	0.85	
re21	X	5.5	180.0	6.2	98.15	4.6	29.4	32.3	0.91	0.93	1.02	3.43e-02	0.95	3.74e-02	0.95	
re7	X	10.3	180.3	6.0	101.06	3.1	27.6	30.4	0.91	0.94	1.02	3.42e-02	0.87	3.70e-02	0.88	
re14	X	10.3	180.3	6.1	99.91	7.5	26.1	28.8	0.91	0.93	1.02	3.03e-02	0.93	3.31e-02	0.94	
re25	X	10.3	179.8	6.3	98.15	4.4	28.2	30.9	0.91	0.92	1.02	2.93e-02	1.06	3.23e-02	1.06	
re27	X	10.3	179.8	6.3	98.17	3.4	26.2	28.7	0.91	0.92	1.02	2.52e-02	1.15	2.81e-02	1.13	
re10	X	10.3	180.3	6.1	100.87	3.8	31.6	34.6	0.91	0.94	1.02	3.59e-02	0.94	3.91e-02	0.95	
re16	X	10.3	180.3	6.1	99.78	7.1	31.4	34.4	0.91	0.94	1.02	3.76e-02	0.91	4.07e-02	0.92	
re24	X	10.3	179.8	6.3	98.15	4.7	32.4	35.5	0.91	0.92	1.02	3.24e-02	1.10	3.58e-02	1.09	
re26	X	10.3	179.9	6.3	98.15	4.0	32.9	36.0	0.91	0.93	1.02	3.52e-02	1.03	3.86e-02	1.03	
re6	XII	19.9	180.4	6.1	101.11	2.2	30.7	33.6	0.91	0.93	1.02	3.35e-02	0.98	3.66e-02	0.98	
re13	XII	19.9	180.3	6.1	100.13	7.8	29.4	32.3	0.91	0.94	1.02	3.55e-02	0.90	3.85e-02	0.91	
re9	XIII	20.0	180.3	6.2	100.90	3.4	30.5	33.4	0.91	0.93	1.02	3.35e-02	0.98	3.66e-02	0.98	
re15	XIII	20.0	180.3	6.2	99.78	8.3	30.0	32.8	0.91	0.92	1.02	2.87e-02	1.14	3.18e-02	1.12	
													Average	1.01		1.01
													Stdev	0.12		0.11

TABLE 4.2b

THE TRANSFER COEFFICIENT RATIOS FROM THE CONVECTIVE DRYING RUNS

Run No.	Sa. No.	b	T _∞ *	v _∞ *	P _∞ *	T _d *	h _c *	h _{cBL} *	K _y *	$\left(\frac{Nu Sc}{Sh_y Pr}\right)$	(K _{yBL}) _{varp} *	$\left(\frac{Nu_{BL} Sc}{Sh_{yBL} Pr}\right)$	$\left(\frac{Sc}{Pr}\right)^{\frac{2}{3}}$	$\left(\frac{Nu_{BL} Sc}{Sh_{yBL} Pr}\right)_{av}$
(.)	(.)	(mm)	(°C)	(m/s)	(kPa)	(°C)	(W/m ² K)	(W/m ² K)	(mole/m ² s)	(4.11)	(mole/m ² s)	(4.23)	(4.24)	(.) Av., Std.
co2	X	10.3	79.9	2.0	99.37	3.0	20.4	21.0	0.79	0.88	0.81	0.88	0.85	80 °C
re18	XII	19.9	79.8	2.0	99.43	2.4	22.2	22.8	0.83	0.92	0.85	0.92	0.85	
co15	IX	5.5	80.2	4.5	99.53	3.0	33.1	34.0	1.33	0.85	1.36	0.85	0.85	
co4	X	10.3	80.5	4.5	99.46	5.2	33.3	34.1	1.00	1.13	1.03	1.12	0.85	
co3	XII	19.9	80.6	4.5	99.46	5.2	36.9	37.8	1.06	1.19	1.09	1.18	0.85	130 °C
co7	X	10.3	130.6	2.2	99.59	3.9	17.7	18.9	0.73	0.82	0.78	0.82	0.82	
co6	XII	19.9	130.7	2.2	99.49	3.4	18.3	19.5	0.62	1.00	0.66	1.00	0.82	
co9	IX	5.5	130.4	5.0	99.54	1.5	29.5	31.3	1.10	0.91	1.16	0.91	0.82	
co12	X	10.3	130.5	4.9	99.63	-1.8	28.3	29.9	0.88	1.09	0.94	1.07	0.82	0.13
co8	XII	19.9	130.4	5.0	99.58	1.6	28.4	30.0	0.82	1.17	0.88	1.15	0.82	180 °C
co11	X	10.3	180.5	2.6	98.79	2.1	17.2	19.1	0.67	0.86	0.75	0.86	0.79	
co10	XII	19.9	180.6	2.6	99.30	1.2	17.1	19.0	0.55	1.05	0.62	1.04	0.79	
re12	IX	5.5	180.5	5.9	100.25	6.6	28.4	31.2	1.32	0.73	1.42	0.74	0.80	
re21	IX	5.5	180.0	6.2	98.15	4.6	29.4	32.3	1.17	0.85	1.27	0.85	0.79	0.10
re7	X	10.3	180.3	6.0	101.06	3.1	27.6	30.4	1.21	0.77	1.31	0.78	0.80	5.5 mm
re14	X	10.3	180.3	6.1	99.91	7.5	26.1	28.8	1.05	0.84	1.15	0.85	0.79	
re25	X	10.3	179.8	6.3	98.15	4.4	28.2	30.9	0.97	0.97	1.07	0.97	0.79	
re27	X	10.3	179.8	6.3	98.17	3.4	26.2	28.7	0.82	1.07	0.92	1.05	0.79	
re10	XI	10.3	180.3	6.1	100.87	3.8	31.6	34.6	1.26	0.85	1.37	0.85	0.79	10.3mm
re16	XI	10.3	180.3	6.1	99.78	7.1	31.4	34.4	1.32	0.80	1.43	0.81	0.79	
re24	XI	10.3	179.8	6.3	98.15	4.7	32.4	35.5	1.08	1.01	1.19	1.00	0.79	
re26	XI	10.3	179.9	6.3	98.15	4.0	32.9	36.0	1.18	0.94	1.30	0.93	0.79	
re6	XII	19.9	180.4	6.1	101.11	2.2	30.7	33.6	1.17	0.88	1.28	0.89	0.79	19.9 mm
re13	XII	19.9	180.3	6.1	100.13	7.8	29.4	32.3	1.25	0.79	1.36	0.80	0.79	
re9	XII	20.0	180.3	6.2	100.90	3.4	30.5	33.4	1.17	0.88	1.28	0.88	0.79	
re15	XII	20.0	180.3	6.2	99.78	8.3	30.0	32.8	0.96	1.05	1.07	1.03	0.79	
Average										0.93		0.93	0.81	
Stdev										0.13		0.12	0.02	

Since the computed means are unchanged by the correction procedure (boundary layer theory), it can be concluded that the intensity of the surface diffusion mass flux does not change significantly the heat and mass transfer analogy in convective drying. This was expected since both transfer coefficients were simultaneously increased approximately by the same amount (between 3 % to 10 %).

4.3.1 COMPARISON WITH THEORETICAL AND PREVIOUS EXPERIMENTAL RESULTS

If one compares the average values obtained for 4.22 and 4.23 (Table 4.2a and b), the trend resulting from the use of the driving force B_K , instead of $\Delta\rho$, is to obtain a verification of the analogy (see the value of 4.24 $((Sc/Pr)_f^{(2/3)})$ in Table 4.2b) written for the case of laminar flow over an isothermal flat plate without mass transfer (Bird et al., 1960):

$$\frac{h_{cBL}^*(c_g)_f}{K_{yBL}^*(\rho_g c_{pg})_f} = \left(\frac{Sc}{Pr}\right)_f^{2/3} \quad (4.24)$$

Bird et al. (1960) did use B_K in their definition of the mass transfer flux because usually K_p^* shows a more complicated dependence on concentration level and mass transfer rate than does K_y^* . Writing 4.24 relies on the assumption that the analogy could be written in terms of the surface average coefficient, a practice commonly adopted in the heat and mass transfer literature.

It is common (Heertjes and Ringens, 1956; Ben Nasrallah et Arnaud 1986; Marseille et al., 1991) to advocate the use of an exponent between (1/2) and (2/3) for the right-hand side of equation 4.24. If one uses 1/2 as the exponent, then in the range of the present experimental results, $Le_f^{(1/2)}$ (Lewis number, $Le=Sc/Pr$) lies between 0.88 and 0.84 (80 °C and 180 °C respectively; average 0.85), whereas with 2/3, it ranges between 0.85 and 0.79 (80 °C and 180 °C respectively; average 0.81). So the range of accepted value for the transfer coefficient ratio (0.80-0.89) is close to the one found experimentally in the present study for 4.23 (0.74-1.18, Table 4.2 b).

For the case of turbulent flow, it is common in heat and mass transfer studies (Eckert and Drake, 1972; Perré, 1987), to assign the value 1 to the right-hand side of equation 4.10, even if the laminar Le deviates from 1. In the present research, the mean of the transfer coefficient ratio in equation 4.10 is 1.01 (last row, Table 4.2a) and agrees very well with such practice.

Hertjees and Ringens (1956) have determined experimentally ($T_{\infty}^* = 47.8$ °C, $v_{\infty}^* = 2.0-4.2$ m/s) h_c^* and K_p^* for water evaporation from a porous earthenware (surface size: 100X50 mm; $b = 20$ mm); from their results the right-hand side of 4.10 can be evaluated to be 1.04 (range 0.83 to 1.28, 9 determinations) with a standard deviation of 0.13. Smolsky and Sergejev (1962) correlated Nu^* and Sh_p^* from carefully controlled liquid evaporation experiment ($T_{\infty}^* = 45-150$ °C, $v_{\infty}^* = 3-15$ m/s) in turbulent flow (surface size: 100 X 176 mm); computing the left-hand side of 4.10 from their correlations gives 0.91. Such values for Nu^* and Sh_p^* were confirmed recently by Adrie et al. (1988) for the case of water evaporation ($T_{\infty}^* =$ room temperature, $v_{\infty}^* = 0.2-6.0$ m/s) from circular discs (90 mm \varnothing) made of filter paper.

The present results (range 0.74-1.25; average 1.01 or 0.93) for the transfer coefficient ratios expressed in terms of K_p^* or K_y^* do fit very well within the range (0.83-1.28; average between 0.82 to 1.04) defined by all the above mentioned results. Some of the referred experimental results have been obtained with similar surface area sample, time and surface average heat and mass transfer coefficient and fully wetted surfaces whereas in the present case the surface was unsaturated.

Preliminary air temperature measurements ($T_{\infty}, T_{\infty i}$ ($i = 1,5$); Figure 3.3) with dried samples when the guard heaters set-points (T_{pi} ($i = 1,2$)) were chosen to equal T_{∞} did show that the thermal gradients were lower than 1 °C from the mid test section level to the test section bottom. Thus the air flow temperature profiles (from $z = 0$ to 50 mm) incident at the sample leading edge can be considered to be uniform (the temperature profile is fully developed). Hence even if the flow in the test section is not fully developed at the sample location, it is probably the simultaneous development of the thermal and concentration boundary layer from the sample leading edge that leads us to a verification of the analogy between

the transfer of heat and mass (Moyné, 1987). For the specific non-hygroscopic capillary porous media ($d = 90\text{-}105\ \mu\text{m}$) used in this study, the analogy between the transfer of heat and mass occurs for S_s value between approximately 0.7 to 0.2 since the reported values of S (last column, Table 4.1) are within the range (0.8-0.6 to 0.4-0.2). Cunningham and Kelly (1980), have shown from experimentally observed moisture content distribution (for $b < 20\ \text{mm}$) that during the P.C.D.R.P. the moisture content is quite uniform throughout the bed thickness; the surface and average moisture content do not differ significantly.

A correlation (Appendix 7) of the heat transfer coefficient (h_{cBL}^*) for comparison in chapter V was developed from the data presented in Table 4.2a. This was necessary since the flow within the test section at the sample location is not fully developed while the flow mixer create a flow with unknown turbulence characteristics. This precluded the use of the correlations published in the literature.

4.3.2 SENSITIVITY STUDY

The average of the right-hand side of 4.23 was computed at constant T_∞^* (last column, Table 4.2b), it was 0.99 (80 °C, 5 evaluations), 0.99 (130 °C, 5 evaluations) and 0.90 (180 °C, 16 evaluations) while their standard deviations were 0.15, 0.13 and 0.10 respectively. Such a decreasing trend for the average may be partially explained by the fact that the theoretical transfer coefficient ratio $(Le)_f^{*(2/3)}$ (Table 4.2b) is also decreasing a function of T_∞^* (0.85 average at 80 °C, 0.79 average at 180 °C).

Similar calculations of the mean were carried out at constant b (last column, Table 4.2b); the average values were found to be 0.84 (5.5 mm, 4 evaluations), 0.92 (10.3 mm, 13 evaluations) and 0.99 (20 mm, 9 evaluations) while their standard deviations were 0.07, 0.11 and 0.13 respectively. Typical distributions of the transfer coefficient ratios from the experimental results (4.23, column 13, Table 4.2b) at constant temperature are given in Figure 4.1a and b for $T_\infty^* = 80\ \text{°C}$ and $T_\infty^* = 130\ \text{°C}$ respectively. In Figure 4.2, similar data are given for $T_\infty^* = 180\ \text{°C}$. A slight effect of b can be observed to exist but it cannot be quantified exactly because few experiments were carried out with the 5.5 mm

sample at each temperature. The overall means (last column, Table 4.2b) for the 10.3 mm (13 experiments) and 19.9 mm (9 experiments) sample are close enough to show that the sample thickness did not affect strongly the transfer coefficient ratios. This is also verified for the mean computed at constant b given in Figure 4.1a and b as well as in Figure 4.2.

A few questions still remain to be answered about the effect of various parameters (E_s , E_t , E_{sc} , T_2^* , T_3^*) on the computed transfer coefficient ratios. A sensitivity analysis was carried due to possible uncertainties on the measured emissivities and of existing differences in recorded wall temperatures. A comparison with results from the film theory as well as penetration theory is also summarized in Table 4.3.

The adopted strategy was to modify each parameter, one at a time, and to calculate the average transfer coefficient ratios. The ranges of E_s values recorded from the emissivity measurement (Appendix 6) were: 1.00-0.95, wet sample surface; 0.91, dry sample surface. Then E_s was chosen as 1.00 (third row, Table 4.3) and 0.91 (second row, Table 4.3). The predicted transfer coefficient ratios for each evaluation were systematically lower (from 0.02 to 0.04) for E_s equal to 1.00 in comparison to the one obtained with E_s equal to 0.91. All these results were within ± 0.02 of the values obtained with E_s equal to 0.95 (first row, Table 4.3). This is also the case for the average values reported in Table 4.3.

The range of E_{sc} measured was (0.11-0.14) but a conservative estimate of an upper boundary for E_{sc} can be taken to be 0.28 (Incropera and De Witt, 1985; Sala, 1986). The average and each values of the transfer coefficient ratio were invariant (or differ by less than 0.02) whether E_{sc} is 0.28 (fourth row, Table 4.3) or 0.13 (first row, Table 4.3). Calculations have shown that the same conclusion can be drawn when E_t was 0.6 (five row, Table 4.3) instead of 0.28 (first row, Table 4.3). 0.6 was selected for E_t because Siegel and Howell (1981) presented such values for a similar aluminized silicone paint.

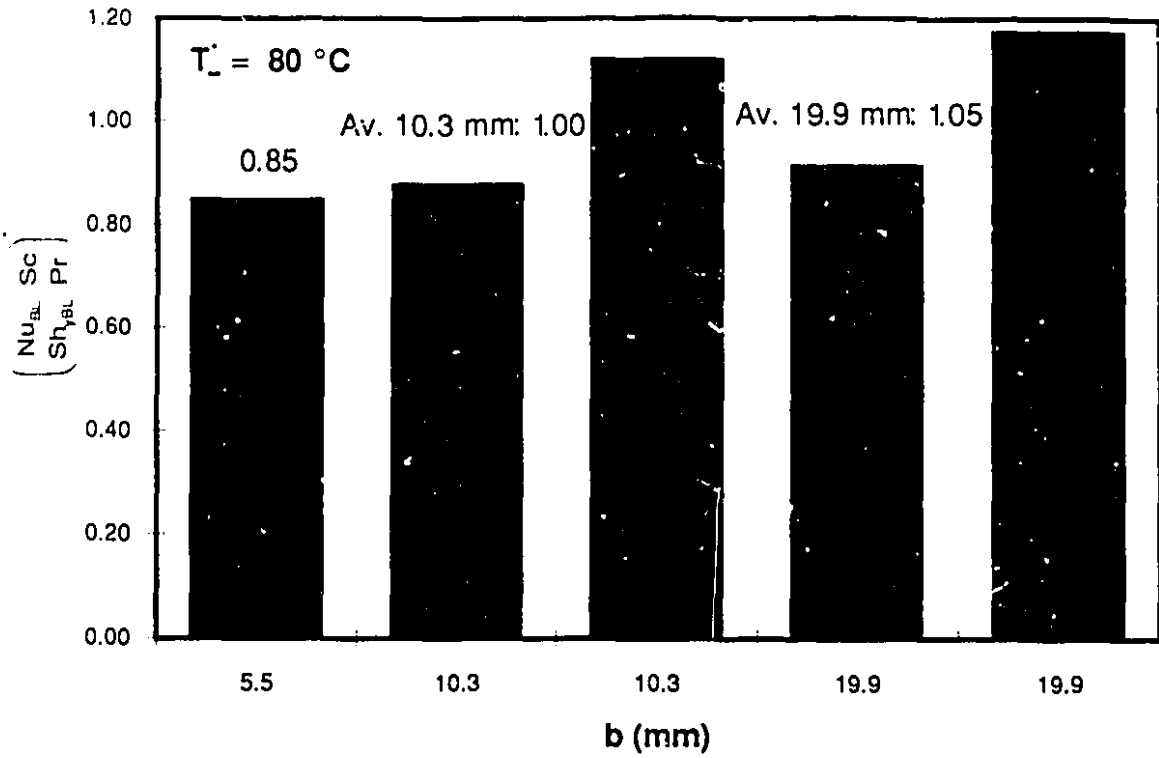


Figure 4.1a A typical transfer coefficient ratio distribution at $T_w = 80 \text{ }^\circ\text{C}$

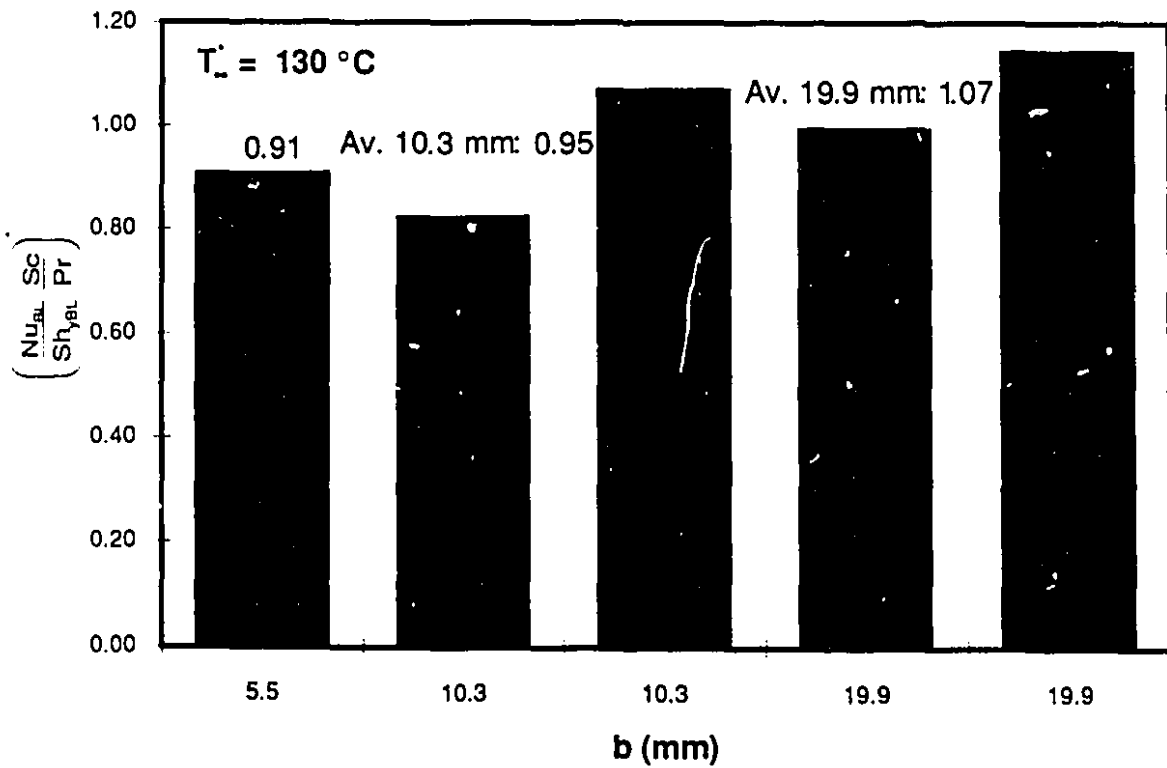


Figure 4.1b A typical transfer coefficient ratio distribution at $T_w = 130 \text{ }^\circ\text{C}$

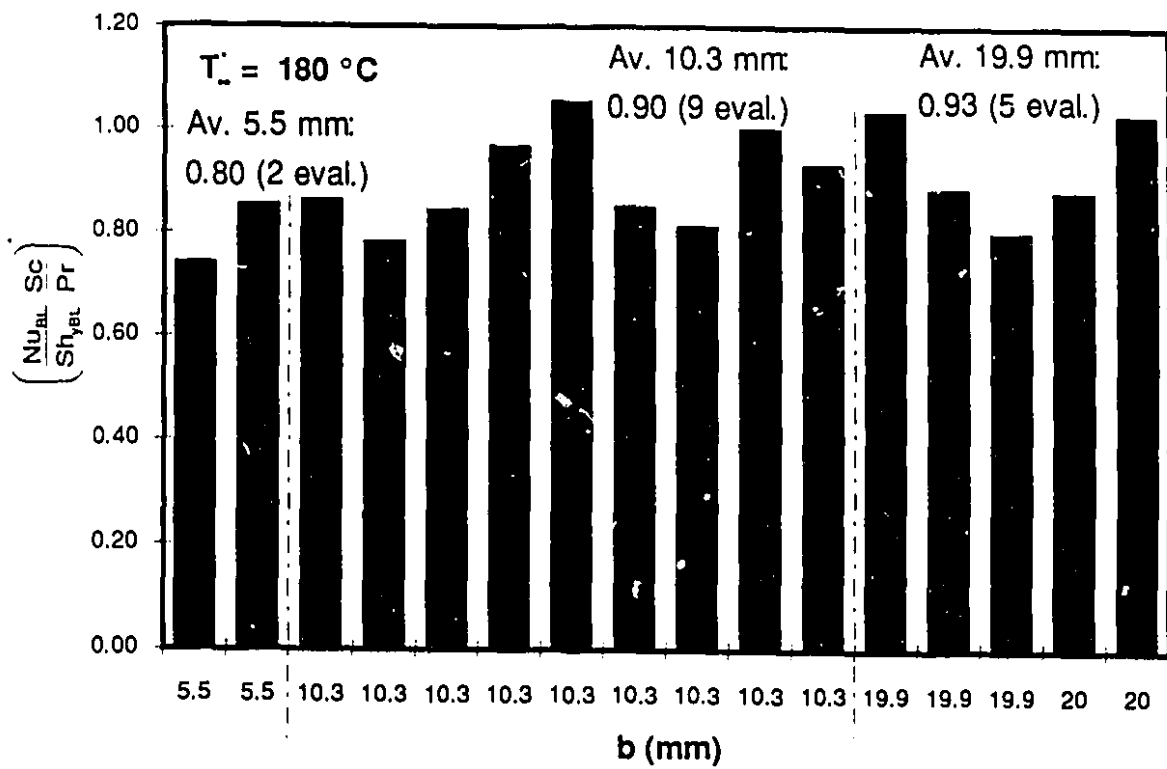


Figure 4.2 A typical transfer coefficient ratio distribution at $T_c = 180 \text{ }^\circ\text{C}$

TABLE 4.3
SENSITIVITY STUDY OF THE TRANSFER COEFFICIENT RATIOS
FROM THE CONVECTIVE DRYING RUNS

Simulation parameters	$\left(\frac{Nu}{Sh_p} \frac{Sc}{Pr}\right)_{av}$ (4.10) Stdev.	$\left(\frac{Nu_{BL}}{Sh_{pBL}} \frac{Sc}{Pr}\right)_{av}$ (4.22) Stdev.	$\left(\frac{Nu}{Sh_y} \frac{Sc}{Pr}\right)_{av}$ (4.11) Stdev.	$\left(\frac{Nu_{BL}}{Sh_{yBL}} \frac{Sc}{Pr}\right)_{av}$ (4.23) Stdev.
$E_s = 0.95, E_{sc} = 0.13, E_l = 0.28$ $T_2^* = \text{Average}(T_{t1}, T_{t3}, T_{t6})$ $T_3^* = \text{Average}(T_{t2}, T_{t4}, T_{t5})$ Boundary Layer Theory	1.01 0.12	1.01 0.11	0.93 0.13	0.93 0.12
$E_s = 0.91$	1.03	1.03	0.95	0.95
$E_s = 1.00$	1.00	1.00	0.92	0.92
$E_{sc} = 0.28$	1.01	1.01	0.93	0.93
$E_l = 0.60$	1.01	1.01	0.93	0.93
$T_2^* = \text{Max}(T_{t1}, T_{t3}, T_{t6})$	1.00	1.00	0.92	0.92
$T_2^* = \text{Min}(T_{t1}, T_{t3}, T_{t6})$	1.03	1.03	0.95	0.94
$T_3^* = \text{Max}(T_{t2}, T_{t4}, T_{t5})$	1.01	1.01	0.93	0.93
$T_3^* = \text{Min}(T_{t2}, T_{t4}, T_{t5})$	1.02	1.01	0.94	0.93
Film Theory	1.01	1.01	0.93	0.93
Penetration Theory	1.01	1.01	0.93	0.93

Maximal temperature differences recorded on surfaces 2 and 3 were always lower than 17 °C and 6 °C respectively. It is possible to bound the temperatures of surface 2 or 3 using the maximum or minimum recorded temperature on each surface. In the case of surface 2, the transfer coefficient ratio was systematically lower (in between 0.02 and 0.04) when using the maximum temperature (six row, Table 4.3) instead of the minimum temperature (seven row, Table 4.3). In the case of surface 3, the transfer coefficient ratios were identical when using the maximum temperature (eight row, Table 4.3) instead of the minimum temperature (ninth row, Table 4.3). The average values of the transfer coefficient ratio using various definition of T_2^* or T_3^* are within ± 0.02 of the reported average values in the first row.

A comparison of the evaluation of the transfer coefficient ratio for each run with the boundary layer (first row, Table 4.3), film (ten row, Table 4.3) or penetration (eleven row, Table 4.3) theories have shown that the differences were less than 0.01. This reflects on the average transfer coefficient ratios which were found to be the same. This result was expected since the θ_h and θ_K for all correction procedures do not show marked differences in the range of values encompassed by B_h ($0.023 < B_h < 0.089$) and B_K ($0.034 < B_K < 0.148$).

The standard deviation of the results given in the first row was unaffected by any of the above mentioned parameter variations.

4.4 CRITICAL MOISTURE CONTENT IN CONVECTIVE DRYING

The critical moisture content X_c , defined according to the procedure described in section 3.4.3, is presented in Table 4.4 where various average X_c values were computed (equivalent average critical saturation S_c are also given). The overall average (last row, Table 4.4) is 0.025 ($S_c = 0.101$) and is comparable to the average computed (last two columns, Table 4.4) with samples having identical thickness b (0.025, 5.5 mm; 0.024, 10.3 mm; 0.024, 20 mm). It may be noted that these averages are all very similar, especially if one accounts for their standard deviation (0.004, overall; 0.005, 5.5 mm; 0.002, 10.3 mm; 0.005, 20 mm).

TABLE 4.4
CRITICAL MOISTURE CONTENT IN CONVECTION DRYING

Run No.	Sa. No.	b	T _∞	v _∞	P _∞	T _d	T _s	q _{ts}	N _v	X _c	S _c	X _{cav} Stdev	S _{cav} Stdev
(.)	(.)	(mm)	(°C)	(m/s)	(kPa)	(°C)	(°C)	(W/m ²)	(kg/m ² s)	(kg/kg)	(.)	(kg/kg)	(.)
co2	X	10.3	79.9	2.0	99.37	3.0	30.6	330	0.55e-03	0.027	0.113	80 °C	
re18	XII	19.9	79.8	2.0	99.43	2.4	30.6	330	0.58e-03	0.022	0.095	0.025	0.105
co15	IX	5.5	80.2	4.5	99.53	3.0	29.3	350	0.83e-03	0.031	0.126		
co4	X	10.3	80.5	4.5	99.46	5.2	32.9	340	0.79e-03	0.025	0.106	0.004	0.015
co3	XII	19.9	80.6	4.5	99.46	5.2	33.2	340	0.85e-03	0.020	0.087		
co7	X	10.3	130.6	2.2	99.59	3.9	40.5	760	0.97e-03	0.019	0.079	130 °C	
co6	XII	19.9	130.7	2.2	99.49	3.4	43.0	740	0.96e-03	0.022	0.096	0.021	0.088
co9	IX	5.5	130.4	5.0	99.54	1.5	39.8	810	1.42e-03	0.022	0.089		
co12	X	10.3	130.5	4.9	99.63	-1.8	42.2	800	1.35e-03	0.022	0.093	0.002	0.007
co8	XII	19.9	130.4	5.0	99.58	1.6	43.3	800	1.32e-03	0.019	0.082		
co11	X	10.3	180.5	2.6	98.79	2.1	48.6	1370	1.50e-03	0.021	0.090	180 °C	
co10	XII	19.9	180.6	2.6	99.30	1.2	51.8	1350	1.47e-03	0.019	0.081	0.025	0.104
re12	IX	5.5	180.5	5.9	100.25	6.6	44.6	1480	2.20e-03	0.021	0.084		
re21	IX	5.5	180.0	6.2	98.15	4.6	46.1	1470	2.23e-03	0.024	0.099	0.004	0.017
re7	X	10.3	180.3	6.0	101.06	3.1	45.3	1490	2.14e-03	0.026	0.112		
re14	X	10.3	180.3	6.1	99.91	7.5	47.0	1480	2.03e-03	0.025	0.106	5.5 mm	
re25	X	10.3	179.8	6.3	98.15	4.4	48.3	1470	2.11e-03	0.026	0.108	0.025	0.100
re27	X	10.3	179.8	6.3	98.17	3.4	50.0	1460	1.99e-03	0.024	0.100	0.005	0.019
re10	XI	10.3	180.3	6.1	100.87	3.8	46.2	1490	2.35e-03	0.024	0.097	10.3 mm	
re16	XI	10.3	180.3	6.1	99.78	7.1	45.7	1490	2.35e-03	0.026	0.110	0.024	0.099
re24	XI	10.3	179.8	6.3	98.15	4.7	48.4	1470	2.36e-03	0.021	0.086		
re26	XI	10.3	179.9	6.3	98.15	4.0	47.0	1480	2.39e-03	0.023	0.093	0.002	0.011
re6	XII	19.9	180.4	6.1	101.11	2.2	46.6	1480	2.25e-03	0.024	0.104	19.9 mm	
re13	XII	19.9	180.3	6.1	100.13	7.8	45.6	1500	2.21e-03	0.028	0.120	0.024	0.104
re9	XII	20.0	180.3	6.2	100.90	3.4	46.6	1490	2.24e-03	0.033	0.140		
re15	XII	20.0	180.3	6.2	99.78	8.3	49.5	1470	2.17e-03	0.031	0.133	0.005	0.022
Average										0.025	0.101		
Stdev										0.004	0.016		

The mean for same T_{∞}^* (last two column, Table 4.3), gives: 0.025 (80 °C), 0.021 (130 °C), 0.025 (180 °C) with similar data scatter (0.004, 80 °C; 0.002, 130 °C; 0.004, 180 °C).

A plot of X_c vs. b , T_{∞}^* , v_{∞}^* , T_d^* , T_s^* , N_v^* , and q_{ts}^* did not show any significant relation between X_c and any of these parameters. A linear increase of X_c with N_v^* has been identified by Wisniak et al. (1967) in convection drying when $d = 44 \mu\text{m}$ ($b = 20 \text{ mm}$, $T_{\infty}^* = 45\text{-}77 \text{ °C}$, $v_{\infty}^* = 2.5\text{-}5.0 \text{ m/s}$) however they also found that X_c was independent of N_v^* when $d = 357 \mu\text{m}$ ($b = 60 \text{ mm}$, $T_{\infty}^* = 38\text{-}74 \text{ °C}$, $v_{\infty}^* = 2.5\text{-}7.5 \text{ m/s}$). Thus the possible dependency of X_c on N_v^* might depend on d or b .

The (X_c/X_{in}) vs. $(N_v^* \cdot b)$ critical point curve (Keey, 1972) is often used to relate X_c to the drying parameters (b , T_{∞}^* , v_{∞}^* , T_d^*) and is given in Figure 4.3 (X_{in} is the initial moisture content). (X_c/X_{in}) does not appear to be a function of $(N_v^* \cdot b)$ although a ten-fold increase of $(N_v^* \cdot b)$ occurs in Figure 4.3. Such behavior has already been reported for $(N_v^* \cdot b)$ values lower than 0.04 kg/mh according to a critical point curve (clay brick, $b = 10\text{-}30 \text{ mm}$, three-fold change in drying rate) presented by Krischer (1963).

The drying rate curves presented by Morgan and Yerazunis (1967) for convective drying of a glass bead bed ($d = 88\text{-}105 \mu\text{m}$, $b = 12.7 \text{ mm}$, $T_{\infty}^* = 66 \text{ °C}$, $v_{\infty}^* = 8.3 \text{ m/s}$) display S_c values in the range 0.2-0.3. Cunningham and Kelly (1980) have found the same range using $112 \mu\text{m}$ \emptyset glass beads ($b = 45 \text{ mm}$, $T_{\infty}^* = 34 - 77 \text{ °C}$). Moyne (1987) reported drying rate curves obtained with $100 \mu\text{m}$ \emptyset glass beads ($2 \text{ mm} \leq h \leq 16 \text{ mm}$, $T_{\infty}^* = 60 \text{ °C}$), S_c can be evaluated to be between 0.22 and 0.28. Two remarks may be made; first a four-fold increase in bed thickness does not change X_c significantly as determined in these studies; the present results are in perfect agreement with this finding (for a similar b range). Second the present average value of S_c (0.101) is lower than the values in the above reported range; this was expected since from the drying rate curve, X_c is usually defined as the average moisture content at the start of the (first) falling rate period whereas in the present study X_c should be considered as an evaluation of the starting point of the (second falling rate period) receding front period (Maneval et al., 1991).

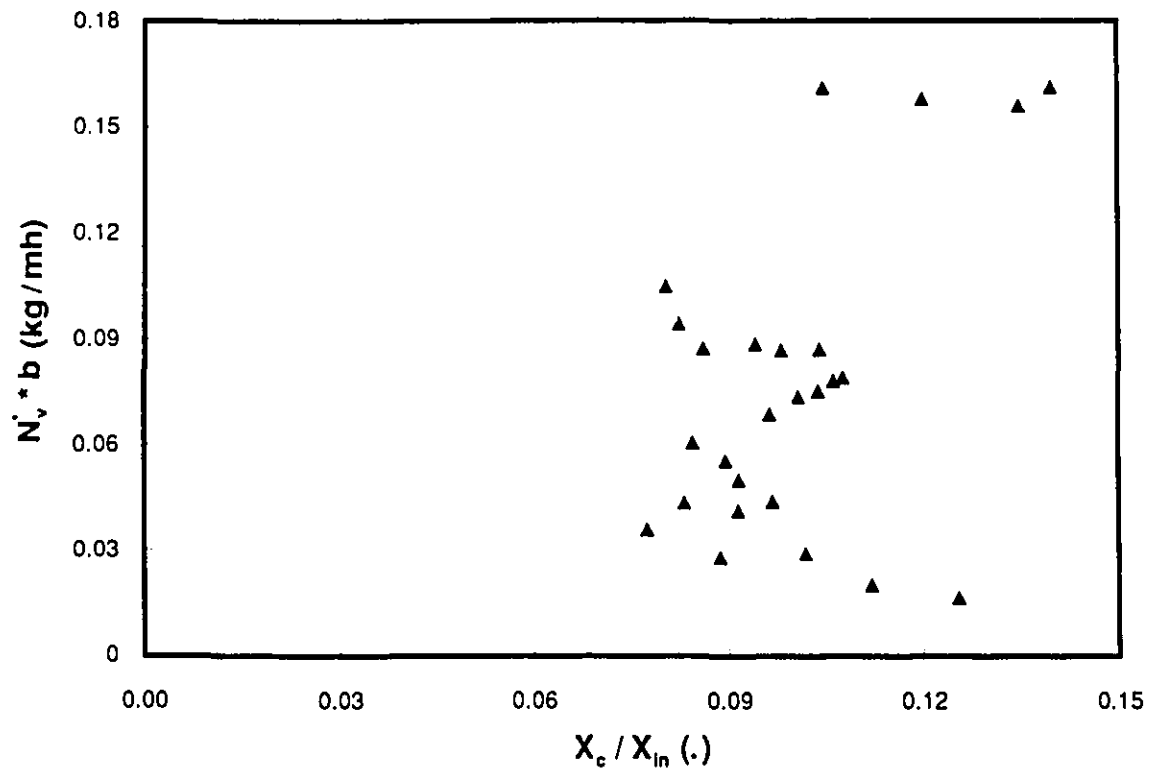


Figure 4.3 The critical point curve from the convective drying results

An experimentally determined curve relating the drying front position (x_f ; from the surface) and the average bed saturation (x_f vs. S) was presented by Morgan and Yerazunis (1967). They concluded that a significant rise in x_f does not occur until S is in the range from 0.08 to 0.17; the present S range (0.079- 0.142) is in close agreement with such a finding.

Cunningham and Kelly (1980) displayed on the S_s vs. S curve, the experimentally determined fact that S is almost constant while S_s goes from S_{ir} (0.10) to zero. In terms of heat transfer, since T_s is usually almost constant as long as water is locally present, more heat is available to be used as sensible heat as S_s goes to zero thus T_s must rise rapidly. Such results suggest that determining the start ($S_s=0$) of the receding front period from a surface temperature measurement is adequate. This is also emphasized by the relatively small spread of S_c found in this research (relatively to X_{in}).

4.5 CONCLUSIONS

Based on the results presented, the following conclusions can be drawn regarding the convective drying process of a capillary porous body (glass beads, $d= 90-105 \mu\text{m}$). In the parameter range investigated ($b = 5.5-20 \text{ mm}$, $T_\infty^* \sim 80-180 \text{ }^\circ\text{C}$, $v_\infty^* \sim 2.0-6.3 \text{ m/s}$, $T_d^* \sim -1.8 - +7.8 \text{ }^\circ\text{C}$):

- (a) The analogy between the heat and mass transfer coefficients has been verified to apply during the pseudo constant drying rate period when the sample surface is unsaturated ($0.2 < S_s < 0.7$). This conclusion applies (within experimental uncertainty) whether the transfer coefficients have been corrected or not to account for the effect of the diffusion mass flux and/or density variation. It was also found that:
 - (i) According to the laminar boundary layer theory correction procedure, unaffected (no mass flux) heat and mass transfer coefficients should be 3 % to 10 % higher than the values

determined experimentally. However, based on the experimental results obtained, it was not possible to determine:

1. The exact magnitude of the heat and mass transfer coefficients decrease due to the diffusion mass flux at the surface
 2. The most appropriate correction procedure to account for the effect of the surface diffusion mass flux on the transfer coefficients.
- (ii) According to the Hanna's correction factor (1962) used to evaluate the effect of density variation between the surface and the flow, unaffected mass transfer coefficients should be 1 % to 3 % lower than the ones predicted with the boundary layer theory for experimentally measured surface temperature ranging from 29 °C to 52 °C. The magnitude of such correction suggests that this effect can be disregarded in convective drying.
- (iii) The very good agreement between the results found and the previous theoretical and experimental findings on the analogy between the transfer of heat and mass (expressed in terms of average heat and mass transfer coefficients ratios) indicates that the experimental test facility built for this research provides a reliable evaluation of the heat and mass transfer coefficients in convective drying.
- (b) The determination of the critical moisture content based on the T_s^* vs. X curve was found to be adequate. It was observed, within experimental uncertainty, that the critical moisture content is independent of the convective drying parameters (T_∞^* , v_∞^* , T_d^*) and sample thickness ($b = 5.5, 10.3$ and 20 mm).

CHAPTER V - COMBINED CONVECTIVE AND INFRARED DRYING EXPERIMENTS

5.1 INTRODUCTION

The objectives of the combined convective and infrared drying experiments are the following:

- a) To verify if the heat and mass transfer analogy² (expressed by the values of the heat and mass transfer coefficient ratios) is applicable to the case of I.R. drying a partially saturated surface within the parameter range investigated;
- b) To determine the critical moisture content in I.R. drying;
- c) To generate combined convective and I.R. drying data for comparison with simulations from the drying front model.

5.2 OVERALL INCIDENT RADIATIVE HEAT FLUX

Attempts to measure the overall incident radiative heat flux q_{iS} (which includes the radiative contributions from the test section walls) using a heat flux transducer were unsuccessful. Thus the water cooled heat flux meter (from Medtherm Corp.; Appendix 3) was calibrated, using a blackbody radiator according to ASTM standard test method E511-73. When inserted in the blackbody radiator opening, the sensor reading was found to rise to a peak value and then decrease significantly (up to 12 %) with time (Figure 5.1). It was also observed that the sensor was very sensitive to lateral heat flux perturbations (conductive or convective) as can be deduced from the heat flux meter temperature (T_h) evolution represented in Figure 5.1.

²See appendix 11 for a discussion concerning the theoretical applicability of the heat and mass transfer analogy in the combined process

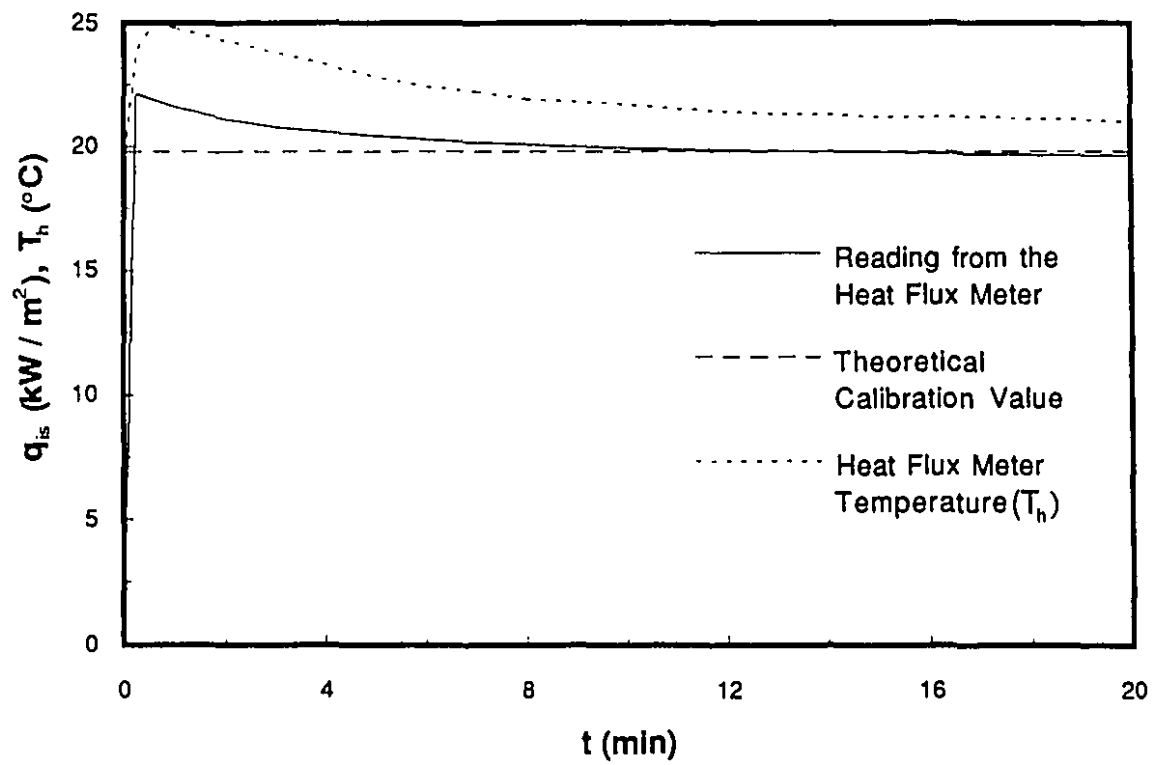


Figure 5.1 A typical q_{is} vs. t curve from the heat flux meter after insertion in the blackbody cavity opening

The conduction heat flux on the meter lateral side was suspected to create the problem as the clearance sensor-opening was very low (~ 1 mm). Baines (1970) advised that such gradient sensor be mounted on a good heat sink to avoid such problems. It is not easy to implement a technical solution within the frame of the calibration procedure. Hence, the incident heat flux and its possible time variations were not measured with this type of heat flux meter for the following reasons:

- a) The reading of the sensor during the calibration is time dependent;
- b) The sensor reading does not stabilize to a fixed value during the calibration procedure (the signal drift still exists after 20 min);
- c) It is not known if the sensor reading under different intensity of lateral heat flux perturbation will be the same for same incident heat flux.

5.2.1 OVERALL INCIDENT RADIATIVE HEAT FLUX IN FREE CONVECTION-I.R. EVAPORATION EXPERIMENTS

A set of I.R. evaporation experiments was undertaken to evaluate q_{is} (W/m^2) with no forced convection present within the test section. Within the frame of this research, such experiments are (for convenience) referred as free convection-I.R. evaporation experiments although no significant convection currents are expected to exist within the test section since the thermal stratification of the air layers between the I.R. heater and the lower test section plate is stable ($T_{sir} \gg T_{pi}$). This type of measurement procedure for q_{is} was also used by Seki et al. (1977) and Shimizu et al. (1990).

The experiments were carried within the test section (with the front panel closed); the fan connected to the ventilation duct (Figure 3.1) was turned off but a slight air evacuation (from the depression created by the central ventilating system) generated v_{∞} lower than 0.1 m/s. In order to "trap" all incident radiation, the vessel (Appendix B) was made of a Pyrex dish (88.5 mm inside \varnothing , 93.5 mm outside \varnothing , internal height 21.5 mm), covered on the outside and on the rim with an aluminium foil ($E_a \sim 0.06$; Incropera, 1985) and painted on the inside with 3M Nextel black paint. This paint was considered to insure that the surface is diffuse (Birkebak, 1972; Enoch, 1984) and a very good absorber ($E_{np} = 0.955$; Enoch, 1984). A Type K stainless steel sheathed thermocouple (0.5 mm \varnothing) was inserted and glued in a hole on the vessel side to measure the water temperature. The position of the measuring bead was at the vessel center, 3 mm from the bottom.

The following assumptions were made to evaluate all the terms in the energy balance equation applicable to the water and vessel:

- a) The air-water interface recession effect is neglected;
- b) The side and bottom surfaces of the vessel are assumed to be adiabatic;
- c) The measured temperature is assumed to be representative of the bed and vessel temperature;
- d) An average free convection heat transfer coefficient is applicable at the vessel surface to evaluate the convective heat transfer loss.

The minimum water thickness found at the end of all experiments was 9 mm (12 mm of height uncovered by water). According to data on the monochromatic absorption coefficient of water (Siegel and Howell, 1981), when $\lambda \geq 2 \mu\text{m}$, the water layer in the vessel can be considered to be optically thick (optical thickness $\gg 1$). It means that the major fraction (~ 89 %) of the heat flux (corresponding to wavelength of a blackbody at $T_s = 850 \text{ }^\circ\text{C}$; $\lambda_{\text{max}} = 2.58 \mu\text{m}$) transmitted through the surface will be absorbed before reaching the bottom of the water layer. Of the remaining 11 % impinging on the 3M Nextel black paint less than about 0.5 % of the originally transmitted heat flux (through the surface water layer) will go back through the water layer and will be refracted as well as reflected at the water-air interface.

A conservative estimate of the side and bottom surface heat loss ($\pm 5 \%$ 2 elements; $\pm 2 \%$ 4, 6 and 8 elements; % given with respect to q_{iS}) was realized through use of the one dimensional conduction heat flux relations (Appendix 8) for planar as well as cylindrical surfaces (Holman, 1981); a radiative energy balance on the dish rim was also taken into account. q_{iS} determined with the energy balance equation 5.3 was increased (or decreased) by only half of these contributions. Since the water layer interface position was not followed during the completion of all experiments, it was not possible to evaluate the size of the uncovered internal side of the vessel, thus the energy lost (radiation or convection) through this area.

Two of the experiments were carried out to quantify the temperature evolutions 3, 9 and 15 mm from the dish bottom as a function of time for 2 and 8 elements. Two additional thermocouples (type K stainless steel sheathed thermocouple, 0.5 mm \varnothing) were inserted from within the test section. In Figure 5.2a and b, the thermocouple readings show the water-air interface reaching 15 mm but not 9 mm before the end of an experiment.

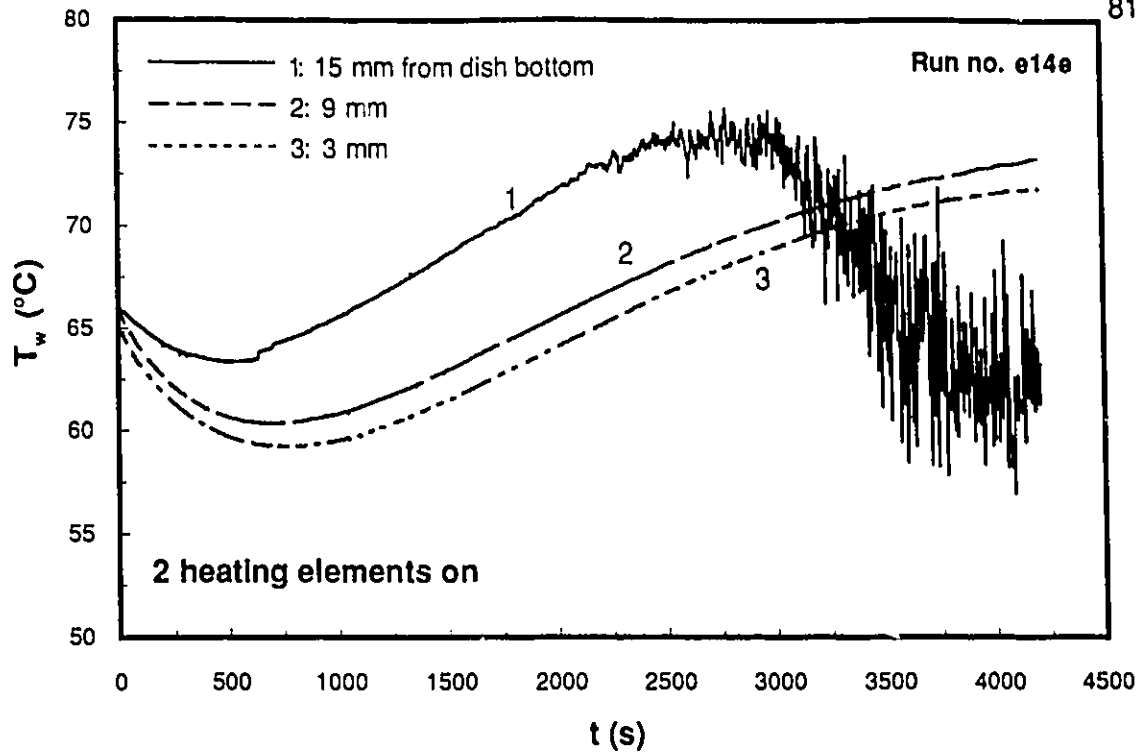


Figure 5.2a Temperature evolution within the water layer during an evaporation experiment (T_w vs. t for 2 heating elements on)

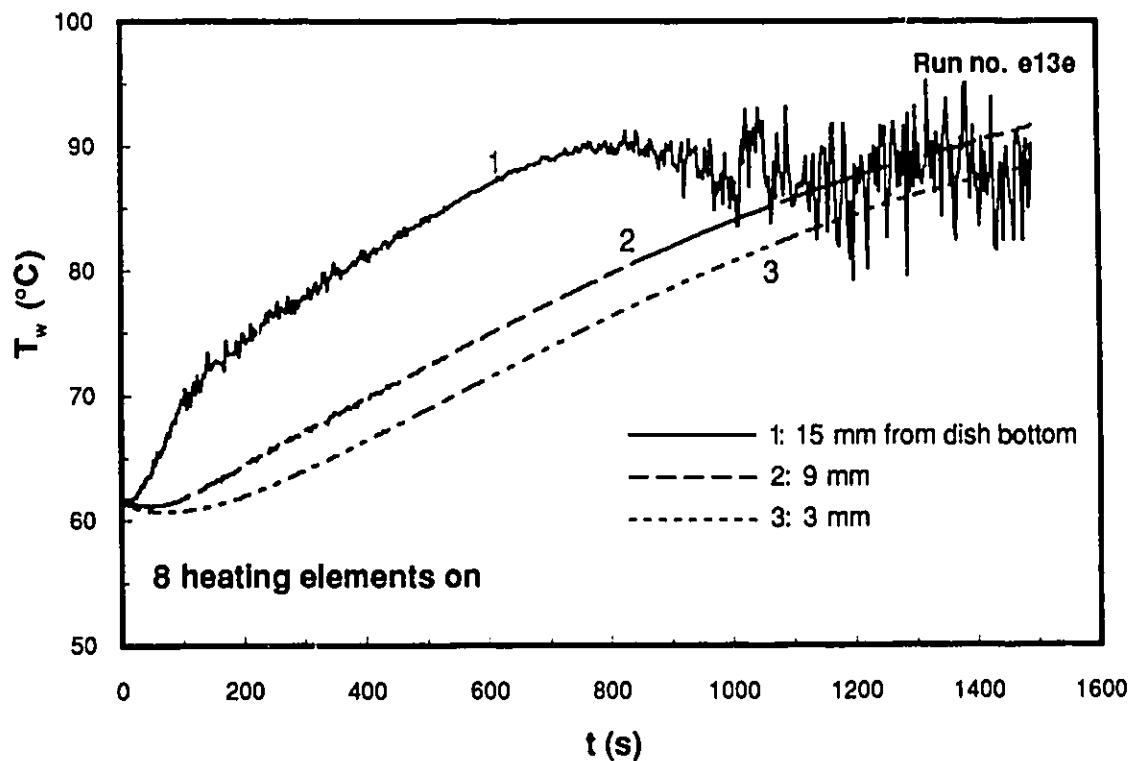


Figure 5.2b Temperature evolution within the water layer during an evaporation experiment (T_w vs. t for 8 heating elements on)

When the thermocouple located at position 1 is uncovered by the water, its reading starts to oscillate because it is submitted to the radiative heat flux close to the evaporation interface. After an initial transient period, it may be noted, that the rates of temperature variation as a function of time are almost the same throughout the water thickness. This suggests that the rate of heat accumulation can be accurately computed through use of the rate of temperature variation as a function of time derived from the temperature measurement at 3 mm from the vessel bottom.

The energy balance for the vessel is still given by equation 4.1. However, Q , the heat transfer by radiation and convection, can now be written (Siegel and Howell, 1981):

$$Q = (E_w q_{ls} - E_w \sigma T_w^4 + h_c (T_3 - T_w)) A_w \quad (5.1)$$

where E_w is the emissivity of water; T_w is the water temperature, K; h_c is the free convection heat transfer coefficient, W/m^2K and A_w the pyrex dish evaporation area (m^2). h_c could be evaluated with the assumption that the heat transfer phenomenon within the test section is one of free convection ($v_\infty < 0.1$ m/s) in an enclosed space where the upper plate is at a higher temperature than the lower plate (Holman, 1981). The average temperature T_3 of surface 3 (Appendix 5) was the arithmetic mean of T_{12} , T_{14} and T_{15} . h_c could not be corrected because the results from the theories to account for high mass transfer rates effect were developed when a velocity profile does exist within the region of interest. h_c was expressed as (Holman, 1981):

$$h_c = \frac{k_a}{e} \quad (5.2)$$

where k_a is the test section air thermal conductivity, W/mK ; e (0.1 m) is the distance separating the upper and bottom plates, m. The evaluation of the convective term is based on the assumption that the conduction heat transfer is between surface 3 and the sample; this should constitute an upper bound for the conduction heat transfer because the temperatures reached by surface 3 as a result of heat transfer to the upper test section plate (Figure 3.3) by conduction

through the stainless steel plate (from the pyramid sides) should be higher than the temperature of the air layer at the upper plate level in front of the source. The latter temperature results almost exclusively from heat transfer by conduction through air since the absorption of radiant energy by the air layer is negligible (Appendix 9). Furthermore, the recorded temperature at the mid test section level (close to the pipe for T_d measurement and shielded with an aluminium foil) did show temperatures close to T_w .

Equations 4.3 and 4.4 are the expressions for Q_v and Q_{ac} . Now, m_b (kg) and c_{pb} (J/kgK) should be considered has the vessel mass (54.38 g) and Pyrex (835 J/kgK; Incropera, 1985) specific heat respectively. q_{is} may be written as:

$$q_{is} = \frac{1}{E_w} \left[-\frac{1}{A_w} \frac{dm_w}{dt} \Delta H_v + \frac{1}{A_w} (m_w c_{pw} + m_b c_{pb}) \frac{dT_w}{dt} - h_c (T_3 - T_w) \right] + \sigma T_w^4 \quad (5.3)$$

E_w was taken to be 0.96 because the water layer can be considered deep as a result of its high monochromatic absorptivity within the wavelength range of the incident radiation (~ 97 % incident energy in the 1-15 μm range), the black coating ($E_{np} = 0.955$) of the vessel (side and bottom) and the thickness of the water layer. Siegel and Howell (1981) gave the normal-total emissivity as 0.96 for water in the temperature range 273-373 K. Shimizu et al (1990) use 0.96 as representative of the hemispherical total emissivity of water when the maximum emissive power of the incident radiation is in between 2.5 to 6 μm and Sala (1986) presented the range 0.95-0.96 (273-373 K) for the hemispherical total emissivity of a 0.1 mm thick water layer.

Each term in equation 5.3 was evaluated according to the procedure defined in sections 3.4.3 and 4.2, from the raw experimental results every 100 s. A typical plot of q_{is} as a function of time is shown in Figure 5.3 (a,b) for the four heat flux levels used; T_{win} defines the initial temperature of the water layer. At the beginning of each experiment, q_{is} values are not presented because the rates of temperature variation were widely different throughout the water layer (Figure 5.2a and b). The duration of experiments with 2, 4, 6 and 8 heating elements on were different and chosen to encompass the whole duration of the experiments

in free convection-I.R. drying of samples (20 mm) using the same number of heating elements.

Experiments for each of the four heat fluxes were conducted using a different hot water temperature ($\sim 60\text{ }^{\circ}\text{C}$ vs. $\sim 20\text{ }^{\circ}\text{C}$) at the start. The results in Figure 5.3 show a decrease of the evaluated q_{is} in the order of only 4 % (2 heating elements), 2 % (4 heating elements), 0 % (6 heating elements) and 4 % (8 heating elements) when using hot water instead of cold water. Thus it is possible to infer that the lack of accuracy on the evaluation of the heat loss by conduction (on the lateral side), convection and radiation (for both, free water surface and lateral uncovered side) has only a small influence on the determination of q_{is} .

In Figure 5.4, at each time step an average value (from all evaluations in Figure 5.3) of q_{is} was computed and correlated through linear regression. The correlation coefficients were 0.950 (2 heating elements), 0.885 (4 heating elements), 0.941 (6 heating elements) and 0.871 (8 heating elements). These correlations are applicable from $t=0$ to the time when the last measurement was reported in Figure 5.3. All q_{is} from the initial experiments in Figure 5.3 were within $\pm 4\%$ (2 and 6 heating elements), $\pm 6\%$ (4 heating elements) and $\pm 7\%$ (8 heating elements) of the values predicted by the correlations.

It may be noted that the slope ($\text{kW}/\text{m}^2\text{s}$) of the q_{is} vs. t curve increases with increase in the heat flux level ($0.210 \cdot 10^{-3}$, 2 heating elements; $0.545 \cdot 10^{-3}$, 4 heating elements; $1.009 \cdot 10^{-3}$, 6 heating elements and $1.417 \cdot 10^{-3}$, 8 heating elements). This is due to the peculiar geometry of the radiative source where activating extra heating elements (symmetrically with respect to the test section symmetry axis) send a greater proportion of energy toward the pyramid internal walls which heat up faster and thus contribute more rapidly (and to a greater extent) to q_{is} .

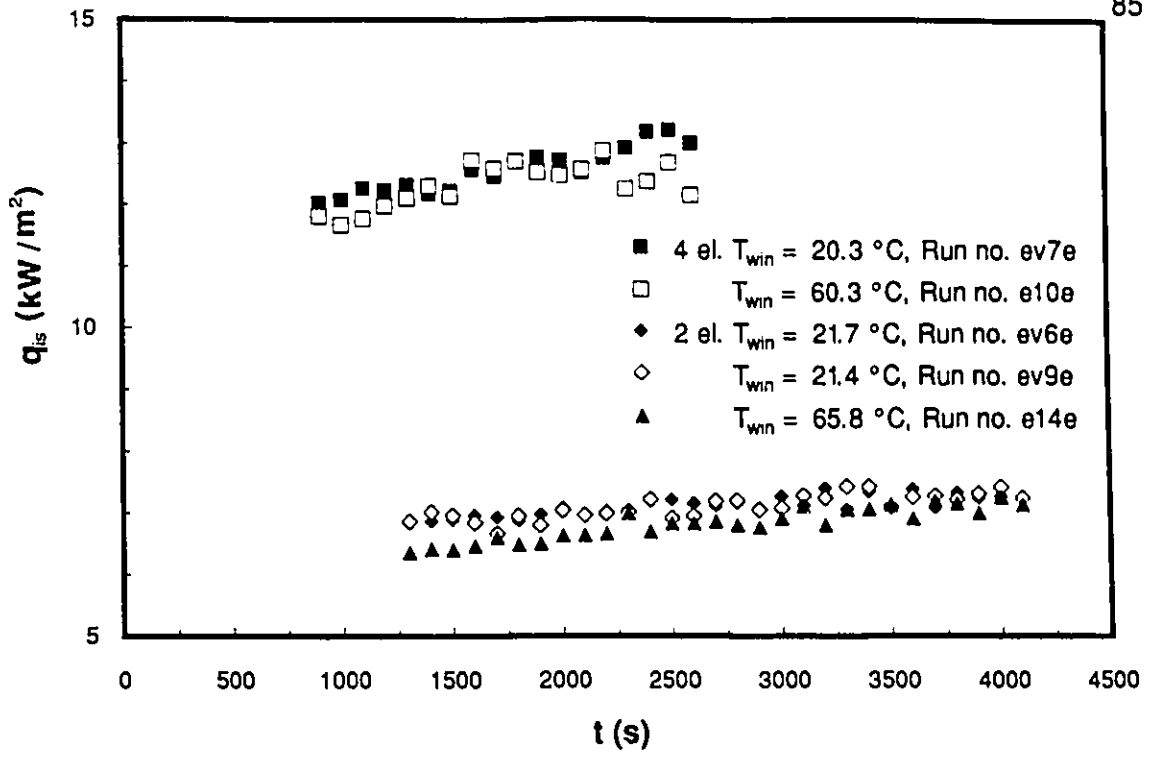


Figure 5.3a The overall incident radiative heat flux from evaporation experiments (q_{is} vs. t for 2 and 4 heating elements on)

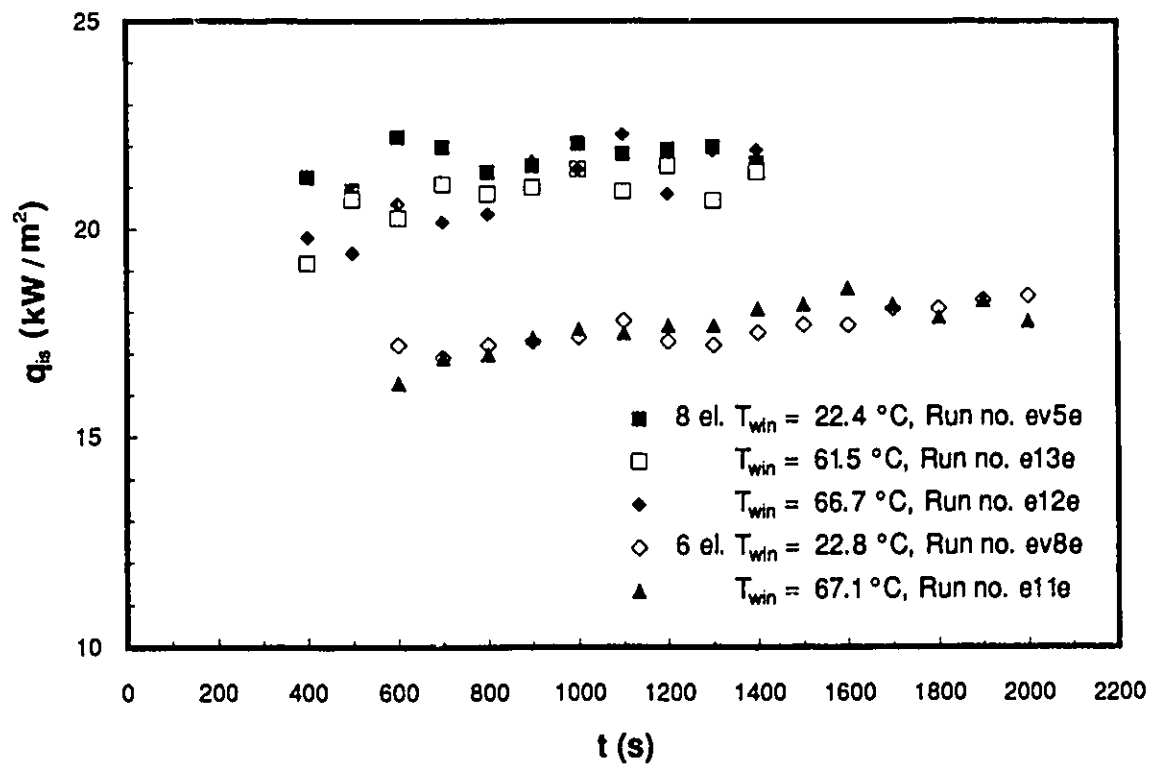


Figure 5.3b The overall incident radiative heat flux from evaporation experiments (q_{is} vs. t for 6 and 8 heating elements on)

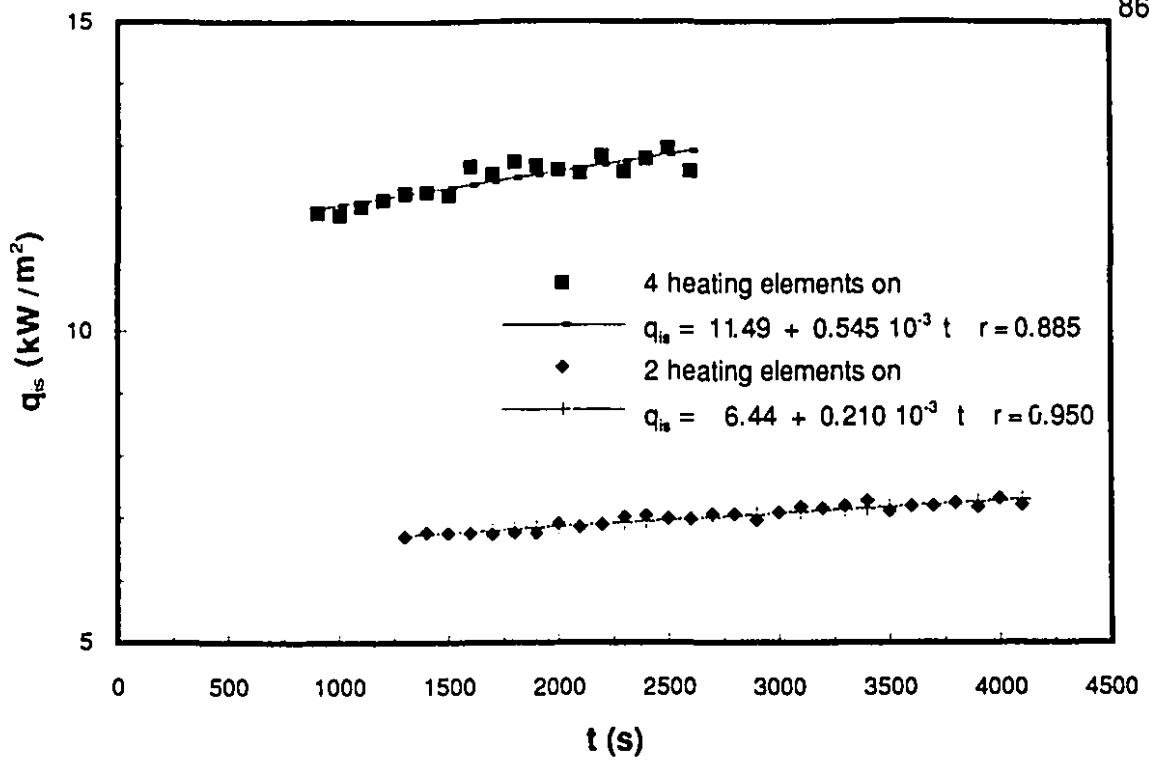


Figure 5.4a Correlation of the overall incident radiative heat flux (q_{is} vs. t for 2 and 4 heating elements on)

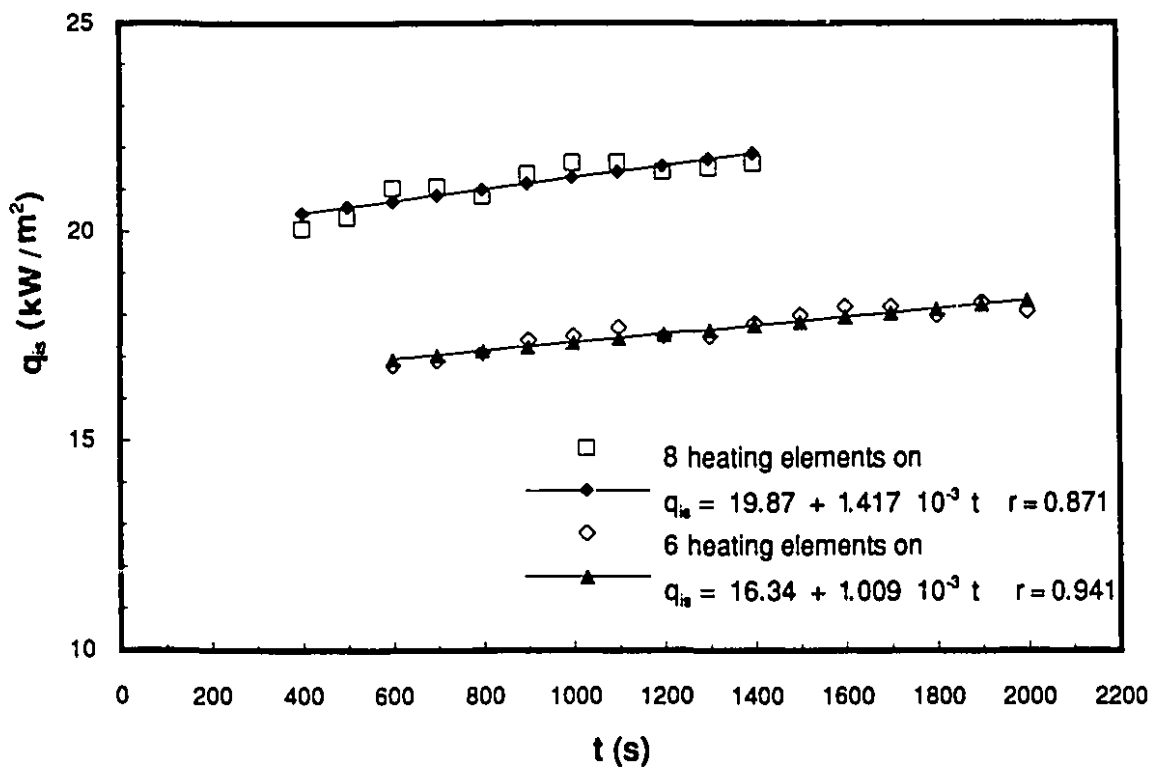


Figure 5.4b Correlation of the overall incident radiative heat flux (q_{is} vs. t for 6 and 8 heating elements on)

That the slope does not increase proportionally with the number of elements results from the fact that P_i (at constant T_{sir}) does not increase proportionally with the number of elements activated (~1320 W, 2 elements; ~ 2220 W, 4 elements; ~ 2860 W, 6 elements; ~ 3330 W, 8 elements). This latter cause is also linked to the already mentioned position effect of the heating elements.

5.2.2 INCIDENT I.R. SOURCE AND TEST SECTION WALL RADIATIVE HEAT FLUXES IN FREE CONVECTION-I.R. EVAPORATION EXPERIMENTS

The overall incident radiative heat flux q_{is} can be written:

$$q_{is} = q_{sir} + q_{its} \quad (5.4)$$

q_{sir} (the radiative contribution of the I.R. source) and q_{its} (the radiative contribution of the test section walls) were deduced from the application of the theory of radiation exchange in an enclosure of diffuse-gray surfaces (section 4.2, Appendix 5). Surface 4 is now a radiating surface with a temperature T_4 adjusted so that q_{is} calculated and measured are identical. The applicability of this concept relies on the assumption that the behavior of the I.R. source cavity can be approximated by using an equivalent flat plate radiating at a lower temperature (T_4). E_4 the equivalent total hemispherical emissivity of the aperture was taken to be 0.92 for the following reasons:

- a) The I.R. source manufacturer (Glenro Inc) reported a value of 0.92 for the hemispherical total emissivity of the corrugated heating elements (oxidized hastelloy);
- b) As a result of the pyramid geometry most of the radiant energy emitted or reflected by the stainless steel pyramid side is directed toward the emitting surface thus increasing its effective emissivity; the ratio of the aperture area (0.023 m^2) to the internal area of the truncated pyramid (0.437 m^2) being $5.3 \cdot 10^{-2}$, the pyramid cavity has a tendency to behave like a blackbody (in terms of emission or absorption of incident energy);

- c) The emissivity of the back-heaters ceramic material is known to be high (0.8-0.95) at high temperature (Wade and Slomp, 1962); according to the manufacturer (Armstrong), clay is one of the major components (together with mineral wool fiber) of the back heaters ceramic and has an emissivity of about 0.86 (Eckert and Drake, 1972; Sala, 1986).
- d) Within the framework of this study, it is the constancy of the value used for E_4 more than an exact evaluation which is important because it determines T_4 level subject to the criterion that the calculated and measured q_{is} values are identical.

The system of equations (Appendix 5) was solved for selected time intervals $[t_1, t_2]$ corresponding to the P.C.D.R.P. for the free convection-I.R. drying of the samples ($b = 5.5, 10.3$ and 19.9 mm). In Table 5.1 (a, b), the run identification name and the number of activated elements, $[t_1, t_2]$, P_∞ , T_d , T_w , T_2 , T_3 , T_4 , q_{is} , q_{sir} , q_{its} and P_i are presented. $q_{its}\%$ is the ratio of q_{its} to q_{sir} expressed in %. $q_{sir}(dr.)$ and $q_{its}(dr.)$ are an estimation of the relative increase of q_{sir} and q_{its} , calculated from the difference between the heat fluxes applicable to the last and first time intervals and divided by the time average value of q_{is} . $P_i(dr.)$ is an evaluation of the relative decrease of P_i computed from the difference between P_i applicable to the last and first time interval and divided by the average value of P_i .

The reproducibility (same time interval) of the computed T_2 and T_3 (sixth and seventh columns in Table 5.1a and b respectively) is ± 8 °C and ± 10 °C respectively.

It is remarkable that the identified values of T_4 (eighth column in Table 5.1a and b) for same time interval and number of elements always differ by less than 2 °C. q_{its} (eleventh column in Table 5.1a and b) is reproducible within less than 3.6 % (2 heating elements), 1.6 % (4 heating elements), 1.9 % (6 heating elements) and 2.4 % (8 heating elements) from a comparison for same $[t_1, t_2]$ and different runs.

TABLE 5.1a

**THE INCIDENT I.R. SOURCE AND TEST SECTION WALLS RADIATIVE
HEAT FLUXES ESTIMATED FROM THE EVAPORATION RUNS**

Run Nb. El.	[t ₁ ,t ₂]	P _∞ *	T _d *	T _w *	T ₂ *	T ₃ *	T ₄ *	q _{is} *	q _{sr} *	q _{its} *	q _{its} %	q _{sr} (dr.)	q _{its} (dr.)	P _i *	P _i (dr.)
(.)	(s)	(kPa)	(° C)	(W/m ²)	(W/m ²)	(W/m ²)	(%)	(%)	(%)	(W)	(%)				
ev6e 2	900-1100	100.90	10.4	43.6	55	102	452	6650	5650	1000	17.7			1341	
	1300-1800		10.4	53.5	67	123	453	6770	5690	1080	19.0			1317	
	2700-3700		10.4	68.1	89	154	458	7110	5860	1250	21.3			1299	
	3000-3900		10.4	69.2	91	156	459	7160	5890	1270	21.6	3.6	4.0	1297	-3.3
ev9e 2	900-1100	102.50	-5.6	42.9	57	106	451	6650	5640	1010	17.9			1339	
	1300-1800		-5.3	52.7	68	126	452	6760	5680	1080	19.0			1318	
	2700-3700		-4.7	67.5	90	154	458	7110	5850	1260	21.4			1305	
	3000-3900		-4.5	68.8	92	156	459	7160	5890	1270	21.6	3.6	3.8	1304	-2.6
e14e 2	900-1100	101.84	4.9	65.5	48	98	452	6650	5680	970	17.1			1347	
	1300-1800		4.6	61.8	60	119	454	6760	5720	1040	18.2			1325	
	2700-3700		4.5	69.6	84	150	459	7110	5890	1220	20.7			1309	
	3000-3900		4.6	70.4	86	153	460	7160	5920	1240	20.9	3.6	4.0	1310	-2.8
ev7e 4	800-1100	100.38	12.7	51.6	70	154	571	12000	10400	1600	15.4			2245	
	1500-2000		13.1	70.0	101	199	574	12440	10560	1880	17.9	1.4	2.2	2172	-3.3
e10e 4	800-1100	101.99	1.4	67.3	73	161	570	12000	10360	1640	15.4			2203	
	1500-2000		1.9	76.3	102	202	574	12440	10540	1900	18.1	1.4	2.2	2161	-1.9

Nb. El.: number of heating elements activated

TABLE 5.1b

**THE INCIDENT I.R. SOURCE AND TEST SECTION WALLS RADIATIVE
HEAT FLUXES ESTIMATED FROM THE EVAPORATION RUNS**

Run Nb. El.	[t ₁ ,t ₂]	P _∞ *	T _d *	T _w *	T ₂ *	T ₃ *	T ₄ *	q _{is} *	q _{sir} *	q _{its} *	q _{its} %	q _{sir} (dr.)	q _{its} (dr.)	P _i *	P _i (dr.)	
(.)	(s)	(kPa)	(° C)	(° C)	(° C)	(° C)	(° C)	(W/m ²)	(W/m ²)	(W/m ²)	(%)	(%)	(%)	(W)	(%)	
ev8e 6	600-800 1100-1300	100.35	12.9 13.5	49.9 69.3	92 117	197 236	648 652	17000 17550	14740 15010	2260 2540	15.6 17.3		1.5 1.7	2930 2840		-3.1
e11e 6	600-800 1100-1300	101.90	1.5 1.8	52.3 80.8	87 117	187 233	649 652	17000 17550	14790 15020	2210 2530	14.9 17.3		1.4 1.8	2969 2870		-3.4
ev5e 8	200-300 300-500 700-1000	100.95	11.4 11.9 13.0	30.7 66.4 63.9	79 92 122	194 215 258	692 693 697	20220 20440 21080	17740 17820 18110	2480 2620 2970	14.1 14.6 16.6			3566 3482 3329		-6.9
e12e 8	200-300 300-500 700-1000	101.70	0.0 0.5 1.5	67.9 70.7 80.0	76 89 121	188 209 253	692 693 697	20220 20440 21070	17760 17850 18130	2440 2590 2940	13.5 14.0 16.3			3555 3475 3341		-6.2
e13e 8	200-300 300-500 700-1000	102.24	0.4 1.2 2.2	76.2 66.4 77.4	78 85 118	181 203 249	693 694 697	20230 20430 21070	17790 17880 18170	2440 2550 2900	13.5 14.0 15.9			3599 3502 3332		-7.7

Nb. El.: number of heating elements activated

q_{its}° % (twelfth column in Table 5.1a and b) is a function of time which increase from about 17.6 % to 21.4 % for 2 elements, 15.4 % to 18.0 % for 4 elements, 14.9 % to 17.1 % for 6 elements and 13.7 % to 16.3 % for 8 elements. The magnitude of these results indicates that the radiative contribution of the test section walls by emission or reflection to q_{is}° is significant and decreases only slightly as more heating elements are used.

q_{sir}° (dr.) (thirteenth column in Table 5.1a and b) establishes that, for the period considered, the average intensity of q_{sir}° increases by about 3.6 % (2 heating elements), 1.4 % (4 heating elements), 1.5 % (6 heating elements) and 1.8 % (8 heating elements). q_{its}° (dr.) (fourteenth column in Table 5.1a and b) reveal that the average intensity of q_{its}° is increased by about 3.9 % (2 heating elements), 2.2 % (4 heating elements), 1.8 % (6 heating elements) and 2.3 % (8 heating elements). The trend of both heat fluxes is to increase at approximately the same rate (for same number of elements). It can be concluded that the overall increase of q_{is}° (Figure 5.4) is due mainly to q_{sir}° increase because q_{sir}° represents between 80 % to 90 % of q_{is}° .

For the same time interval $[t_1, t_2]$, P_i° (fifteenth column in Table 5.1a and b) was found reproducible within less than 1.0 % (2 heating elements), 1.9 % (4 heating elements), 1.3 % (6 heating elements) and 1.2 % (8 heating elements). The average P_i° (P_i° (dr.); last column of Table 5.1a and b) decrease, for the period considered, as a function of time is 2.9 % (2 heating elements), 2.6 % (4 heating elements), 3.3 % (6 heating elements) and 6.9 % (8 heating elements). Since T_{sir} is kept constant (by controlling P_i) and P_i is observed to decrease (Table 5.1, Figure 5.6), it can be deduced that the temperature increase of the ceramic and stainless steel pyramid walls must be sufficient to generate an increase in q_{sir}° and q_{its}° .

Maximal temperature differences recorded on surface number 2 (Appendix 5) were always less than 38 °C (2 elements), 48 °C (4 elements), 51 °C (6 elements) and 53 °C (8 elements). For surface 3, it was always lower than 29 °C (2 elements), 56 °C (4 elements), 70 °C (6 elements) and 82 °C (8 elements). It was decided to test the sensitivity of the evaluation of T_4° to an appropriate determination of T_2° and T_3° . If one selects, as representative of

surface 2, the maximum recorded temperature to estimate T_4^* and compares those values to the one obtained when choosing the minimum temperature, T_4^* is decreased between 2 to 5 °C (2 elements), between 2 to 5 °C (4 elements), between 3 to 4 °C (6 elements) and between 2 to 4 °C (8 elements). The range given for the changes in T_4^* represents the minimal and maximal temperature differences that were computed (from run to run, same $[t_1, t_2]$ and number of elements). Such decrease of T_4^* generates a maximal increase of 13 % for q_{its}^* and a maximum decrease of 1 % for q_{sir}^* (with respect to their average value).

For surface 3, the estimation was carried out with the maximal temperature (T_{12}^*) and a minimum temperature computed as the average of T_{11}^* , T_{13}^* , T_{14}^* and T_{15}^* . T_{11}^* and T_{13}^* being around surface 3 insure that this temperature is the lowest possible average temperature representative of surface 3. In such a case, T_4^* decreases in the order of 2-3 °C (2 elements), 3-4 °C (4 elements), 3-4 °C (6 elements) and 3-5 °C (8 elements). Such decrease of T_4^* create a maximal increase of 12 % for q_{its}^* and a maximum decrease of 1 % for q_{sir}^* .

In the present study, T_2^* is calculated as the average of T_{11}^* , T_{13}^* and T_{16}^* ; this method of determination constrain T_2^* to be close to T_{11}^* and T_{13}^* (the highest temperatures on surface 3). As the radiative heat transfer depends on the fourth power of temperature, the use of a temperature closer to the highest on the surface should give us a better approximation of T_4^* and q_{its}^* . Furthermore, T_{11}^* and T_{13}^* characterize the surface temperature of the fraction of surface 2 (upper test section plate) which has the highest shape factor with respect to the sample surface (1). For surface 3, since T_{12}^* is measured close to surface 4 (10 mm), an average based on T_{12}^* , T_{14}^* and T_{15}^* gives a T_3^* close to T_{14}^* and T_{15}^* which are more representative of surface 3 because their location is almost halfway in between the aperture and the external boundaries of surface 3.

These remarks and the evaluation given in the preceding paragraph suggest that an accurate determination of T_4^* has been carried out with maximal variation in the order of ± 5 °C which creates an uncertainty in the assessment of q_{its}^* in the order of ± 12 % and of q_{sir}^* in the order of ± 1 %. Taking into account data from Tables 5.3 (q_{its}^* %), the resulting maximal q_{is}^* uncertainty is in the order of ± 4 %.

During the combined convection-I.R. drying runs the temperature differences on surface 2 and 3 recorded were equal or lower than the one used for the above computations. Thus the same uncertainty level are applicable to the combined convective-I.R. drying runs.

5.3 TEST SAMPLE SURFACE ABSORPTIVITY UNDER I.R. HEAT FLUX

Before deducing experimentally the heat and mass transfer coefficients applicable in combined convective-I.R. drying, it is essential to know the hemispherical total absorptivity of the sample surface under the I.R. heat flux.

In section 4.2 the sample emissivity E_s was taken as 0.95 in the wavelength range 8-14 μm (wavelength range of the pyrometer). Since the incident radiation coming from the cavity walls is for the major fraction in the same range (80 °C, $\lambda_{\text{max}} = 8.21 \mu\text{m}$; 180 °C, $\lambda_{\text{max}} = 6.39 \mu\text{m}$) it was justified to use this value of E_s as representative of the emission and absorption characteristics of the sample surface. However, in the present case the wavelength range of the incident radiation is shifted toward much shorter wavelengths (850 °C, $\lambda_{\text{max}} = 2.58 \mu\text{m}$); it is no longer possible to assimilate the measured emissivity and the absorptivity of the surface under I.R. radiation. A complete characterization of the absorptivity as a function of wavelength would necessitate to quantify (under the gray surface behavior assumption) the spectral emittance with an environmental chamber-spectrophotometer as described by Birkebak (1972) or Navarri (1991). Consequently, it was decided to determine an overall equivalent emissivity (under the assumption of diffuse gray surface behavior) through use of equation 4.1, modified as in the previous section and integrated over $[t_1, t_2]$:

$$E_s^* = \frac{1}{(q_b^* - \sigma T_s^{*4})} \left\{ \frac{1}{(t_2 - t_1)} \left[\int_{t_1}^{t_2} \left(-\frac{1}{A_s} \frac{dm_w}{dt} \Delta H_v \right) dt + \int_{t_1}^{t_2} \frac{1}{A_s} (m_w c_{pw} + m_b c_{pb}) \frac{dT_s}{dt} dt \right] - h_c (T_3^* - T_s^*) \right\} \quad (5.5)$$

As a result of the good reproducibility obtained in terms of temperature and heat flux levels for the free convection experiments (section 5.2.2), q_{is}^* may be computed from the correlation in Figure 5.4 and the time in the middle of the P.C.D.R.P (defined from the time interval $[t_1, t_2]$). Hence, free convection-I.R. drying experiments (no forced flow present) with various sample and thickness were carried out under similar conditions as the ones used in section 5.2.1.

In Table 5.2, the run identification name and the number of activated elements, $[t_1, t_2]$, the sample number, b , P_∞^* , T_d^* , T_s^* , T_3^* , N_v^* , q_{ac}^* , q_c^* , q_{is}^* and E_s^* are presented. q_{ac}^* is the second term in the right-hand side of equation 5.5. q_c^* is the average convection heat flux during the P.C.D.R.P. identified as the last term of the right-hand side of equation 5.3.

T_s^* (eighth column, Table 5.2) reaches the boiling point for the 19.9 mm sample (why the measured value is slightly higher than 100 °C will be discussed in section 5.5). This phenomenon occurs as a result of the formation of an additional mass transfer resistance at the sample surface level as explained in section 5.4.3. At this point the mass flux is no more diffusion controlled; bulk flow of the vapor occurs at the surface because the surface vapor pressure is higher than P_∞^* .

For the 5.5 and 10.3 mm samples, T_s^* did not reach the boiling point temperature whatever the value of q_{is}^* applied although T_s^* was always higher for the 10.3 mm than for the 5.5 mm sample (eight column Table 5.2). T_s^* recorded for the 5.5 and 10.3 mm thick samples are increasing functions of the heat flux as shown in Figure 5.5a where a linear correlation of T_s^* as a function of q_{is}^* can be drawn ($r=0.983$) for the 10.3 mm sample. Data ($T_s^* = 92$ °C) from Navarri (1991) for free convection-I.R.drying (sea sand, $d = 200-250$ μm , $b = 7$ mm, $q_{is}^* = 18.5$ kW/m^2 (Near Infrared Radiation)) is in good agreement with the present value range.

Comparing data from the different time intervals corresponding to the P.C.D.R.P. of the 5.5 mm and 19.9 mm samples, N_v^* (tenth column, Table 5.2) was found to increase by about 6 % (2 elements), 17 % (4 elements), 18 % (6 elements) and 9 % (8 elements). This is a consequence of the observed increase of q_{is}^* as a

TABLE 5.2
EVALUATION OF THE SAMPLE EQUIVALENT HEMISPHERICAL TOTAL
EMISSIVITY UNDER I.R. HEAT FLUX

Run No.	Nb. El. (.)	[t ₁ , t ₂] (s)	Sa. No.	b (mm)	P _∞ (kPa)	T _d (°C)	T _s (°C)	T ₃ (°C)	N _v (kg/m ² s)	q _{ac} (W/m ²)	q _c (W/m ²)	q _{is} (W/m ²)	E _s (.)
ir24	2	900-1100	X	5.5	102.56	-3.2	75.4	99	2.06e-03	30	10	6650	0.82
i79h	2	1300-1800	X	10.3	99.69	19.3	84.5	125	2.08e-03	120	20	6760	0.84
i72h	2	3000-3900	XI	19.9	100.39	17.6	101.6	161	2.13e-03	0	30	7160	0.79
i73h	2	2700-3700	XI	19.9	100.39	15.0	101.6	161	2.18e-03	0	30	7110	0.82
ir22	4	800-1100	X	10.3	102.10	2.8	90.8	149	3.64e-03	240	30	12030	0.77
i81h	4	1500-2000	XI	19.9	102.16	1.8	102.1	205	4.34e-03	20	60	12440	0.86
ir23	6	600-800	X	10.3	102.10	3.2	94.6	167	4.98e-03	460	40	17030	0.73
i82h	6	1100-1300	XI	19.9	102.63	2.2	102.1	222	5.97e-03	50	70	17550	0.82
ir25	8	200-300	X	5.5	102.55	-3.6	92.6	192	6.44e-03	370	50	20240	0.78
i80h	8	300-500	X	10.3	99.69	19.2	96.0	243	6.43e-03	730	80	20460	0.79
i74h	8	700-1000	XI	19.9	100.78	14.3	101.7	271	6.88e-03	320	100	21070	0.79
i75h	8	800-1000	XI	19.9	100.83	13.5	101.6	263	7.07e-03	360	90	21120	0.81
Average													0.80
Stdev.													0.03

Nb. El.: number of heating elements activated

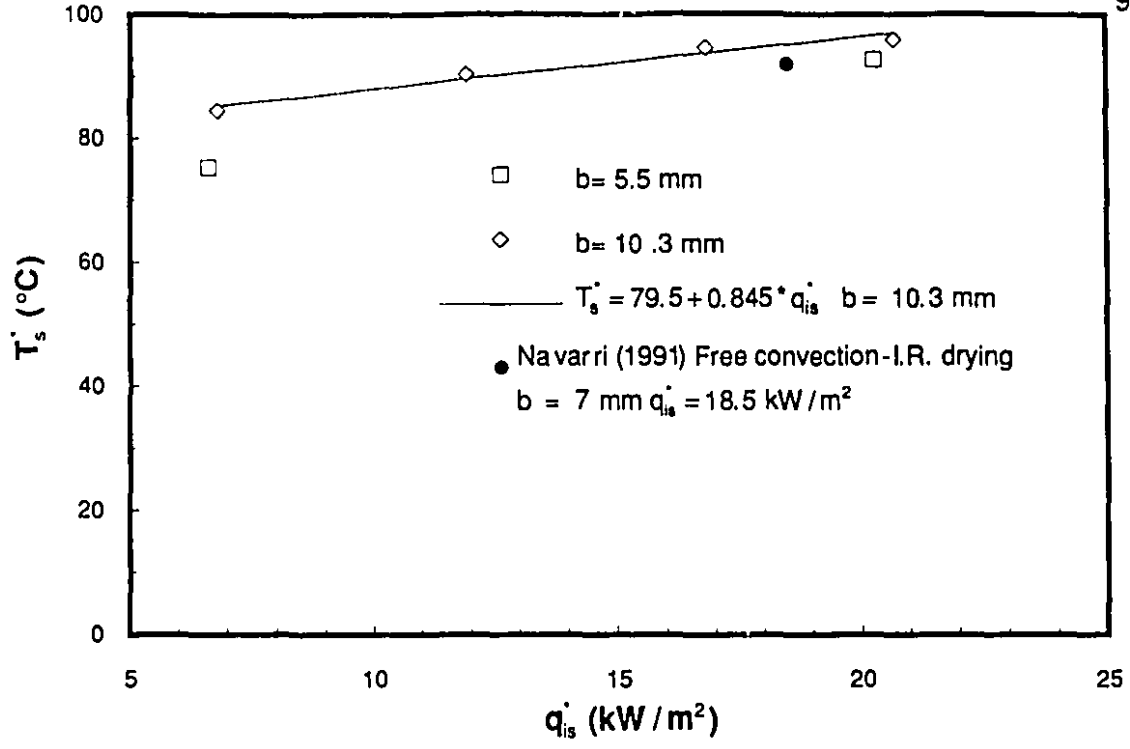


Figure 5.5a The sample surface temperature as a function of the overall incident heat flux from free convection IR. drying runs (T_s vs. q'_{is})

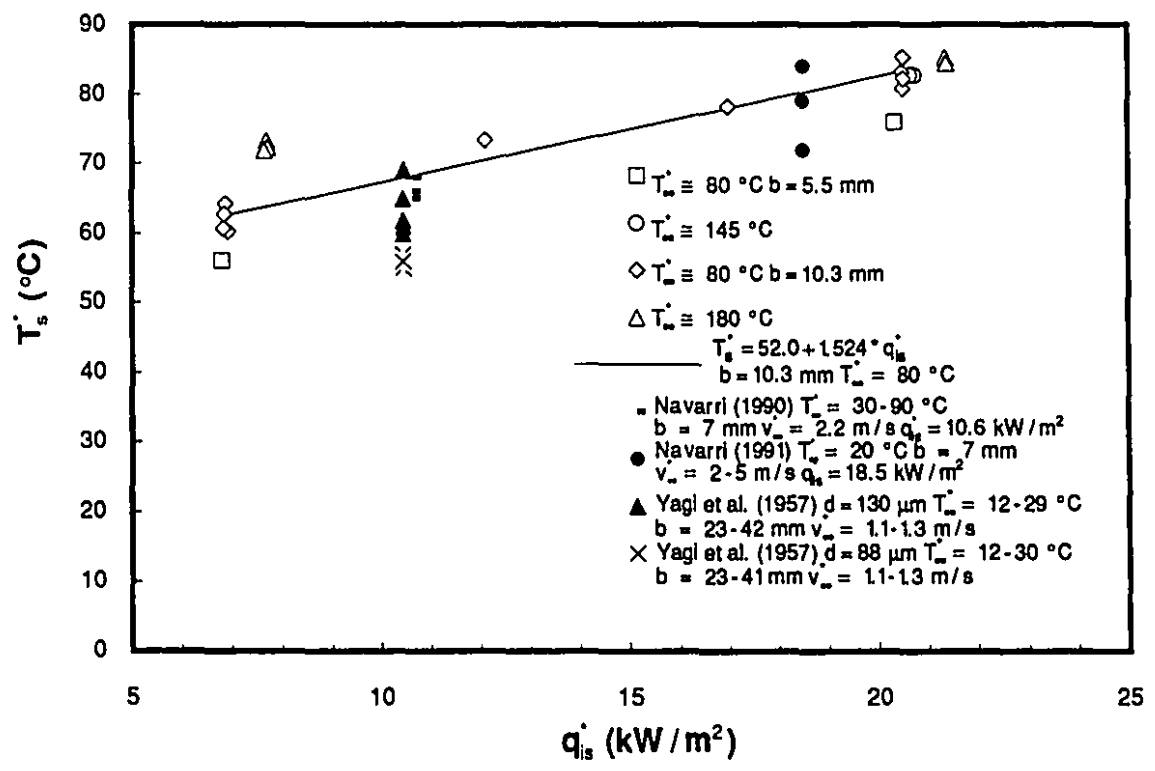


Figure 5.5b The sample surface temperature as a function of the overall incident heat flux from forced convection IR. drying runs (T_s vs. q'_{is})

function of time (section 5.3) and the mass flux reproducibility with different samples (section 3.5).

The computed value of q_c^* (twelfth column, Table 5.2) and q_{ac}^* (eleventh column, Table 5.2) are always less than 0.5 % and 3.6 % of q_{is}^* , respectively.

The average value of E_s^* (last row, Table 5.2) is 0.8 with a standard deviation of 0.03. Except for two values (runs i81h and ir23) the determined values are well grouped around the mean. The mean of E_s^* (for same number of elements) has a slight tendency to decrease with increase in the heat flux level; however the scatter in the results does not allow us to present it as a final conclusion.

5.4 CONVECTIVE HEAT TRANSFER COEFFICIENTS IN COMBINED CONVECTION-I.R. DRYING

The wall temperatures in forced and free convection experiments were different, thus it was necessary to evaluate q_{is}^* for each of the combined convective and I.R. drying experiments. In order to apply the theory of radiation exchange in an enclosure of diffuse-gray surfaces, one must know T_4^* . An alternative would be to know q_{sir}^* .

5.4.1 OVERALL INCIDENT RADIATIVE HEAT FLUX IN COMBINED CONVECTION-I.R. DRYING EXPERIMENTS

In Figure 5.6 (a, b) are displayed characteristics P_i vs. t curves for 2 heating elements (a) and 8 heating elements (b) from representative experimental conditions: convection with $T_\infty^* \sim 80$ °C, $v_\infty^* = 2.1-4.5$ m/s; $T_\infty^* \sim 180$ °C, $v_\infty^* = 2.6-6.2$ m/s and in free convection (no forced flow present). Despite widely different convective conditions within the test section, the differences existing between the recorded P_i at any specific time, are always less than 7 % (2 elements) and 12 % (8 elements). An increase of P_i occurs, in most cases, when T_∞^* is decreased or v_∞^* is increased (other conditions being constant); this is exemplified in Figure 5.7a and b where the differences (less than 6 % (2 elements) and 10 % (8 elements)) between the P_i curves are scaled-up (and taken from representative time intervals).

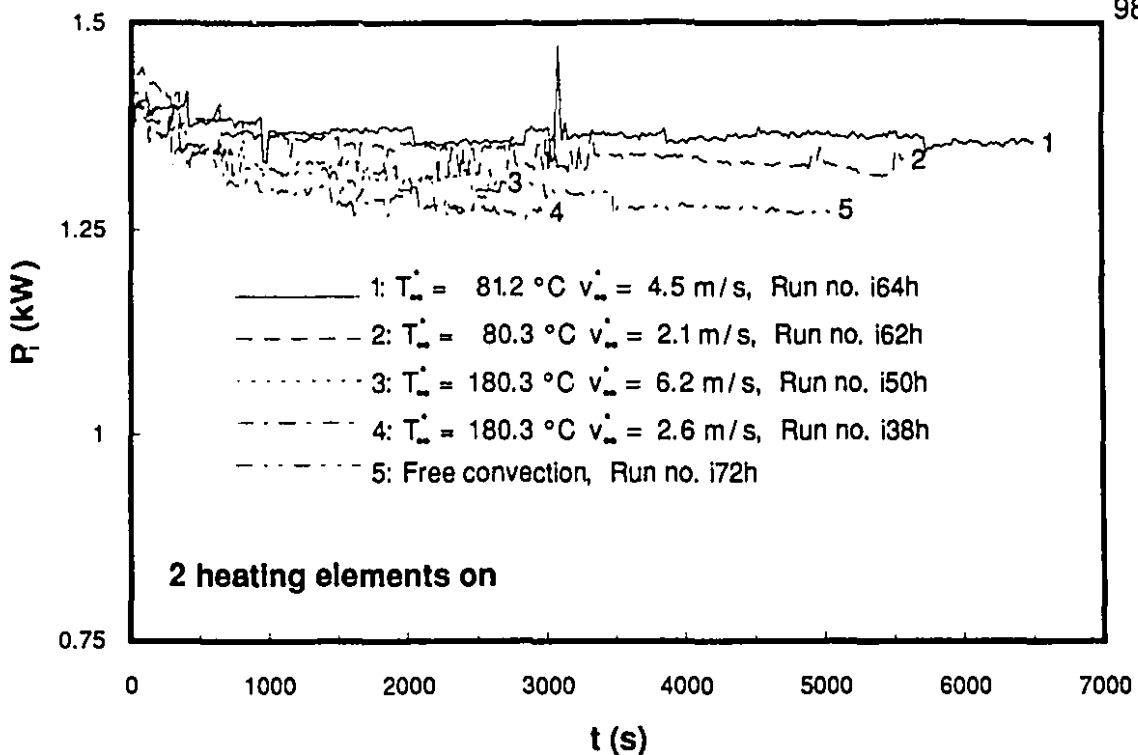


Figure 5.6a Characteristic power input curves from the combined convective and IR. drying runs (P_i vs. t for 2 heating elements on)

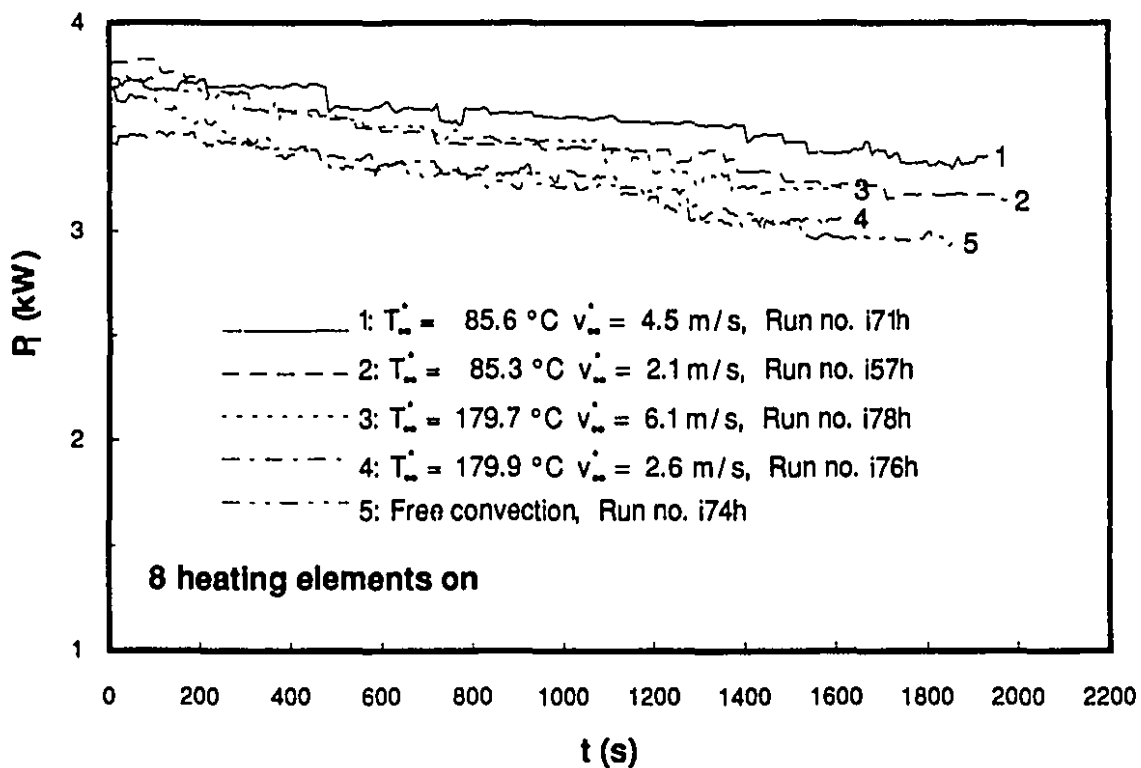


Figure 5.6b Characteristic power input curves from the combined convective and IR. drying runs (P_i vs. t for 8 heating elements on)

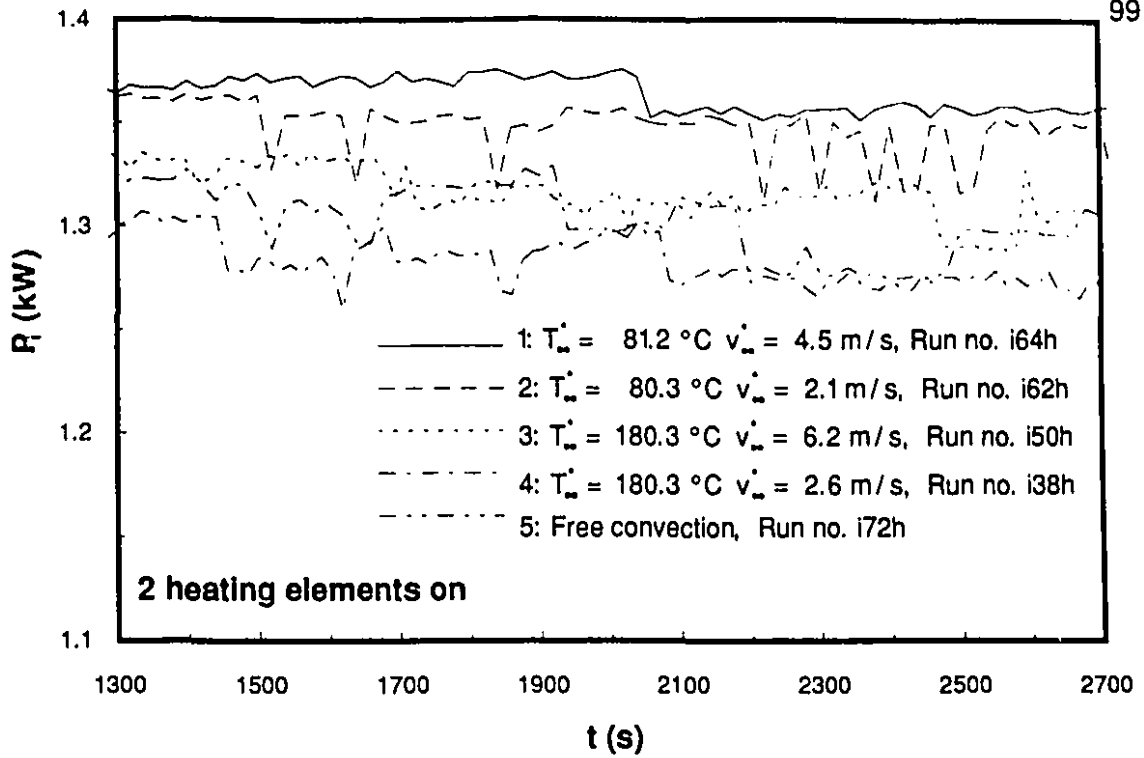


Figure 5.7a A typical scaled-up fraction of characteristic power input curves from the combined convective and LR. drying runs (P_i vs. t for 2 heating elements on)

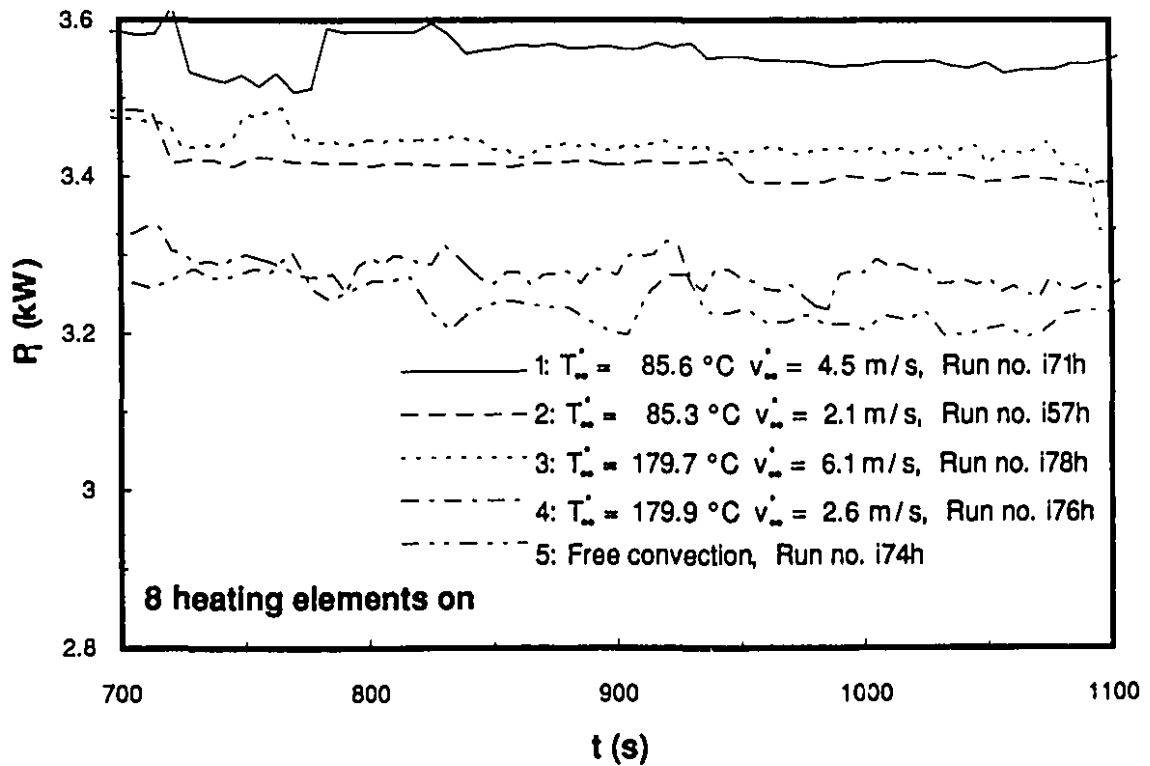


Figure 5.7b A typical scaled-up fraction of characteristic power input curves from the combined convective and LR. drying runs (P_i vs. t for 8 heating elements on)

The following classification in terms of input power (ranked from the highest to the lowest) of the curves taken from Figure 5.6a and b shows the links existing between P_i and T_{∞}^* or v_{∞}^* :

2 elements

- 1: $T_{\infty}^* \sim 80 \text{ }^{\circ}\text{C}$, $v_{\infty}^* = 4.5 \text{ m/s}$, run no. i64h
- 2: $v_{\infty}^* = 2.1 \text{ m/s}$, run no. i62h
- 3: $T_{\infty}^* \sim 180 \text{ }^{\circ}\text{C}$, $v_{\infty}^* = 6.2 \text{ m/s}$, run no. i50h
- 4: Free convection, run no. i72h
- 5: $T_{\infty}^* \sim 180 \text{ }^{\circ}\text{C}$, $v_{\infty}^* = 2.6 \text{ m/s}$, run no. i38h

The differences between 4 and 5 are very small (in the order of 1 to 2 % of P_i).

8 elements

- 1: $T_{\infty}^* \sim 85 \text{ }^{\circ}\text{C}$, $v_{\infty}^* = 4.5 \text{ m/s}$, run no. i71h
- 2: $v_{\infty}^* = 2.1 \text{ m/s}$, run no. i57h
- 3: $T_{\infty}^* \sim 180 \text{ }^{\circ}\text{C}$, $v_{\infty}^* = 6.1 \text{ m/s}$, run no. i78h
- 4: $v_{\infty}^* = 2.6 \text{ m/s}$, run no. i76h
- 5: Free convection, run no. i74h

The differences between 2 and 3 are very low (in the order of 1 to 2 % of P_i).

The spikes present in these curves (Figure 5.6 and 5.7) were generated because P_i was manually controlled to keep T_{sir} constant throughout the experiments. These P_i variations, in the order of 1 to 2 % (nominal value), produced maximal changes of T_{sir} in the order of $\pm 5 \text{ }^{\circ}\text{C}$ but their effects on q_{iS} was negligible because it was corrected rapidly. As a first approximation it is justified to assume that the T_4^* values determined in section 5.2.2 are not affected strongly by the forced convection conditions within the test section since the instantaneous P_i

values do not differ strongly and seems to be correlated with an increase of the convective heat transfer with the test section walls (when v_{∞}^* is increased or T_{∞}^* is decreased). Consequently, T_4 was correlated as a function of time from the values identified in Table 5.1. The following expressions were found:

2 elements:

$$T_4 = 448.4 + 3.140 \cdot 10^{-3} \cdot t \quad (5.6)$$

4 elements:

$$T_4 = 566.3 + 4.375 \cdot 10^{-3} \cdot t \quad (5.7)$$

6 elements:

$$T_4 = 643.6 + 7.000 \cdot 10^{-3} \cdot t \quad (5.8)$$

8 elements:

$$T_4 = 690.3 + 7.864 \cdot 10^{-3} \cdot t \quad (5.9)$$

The correlation coefficient r for these relations were 0.99 (2 heating elements) and 1.00 (4 heating elements, 6 heating elements and 8 heating elements).

The theory of radiation exchange in an enclosure of diffuse-gray surfaces (Appendix 5) was applied with these correlations for T_4 and the data recorded from each run. In Table 5.3, the sample number, b , the run identification name, the time in the middle of the P.C.D.R.P. t_{av} , the number of activated elements, T_{∞}^* , v_{∞}^* , P_{∞}^* , T_d^* , T_s^* , T_2^* , T_3^* , T_4^* , q_{is}^* , q_{sir}^* and q_{its}^* are given. $q_{its}^*\%$ is the ratio of q_{its}^* to q_{sir}^* expressed in %.

The analysis summarized by the results in Table 5.3 gives us the opportunity to evaluate the radiative (Q_R^*) and convective (Q_C^*) overall heat transfer rate from surfaces 2 and 3. Q_R^* is the sum of the radiative heat transfer rates from surface 2 and surface 3 (Appendix 5):

$$Q_R^* = Q_2^* + Q_3^* \quad (5.10)$$

In Figure 5.8a is displayed Q_R^* (for 2 and 8 elements, $b=10.3$ and 19.9 mm) as a function of h_{cc}^* , the convective heat transfer coefficient predicted with equation A7.2 (Appendix 7), v_{∞}^* and the temperatures (air and surfaces). It can be noted that:

- Q_R^* values for 8 elements are about 3.2 to 3.6 times higher than for 2 elements;
- Q_R^* does not change significantly with increasing h_{cc}^* (or v_{∞}^*);
- Q_R^* is increased between 11 % to 14 % (2 heating elements) and 4 % to 5 % (8 heating elements) when T_{∞}^* is increased from 80 °C to 180 °C;
- Q_R^* increase slightly as a function of time (t_{av} ; Table 5.3) since its value is higher for a 19.9 mm than for a 10.3 mm sample.

Q_C^* is the sum of the convective heat transfer rates from surface 2 and 3:

$$Q_C^* = h_{cc}^* (T_2^* - T_{\infty}^*) + h_{cc}^* (T_3^* - T_{\infty}^*) \quad (5.11)$$

In Figure 5.8b is sketched Q_C^* as a function of h_{cc}^* . It is observed that:

- The equality between Q_C^* and Q_R^* is not always respected due to local variations of h_{cc} and T_{ti} and the imperfect insulation of the test section;
- Q_C^* values for 8 elements are about 0.3 to 8.0 time higher than for 2 elements.
- Q_C^* increase significantly between 15 % and 89 % for 8 elements with increasing h_{cc}^* (or v_{∞}^*);
- Q_C^* increase significantly between 38 % and 86 % for 2 elements with increasing h_{cc}^* (or v_{∞}^*) except for the cases with $T_{\infty}^* \sim 80$ °C where there is no increase or a 38 % decrease ($T_{\infty}^* \sim 80$ °C, $b = 19.9$ mm);

TABLE 5.3a

**THE INCIDENT I.R. SOURCE AND TEST SECTION RADIATIVE WALL HEAT FLUXES
FROM COMBINED CONVECTIVE AND I.R. DRYING RUNS**

Sa. No.	b (mm)	Run No.	t _{av} (s)	Nb. El. (.)	T _∞ [*] (°C)	v _∞ [*] (m/s)	P _∞ [*] (kPa)	T _d [*] (°C)	T _s [*] (°C)	T ₂ [*] (°C)	T ₃ [*] (°C)	T ₄ [*] (°C)	q _{is} [*] (W/m ²)	q _{sir} [*] (W/m ²)	q _{its} [*] (W/m ²)	q _{its} [*] %
X	5.5	ir17	1170	2	79.2	2.0	100.10	8.3	56.0	83	110	452	6810	5670	1140	20.0
		ir18	210	8	86.1	2.0	99.98	12.2	76.0	96	184	692	20340	17750	2590	14.6
		i85h	210	8	145.0	3.5	101.98	-4.0	82.8	146	210	692	20740	17770	2900	16.7
		i83h	200	8	141.7	5.2	101.19	-10.6	82.7	146	222	692	20770	17760	2980	16.9
X	10.3	ir2	770	4	81.1	2.1	98.78	5.2	73.3	96	151	570	12110	10350	1760	16.9
		ir3	550	6	83.1	2.1	98.73	6.4	78.2	99	166	648	16980	14730	2250	15.3
		ir1	1360	2	80.0	2.1	98.97	3.9	60.3	93	135	452	6930	5700	1230	21.6
		ir5	1270	2	79.9	2.1	99.51	12.3	64.2	90	128	452	6890	5690	1200	21.1
		ir7	1210	2	79.8	3.2	99.93	6.7	62.7	89	123	452	6860	5680	1180	20.8
		ir9	1120	2	79.8	4.5	99.86	7.8	60.7	87	119	452	6840	5670	1170	20.6
		ir4	450	8	86.7	2.1	98.74	4.4	85.3	102	181	694	20520	17900	2620	14.7
		ir6	450	8	85.6	2.1	99.50	13.9	80.8	101	177	694	20510	17900	2610	14.6
		ir8	440	8	83.0	3.3	100.06	7.1	83.1	100	176	694	20490	17890	2600	14.6
		ir10	460	8	83.7	4.5	99.87	9.2	82.3	101	178	694	20510	17900	2610	14.6
		ir11	860	2	180.0	2.6	100.81	2.9	73.3	180	199	451	7660	5680	1980	34.8
		ir13	810	2	180.0	4.3	100.79	2.5	72.4	182	209	451	7710	5680	2030	35.7
		ir15	720	2	179.8	6.1	100.79	4.1	71.8	180	202	451	7660	5670	1990	35.0
		ir12	310	8	183.3	2.6	100.79	5.1	85.2	188	259	693	21370	17850	3520	19.7
		ir14	300	8	181.1	4.3	100.81	1.9	84.4	190	258	693	21370	17840	3530	19.7
		ir16	310	8	180.1	6.1	100.79	5.8	84.4	190	259	693	21380	17850	3530	19.8

Nb. El.: number of heating elements activated

TABLE 5.3b

**THE INCIDENT I.R. SOURCE AND TEST SECTION RADIATIVE WALL HEAT FLUXES
FROM COMBINED CONVECTIVE AND I.R. DRYING RUNS**

Sa.	b	Run	t_{av}	Nb. El.	T_{∞}	v_{∞}	P_{∞}	T_d	T_s	T_2	T_3	T_4	q_{is}	q_{sir}	q_{its}	$q_{its} \%$
No.	(mm)	No.	(s)	(.)	(°C)	(m/s)	(kPa)	(°C)	(°C)	(°C)	(°C)	(°C)	(W/m ²)	(W/m ²)	(W/m ²)	%
XII	19.9	i62h	4090	2	80.3	2.1	99.79	17.9	100.8	96	145	461	7260	5970	1290	21.7
		i63h	4010	2	81.3	2.1	99.67	17.1	100.9	98	146	461	7270	5960	1310	21.9
		i64h	4490	2	81.2	4.5	99.57	16.9	100.6	88	123	462	7220	6000	1220	20.3
		i57h	970	8	85.3	2.1	99.69	16.2	101.7	119	231	698	21130	18220	2910	15.9
		i58h	980	8	84.2	2.1	99.79	16.2	101.8	116	226	698	21100	18230	2870	15.8
		i56h	990	8	84.2	2.6	99.71	16.5	101.7	115	220	698	21080	18230	2850	15.6
		i55h	1000	8	84.1	3.4	99.78	15.9	101.5	111	205	698	21010	18230	2780	15.2
		i68h	1040	8	82.9	4.5	99.99	14.1	101.6	106	198	699	20990	18260	2730	15.0
		i69h	1050	8	84.1	4.5	99.99	13.7	101.6	107	198	699	21000	18260	2740	15.0
		i70h	1010	8	84.9	4.5	100.06	13.7	101.7	109	200	698	20990	18240	2750	15.1
		i71h	980	8	85.6	4.5	100.18	14.0	101.6	110	203	698	20980	18220	2760	15.2
		i38h	2000	2	180.3	2.6	99.99	11.8	101.2	186	221	454	7920	5800	2120	36.5
		i45h	1790	2	180.2	6.2	99.71	14.7	100.5	184	215	454	7860	5780	2080	36.0
		i49h	1810	2	180.2	6.2	98.90	14.0	100.4	185	216	454	7870	5780	2090	36.2
		i50h	1860	2	180.3	6.2	99.11	12.0	100.5	185	216	454	7880	5780	2100	36.2
		i76h	700	8	179.9	2.6	100.63	8.7	101.1	204	306	696	22020	18100	3920	21.7
		i77h	700	8	179.9	2.6	100.61	9.7	101.1	208	315	696	22110	18100	4010	22.1
		i52h	720	8	180.3	6.2	99.51	6.6	100.9	198	280	696	21830	18100	3730	20.6
i78h	630	8	179.7	6.1	100.31	12.1	101.5	196	276	696	21770	18080	3690	20.4		

Nb. El.: number of heating elements activated

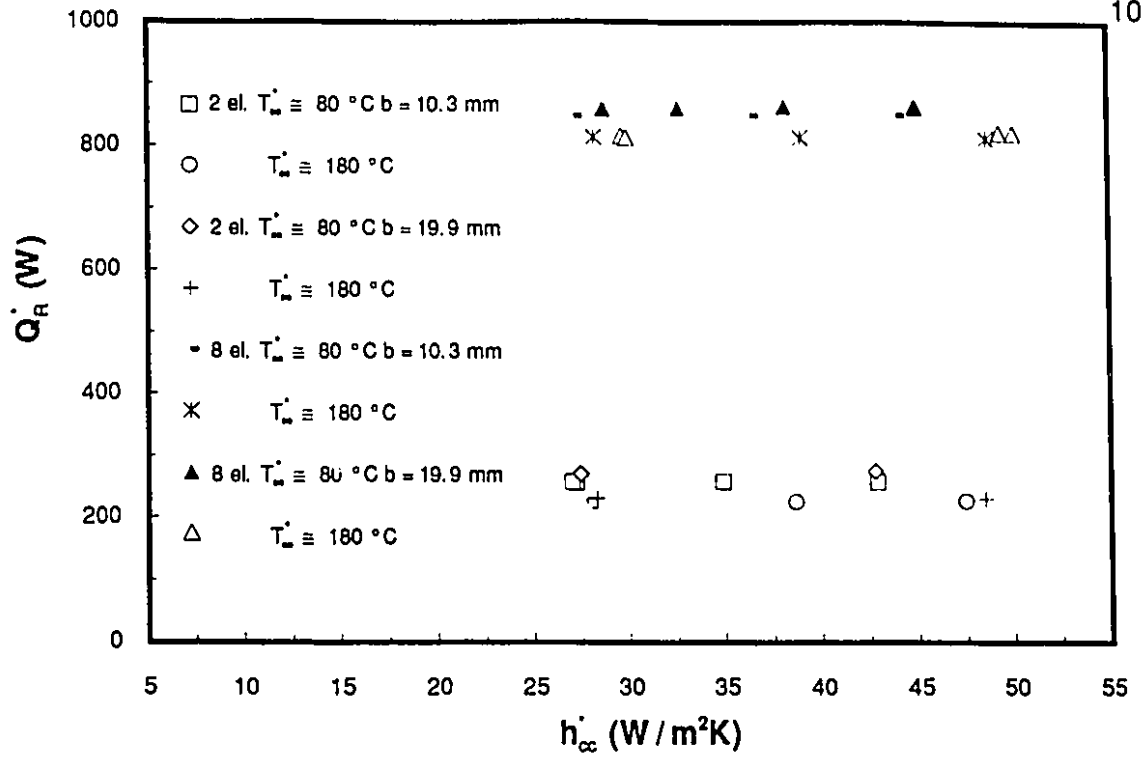


Figure 5.8a The radiative heat transfer rate within the test section as a function of the convective heat transfer coefficient (\dot{Q}_R vs. h_{cc})

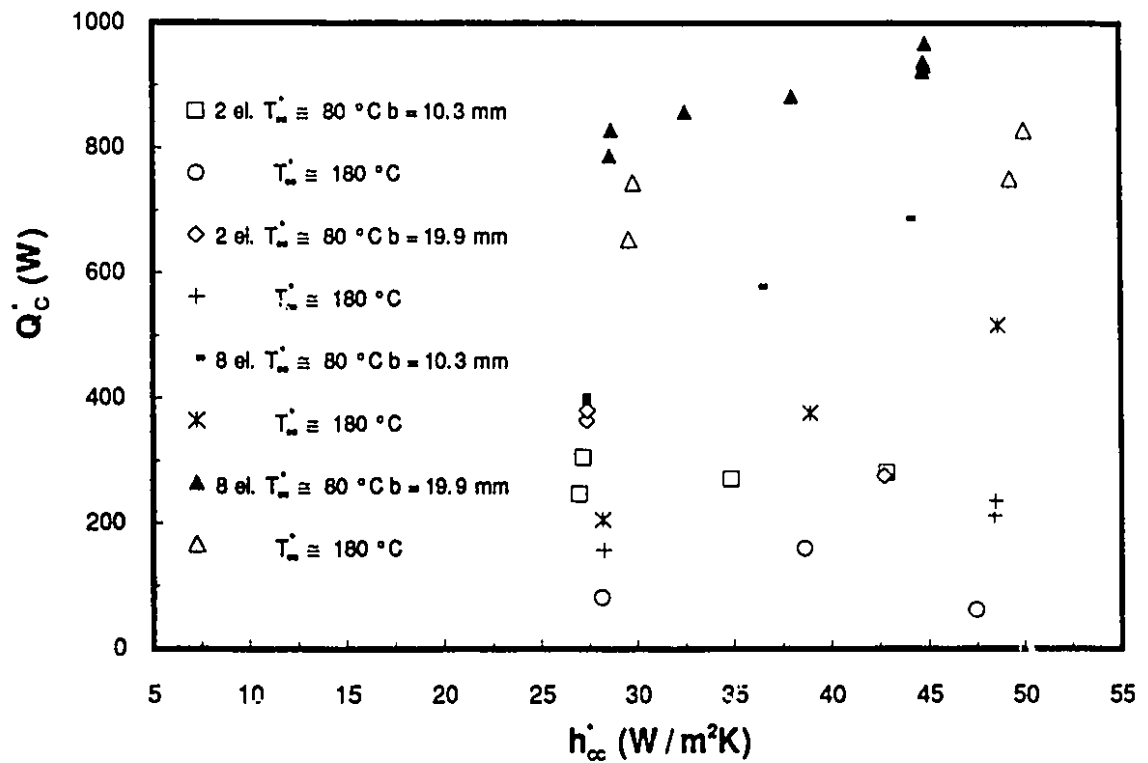


Figure 5.8b The convective heat transfer rate within the test section as a function of the convective heat transfer coefficient (\dot{Q}_c vs. h_{cc})

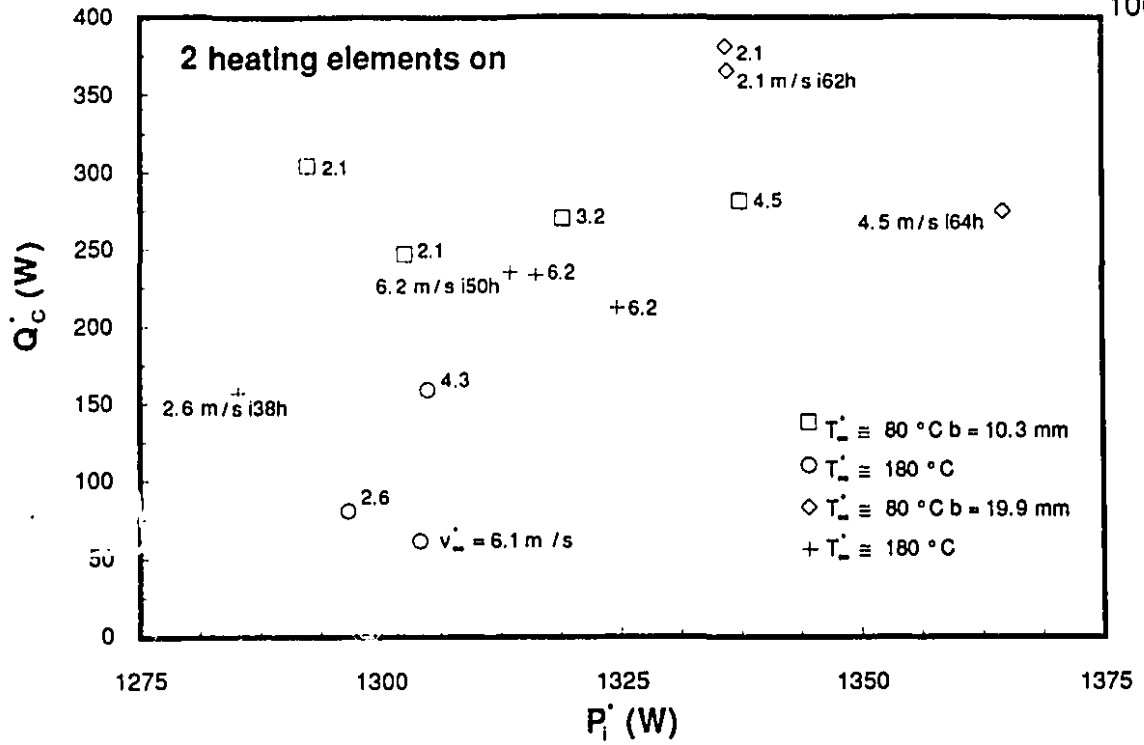


Figure 5.9a The convective heat transfer rate within the test section as a function of the power input for 2 heating elements on (Q_c vs. P_i)

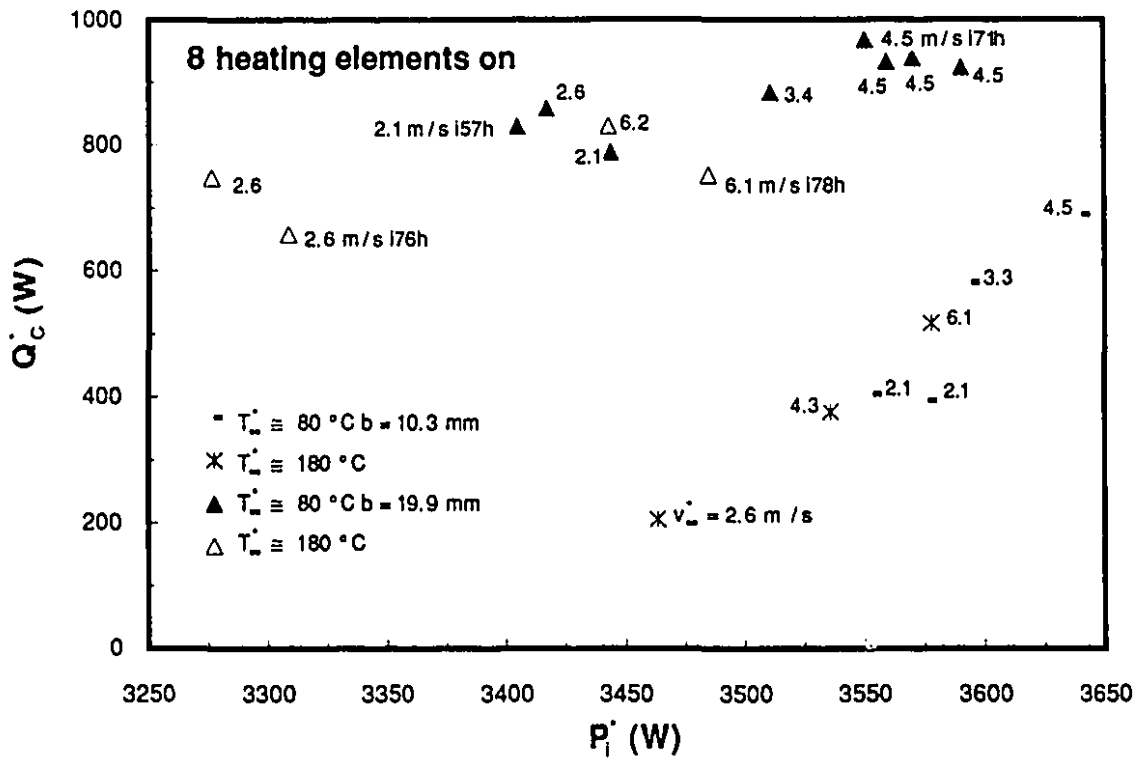


Figure 5.9b The convective heat transfer rate within the test section as a function of the power input for 8 heating elements on (Q_c vs. P_i)

- e) Q_C^* is increased between 0 % to 170 % (2 heating elements) and 16 % to 65 % (8 heating elements) when T_∞^* is decreased from 180 °C to 80 °C.

In figure 5.9a and b are presented Q_C^* as a function of P_i^* for 2 and 8 elements respectively. It can be noted that an increase of P_i^* in the range 1 % to 3 % (2 elements) and 3 % to 6 % (8 elements) occurs when v_∞^* (given close to the data points) is increased from its minimum to its maximum value. It is also possible to observe that an increase of P_i^* in the range 0 % to 4 % (2 elements) and 3 % to 4 % (8 elements) do occur when T_∞^* is decreased from 180 °C to 80 °C (same velocity). Runs in Figure 5.6 and 5.7 are indicated in Figure 5.9; it can be observed that we obtain a similar classification in terms of the highest P_i .

Considering the uncertainty level on the temperature measurement and the possible local variations within the test section of h_{cc} , all these results demonstrate that:

- a) Q_R^* is practically time independent and only slightly affected by the convective heat transfer (only through T_∞^*). Thus it is not responsible for the P_i differences that were observed in Figures 5.6 and 5.7.
- b) In most cases Q_C^* behaves exactly like P_i^* ; it increases when T_∞^* is decreased or v_∞^* is increased. Furthermore, the P_i^* increase can be for a significant fraction explained quantitatively by the variations in T_∞^* or v_∞^* .

When T_∞^* is decreased, the thermal gradient between the inside of the pyramid and the upper cavity (Figure 3.3) is increased (also the conductive heat losses). Thus P_i must be increased to keep T_{sir} constant (for same number of elements). When v_∞^* is increased, the air renewal rate within the upper cavity is increased (also the convective heat losses on the outside of the pyramid) thus P_i must be increased to keep T_{sir} constant. This qualitative evaluation does show that the fraction of the P_i increase that was not explained by higher convective losses within the test section are likely to be due to higher conductive heat transfer loss through the pyramid's walls, I.R. source ceramic and frame.

These arguments constitute *a posteriori* justification of the assumption of T_4 being the same function for all the I.R. drying runs in free or forced convection.

The reproducibility of the data in Table 5.3 (at constant T_∞^* and number of elements) of the determination of q_{is}^* and q_{its}^* (2 and 8 elements) was $\pm 1.5\%$ and $\pm 7.2\%$ respectively. It should be noted that q_{its}^* does not appear to be a function of v_∞^* (the same behavior was found for Q_R^*). On the other hand, it decreases when the number of elements is increased or T_∞^* decreased. Same results were found in Figure 5.8a. q_{its}^* is between 14.6% to 36.5%. At $T_\infty^* \sim 80^\circ\text{C}$ or 180°C (8 elements), q_{its}^* are in the same range (15% to 22%) as the one obtained for all the free convection-I.R. evaporation experiments (Table 5.1); at $T_\infty^* \sim 180^\circ\text{C}$ and 2 heating elements, q_{its}^* in Table 5.3 are much higher (35% to 37%). All q_{its}^* when the same conditions are used (Table 5.3) differ by less than 1.6%.

5.4.2 CONVECTIVE HEAT TRANSFER COEFFICIENTS

From equation 5.3 and the above evaluation of q_{is}^* , the average experimental convective heat transfer coefficient h_c^* corrected for radiation from the cavity walls and I.R. heat source during the P.C.D.R.P. (S values between 0.5 to 0.2; Table 5.9) is:

$$h_c^* = \frac{1}{(T_\infty^* - T_s^*)} \left\{ \frac{1}{(t_2 - t_1)} \left[\int_{t_1}^{t_2} \left(-\frac{1}{A_s} \frac{dm_w}{dt} \Delta H_v \right) dt + \int_{t_1}^{t_2} \frac{1}{A_s} (m_w c_{pw} + m_b c_{pb}) \frac{dT_s}{dt} dt \right] - E_s (q_{is}^* - \sigma T_s^{*4}) \right\} \quad (5.12)$$

The convective heat transfer coefficients h_{cc}^* could be predicted from the correlation developed in Appendix 7 for the flow variables (T_∞^* , v_∞^* , T_d^*) and T_s^* given in Table 5.3.

Moreover, h_{cc}^* was corrected for high mass transfer rate effects to yield the predicted heat transfer coefficient h_{cp}^* (it is the heat transfer coefficient diminished as a result of the measured evaporation rate) according to:

$$h_{cp}^* = h_{cc}^* \cdot \theta_h \quad (5.13)$$

However, the relation which gives θ_h is expressed in terms of the rate factor ϕ_h as (Bird et al., 1960):

$$\phi_h = \frac{N_v (c_{pv})_s}{h_{cc}^*} \quad (5.14)$$

θ_h (Bird et al. (1960)) was correlated as a function of ϕ_h (polynomial regression):

Boundary layer theory:

if $-1.0 < \phi_h < 1.0$

$$\theta_h = 1.0008 - 0.76844 \cdot \phi_h + 4.07 \cdot 10^{-2} \cdot \phi_h^2 \quad (5.15)$$

Film theory:

if $-1.0 < \phi_h < 1.0$

$$\theta_h = 1.0005 - 0.49974 \cdot \phi_h + 8.2279 \cdot 10^{-2} \cdot \phi_h^2 \quad (5.16)$$

Penetration theory:

if $-1.0 < \phi_h < 1.0$

$$\theta_h = 0.99875 - 0.62973 \cdot \phi_h + 8.5464 \cdot 10^{-2} \cdot \phi_h^2 \quad (5.17)$$

The correlation coefficient r for these expressions was 1.00. In Table 5.4, the sample number, b , the run identification name, the number of activated elements, T_{∞}^* , v_{∞}^* , P_{∞}^* , T_d^* , T_s^* , q_{is}^* , N_v^* , q_{ac}^* , q_{ac}^* %, h_c^* , h_{cp}^* , h_{cc}^* and θ_h are given. The computed θ_h values were obtained using equations 5.14 and 5.15.

5.4.3 DISCUSSION OF RESULTS

A close look at Table 5.4 (a and b) allows us to make the following observations. When the drying rate gets close to a constant value (P.C.D.R.P.), the surface evaporation temperature T_s^* (eight column) when $b = 19.9$ mm reaches the boiling point whatever the external drying conditions (T_{∞}^* , v_{∞}^* , T_d^* , q_{is}^*). Moreover, for $b \leq 10.3$ mm it is obvious that whatever T_{∞}^* , v_{∞}^* , T_d^* and q_{is}^* ; T_s^* does not reach the boiling point temperature. A similar behavior was previously observed in section 5.3 for the free convection-I.R. drying experiments. This phenomenon necessitates a careful explanation.

The relevant experimental phase was carried out through completion of the following experimental schedule:

- a) Convective drying runs with $b = 5.5, 10.3$ and 19.9 mm;
- b) Combined convective-I.R. drying runs for the 10.3 mm sample;
- c) Combined convective-I.R. drying runs for the 19.9 mm sample;
- d) Combined convective-I.R. drying runs for the 5.5 mm sample and free convection-I.R. drying runs.

Up to step 3, the recorded T_s^* and N_v^* were reproducible and comparable for fixed external conditions. However, after a few combined convective and I.R. ($T_{\infty}^* \sim 80-180$ °C, $v_{\infty}^* \sim 2.1-6.2$ m/s, $q_{is}^* \sim 7260-21080$ W/m²) drying runs (6 for $b = 19.9$ mm (No. XII) and 3 for $b = 20$ mm (No. XIII)) for which it was observed that the T_s^* and N_v^* were similar to the ones already found for the 10.3 mm sample (No. X). It appeared, as additional runs were carried out for same heating conditions (T_{∞}^* , v_{∞}^* , q_{is}^*), that the recorded T_s^* were getting progressively higher than for the initial observations.

TABLE 5.4a
HEAT TRANSFER COEFFICIENTS FROM THE COMBINED
CONVECTIVE AND I.R. DRYING RUNS

Sa. No. b (mm)	Run No.	Nb. El.	T_{∞}^*	v_{∞}^*	P_{∞}^*	T_d^*	T_s^*	q_{is}^*	N_v^*	q_{ac}^*	$q_{ac}^* \%$	h_c^*	h_{cp}^*	h_{cc}^*	θ_h
			(°C)	(m/s)	(kPa)	(°C)	(°C)	(W/m ²)	(kg/m ² s)	(W/m ²)	%	(W/m ² K)	(W/m ² K)	(W/m ² K)	(.)
K 5.5	ir17	2	79.2	2.0	100.10	8.3	56.0	6810	2.25e-03	110	2.0	22	20	23	0.86
	ir18	8	86.1	2.0	99.98	12.2	76.0	20340	6.63e-03	500	3.2	27	14	24	0.60
	i85h	8	145.0	3.5	101.98	-4.0	82.8	20740	6.82e-03	510	3.2	5	18	29	0.65
	i83h	8	141.7	5.2	101.19	-10.6	82.7	20770	7.06e-03	550	3.4	15	26	37	0.72
X 10.3	ir2	4	81.1	2.1	98.78	5.2	73.3	12110	3.88e-03	300	3.3	-	19	25	0.77
	ir3	6	83.1	2.1	98.73	6.4	78.2	16980	5.14e-03	550	4.6	-	17	25	0.70
	ir1	2	80.0	2.1	98.97	3.9	60.3	6930	2.25e-03	110	2.2	22	20	24	0.86
	ir5	2	79.9	2.1	99.51	12.3	64.2	6890	2.29e-03	130	2.3	36	21	24	0.86
	ir7	2	79.8	3.2	99.93	6.7	62.7	6860	2.28e-03	140	2.6	35	29	32	0.90
	ir9	2	79.8	4.5	99.86	7.8	60.7	6840	2.29e-03	170	3.1	34	35	39	0.91
	ir4	8	86.7	2.1	98.74	4.4	85.3	20520	6.16e-03	850	6.0	-	16	25	0.64
	ir6	8	85.6	2.1	99.50	13.9	80.8	20510	6.01e-03	760	5.4	-	16	25	0.65
	ir8	8	83.0	3.3	100.06	7.1	83.1	20490	6.15e-03	790	5.6	-	25	34	0.73
	ir10	8	83.7	4.5	99.87	9.2	82.3	20510	5.82e-03	750	5.6	-	32	41	0.79
	ir11	2	180.0	2.6	100.81	2.9	73.3	7660	3.34e-03	270	3.5	24	16	20	0.76
	ir13	2	180.0	4.3	100.79	2.5	72.4	7710	3.67e-03	270	3.1	31	22	28	0.81
	ir15	2	179.8	6.1	100.79	4.1	71.8	7660	3.66e-03	290	3.4	31	29	35	0.85
	ir12	8	183.3	2.6	100.79	5.1	85.2	21370	7.24e-03	1180	7.1	15	10	21	0.49
	ir14	8	181.1	4.3	100.81	1.9	84.4	21370	7.37e-03	1260	7.4	19	18	29	0.62
	ir16	8	180.1	6.1	100.79	5.8	84.4	21380	7.32e-03	1110	6.6	16	25	36	0.70

Nb. El.: number of heating elements activated

TABLE 5.4b
HEAT TRANSFER COEFFICIENTS FROM THE COMBINED
CONVECTIVE AND I.R. DRYING RUNS

Sa. No. b (mm)	Run No.	Nb. El.	T_{∞}^*	v_{∞}^*	P_{∞}^*	T_d^*	T_s^*	q_{is}^*	N_v^*	q_{ac}^*	$q_{ac}^* \%$	h_c^*	h_{cp}^*	h_{cc}^*	θ_h
			(° C)	(m/s)	(kPa)	(° C)	(° C)	(W/m ²)	(kg/m ² s)	(W/m ²)	%	(W/m ² K)	(W/m ² K)	(W/m ² K)	(.)
XII 19.9	i62h	2	80.3	2.1	99.79	17.9	100.8	7260	1.75e-03	0	0.0	48	24	27	0.91
	i63h	2	81.3	2.1	99.67	17.1	100.9	7270	1.80e-03	0	0.0	45	24	27	0.90
	i64h	2	81.2	4.5	99.57	16.9	100.6	7220	1.49e-03	0	0.0	79	42	44	0.95
	i57h	8	85.3	2.1	99.69	16.2	101.7	21130	6.60e-03	510	3.4	39	17	27	0.63
	i58h	8	84.2	2.1	99.79	16.2	101.8	21100	6.53e-03	470	3.2	46	17	27	0.64
	i56h	8	84.2	2.6	99.71	16.5	101.7	21080	6.37e-03	440	3.1	68	21	31	0.69
	i55h	8	84.1	3.4	99.78	15.9	101.5	21010	6.26e-03	550	3.9	73	27	37	0.75
	i68h	8	82.9	4.5	99.99	14.1	101.6	20990	6.23e-03	230	1.6	88	34	44	0.79
	i69h	8	84.1	4.5	99.99	13.7	101.6	21000	6.24e-03	310	2.2	89	34	44	0.79
	i70h	8	84.9	4.5	100.06	13.7	101.7	20990	6.34e-03	290	2.0	80	34	43	0.79
	i71h	8	85.6	4.5	100.18	14.0	101.6	20980	6.33e-03	330	2.3	82	34	43	0.79
	i38h	2	180.3	2.6	99.99	11.8	101.2	7920	3.13e-03	220	3.1	23	18	22	0.79
	i45h	2	180.2	6.2	99.71	14.7	100.5	7860	3.55e-03	110	1.3	34	33	38	0.86
	i49h	2	180.2	6.2	98.90	14.0	100.4	7870	3.36e-03	160	2.2	29	33	38	0.87
	i50h	2	180.3	6.2	99.11	12.0	100.5	7880	3.57e-03	70	0.9	34	33	38	0.86
	i76h	8	179.9	2.6	100.63	8.7	101.1	22020	7.79e-03	990	5.6	23	11	22	0.48
	i77h	8	179.9	2.6	100.61	9.7	101.1	22110	7.70e-03	1010	5.8	20	11	22	0.48
	i52h	8	180.3	6.2	99.51	6.6	100.9	21830	7.64e-03	1510	8.7	27	27	38	0.70
i78h	8	179.7	6.1	100.31	12.1	101.5	21770	7.98e-03	940	5.2	31	26	38	0.69	

Nb. El.: number of heating elements activated

During the period of these experiments (within 3 days), four convective drying runs ($T_{\infty}^* \sim 180^{\circ}\text{C}$, $v_{\infty}^* \sim 2.6$ and 6.1 m/s and $T_d^* \sim 13.6$ - 16.3°C) showed a similar increase of T_s^* (68°C , 72°C , 78°C and 86°C) in convection drying which confirmed the existence of this phenomenon. As these temperatures are significantly higher than the ones presented in section 4.2 for similar conditions ($T_s^* \sim 45$ - 51°C), it can be concluded that an additional mass transfer resistance was probably being built close to the sample surface (crust formation). This is quantified in Table 5.5 where an evaluation of the mass transfer coefficient $(K_{yBL}^*)_{\text{varp}}$ (from the experimental N_v^* , application of the boundary layer theory and density variation corrections) is compared with the one presented in section 4.3 (Table 4.2). For sample no. XIII, the ratio of these mass transfer coefficients evolves from 2.4 (run no. i37h) to 5.2 (run no. i46h). As T_s^* for sample no. XII during the combined convective-I.R. drying runs was already stabilized to the boiling point temperature when run no. i47h was realized, it is likely that the value reached is also stabilized (it is about 6.2 time lower than its initial value). h_{cBL}^* is also computed in Table 5.5 and show similar values as the one from Table 4.2. This underlines the point that a much higher mass transfer resistance exists at the surface which has no major influence on the heat transfer resistance.

In Figure 5.10a, a photograph of sample no. X surface can be compared to sample no. XII surface (Figure 5.10b). It is observed that the surface of no. XII displays brown and darker areas than the surface of no. X which means that it was "contaminated". Also in Figure 5.11a and b, a typical fraction of these surfaces are magnified (X 40) which shows that the pores of sample no. XII surface (Figure 5.11b) are obstructed whereas for sample X this does not seem to be the case (Figure 5.11a). However, as the total amount of water absorbed by sample no. XII was not different during the convective and combined convective-I.R. drying experiments, the additional mass transfer resistance is not likely to affect the internal moisture transport as it is mainly a surface phenomenon. Since only distilled-ion free water (conductivity: $5.6 \cdot 10^{-8}$ mho/cm) was used throughout, it is probably due to an improper glue mixture which did not resist fully to the very high temperature and stresses to which it was submitted under repeated wetting and drying with I.R. heating (overheating).

TABLE 5.5

COMPARISON OF $(K_{yBL})_{varp}$ AND h_{cBL} AFTER (COMBINED CONVECTIVE-I.R. DRYING RUNS) AND BEFORE (CONVECTIVE RUNS): THE EFFECT OF CRUST FORMATION ON SAMPLE NO. XII AND XIII FROM CONVECTIVE DRYING RUNS

Run No.	Sa. No.	b	T_{∞}	v_{∞}	P_{∞}	T_d	T_s	N_v	After $(K_{yBL})_{varp}$	Before $(K_{yBL})_{varp}$	After h_{cBL}	Before h_{cBL}
(.)	(.)	(mm)	(°C)	(m/s)	(kPa)	(°C)	(°C)	(kg/m ² s)	(mole/m ² s)	(mole/m ² s)	(W/m ² K)	(W/m ² K)
i37h	XIII	20.0	180.5	2.6	100.05	13.6	68	1.31e-03	0.26	0.62	18	19
i42h	XIII	20.0	180.3	6.1	99.73	14.2	72	1.53e-03	0.25	1.18	24	33
i46h	XIII	20.0	180.6	2.6	99.41	16.0	78	9.93e-04	0.12	0.62	13	19
i47h	XII	19.9	180.5	2.6	99.13	16.3	86	1.18e-03	0.10	0.62	19	19

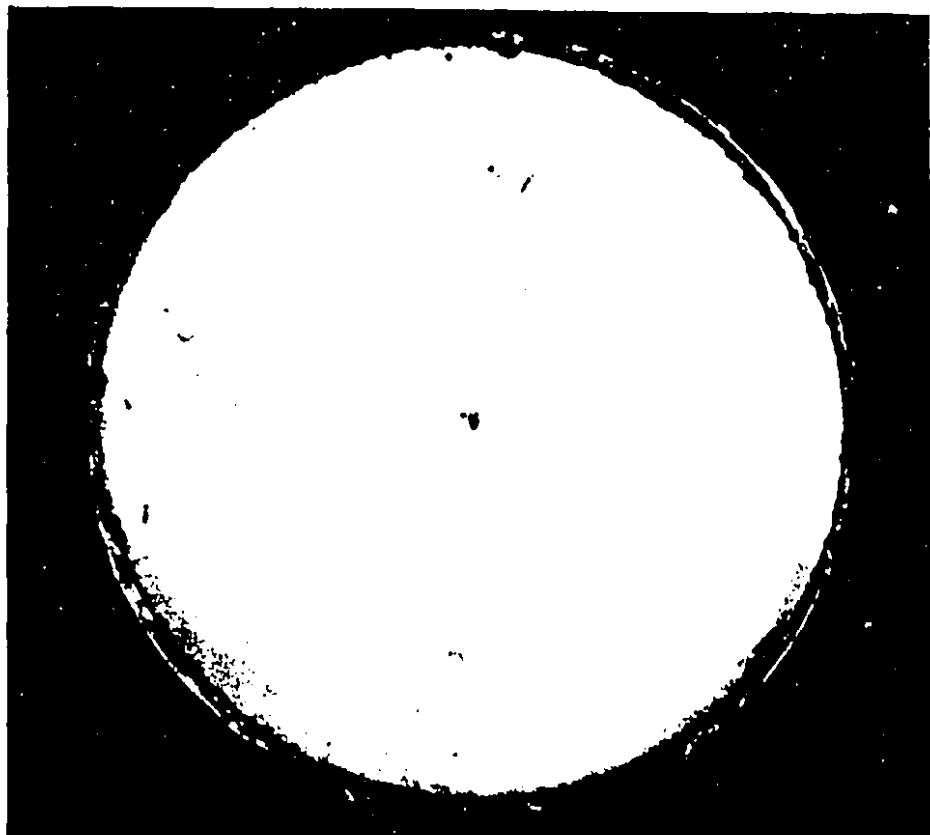


Figure 5.10 a Photograph of sample No. X after completion of the experimental schedule: overall view of the surface



Figure 5.10b Photograph of sample No. XII after completion of the experimental schedule: overall view of the surface

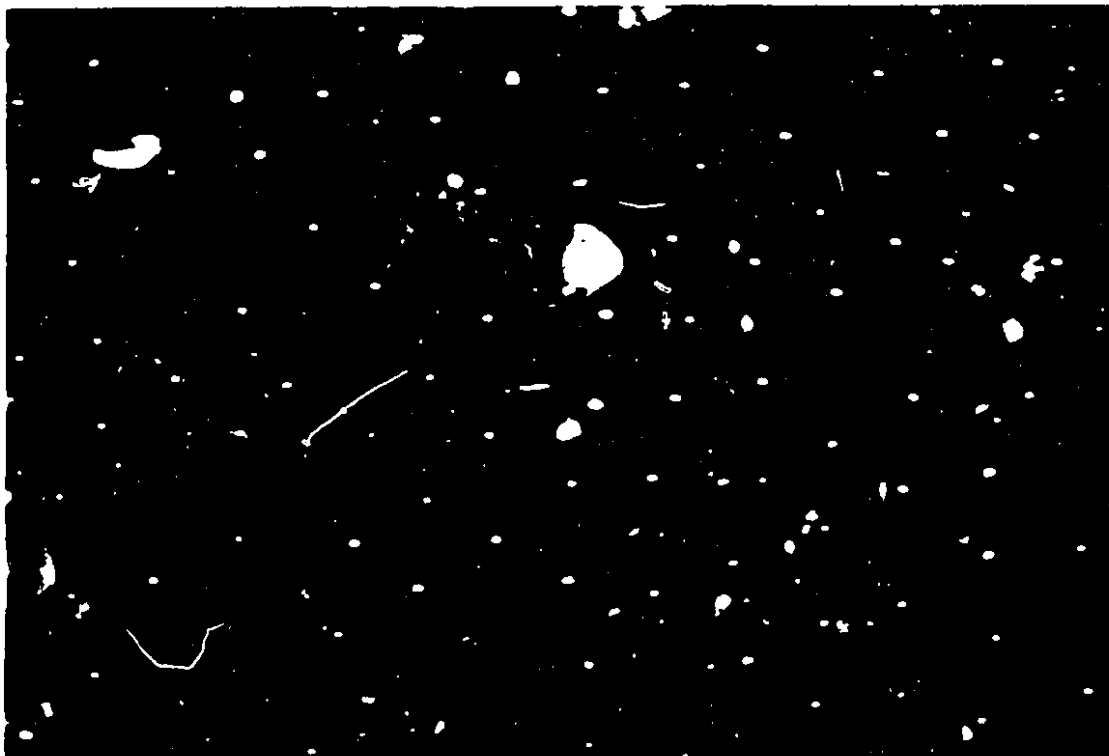


Figure 5.1 1a Photograph of sample No. X after completion of the experimental schedule: a typical fraction of the surface magnified (X 40)

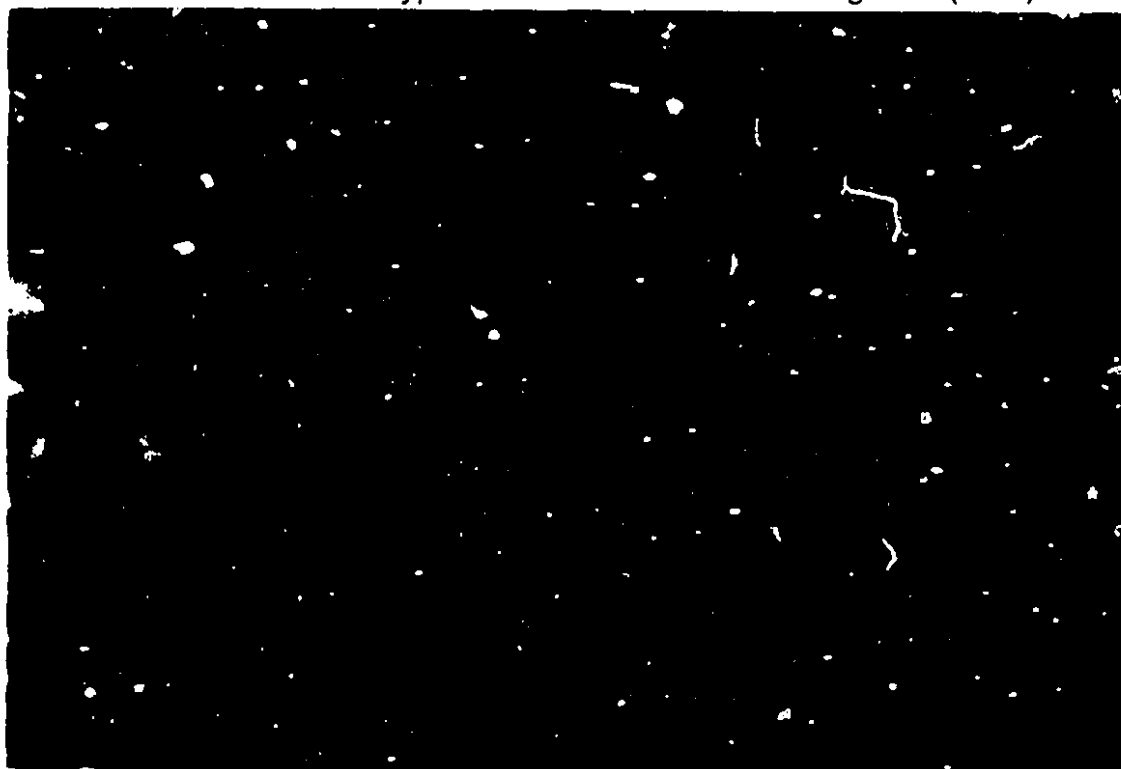


Figure 5.1 1b Photograph of sample No. XII after completion of the experimental schedule: a typical fraction of the surface magnified (X 40)

The reported results for the combined convective-I.R. drying runs performed with sample no. XII (19.9 mm) are the ones for which the T_s^* values stabilized to a value close to 100 °C for all q_{is}^* used and N_v^* was observed to be reproducible. These data were analyzed since:

- a) It probably corresponds to data ($T_s^* \sim 100$ °C) for a very low permeability porous medium or colloidal material such as porcelain clay ($d < 43$ μm , $b = 28\text{-}31$ mm, $T_\infty^* = 8$ °C, $v_\infty^* = 1.3$ m/s, $q_{is}^* = 9260$ W/m², $T_s^* = 100$ °C) as reported by Yagi et al. (1957);
- b) It characterizes extreme conditions in terms of mass transfer rate and presents a good test for the applicability of the correction procedures.

As can be seen from the 10.3 mm sample data ($T_\infty^* \sim 80$ °C, $v_\infty^* \sim 2.1$ m/s, $T_d^* \sim 3.9\text{-}6.4$ °C), when q_{is}^* is increased in the range 6.9, 12.1, 17.0 and 20.5 kW/m²; T_s^* increases in the range 60, 73, 78 and 85 °C respectively (Figure 5.5b). A very good linear correlation ($r=0.983$) between T_s^* and q_{is}^* is displayed in Figure 5.5b for $T_\infty^* \sim 80$ °C. Yagi et al. (1957) have found T_s^* in the range 46-69 °C for various granular porous media (river and standard sand, $d = 9\text{-}740$ μm , $b = 7\text{-}61$ mm, $T_\infty^* \sim 8\text{-}33$ °C, $v_\infty^* \sim 1.1\text{-}1.3$ m/s, $q_{is}^* = 5110\text{-}10450$ W/m²). Their results for $d=88$ μm and 130 μm and the one provided by Navarri (1990, 1991) for silica sand (quarry sand or sea sand, $d = 250\text{-}400$ or $200\text{-}250$ μm , $b = 5$ or 7 mm, $T_\infty^* \sim 30\text{-}90$ °C, $v_\infty^* \sim 2.1\text{-}6.0$ m/s, $q_{is}^* = 10.0$ and 18.5 kW/m² (N.I.R.)) are also sketched in the same figure; they confirm the temperature level found in the present study. Hasatani et al. (1983, 1988) studying the case of silica sand layers ($d = 320$ μm , $b = 20$ mm, $T_\infty^* = 30\text{-}80$ °C, $v_\infty^* \sim 0.60\text{-}1.1$ m/s and $q_{is}^* = 290\text{-}1400$ W/m²) observed T_s^* in the range 32-34 °C. This is probably a result of the low q_{is}^* values used during their experiments which were comparable in magnitude to the radiative heat fluxes from the test section walls found in the convective drying experiments summarized in Table 4.1.

In Table 5.4a, for $T_\infty^* \sim 80$ °C, $v_\infty^* \sim 2.1$ m/s and $q_{is}^* \sim 6.9$ kW/m², an increase of 8 °C of T_d^* (3.9 °C vs. 12.3 °C) produces a T_s^* increase of about 4 °C whereas for $T_\infty^* \sim 86$ °C, $v_\infty^* \sim 2.1$ m/s and $q_{is}^* \sim 20.5$ kW/m², an increase of

9 °C of T_d^* (4.4 °C vs. 13.9 °C) produce a T_s^* decrease of about 4 °C. Thus, it seems that there is no systematic effect of T_d^* on T_s^* .

No apparent effect of v_∞^* on T_s^* level can be identified with certainty in Table 5.4a. If it exists, it might be a very low decrease (~ 1 °C when the velocity is doubled). At low q_{is}^* (6.9-7.9 kW/m²) a significant increase in surface temperature (~ 10 °C) occur when T_∞^* is increased from 80 °C to 180 °C. However, at high q_{is}^* (20.5-21.4 kW/m²) the same increase of T_∞^* do not promote any meaningful effect on T_s^* (Figure 5.5b).

It is interesting to note that T_s^* values reached in free convection-I.R. drying (Figure 5.5a) are higher than the ones in forced convection-I.R. drying (Figure 5.5b). In forced convection conditions, the diffusion path (for the water vapor molecules) through the boundary layer is smaller. This result in a lower diffusion resistance, which, for similar mass flux, necessitates a lower surface concentration and thus a lower surface temperature.

It can be concluded that for $b = 10.3$ mm, T_s^* during the P.C.D.R.P. is only an increasing function of q_{is}^* while it is also an increasing function of T_∞^* at low q_{is}^* (6.9-7.9 kW/m²).

T_s^* reached for the 5.5 mm sample ($T_\infty^* \sim 80$ °C, $v_\infty^* \sim 2.0$ m/s, $T_d^* \sim 8.3$ -12.2 °C) is about 4 °C to 9 °C (Figure 5.5b) lower than for the 10.3 mm sample (56 °C vs. 60-64 °C; 76 °C vs. 81-85 °C) under almost the same incident heat fluxes ($q_{is}^* \sim 6.8$ -20.3 kW/m²). A portion of this difference is probably due to the effect of the thermocouple on the surface temperature measurement as discussed in section 6.6.2 and 6.7.1.

In Figure 5.12a and b, a representation of N_v^* as a function of q_{is}^* is displayed for free (no forced flow present) and forced convection I.R. drying respectively ($b = 19.9$ mm). In forced convection (Figure 5.12b), N_v^* is relatively more sensitive to v_∞^* changes at low q_{is}^* values because the spread of the data (a measure of the effect of v_∞^*) is about the same at low and high heat flux.

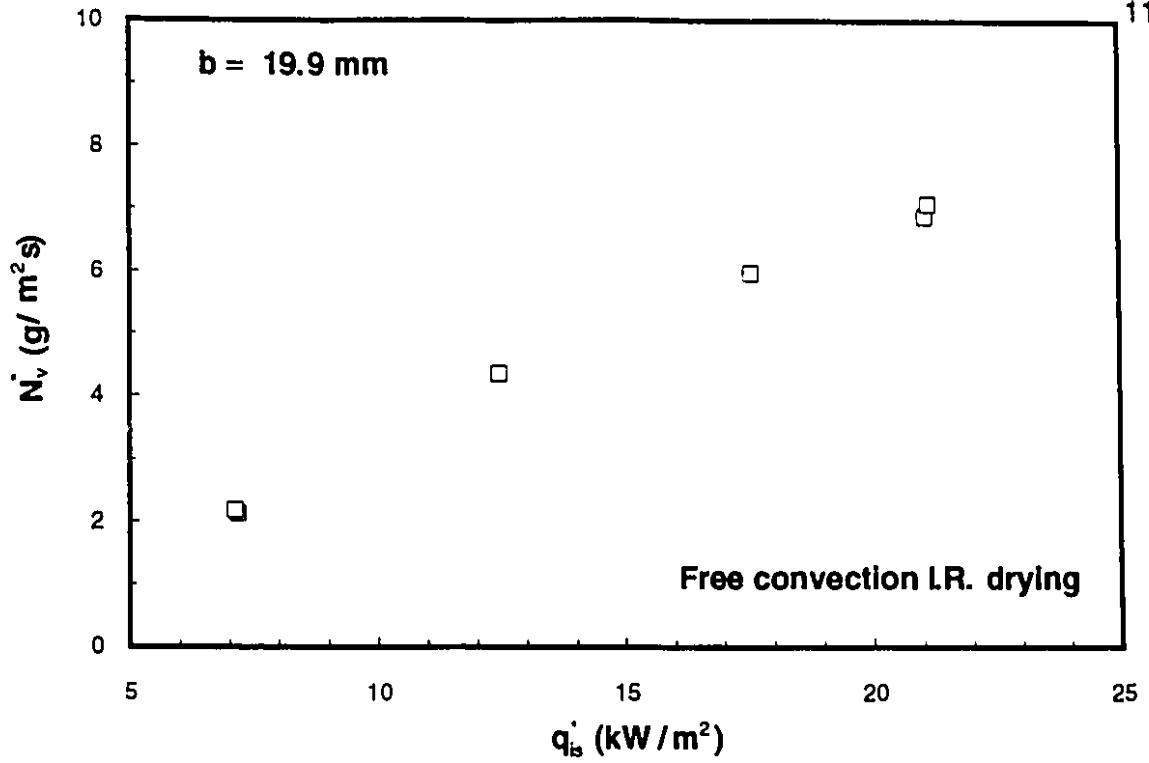


Figure 5.12a The drying rate as a function of the overall incident heat flux from free convection L.R. drying runs (N_v vs. q'_{is})

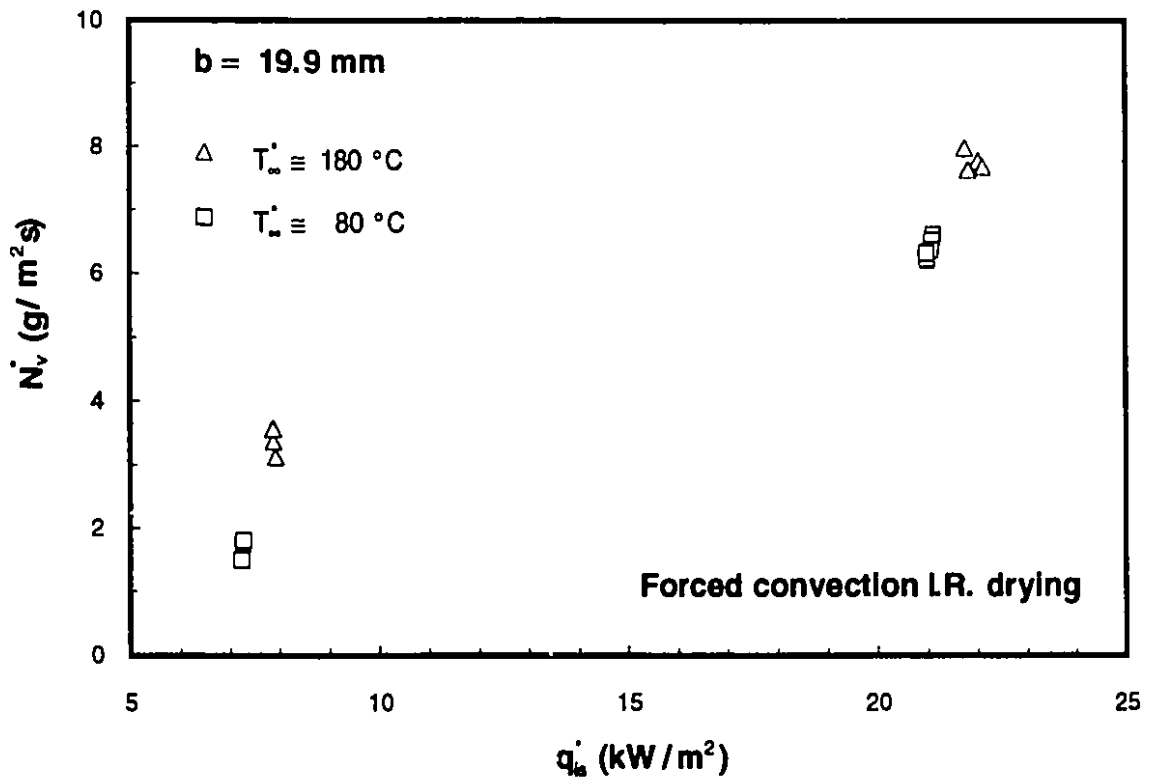


Figure 5.12b The drying rate as a function of the overall incident heat flux from forced convection L.R. drying runs (N_v vs. q'_{ib})

Since N_v^* and q_{is}^* were obtained independently (forced and free convection-I.R. experiments respectively), the relatively small spread of the data (at constant T_∞^*) emphasize the fact that the experimental procedure to obtain q_{is}^* and E_s^* is accurate.

q_{ac}^* % (twelfth column, Table 5.4a and b) range from 0.0 % ($T_\infty^* \sim 80^\circ\text{C}$, $q_{is}^* \sim 7.3 \text{ kW/m}^2$, $b = 19.9 \text{ mm}$) to 8.7 % ($T_\infty^* \sim 180^\circ\text{C}$, $q_{is}^* \sim 21.8 \text{ kW/m}^2$, $b = 19.9 \text{ mm}$). At constant T_∞^* , when q_{is}^* increases from about 7 kW/m^2 to 21 kW/m^2 , q_{ac}^* % increases between 2 to 4 %. At almost constant q_{is}^* , increasing T_∞^* by 100°C creates approximately a 1 % increase of q_{ac}^* %. q_{ac}^* % is a very weak function of v_∞^* (changes are less than 1 % when v_∞^* is doubled).

h_c^* (thirteenth column, Table 5.4a and b) could not be calculated accurately when $q_{is}^* \geq 12.1 \text{ kW/m}^2$ ($b = 10.3 \text{ mm}$, $T_\infty^* \sim 80^\circ\text{C}$) because when the denominator ($T_\infty^* - T_s^*$) of the left-hand side in equation 5.12 is too low ($-0.1 \leq T_\infty^* - T_s^* \leq 7.8^\circ\text{C}$), h_c^* is more sensitive to errors which occur in the determination of the drying rate, heat of accumulation, sample total hemispherical emissivity or incident heat flux.

When $T_s^* > T_\infty^*$ ($b = 19.9 \text{ mm}$, $T_\infty^* \sim 80^\circ\text{C}$), it is remarkable to observe that h_c^* (thirteenth column, Table 5.4b) is about twice h_{cp}^* (fourteenth column, Table 5.4b). This heat transfer coefficient increase is contrary to what can be predicted with the correction procedures (boundary layer, film or penetration theories) presented in section 4.3. A decrease should be expected like in evaporation from a heated wall (Bird et al. 1960; Kast, 1984). This phenomenon results in higher than expected convective heat losses and lower N_v^* . It may be noted that:

- a) At constant q_{is}^* , for same v_∞^* (2.1 m/s or 4.5 m/s) the maximum scatter on these h_c^* data is relatively low ($\sim 17\%$);
- b) At constant v_∞^* , for different q_{is}^* (7.3 kW/m^2 vs. 21.1 kW/m^2) a comparison of determined h_c^* values show differences less than 20 %;

- c) The usual behavior of h_c^* increasing function of v_∞^* increasing is shown by these data; for both heat fluxes (7.3 kW/m² and 21.1 kW/m²) multiplying the velocity by 2.1 gives a h_c^* multiplied by a factor between 1.7 and 2.0. In chapter IV, the experimentally determined h_c^* was similarly observed to be multiplied by 1.5 when the velocity is multiplied by about 2.3;
- d) The determination of h_c^* (Table 5.4b) was reproduced 4 times for same drying conditions ($b=19.9$ mm, $T_\infty^* \sim 84$ °C, $v_\infty^* = 4.5$ m/s, $T_d^* \sim 14$ °C, $q_{is}^* \sim 21.1$ kW/m²), the resulting h_c^* was reproducible within ± 11 %. Moreover, T_s^* was found reproducible within ± 0.1 °C.

When $T_s^* < T_\infty^*$ ($b = 5.5$ or 10.3 mm; $b = 19.9$ mm and $T_\infty^* \sim 180$ °C) the range of h_c^* (5-36 W/m²K) is comparable to the range of h_{cc}^* (21-44 W/m²K; fifteenth column, Table 5.4a and b). This means that I.R. heating (medium-to-long wavelength range) does not change the order of magnitude of the convective heat transfer coefficient ($T_s^* < T_\infty^*$). In most reported cases in Table 5.4, an increase of h_c^* results from a v_∞^* increase although the scatter in the results does mask partly this effect.

For convection-I.R. drying, the range of θ_h (0.48-0.95; last column, Table 5.4a and b) extends to lower θ_h values as compared to the one found in convection drying (0.94-0.98). The overall behavior of θ_h is a decrease with an increase in q_{is}^* (Figure 5.13a). In Table 5.4, θ_h increases by up to 0.15 as T_∞^* is decreased by 100 °C (at constant q_{is}^* ; Figure 5.13a). θ_h is increased when v_∞^* is increased (by as much as 0.2 when v_∞^* is doubled). The range of θ_h predicted by the boundary layer theory implies a significant decrease (5 % to 52 %) of the heat transfer coefficient in the case of combined convective-I.R. drying over the operating range investigated.

In order to verify (when $T_s^* < T_\infty^*$) if the boundary layer correction could be applied successfully to h_{cc}^* to predict the convective heat transfer coefficient h_{cp}^* corrected for high mass transfer rate effect, the differences $h_c^* - h_{cp}^*$ (Δh_1) and $h_c^* - h_{cc}^*$ (Δh_2) were computed ($n = 22$ cases; Table 5.6).

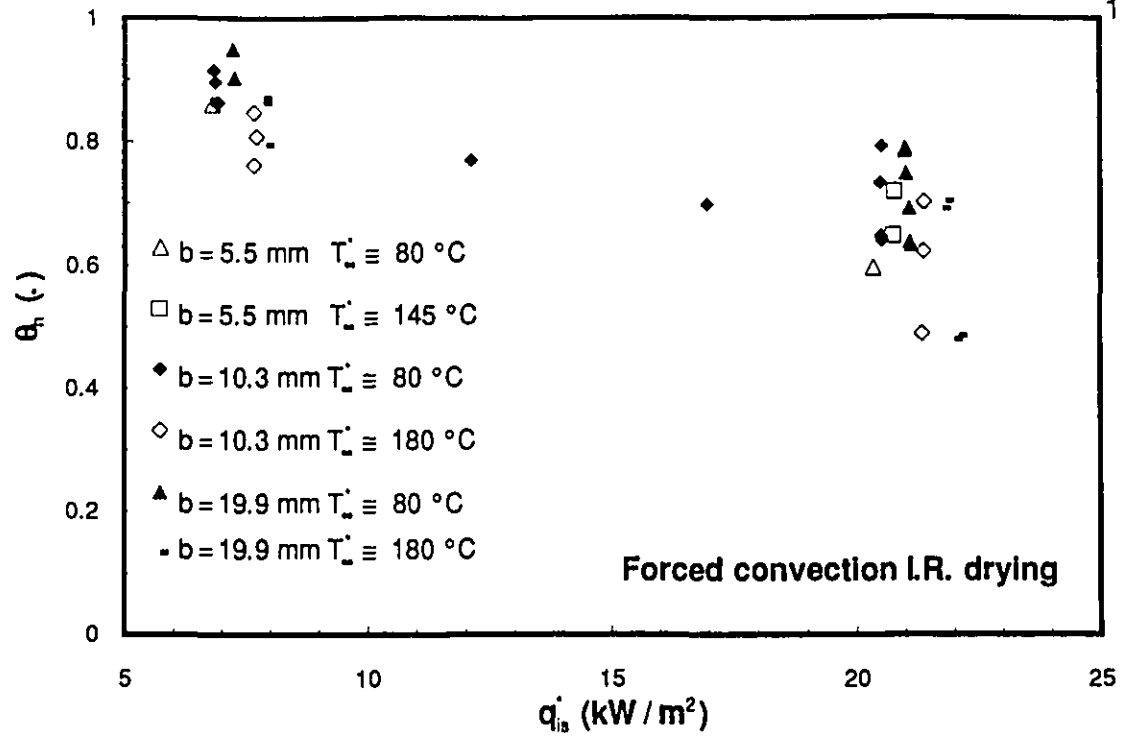


Figure 5.13a The heat transfer coefficient correction factor as a function of the overall incident heat flux from forced convection IR. drying runs (θ_h vs. q_{is})

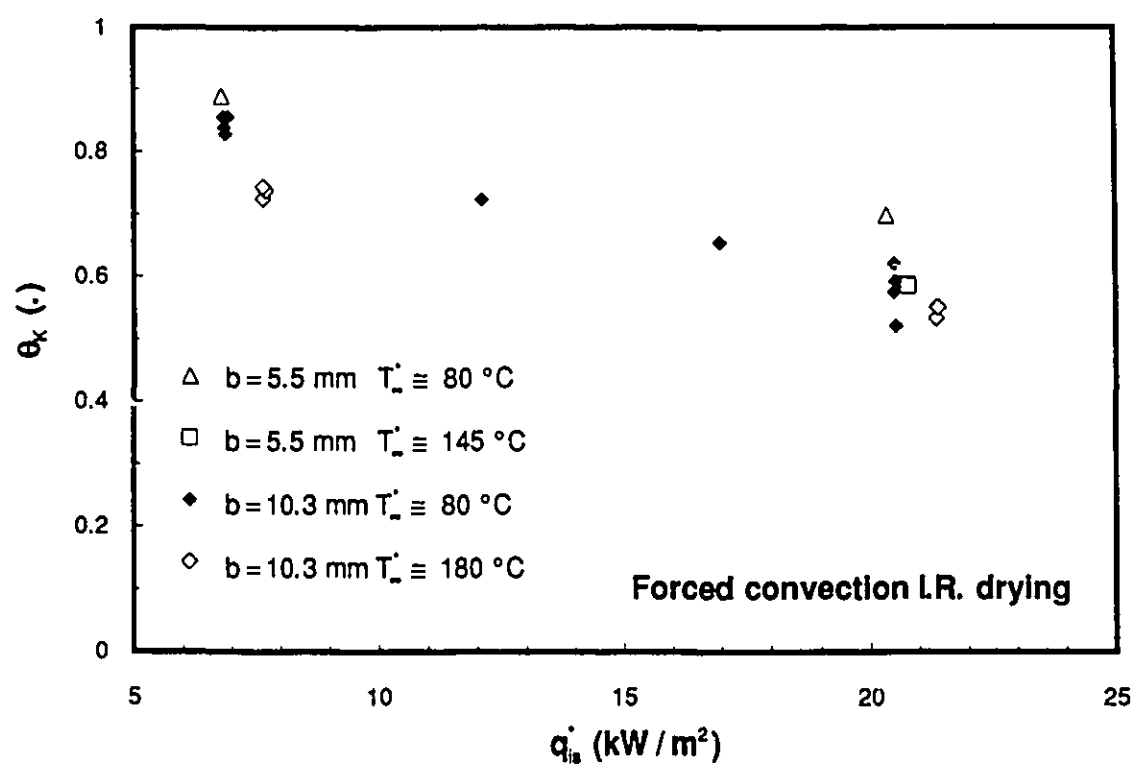


Figure 5.13b The mass transfer coefficient correction factor as a function of the overall incident heat flux from forced convection IR. drying runs (θ_K vs. q_{is})

TABLE 5.6

TEST ON THE PREDICTION OF THE HEAT TRANSFER COEFFICIENT WITH THE BOUNDARY

LAYER THEORY FROM THE COMBINED CONVECTIVE AND I.R. DRYING RUNS

Sa. No.	Run b (mm)	Nb. No.	Nb. El.	T_{∞}^*	v_{∞}^*	P_{∞}^*	T_d^*	T_s^*	q_{is}^*	Δh_1	Δh_2	Δh_1	Δh_2	Δh_1	Δh_2	
				(°C)	(m/s)	(kPa)	(°C)	(°C)	(W/m ²)	2 and 8	2 and 8	2	2	8	8	
X 5.5	ir17	2		79.2	2.0	100.10	8.3	56.0	6810	2	-2	2	-2			
	ir18	8		86.1	2.0	99.98	12.2	76.0	20340	12	2			12	2	
	i85h	8		145.0	3.5	101.98	-4.0	82.8	20740	-13	-23			-13	-23	
	i83h	8		141.7	5.2	101.19	-10.6	82.7	20770	-11	-22			-11	-22	
X 10.3	ir1	2		80.0	2.1	98.97	3.9	60.3	6930	1	-2	1	-2			
	ir5	2		79.9	2.1	99.51	12.3	64.2	6890	15	12	15	12			
	ir7	2		79.8	3.2	99.93	6.7	62.7	6860	6	3	6	3			
	ir9	2		79.8	4.5	99.86	7.8	60.7	6840	-2	-5	-2	-5			
	ir11	2		180.0	2.6	100.81	2.9	73.3	7660	8	4	8	4			
	ir13	2		180.0	4.3	100.79	2.5	72.4	7710	8	3	8	3			
	ir15	2		179.8	6.1	100.79	4.1	71.8	7660	1	-4	1	-4			
	ir12	8		183.3	2.6	100.79	5.1	85.2	21370	4	-6			4	-6	
ir14	8		181.1	4.3	100.81	1.9	84.4	21370	1	-10			1	-10		
ir16	8		180.1	6.1	100.79	5.8	84.4	21380	-9	-20			-9	-20		
XI 19.9	i38h	2		180.3	2.6	99.99	11.8	101.2	7920	5	1	5	1			
	i45h	2		180.2	6.2	99.71	14.7	100.5	7860	1	-4	1	-4			
	i49h	2		180.2	6.2	98.90	14.0	100.4	7870	-4	-9	-4	-9			
	i50h	2		180.3	6.2	99.11	12.0	100.5	7880	1	-4	1	-4			
	i76h	8		179.9	2.6	100.63	8.7	101.1	22020	12	1			12	1	
	i77h	8		179.9	2.6	100.61	9.7	101.1	22110	9	-3			9	-3	
	i52h	8		180.3	6.2	99.51	6.6	100.9	21830	0	-11			0	-11	
	i78h	8		179.7	6.1	100.31	12.1	101.5	21770	4	-8			4	-8	
										Δh_{mi}	2.5	-4.8	3.7	-0.6	1.0	-9.9
										Stdev.	7.3	8.6	5.2	5.5	9.4	9.1

Nb. El.: number of heating elements activated

Δh_1 mean value (Δh_{m1}) was 2.5 (standard deviation $\sigma_1 = 7.3$) and Δh_2 mean value (Δh_{m2}) was -4.8 (standard deviation $\sigma_2 = 8.6$). Assuming a normal distribution (Bragg, 1974) for Δh_1 and Δh_2 , a student's t test (Audet et al., 1986) was carried out to check if these mean values were significantly different from 0. The formula for t is given by (Audet et al., 1986):

$$t = \frac{\Delta h_{mi} - 0}{\sigma_i / \sqrt{n}} \quad (5.18)$$

where Δh_{mi} is the mean to be tested (Δh_{m1} or Δh_{m2}), 0 is the assumed average of the whole population, σ_i the standard deviation computed from the evaluation of Δh_1 or Δh_2 and $(n-1)$ is the test number of degrees of freedom for the test. With 21 as the degree of freedom, a "student's t " value of 1.72 for a probability $P = 0.05$ is found (Audet et al., 1986). The " t " values from equation 5.18 were 1.6 for Δh_1 and -2.6 for Δh_2 . Then, it can be concluded that within a 95 % confidence limit interval, Δh_{m1} does not differ significantly from 0 whereas Δh_{m2} differs significantly from 0.

In Table 5.6 are also provided the Δh_{m1} and Δh_{m2} values for low (6.8-7.9 kW/m²; 2 heating elements) and high (20.3-22.1 kW/m²; 8 heating elements) heat flux data. The student's t test was applied to each of these categories.

For the low heat flux data, the degrees of freedom is 11 and a "student's t " value of 1.80 for a probability $P = 0.05$ is found (Audet et al., 1986). The " t " values from equation 5.18 were 2.5 for Δh_1 and -0.4 for Δh_2 . Then, it can be concluded that within a 95 % confidence limit interval, Δh_{m2} does not differ significantly from 0 whereas Δh_{m1} differs significantly from 0.

For the high heat flux data, the degrees of freedom is 9 and a "student's t " value of 1.83 for a probability $P = 0.05$ is found (Audet et al., 1986). The " t " values from equation 5.18 were 0.3 for Δh_1 and -3.2 for Δh_2 . Then, it can be concluded that within a 95 % confidence limit interval, Δh_{m1} does not differ significantly from 0 whereas Δh_{m2} differs significantly from 0 when 8 elements are used.

Since the correction procedures were developed under the assumption that vapor diffusion occurs at the interface it is interesting to verify if, when T_s^* is equal to the boiling point temperature and $T_s^* < T_\infty^*$, their predictions are still valid. A test can be carried with the values obtained for $b = 19.9$ mm and $T_\infty^* \sim 180$ °C.

When T_s^* is equal to the boiling point temperature ($b = 19.9$ mm and $T_\infty^* \sim 180$ °C; Table 5.4b), with 7 degrees of freedom a "student's t " value of 2.00 for a probability $P = 0.05$ is found (Audet et al., 1986). The " t " values from equation 5.18 were 1.7 for Δh_1 and -2.9 for Δh_2 . Then, it can be concluded that within a 95 % confidence limit interval, Δh_{m1} does not differ significantly from 0 whereas Δh_{m2} differs significantly from 0 when T_s^* is equal to the boiling point temperature and $T_s^* < T_\infty^*$. The boundary layer theory can be applied to predict the convective heat transfer coefficient when the surface temperature reaches the boiling temperature and $T_s^* < T_\infty^*$. Yagi et al (1957) have presented results for a colloidal medium (porcelain clay, $d < 43$ μ m, $b = b = 28-31$ mm, $T_\infty^* = 8$ °C, $v_\infty^* = 1.3$ m/s, $q_{is}^* = 9260$ W/m²) for which T_s^* reach the boiling point temperature and N_v^* is half its value obtained for non-hygroscopic porous media under similar conditions. This might be a consequence of a low E_s and/or an increase of h_c^* as observed in the present study.

At low q_{is}^* scatter in the results does not allow us to make a definitive test about the appropriateness of the boundary layer theory to account for the effect of high mass transfer rate on the heat transfer coefficient. In such cases, the magnitude of the expected correction being low (between 5 % and 21 %) relatively small differences between h_c^* , h_{cp}^* and h_{cc}^* are apparent in Table 5.4. When the corrections for high mass transfer rate effect (highest N_v^*) on the heat transfer coefficient are the highest (between 21 % and 52 %), the boundary layer theory appears to be well suited to account for these effects. Hence, it is possible to infer that the magnitude of the high mass transfer rate effect appearing in combined convection-I.R. drying ($T_s^* < T_\infty^*$) on the heat transfer coefficient is quantitatively well predicted by the laminar boundary layer theory (Bird et al, 1960). A test on the film as well as penetration theories to predict h_c^* did show that they were also acceptable.

5.5 TEST OF THE ANALOGY BETWEEN THE HEAT AND MASS TRANSFER IN COMBINED CONVECTION-I.R. DRYING

The mass transfer coefficients K_p^* and K_y^* were computed with equation 4.8 and 4.9 as well as corrected with equations 4.14, 4.15 and 4.19 to give $(K_{pBL}^*)_{varp}$ and $(K_{yBL}^*)_{varp}$. K_y^* could not be computed when T_s^* is near the boiling point temperature because y_{vs}^* is close to unity thus B_K (section 4.3) increases to very large values (positive or negative) where the various correction procedures become meaningless. In terms of the physical phenomena, this is usually associated with a boundary layers separation at the surface (Greiner and Winter, 1978). The experimentally determined h_c^* can be corrected (equation 4.20) for high mass transfer rate effect and h_{cBL}^* was obtained. Here θ_h was obtained with equation 4.21 (for B_h) and the correlation 4.16 from the boundary layer theory results. Then all the transfer coefficient ratios described in section 4.3 (4.10, 4.11, 4.22, 4.23) are computed for the 5.5 mm and 10.3 mm samples. The missing h_{cBL}^* (to compute ratios 4.22 and 4.23) values (due to too small $(T_\infty^* - T_s^*)$; section 5.4.3) were replaced by h_{cc}^* (6 cases) since it has been demonstrated in the previous section that the experimental convective correlation (Appendix7) and the boundary layer theory could be used to predict the heat transfer coefficient corrected for high mass transfer rate effect. The ratios 4.10 and 4.11 were evaluated with h_c^* or h_{cp}^* (6 cases) respectively.

In Table 5.7, the sample number, b, the run identification name, the number of activated elements, T_∞^* , v_∞^* , P_∞^* , T_d^* , T_s^* , q_{is}^* , h_{cBL}^* or h_{cc}^* , K_p^* , $(K_{pBL}^*)_{varp}$, 4.22, K_y^* , $(K_{yBL}^*)_{varp}$, 4.23, θ_K and H_c are given. This Table is given as a reference for comparison with Table 5.8, where the same variables are presented when T_s^* is corrected. Indeed, an important observation concerns the fact that T_s^* values reported in Table 5.4b (also in Table 5.2 for $b = 19.9$ mm) are greater than 100 °C, the boiling point temperature at atmospheric pressure. Furthermore, the level reached by T_s^* is a function of the number of activated heating elements (2 elements average T_s^* : 100.7 °C, 8 elements average T_s^* : 101.5 °C; T_s^* standard deviation: 0.3 °C). Since the thermocouples used for T_s^* measurements have been calibrated to 0.5 °C, it is possible to ascribe the I.R. heat flux penetration below the surface as being responsible for the observed systematically too high T_s^* values. It can be assumed that the same phenomena do occur for the case of

the 5.5 and 10.3 mm sample since the making of all samples was the same. Then, T_s^* can be decreased (0.7 °C 2 elements, 1.0 °C 4 elements, 1.3 °C 6 elements, 1.5 °C 8 elements) and all variables in Table 5.7 can be computed again (Table 5.8).

When $T_s^* < 100$ °C, θ_K (Table 5.8) is in the range 0.52 to 0.89. θ_K appears to be a decreasing function of q_{is}^* (Figure 5.13b). θ_K is decreased when T_∞^* is increased (up to 0.15 at low q_{is}^* and 0.05 at high q_{is}^*). The effects of v_∞^* on θ_K are low (usually < 0.03). The range for θ_K predicted by the boundary layer theory implies a significant decrease (11 % to 48 %) of the mass transfer coefficient for the case of combined convective and I.R. drying over the operating range investigated.

H_C (Table 5.8) ranges from 1.03 to 1.12. It seems to increase with q_{is}^* (Figure 5.14a). H_C is slightly increased when T_∞^* is increased (by about 0.03 at low q_{is}^* and almost invariant at high q_{is}^*). The effects of v_∞^* on θ_K are low (usually < 0.02). The range for H_C implies an increase between 3 % to 12 % of the mass transfer coefficient in case of combined convective and I.R. drying over the operating range investigated.

The transfer coefficient ratios mean (20 cases) of 4.22 and 4.23 computed from all experimental results reported in Table 5.8 are 0.97 and 1.46 while their standard deviation are 0.42 and 0.44 respectively. The increase of the scatter in the transfer coefficient ratios (as compared to the one found for the convective results) is mainly due to the additional uncertainty brought into equation 5.12 by the experimental determination of the radiative heat transfer characteristics: E_s^* and q_{is}^* . Only 2 ($T_\infty^* \sim 80$ °C, $v_\infty^* \sim 2.1$ m/s, $q_{is}^* \sim 6.9$ or 20.5 kW/m²) of the 20 cases were carried under similar conditions and their transfer coefficient ratio do show a similar scatter as the whole of the data. The mean of 4.22 and 4.23 (Table 5.7) were 1.00 and 1.56 while their standard deviation is slightly increased (0.45 and 0.46 respectively) before the T_s^* correction was made, so it is possible to say that the transfer coefficient ratios are quite sensitive to small T_s^* variations (0.7 °C to 1.5 °C).

TABLE 5.7

THE TRANSFER COEFFICIENT RATIOS FROM THE COMBINED

CONVECTIVE AND I.R. DRYING RUNS (RAW DATA)

Sa. No.	Run No.	Nb El.	T _∞ [*]	v _∞ [*]	P _∞ [*]	T _d [*]	T _s [*]	q _{is} [*]	h _{cBL} [*] (h _{cc})	K _p [*]	(K _{pBL}) _{varp} [*]	($\frac{Nu_{BL} Sc}{Sh_{pBL} Pr}$) [*]	K _y [*]	(K _{yBL}) _{varp} [*]	($\frac{Nu_{BL} Sc}{Sh_{yBL} Pr}$) [*]	θ _K	H _C
b (mm)	(.)	(.)	(° C)	(m/s)	(kPa)	(° C)	(° C)	(W/m ²)	(W/m ² K)	(m/s)	(m/s)	(4.22)	(mole/m ² s)	(mole/m ² s)	(4.23)	(.)	(.)
K 5.5	ir17	2	79.2	2.0	100.10	8.3	56.0	6810	25	2.20e-02	2.57e-02	0.92	0.68	0.79	1.06	0.88	1.03
	ir18	8	86.1	2.0	99.98	12.2	76.0	20340	36	2.75e-02	4.41e-02	0.79	0.57	0.91	1.30	0.68	1.08
	i85h	8	145.0	3.5	101.98	-4.0	82.8	20740	15	2.13e-02	4.25e-02	0.36	0.35	0.70	0.69	0.56	1.11
	i83h	8	141.7	5.2	101.19	-10.6	82.7	20770	25	2.21e-02	4.43e-02	0.58	0.36	0.72	1.12	0.55	1.11
X 10.3	ir2	4	81.1	2.1	98.78	5.2	73.3	12110	(25)	1.77e-02	2.68e-02	0.90	0.39	0.59	1.40	0.71	1.07
	ir3	6	83.1	2.1	98.73	6.4	78.2	16980	(25)	1.94e-02	3.35e-02	0.73	0.36	0.63	1.31	0.63	1.09
	ir1	2	80.0	2.1	98.97	3.9	60.3	6930	25	1.78e-02	2.18e-02	1.11	0.51	0.62	1.35	0.85	1.04
	ir5	2	79.9	2.1	99.51	12.3	64.2	6890	39	1.57e-02	2.00e-02	1.89	0.42	0.54	2.43	0.82	1.05
	ir7	2	79.8	3.2	99.93	6.7	62.7	6860	38	1.64e-02	2.05e-02	1.77	0.45	0.57	2.22	0.83	1.04
	ir9	2	79.8	4.5	99.86	7.8	60.7	6840	37	1.80e-02	2.21e-02	1.59	0.52	0.63	1.94	0.85	1.04
	ir4	8	86.7	2.1	98.74	4.4	85.3	20520	(25)	1.77e-02	4.12e-02	0.61	0.24	0.56	1.48	0.49	1.13
	ir6	8	85.6	2.1	99.50	13.9	80.8	20510	(25)	2.03e-02	3.87e-02	0.63	0.36	0.67	1.24	0.59	1.10
	ir8	8	83.0	3.3	100.06	7.1	83.1	20490	(34)	1.92e-02	3.94e-02	0.83	0.30	0.62	1.79	0.54	1.12
	ir10	8	83.7	4.5	99.87	9.2	82.3	20510	(41)	1.88e-02	3.73e-02	1.07	0.31	0.61	2.21	0.56	1.11
	ir11	2	180.0	2.6	100.81	2.9	73.3	7660	29	1.51e-02	2.27e-02	1.37	0.34	0.51	1.83	0.72	1.07
	ir13	2	180.0	4.3	100.79	2.5	72.4	7710	36	1.72e-02	2.54e-02	1.52	0.40	0.59	1.99	0.73	1.07
	ir15	2	179.8	6.1	100.79	4.1	71.8	7660	36	1.76e-02	2.56e-02	1.52	0.41	0.60	1.96	0.74	1.07
	ir12	8	183.3	2.6	100.79	5.1	85.2	21370	25	2.08e-02	4.69e-02	0.58	0.30	0.67	1.20	0.50	1.13
	ir14	8	181.1	4.3	100.81	1.9	84.4	21370	29	2.18e-02	4.72e-02	0.67	0.33	0.71	1.34	0.52	1.12
	ir16	8	180.1	6.1	100.79	5.8	84.4	21380	27	2.17e-02	4.69e-02	0.61	0.32	0.70	1.23	0.52	1.12
Average												1.00			1.56		
Stdev.												0.45			0.46		

Nb. El.: number of heating elements activated

TABLE 5.8

**THE TRANSFER COEFFICIENT RATIOS FROM THE COMBINED
CONVECTIVE AND I.R. DRYING RUNS (T_s^* CORRECTED)**

Sa. No.	Run No.	Nb. El.	T_∞^*	v_∞^*	P_∞^*	T_d^*	T_s^*	q_{is}^*	h_{cBL}^* (h_{cc})	K_p^*	$(K_{pBL}^*)_{varp}$	$\left(\frac{Nu_{BL} Sc}{Sh_{pBL} Pr}\right)^*$	K_y^*	$(K_{yBL}^*)_{varp}$	$\left(\frac{Nu_{BL} Sc}{Sh_{yBL} Pr}\right)^*$	θ_K	H_c
b (mm)	(.)	(.)	(°C)	(m/s)	(kPa)	(°C)	(°C)	(W/m ²)	(W/m ² K)	(m/s)	(m/s)	(4.22)	(mole/m ² s)	(mole/m ² s)	(4.23)	(.)	(.)
K 5.5	ir17	2	79.2	2.0	100.10	8.3	55.3	6810	24	2.28e-02	2.64e-02	0.87	0.70	0.82	1.00	0.89	1.03
	ir18	8	86.1	2.0	99.98	12.2	74.5	20340	34	2.92e-02	4.50e-02	0.72	0.63	0.97	1.14	0.70	1.08
	ir85h	8	145.0	3.5	101.98	-4.0	81.3	20740	15	2.25e-02	4.24e-02	0.36	0.40	0.75	0.65	0.59	1.11
	ir83h	8	141.7	5.2	101.19	-10.6	81.2	20770	25	2.33e-02	4.41e-02	0.58	0.41	0.77	1.05	0.58	1.11
X 10.3	ir2	4	81.1	2.1	98.78	5.2	72.3	12110	(25)	1.84e-02	2.73e-02	0.88	0.41	0.61	1.33	0.72	1.07
	ir3	6	83.1	2.1	98.73	6.4	76.9	16980	(25)	2.04e-02	3.39e-02	0.72	0.40	0.66	1.24	0.65	1.09
	ir1	2	80.0	2.1	98.97	3.9	59.6	6930	24	1.84e-02	2.23e-02	1.05	0.53	0.64	1.26	0.86	1.04
	ir5	2	79.9	2.1	99.51	12.3	63.5	6890	37	1.62e-02	2.04e-02	1.77	0.44	0.56	2.25	0.83	1.04
	ir7	2	79.8	3.2	99.93	6.7	62.0	6860	36	1.69e-02	2.10e-02	1.66	0.47	0.59	2.07	0.84	1.04
	ir9	2	79.8	4.5	99.86	7.8	60.0	6840	35	1.86e-02	2.26e-02	1.50	0.54	0.65	1.82	0.86	1.04
	ir4	8	86.7	2.1	98.74	4.4	83.8	20520	(25)	1.87e-02	4.03e-02	0.62	0.27	0.59	1.39	0.52	1.12
	ir6	8	85.6	2.1	99.50	13.9	79.3	20510	(25)	2.20e-02	3.89e-02	0.63	0.40	0.71	1.16	0.62	1.10
	ir8	8	83.0	3.3	100.06	7.1	81.6	20490	(34)	2.03e-02	3.92e-02	0.83	0.34	0.66	1.68	0.57	1.11
	ir10	8	83.7	4.5	99.87	9.2	80.8	20510	(41)	1.99e-02	3.72e-02	1.06	0.35	0.65	2.07	0.59	1.10
	ir11	2	180.0	2.6	100.81	2.9	72.6	7660	28	1.56e-02	2.30e-02	1.34	0.36	0.53	1.77	0.72	1.07
	ir13	2	180.0	4.3	100.79	2.5	71.7	7710	35	1.77e-02	2.57e-02	1.49	0.42	0.61	1.92	0.74	1.07
	ir15	2	179.8	6.1	100.79	4.1	71.1	7660	36	1.81e-02	2.60e-02	1.49	0.43	0.62	1.89	0.74	1.07
	ir12	8	183.3	2.6	100.79	5.1	83.7	21370	25	2.20e-02	4.60e-02	0.59	0.34	0.71	1.13	0.53	1.12
	ir14	8	181.1	4.3	100.81	1.9	82.9	21370	29	2.30e-02	4.66e-02	0.68	0.37	0.75	1.26	0.55	1.11
	ir16	8	180.1	6.1	100.79	5.8	82.9	21380	26	2.29e-02	4.63e-02	0.62	0.37	0.75	1.15	0.55	1.11
Average												0.97			1.46		
Stdev.												0.42			0.44		

Nb. El.: number of heating elements activated

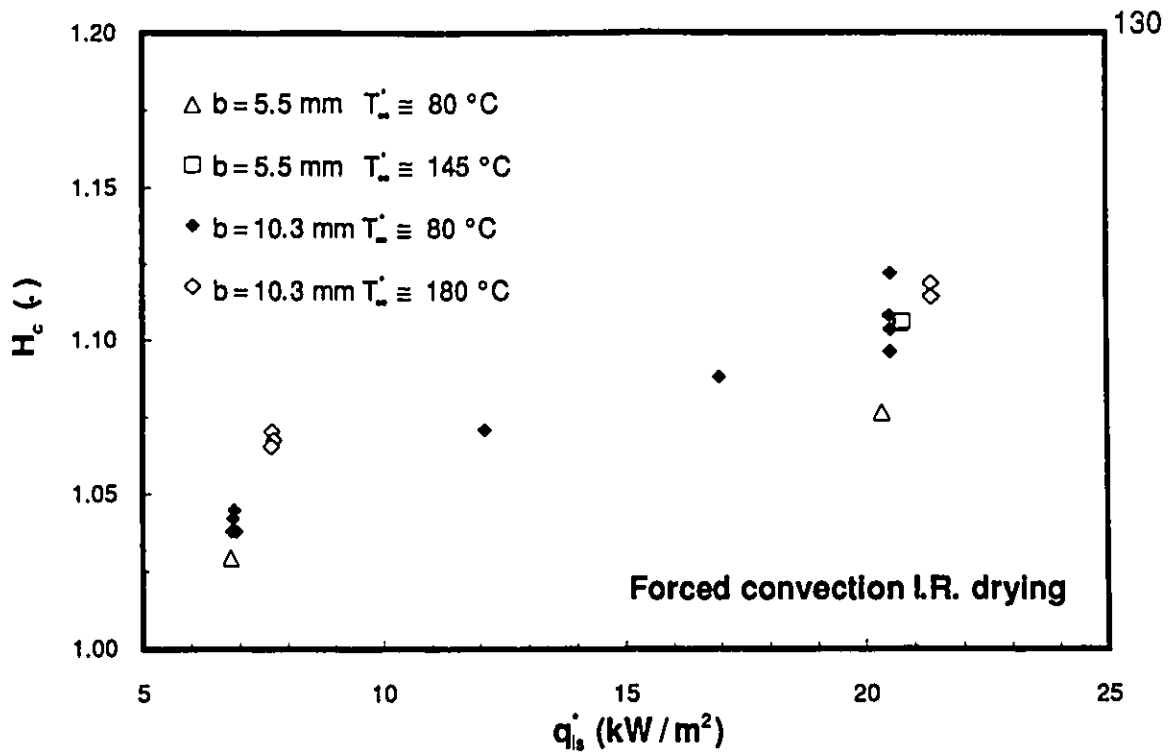


Figure 5.14a Hanna's correction factor as a function of the overall incident heat flux from forced convection I.R. drying runs (H_c vs. q'_{is})

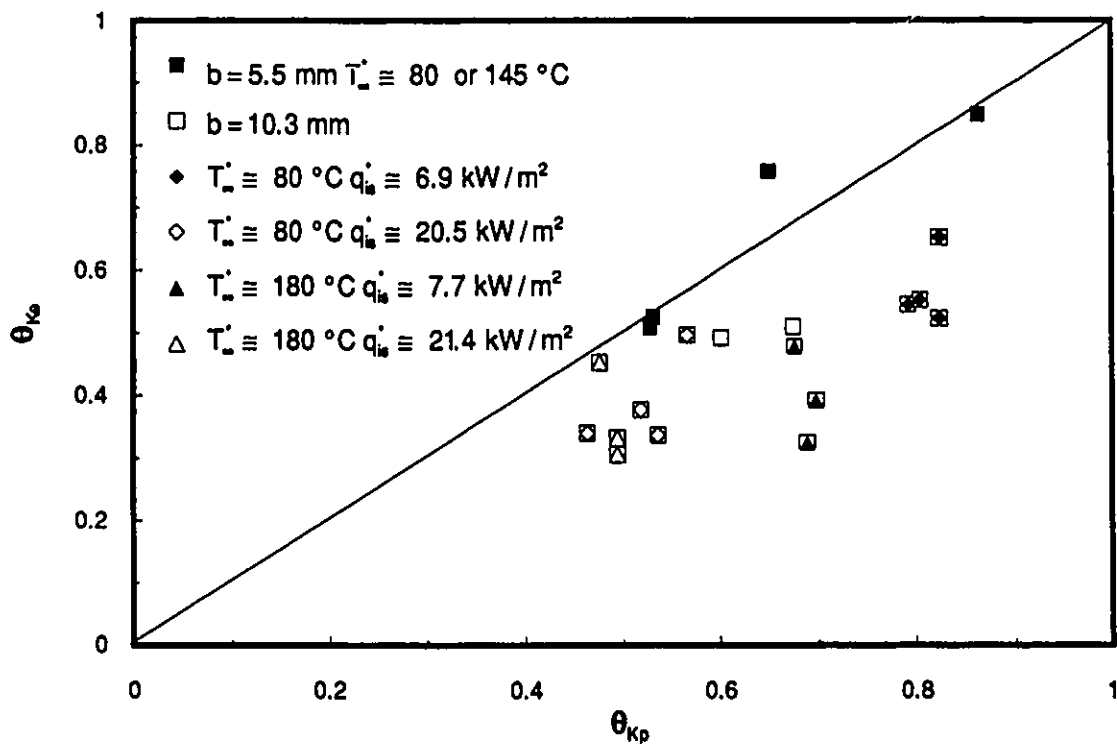


Figure 5.14b The ratio of experimental mass transfer coefficients from I.R. drying to unaffected mass transfer coefficient from convective drying as a function of the predicted mass transfer coefficient ratio (θ_{Ke} vs. θ_{Kp})

It is interesting to note that the transfer coefficient ratio 4.22 is about three times less sensitive to T_s^* variations than is the transfer coefficient ratio 4.23.

The intensity of the correction procedures (in Table 5.8) on the transfer coefficient ratios (4.10 and 4.11) can be visualized through use of frequency graphs. 0.2 width intervals are defined and all transfer coefficient ratios falling within that interval are given the same average values (x value) while the total number of case that have the same x value are recorded (y value). For example, all values (y value) within the interval 0.4-0.6 are taken to have the value 0.5 (x value), all values within the interval 0.6-0.8 are taken to have the value 0.7, etc. In Figure 5.15a and b are represented the transfer coefficient ratios 4.10 and 4.22 respectively while in Figure 5.16a and b are represented the transfer coefficient ratios 4.11 and 4.23 respectively. It can be observed that:

- a) The scatter of the data is significantly reduced (0.42 vs.0.52 and 0.44 vs. 0.64) by using the boundary layer theory and density variation procedures to correct the heat and mass transfer coefficients;
- b) The average transfer coefficient ratio is shifted toward lower values (0.97 vs.1.16 and 1.46 vs. 1.77).

A bimodality effect seems to exist according to data in Figure 5.15 and 5.16. From the results in Table 5.8, the mean of 4.23 for 2 and 8 elements can be calculated, we find 1.75 (standard deviation 0.42) and 1.27 (standard deviation 0.38) respectively. Heat losses in percent evaluated for 2 elements in section 5.2.1 are about twice the one found for 4, 6 or 8 elements thus the uncertainty in the determination of q_{is}^* is likely to be higher in that case. If for instance q_{is}^* is underestimated by only 2 % (real heat losses being higher than estimated as a result of radiative loss from the vessel internal side) for 2 elements than the means of 4.23 for 2 elements and all cases (2 elements and 8 elements) are now 1.54 (standard deviation 0.41) and 1.38 (standard deviation 0.39) respectively (instead of 1.75 (0.42) and 1.46 (0.44)). This could explain partially the discrepancies observed between the results at high and low q_{is}^* values.

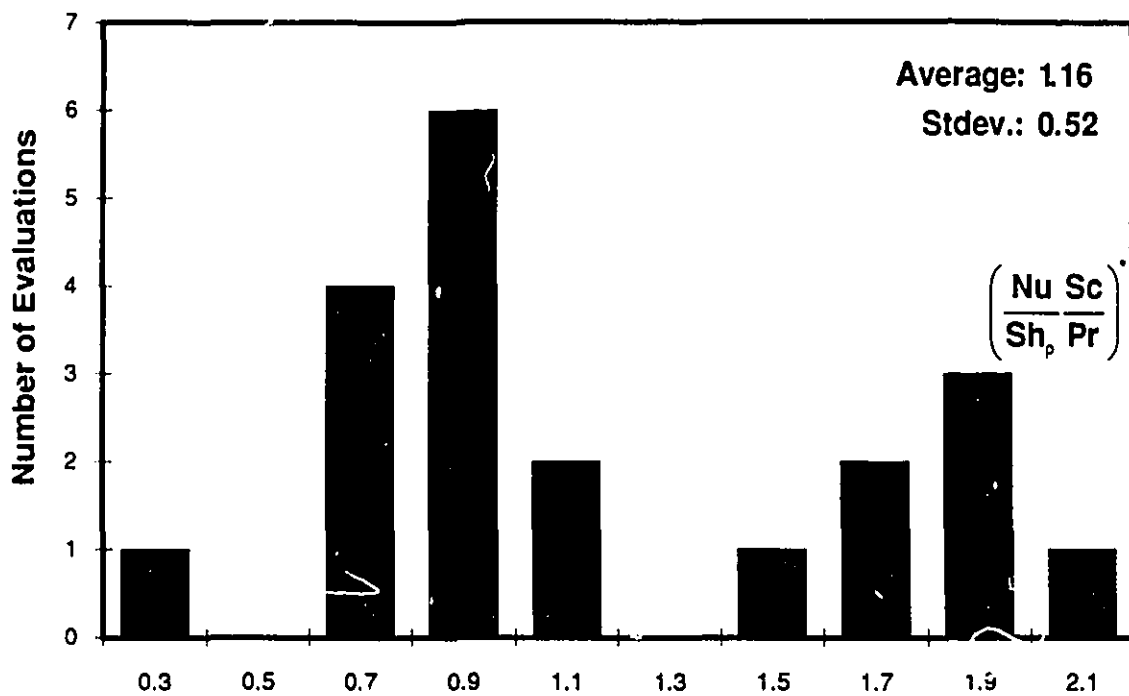


Figure 5.15a A frequency distribution for $\left(\frac{Nu Sc}{Sh_p Pr} \right)$ from the combined convective and LR. drying runs

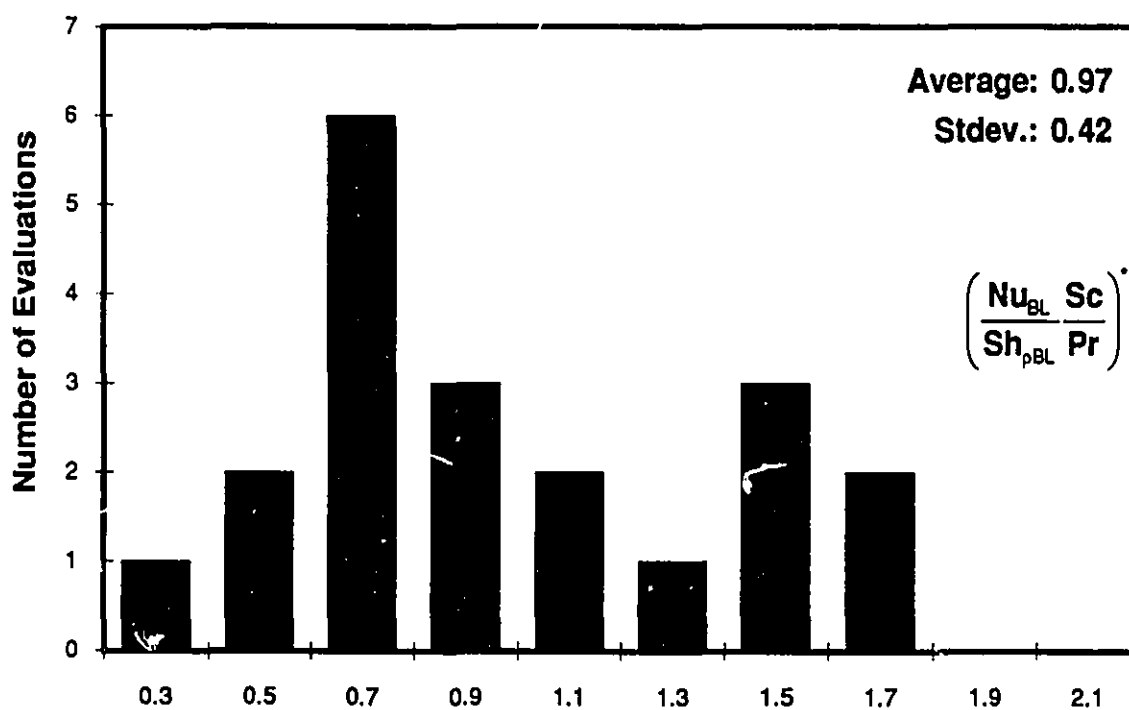


Figure 5.15b A frequency distribution for $\left(\frac{Nu_{BL} Sc}{Sh_{pBL} Pr} \right)$ from the combined convective and LR. drying runs

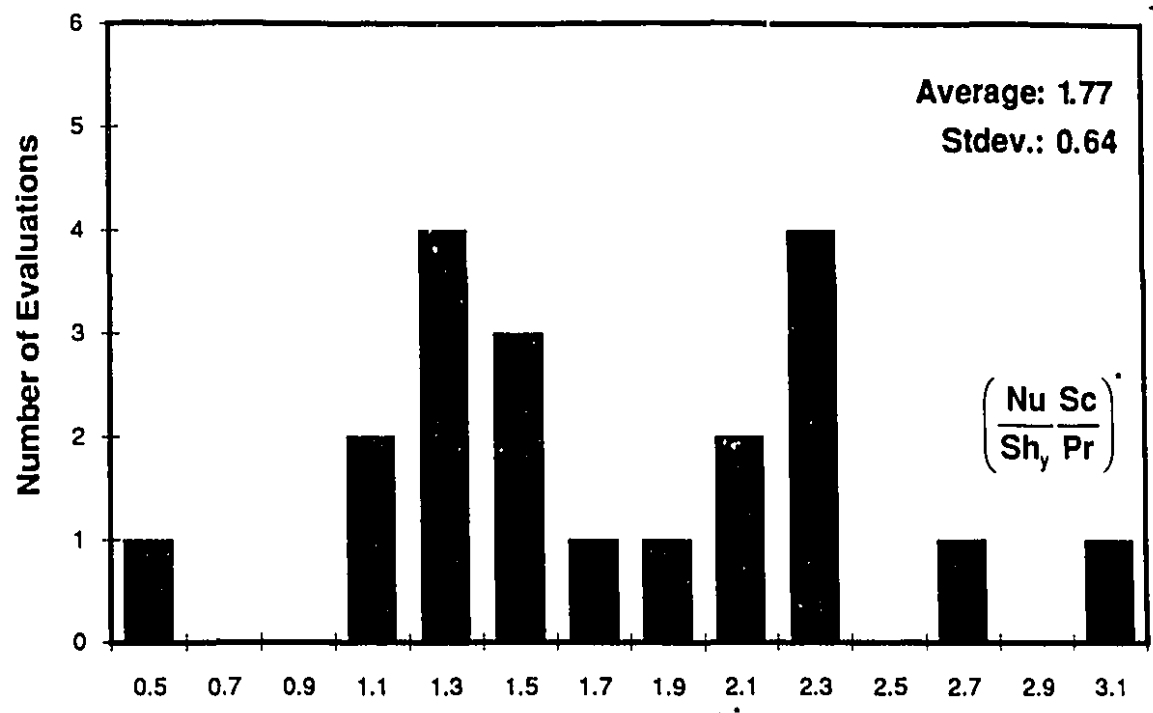


Figure 5.16a A frequency distribution for $\left(\frac{Nu Sc}{Sh_y Pr}\right)$ from the combined convective and I.R. drying runs

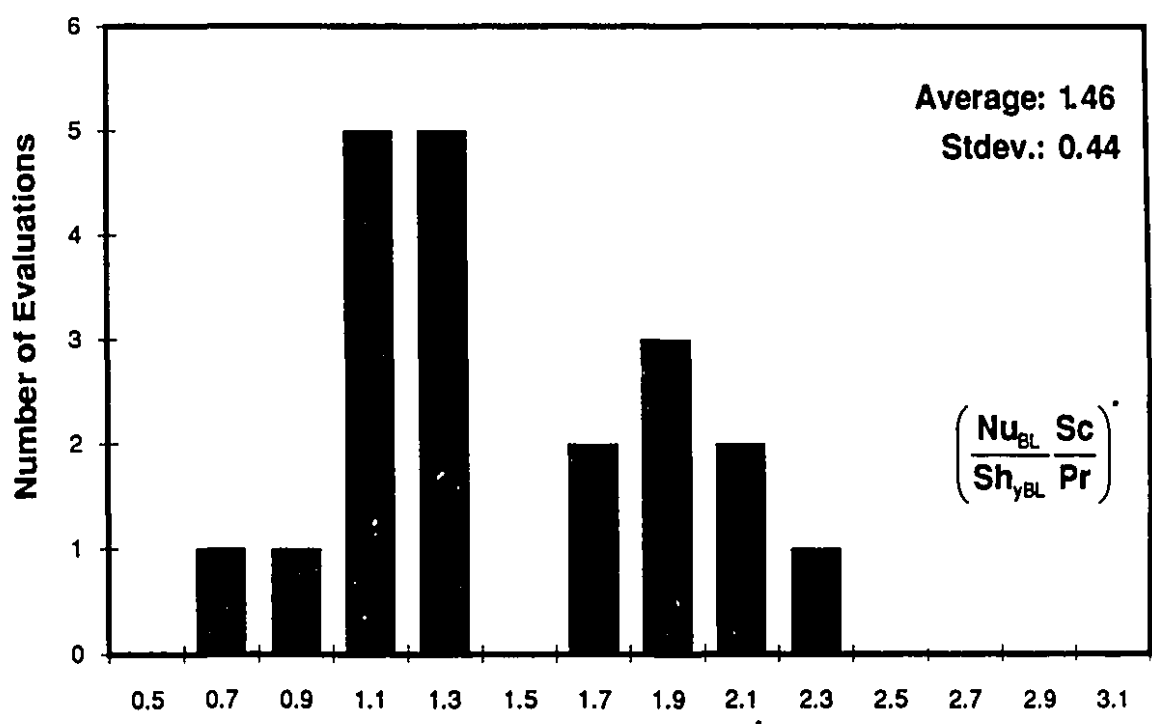


Figure 5.16b A frequency distribution for $\left(\frac{Nu_{BL} Sc}{Sh_{yBL} Pr}\right)$ from the combined convective and I.R. drying runs

I

TABLE 5.9

THE TRANSFER COEFFICIENT RATIOS FROM THE COMBINED
CONVECTIVE AND I.R. DRYING RUNS AND THE
CORRECTION PROCEDURES

Simulation parameters	$\left(\frac{Nu Sc}{Sh_p Pr}\right)_{av}$ (4.10) Stdev.	$\left(\frac{Nu_{BL} Sc}{Sh_{pBL} Pr}\right)_{av}$ (4.22) Stdev.	$\left(\frac{Nu Sc}{Sh_y Pr}\right)_{av}$ (4.11) Stdev.	$\left(\frac{Nu_{BL} Sc}{Sh_{yBL} Pr}\right)_{av}$ (4.23) Stdev.
$E_s = 0.80, E_4 = 0.92, E_1 = 0.28$ $T_2 = \text{Average}(T_{11}, T_{13}, T_{16})$ $T_3 = \text{Average}(T_{12}, T_{14}, T_{15})$ Boundary Layer Theory	1.16 0.52	0.97 0.42	1.77 0.64	1.46 0.44
Film Theory	1.20 0.51	0.93 0.43	1.84 0.68	1.39 0.47
Penetration Theory	1.19 0.51	0.95 0.43	1.82 0.66	1.43 0.46

A quantitative evaluation of both correction procedures (boundary layer theory, density variations) may now be made. The mean of 4.23 (Table 5.8) when the transfer coefficients are uncorrected is 1.77 (standard deviation 0.64). When the boundary layer theory correction is applied a mean value of 4.23 (without density correction) is found to be 1.58 (standard deviation 0.45). This represents an 11 % decrease (1.58 vs. 1.77) while the data standard deviation is decreased by about 35 % (0.48 vs. 0.71). Once Hanna's correction factor is applied the mean 1.58 with standard deviation 0.45 gives 1.46 (the mean presented in Table 5.8) with a standard deviation of 0.44; this represents a decrease of 8 % and 2 % respectively in the result.

Table 5.9 presents a comparison of the mean transfer coefficient ratios obtained from the various correction procedures (boundary layer, film and penetration theories). It appears from these results (especially on 4.23) that the magnitude of the correction provided by the film theory seems to better predict the high mass transfer rate effect in combined convective-I.R. drying. The small differences between the transfer coefficients ratios (4.10, 4.11) computed with uncorrected transfer coefficients result from the use of h_{cp}^* instead of h_c^* that could not be evaluated for six runs. For the transfer coefficient ratio 4.22, all correction procedures seem to offer an acceptable correction of the transfer coefficients.

Three additional explanations can be put forward to explain the differences still existing between the mean transfer coefficients ratio 1.46 (equation 4.23; Table 5.8; Table 5.8) and its value in convection drying (0.93; Table 4.2b):

- a) The laminar boundary layer theory might not model adequately the high mass transfer rate effect in case of turbulent flow; according to the transfer coefficient ratios computed with the film and penetration theory, it seems that the correction to the transfer coefficients should be lower. Kast (1982) underlined the point that for a turbulent boundary layer no specific correction other than empirical have been developed. The relation between θ_h and ϕ_h derived from heat transfer experimental results (transpiration cooling) and presented by Eckert and Drake (1972) as well as Kast (1982) shows that θ_h should

A quantitative evaluation of both correction procedures (boundary layer theory, density variations) may now be made. The mean of 4.23 (Table 5.8) when the transfer coefficients are uncorrected is 1.77 (standard deviation 0.64). When the boundary layer theory correction is applied a mean value of 4.23 (without density correction) is found to be 1.58 (standard deviation 0.45). This represents an 11 % decrease (1.58 vs. 1.77) while the data standard deviation is decreased by about 35 % (0.48 vs. 0.71). Once Hanna's correction factor is applied the mean 1.58 with standard deviation 0.45 gives 1.46 (the mean presented in Table 5.8) with a standard deviation of 0.44; this represents a decrease of 8 % and 2 % respectively in the result.

Table 5.9 presents a comparison of the mean transfer coefficient ratios obtained from the various correction procedures (boundary layer, film and penetration theories). It appears from these results (especially on 4.23) that the magnitude of the correction provided by the film theory seems to better predict the high mass transfer rate effect in combined convective-I.R. drying. The small differences between the transfer coefficients ratios (4.10, 4.11) computed with uncorrected transfer coefficients result from the use of h_{cp}^* instead of h_c^* that could not be evaluated for six runs. For the transfer coefficient ratio 4.22, all correction procedures seem to offer an acceptable correction of the transfer coefficients.

Three additional explanations can be put forward to explain the differences still existing between the mean transfer coefficients ratio 1.46 (equation 4.23; Table 5.8; Table 5.8) and its value in convection drying (0.93; Table 4.2b):

- a) The laminar boundary layer theory might not model adequately the high mass transfer rate effect in case of turbulent flow; according to the transfer coefficient ratios computed with the film and penetration theory, it seems that the correction to the transfer coefficients should be lower. Kast (1982) underlined the point that for a turbulent boundary layer no specific correction other than empirical have been developed. The relation between θ_h and ϕ_h derived from heat transfer experimental results (transpiration cooling) and presented by Eckert and Drake (1972) as well as Kast (1982) shows that θ_h should

be greater than the one derived from the film theory for the case of turbulent flow;

- b) The heat transfer coefficient could not be corrected for the effect of density variation because at the present time such correction has not been found.

In Figure 5.14b is shown the ratio of the experimental θ_{K_e} (ratio of K_y^* (Table 5.8) to $(K_y^*)_{varp}$ (Table 4.2b; $b= 5.5$ and 10.3 mm)) to the predicted θ_{Kp} (ratio of θ_K to H_c). The following remarks may be made:

- a) The order of magnitude of the mass transfer coefficient correction is correctly evaluated;
- b) The experimental K_y^* appears to be lower than could be predicted with $(K_y^*)_{varp}$, θ_K and H_c ;
- c) As q_{is}^* increases the agreement between the theoretical prediction and the experimental observations is better whatever T_∞^* ;
- d) For the 5.5 mm sample the agreement is fairly good.

An additional comments can be made on T_s^* for the 10.3 mm sample:

- a) Though T_s^* of sample no. X seems to be comparable to T_s^* found in previous studies (Figure 5.5b), the experimental results of Yagi et al. (1957) indicates that the evaporation temperature should be independent of b while it has been found in section 5.4.3 that T_s^* for $b= 5.5$ mm is less than T_s^* for $b= 10.3$ mm.

These observations suggest that the surface of the 10.3 mm sample was probably contaminated but to a lesser extend than the one of the 19.9 mm sample since the evaporation temperatures are much lower for $b= 10.3$ mm than for $b= 19.9$ mm. If one uses $(K_y^*)_{varp}$ deduced from the convective runs (Table 4.2 b; $b= 5.5$ and 10.3 mm) and h_{cBL}^* from the I.R drying runs, the average (14 runs, Table 5.8) transfer coefficient ratio 4.23 gives 1.07 (standard deviation: 0.26); this is close to its value in convection (0.93; standard

deviation: 0.12). This emphasizes the fact that the deviation in I.R. drying of 4.23 from its value in convection drying is probably caused by surface contamination which was shown (Table 5.5), in the case of the 19.9 mm sample, to decrease K_y^* . Thus it can be concluded that:

- a) The heat and mass transfer analogy is not exactly verified if the mass transfer coefficient is reduced as a result of crust formation;
- b) When the mass transfer resistance is mainly determined by the external boundary layer (as is the case for the 5.5 mm sample which was used only 8 times during the experimental phase and submitted to much lower thermal stresses), the heat and mass transfer analogy appears to be verified quite well in the combined convective-I.R. drying process.

Arai et al. (1979 a and b) have experimentally demonstrated in the case of natural convection heat and mass transfer from a horizontal upward facing plane surface heated by radiation ($q_{is}^* \sim 290 \text{ W/m}^2$ to 1740 W/m^2) that the analogy between the transfer of heat and mass is valid at low q_{is}^* although the heat and mass transfer coefficient were not corrected for the effect of high mass transfer rate. The present results extends such conclusions to the case of forced convection I.R. drying for much higher radiative and convective heat flux levels.

5.6 CRITICAL MOISTURE CONTENT IN COMBINED CONVECTIVE AND RADIATIVE DRYING

The critical moisture content X_c , defined according to the procedure described in section 3.4.4, is presented in Table 5.10 where various average X_c were computed (equivalent average critical saturation S_c are also given). The overall average is 0.021 ($S_c = 0.089$; Table 5.10b) and is comparable to the average computed with only samples with same thickness b (0.025, 5.5 mm; 0.019, 10.3 mm; 0.022, 19.9 mm). It can be noted that these averages are all very similar, especially if one accounts for their standard deviation (0.006, overall; 0.004, 5.5 mm; 0.005, 10.3 mm; 0.006, 19.9 mm). It is interesting to observe that even though the surface mass transfer characteristics of sample no. XII were changed

(section 5.4.3) for these experiments (as compared to the case of the convective experiments), its average X_c and standard deviation remain almost unchanged (this is also true for sample no. X). Averaging for same T_∞^* , gives: 0.021 (80 °C) and 0.021 (180 °C) again the point scatter (0.004, 80 °C; 0.007, 180 °C). are comparable. Averaging for same q_{is}^* , gives: 0.017 (2 elements) and 0.024 (8 elements) with similar standard deviations (0.006, 2 elements; 0.004, 8 elements). The average critical moisture content of the free convection-I.R. drying experiments presented in Table 5.2 is 0.018 with a standard deviation of 0.007; again these results are not significantly different from the one found when convection is present.

A plot of X_c vs. b , T_∞^* , v_∞^* , T_d^* , T_s^* , N_v^* , and q_{is}^* did not show any significant relation between X_c and any of these parameters. The (X_c/X_{in}) vs (N_v^*b) critical point curve (Keey, 1972) was used to compare the results found in convection drying and in combined convection I.R. drying (Figure 5.17). (X_c/X_{in}) does not appear to be a strong function of (N_v^*b) although a thirty five-fold increase of (N_v^*b) occurs in Figure 5.17.

Yagi et al. (1957) have presented a curve of S_c for river and standard sand as a function of the particle diameter d (Figure 5.18) which clearly shows ($b= 20-40$ mm, $T_\infty^* = 9-34$ °C, $v_\infty^* = 1.14-1.34$ m/s and $q_{is}^* = 5110-10450$ W/m²), that S_c (defined from the drying rate curve) is not a function of these parameters. The two curves drawn in Figure 5.18 correspond to S_{c1} the first and S_{c2} the second critical point as defined by Keey (1972). Yagi et al. (1957) have found that S_{c1} and S_{c2} were the same as long as d is greater than 100 μm . It is possible to observe that for $d = 100$ μm , Yagi et al. (1957) report S_c between 0.20 and 0.35, this is in almost exactly the range that researchers (Morgan and Yerazunis, 1967; Cunningham and Kelly, 1980; Moyne, 1987) in the field of convective drying at low mass flux have reported for same d . Although S_c (between 0.042 to 0.125) in the present study (Figure 5.18) are in a lower range (the reason is explained in section 4.4), the range for which S_c can be considered to be independent of b , T_∞^* , v_∞^* and q_{is}^* has been extended.

TABLE 5.10a
CRITICAL MOISTURE CONTENT FROM THE COMBINED
CONVECTIVE AND I.R. DRYING RUNS

Sa. No.	Run No.	Nb. El.	T_{∞}	v_{∞}	P_{∞}	T_d	T_s	q_{lis}	N_v	S	X_c	S_c	X_{cav} Stdev	S_{cav} Stdev
b (mm)	(.)	(.)	(° C)	(m/s)	(kPa)	(° C)	(° C)	(W/m ²)	(kg/m ² s)	(.)	(kg/kg)	(.)	(kg/kg)	(.)
X 5.5	ir17	2	79.2	2.0	100.10	8.3	56.0	6810	2.25e-03	0.55-0.29	0.020	0.086	5.5 mm	
	ir18	8	86.1	2.0	99.98	12.2	76.0	20340	6.63e-03	0.54-0.32	0.026	0.111		
	i85h	8	145.0	3.5	101.98	-4.0	82.8	20650	6.82e-03	0.51-0.27	0.028	0.113	0.025	0.105
	i83h	8	141.7	5.2	101.19	-10.6	82.7	20740	7.06e-03	0.56-0.29	0.027	0.108	0.004	0.013
X 10.3	ir2	4	81.1	2.1	98.78	5.2	73.3	12110	3.88e-03	0.45-0.24	0.022	0.093	10.3 mm	
	ir3	6	83.1	2.1	98.73	6.4	78.2	16980	5.14e-03	0.46-0.26	0.024	0.100	0.019	0.081
	ir1	2	80.0	2.1	98.97	3.9	60.3	6930	2.25e-03	0.43-0.20	0.021	0.090	0.005	0.020
	ir5	2	79.9	2.1	99.51	12.3	64.2	6890	2.29e-03	0.48-0.24	0.020	0.084	80 °C	
	ir7	2	79.8	3.2	99.93	6.7	62.7	6860	2.28e-03	0.51-0.21	0.017	0.072	0.021	0.090
	ir9	2	79.8	4.5	99.86	7.8	60.7	6840	2.29e-03	0.57-0.28	0.024	0.101	0.004	0.018
	ir4	8	86.7	2.1	98.74	4.4	85.3	20520	6.16e-03	0.48-0.26	0.025	0.105	180 °C	
	ir6	8	85.6	2.1	99.50	13.9	80.8	20510	6.01e-03	0.53-0.25	0.018	0.076	0.021	0.092
	ir8	8	83.0	3.3	100.06	7.1	83.1	20490	6.15e-03	0.48-0.25	0.020	0.084	0.007	0.032
	ir10	8	83.7	4.5	99.87	9.2	82.3	20510	5.82e-03	0.44-0.23	0.025	0.105	2 Elements	
	ir11	2	180.0	2.6	100.81	2.9	73.3	7630	3.34e-03	0.47-0.23	0.011	0.047	0.017	0.075
	ir13	2	180.0	4.3	100.79	2.5	72.4	7950	3.67e-03	0.42-0.24	0.010	0.042	0.006	0.027
	ir15	2	179.8	6.1	100.79	4.1	71.8	7660	3.66e-03	0.49-0.25	0.011	0.047	8 Elements	
	ir12	8	183.3	2.6	100.79	5.1	85.2	21370	7.24e-03	0.58-0.33	0.020	0.086		
ir14	8	181.1	4.3	100.81	1.9	84.4	21370	7.37e-03	0.66-0.26	0.021	0.091	0.024	0.098	
ir16	8	180.1	6.1	100.79	5.8	84.4	21380	7.32e-03	0.56-0.30	0.019	0.080	0.004	0.017	

Nb. El.: number of heating elements activated

TABLE 5.10b
CRITICAL MOISTURE CONTENT FROM THE COMBINED
CONVECTIVE AND I.R. DRYING RUNS

Sa. No.	Run No.	Nb. El.	T_{∞}^*	v_{∞}^*	P_{∞}^*	T_d^*	T_s^*	q_{is}^*	N_v^*	S	X_c	S_c	X_{cav} Stdev	S_{cav} Stdev
b (mm)	(.)	(.)	(° C)	(m/s)	(kPa)	(° C)	(° C)	(W/m ²)	(kg/m ² s)	(.)	(kg/kg)	(.)	(kg/kg)	(.)
XI 19.9	i62h	2	80.3	2.1	99.79	17.9	100.8	7260	1.75e-03	0.33-0.15	0.011	0.049	19.9 mm	
	i63h	2	81.3	2.1	99.67	17.1	100.9	7270	1.80e-03	0.29-0.12	0.011	0.048	0.022	0.092
	i64h	2	81.2	4.5	99.57	16.9	100.6	7220	1.49e-03	0.29-0.14	0.015	0.065	0.006	0.026
	i57h	8	85.3	2.1	99.69	16.2	101.7	21130	6.60e-03	0.41-0.23	0.022	0.094	5.5, 10.3 and 19.9	
	i58h	8	84.2	2.1	99.79	16.2	101.8	21100	6.53e-03	0.42-0.24	0.021	0.091	0.021	0.089
	i56h	8	84.2	2.6	99.71	16.5	101.7	21080	6.37e-03	0.41-0.24	0.022	0.095	0.006	0.024
	i55h	8	84.1	3.4	99.78	15.9	101.5	21010	6.26e-03	0.41-0.24	0.024	0.104		
	i68h	8	82.9	4.5	99.99	14.1	101.6	20990	6.23e-03	0.39-0.21	0.026	0.111		
	i69h	8	84.1	4.5	99.99	13.7	101.6	21000	6.24e-03	0.42-0.24	0.023	0.099		
	i70h	8	84.9	4.5	100.06	13.7	101.7	20990	6.34e-03	0.41-0.22	0.021	0.091		
	i71h	8	85.6	4.5	100.18	14.0	101.6	20980	6.33e-03	0.42-0.24	0.025	0.107		
	i38h	2	180.3	2.6	99.99	11.8	101.2	7920	3.13e-03	0.40-0.20	0.029	0.125		
	i45h	2	180.2	6.2	99.71	14.7	100.5	7860	3.55e-03	0.44-0.20	0.021	0.091		
	i49h	2	180.2	6.2	98.90	14.0	100.4	7870	3.36e-03	0.52-0.19	0.020	0.085		
	i50h	2	180.3	6.2	99.11	12.0	100.5	7880	3.57e-03	0.41-0.24	0.018	0.078		
	i76h	8	179.9	2.6	100.63	8.7	101.1	22020	7.79e-03	0.49-0.27	0.030	0.128		
	i77h	8	179.9	2.6	100.61	9.7	101.1	22110	7.70e-03	0.49-0.27	0.030	0.129		
	i52h	8	180.3	6.2	99.51	6.6	100.9	21830	7.64e-03	0.47-0.27	0.026	0.111		
i78h	8	179.7	6.1	100.31	12.1	101.5	21770	7.98e-03	0.50-0.29	0.033	0.142			

Nb. El.: number of heating elements activated

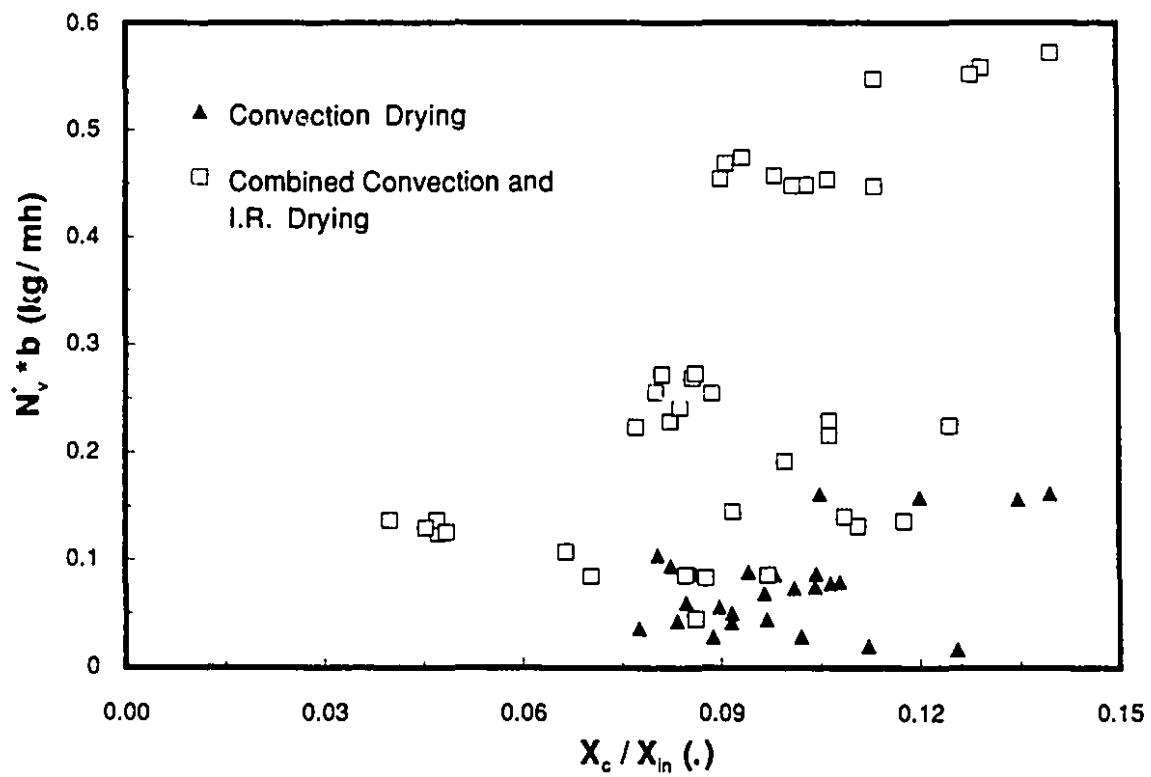


Figure 5.17 The critical point curve from the convective and combined convective I.R. drying runs

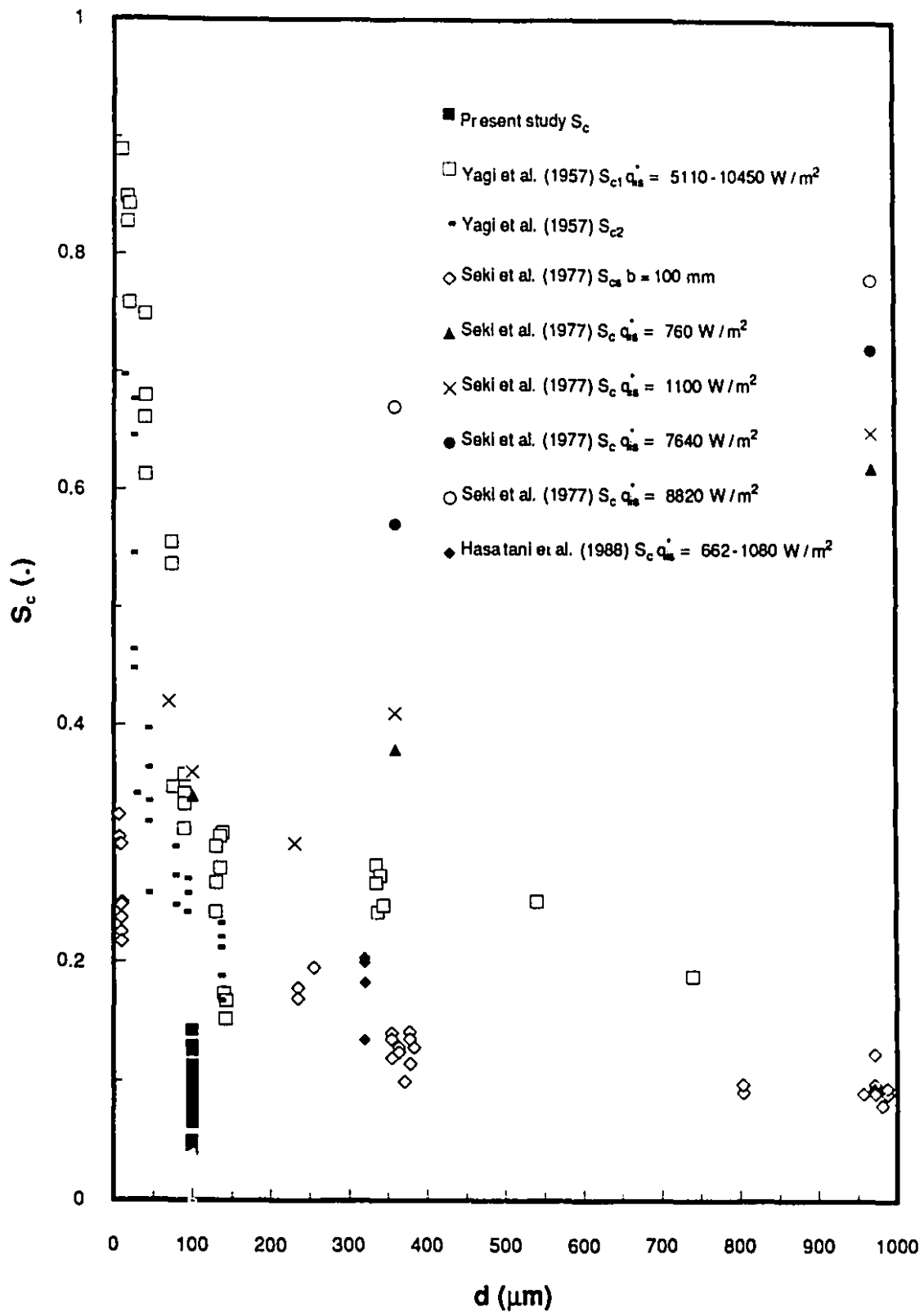


Figure 5.18 The critical saturation from convective, I.R. and combined convective I.R. drying runs from various studies

Evaluating X_c on the T_s^* vs. X curve does not appear to add extra scatter to the determination of X_c as compared to scatter that is present in the Yagi et al. (1957) results.

In Figure 5.18, it can be observed that the surface critical moisture content X_{cs} in free convection-I.R. drying (Seki et al., 1977) are only slightly higher than X_c in the present results. Since the decrease of the drying rate (a surface phenomena) is always linked to a critical value for the surface moisture content which is likely to be mainly a function of d , this equality might result from the fact that in the present study X_{cs} is more or less equivalent to X . Seki et al. (1977) have shown however that the average S_c for their thick bed ($b = 100$ mm) was an increasing function of q_{is}^* (Figure 5.18). In the present study, the values for S_c (between 0.042 to 0.125) are in a lower range than theirs because:

- a) In their study, b is much higher which results in highly non uniform moisture distribution within the material (such distributions have been presented by Seki et al.(1977)); comparable non-uniformity have not been observed to occur for $b = 20$ mm (see Cunningham and Kelly.(1980));
- b) The determination of S_c is based on the drying rate curves in Seki et al. (1977) results.

Hasatani et al. (1988) studying the case of a silica sand layer at low q_{is}^* ($d = 320$ μ m, $b = 20$ mm, $T_\infty^* = 50-72$ $^\circ$ C, $v_\infty^* \sim 0.60$ m/s and $q_{is}^* = 660-1080$ W/m²) have found, S_c (between 0.12 to 0.21; Figure 5.18) to be linearly correlated with N_v^* (between $0.20 \cdot 10^{-3}$ to $0.46 \cdot 10^{-3}$ kg/m²s). Such behavior is uncommon for low ($N_v^* \cdot b$) values (0.033 kg/mh) according to a critical point curve (clay brick, $b = 10-30$ mm, three-fold change in drying rate) presented by Krischer (1963) where it can be observed that for ($N_v^* \cdot b$) lower than 0.04 kg/mh the critical point is not a function of N_v^* .

5.7 CONCLUSIONS

According to the results presented, the following conclusions can be drawn regarding the combined convective and I.R. drying process of a capillary porous body (glass beads, $d = 90\text{-}105 \mu\text{m}$). In the parameter range investigated ($b = 5.5\text{-}19.9 \text{ mm}$, $T_{\infty}^{\circ} = 80\text{-}180 \text{ }^{\circ}\text{C}$, $v_{\infty}^{\circ} = 2.0\text{-}6.2 \text{ m/s}$, $T_d^{\circ} = -10.6\text{-}+17.9 \text{ }^{\circ}\text{C}$, $q_{is}^{\circ} = 6810\text{-}22020 \text{ W/m}^2$):

- (a) It was observed that the evaporation temperature of a 19.9 mm sample can reach the boiling point whatever set of external drying conditions (T_{∞}° , v_{∞}° , T_d° , q_{is}°) are used when an additional surface mass transfer resistance exists due to crust formation.
- (b) A significant increase (up to 100 %) of the convective heat transfer coefficient was observed when T_s° reached the boiling point temperature ($b = 19.9 \text{ mm}$) and is higher than T_{∞}° . This effect decreases the drying rate and leads to a lower efficiency of the I.R. heating process.
- (c) A decrease in the heat transfer coefficient was observed for the combined convective and I.R. drying process. It was also found that:
 - (i) The necessity to take into account the effect of high mass transfer flux on the heat transfer coefficient (when convection is combined with I.R. heating) has been demonstrated. Using the laminar boundary layer theory, corrected heat transfer coefficients should be 5 % to 52 % lower than heat transfer coefficients applicable when there is no mass flux. However, based on the experimental results obtained, it was not possible to determine the most appropriate correction procedure to account for the effect of the surface diffusion mass flux on the heat and mass transfer coefficients.

- (ii) According to the Hanna's correction factor (1962) used to evaluate the effect of density variation between the surface and the flow, unaffected mass transfer coefficients should be 3 % to 13 % lower than the one predicted with the boundary layer theory for experimentally measured surface temperature ranging from 56 °C to 85 °C. From a practical point of view, the magnitude of such correction suggests that this effect is negligible in combined convective-I.R. drying.
- (c) From the experimental results obtained, the following observations were found to characterize the analogy between the heat and mass transfer coefficients (expressed in terms of average heat and mass transfer coefficients ratios) when the sample surface is unsaturated ($0.2 < S_s < 0.5$):
- (i) When the mass transfer resistance is mainly determined by the external boundary layer, the heat and mass transfer analogy appears to be verified quite well. This results is in agreement with applicable theoretical results in case of a laminar boundary layer (Appendix 11).
 - (ii) The heat and mass transfer analogy is not exactly verified if the equivalent mass transfer coefficient is reduced as a result of crust formation.
- (d) It was observed, within experimental uncertainty, that the critical moisture content is independent of the convective drying parameters (T_∞^* , v_∞^* , T_d^*), sample thickness ($b = 5.5, 10.3$ and 19.9 mm), overall incident heat flux ($q_{iS}^* = 6810-22020$ W/m²) and surface contamination.

CHAPTER VI - COMBINED CONVECTIVE AND INFRARED DRYING MODELLING

6.1 INTRODUCTION

Up to date there have been very few attempts to use and/or build a model for predicting the combined convective-I.R. drying of capillary porous media. Most of these works have been conducted by researchers working in the range of low to medium heat fluxes ($q_{is}^* < 8800 \text{ W/m}^2$, $T_{\infty}^* < 80 \text{ }^{\circ}\text{C}$). Basically two types of models have been developed to study the free (no forced flow present) and forced convection-I.R. drying:

- a) Complete model (Whitaker, 1977) with the simultaneous solution of the moisture content, temperature and pressure distributions in wet and dried regions separated by a front (Min and Emmons, 1972; Seki et al., 1977);
- b) Reduced model (energy conservation equation) calibrated with experimental drying rate (Hasatani et al., 1983; Hasatani et al., 1988).

Min and Emmons (1972) solved a simplified version of the model originally presented by Philip and De Vries (1957), Krischer (1963) and Luikov (1966) though the gaseous phase continuity equation was included. The assumptions of the existence of a front at the surface (at the start) and no liquid moisture movement decreased the amount of necessary experimental internal heat and mass transfer coefficients. The numerical solution of the system of 3 coupled non-linear differential equations (in each zone) was carried through use of an explicit finite difference discretization while the various derivatives at the front were expressed in the manner suggested by Murray and Landis (1959) for a fixed spatial network. A qualitatively good agreement can be observed for the T vs. t , P vs. t as well as pressure and temperature distributions for the free convection-I.R. drying experiments (alumina powder, $b = 54 \text{ mm}$, $T_{\infty}^* = 20 \text{ }^{\circ}\text{C}$, $q_{is}^* = 6270 \text{ W/m}^2$) though some differences are greater than the uncertainty in

experimental results. The hypothesis limit the model applicability to low moisture content materials or to predict the receding front period.

Though Seki et al. (1977) did not consider the gaseous phase conservation equation, they extended the application of the previous model to include the constant drying rate period of free convection-I.R. drying (glass beads, $d = 360\text{-}970 \mu\text{m}$, $T_{\infty}^{\circ} = 20 \text{ }^{\circ}\text{C}$, $q_{is}^{\circ} = 750\text{-}8800 \text{ W/m}^2$) of an initially saturated ($S_{in} = 1$) thick bed ($b = 0.1 \text{ m}$). Gravity and capillary pressure were used as driving forces for the liquid flux in the wet zone. Energy as well as mass conservation equations at the front link the system of equations in the wet and dry zones. No details were provided with respect to the numerical solution technique used and how the front was followed. The assumption of $S_s = 0$ when the front start to recede was found to generate smaller values for the average S_c than the one identified from the experimental drying rate curves. Simulations were found to predict more extensive constant drying rate period than observed experimentally while the overall behavior of drying rate curves is very well predicted. Considering the accuracy of the slicing technique to evaluate the moisture distribution, a qualitatively good prediction of the moisture distribution was performed. Only a few drying curves and temperatures distributions were reproduced, probably within experimental uncertainty.

The comparison reported by Min and Emmons (1972) and Seki et al. (1977) underlined the fact that a quantitative prediction of the moisture and pressure distribution with a complete model is impeded by:

- a) The uncertainty associated with the distribution measurement techniques;
- b) The uncertainty on the experimental or theoretical determination of the internal heat and mass transfer coefficients (Bories, 1968).

Hasatani et al. (1983) used a simpler model which include only an energy balance equation to evaluate the temperature distribution during the preheating and constant drying rate period of a wet silica sand, a slurry of activated sludge and a water suspension of graphite particles ($d = 5 \mu\text{m}$, $b = 20 \text{ mm}$, $T_{\infty}^{\circ} = 30\text{-}$

80 °C, $v_{\infty}^* \sim 1.1$ m/s, $q_{is}^* = 290-1400$ W/m²). In the first version, q_{is}^* was absorbed on the surface (opaque drying model) and in the second q_{is}^* absorption was throughout the wetted layer (semitransparent drying model). It was found that the opaque version of the model was adequate in predicting the drying rate and surface temperature rise when the suspension concentration is greater than 2 kg/m³. This model was extended (Hasatani et al., 1988) to predict the first falling rate and receding front periods for coal, silica sand and brick ($d = 320$ μ m, $b = 20$ mm, $T_{\infty}^* = 27-72$ °C, $v_{\infty}^* \sim 0.5$ m/s, $q_{is}^* = 0-1080$ W/m²). During the first falling rate period the drying rate had to be computed from the drying rate during the constant drying rate period and an experimentally determined function of X dependent on the specific material dried. The predicted receding front period necessitated the knowledge of the front position which was taken to be a function of X calibrated from each experimental result. Nevertheless, a good prediction of the T vs. t and X vs. t curves was obtained although the question of experimental uncertainty remains opened.

Recently, Dostie (1991) developed a drying front model which can predict the drying rate without using the information from the whole drying rate curve. In comparison, the complete model of Seki et al.(1977) necessitate the knowledge (thus the determination) of the following physical properties of the material:

- a) The gas and liquid relative permeability as a function of S ;
- b) The capillary pressure as a function of S ;
- c) The diffusion coefficient as a function of S .

Their determination requires difficult and time-consuming experiments and the availability of special equipments. Another drawback of such models is the high computing time needed to perform a run.

The purpose of this chapter is to evaluate the predictive capability of the drying front model (Dostie, 1991) for the case of high temperature convection drying ($d = 90-105$ μ m, $b = 5-20$ mm, $T_{\infty}^* = 80-180$ °C, $q_{is}^* \sim 330-1500$ W/m²) and combined high temperature convection-I.R. drying ($d = 90-105$ μ m, $b = 5-$

20 mm, $T_{\infty}^* = 80-180$ °C, $v_{\infty}^* = 2.0-6.3$ m/s, $q_{is}^* = 6810-22020$ W/m²) of a capillary porous media (glass beads).

6.2 HYPOTHESES

The idea behind the development of this model (Dostie, 1991) was to use a minimum of physical properties to be evaluated. A description of this model is now summarized starting from the following hypotheses regarding the external boundary conditions:

- a) No detailed computation of the external flow is carried out (heat and mass transfer coefficient from correlation or experimental results will be used);
- b) The overall incident radiative heat flux q_{is}^* is absorbed at the surface (opaque model);
- c) The model is one dimensional and applied to the planar geometry with asymmetrical boundary conditions (drying at the surface and the bottom is adiabatic and impervious).

Additional hypotheses concern the heat and mass transfer processes within the material:

- a) It is postulated that two drying regimes exist (Keey, 1972); the funicular regime when only a wet zone exists and a pendular regime when wet and dry zones coexist (Figure 6.1a);
- b) The transition between the two regimes occurs at an average critical moisture content X_c when a drying front starts to recede within the material;
- c) The moisture content distribution is always uniform within the wet zone;
- d) The model is restricted to non-hygroscopic material;

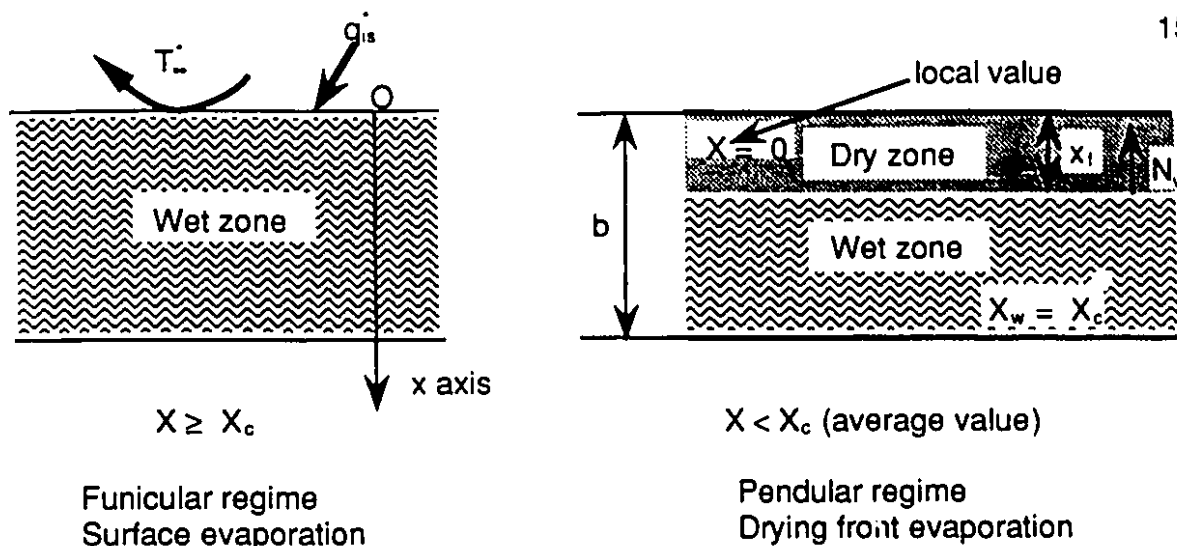


Figure 6.1a The funicular and pendular drying regimes

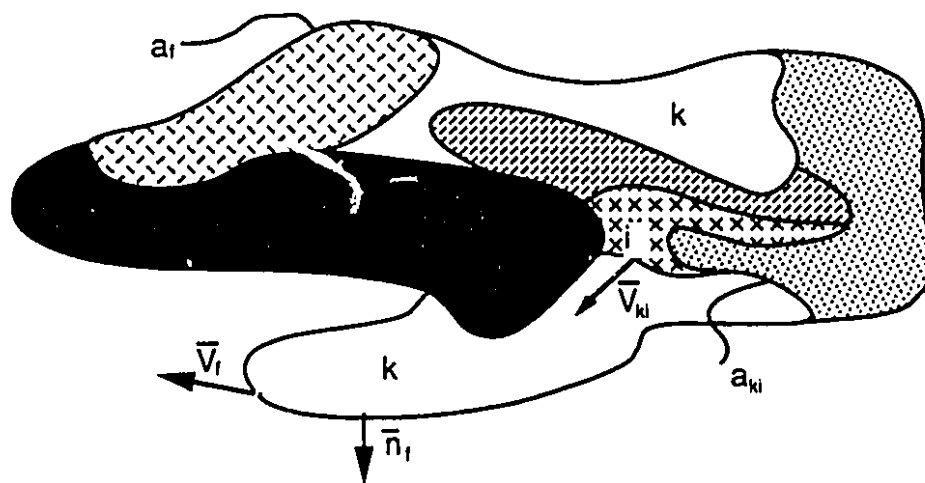


Figure 6.1b The elementary control volume

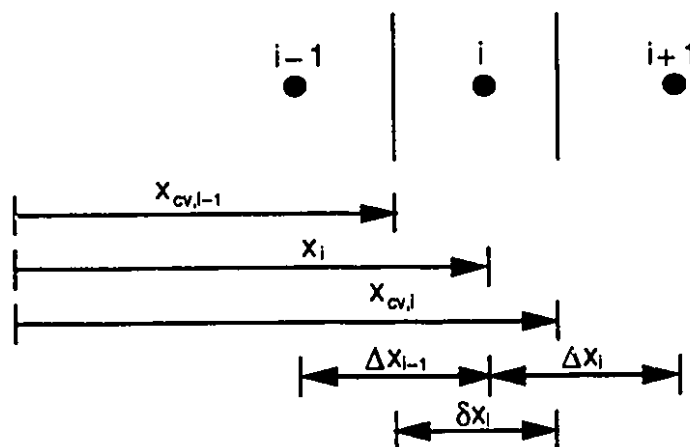


Figure 6.1c The control volume grid

- e) The sensible heat increase of the vapour or air going through the dry zone is negligible;
- f) Mass transfer at the drying front consists of diffusive and convective components;
- g) The front position is corrected through a unique function (material and experiment independent) in order to evaluate the heat and mass transfer resistance throughout the dry region;
- h) The porous matrix does not shrink;
- i) Gravity effects are neglected.

6.3 MASS CONSERVATION EQUATIONS

The adopted sign rule is that fluxes leaving the wet zone are considered negative. At the front (Figure 6.1a) a mass conservation equation on the water gives:

$$N_v = \frac{1}{A_s} \frac{dm_w}{dt} \quad (6.1)$$

where the right-hand side is the water mass evaporation rate per unit area ($\text{kg/m}^2\text{s}$) and N_v is the front vapor flux ($\text{kg/m}^2\text{s}$). N_v is the sum of a diffusive and a convective contribution, it can be approximated as:

$$N_v = -\frac{\frac{y_{vs} - y_{vf}}{1 - \left(\frac{y_{vf} + y_{vs}}{2}\right)}}{R_{D2}} + \frac{P_\infty - p_{vf}}{R_c} \quad (6.2)$$

where y_v is the vapor mole fraction (variable with f or ∞ as subscripts are evaluated at the front or in the external flow respectively), P_∞ the flow gas pressure and p_{vf} the vapor pressure at the front. The first term represents the vapor diffusion flux between the front and the surface as approximated by Fick's first law (Bird et al., 1960) applied to the diffusion in the porous dried layer

(with an effective diffusion coefficient). The second term results from the application of Darcy's law (Kaviany, 1991) for the vapor evaporating at the front with the assumption that the surface pressure is P_{∞} . Min and Emmons (1972) have already identified the molecular diffusion of the gaseous component and the pressure driven convective flow as the principal mechanisms of mass transfer in case of a drying front formulation from their experimental results where the pressure distribution was measured. R_{D2} is the diffusion resistance coefficient of the vapor through the dried layer (m^2s/kg):

$$R_{D2} = \frac{x_f'}{M_v \cdot (c_g \cdot D_e)_{av}} \quad (6.3)$$

where x_f' is the corrected front position to evaluate the mass transfer resistance (m), M_v is the vapor molecular weight (kg/mole), c_g the total molar concentration (mole/ m^3) and D_e the effective diffusion coefficient (m^2/s); their product is evaluated at the average conditions between the surface and front. The convective resistance coefficient R_c (m/s) is:

$$R_c = \frac{x_f'}{\kappa} \left(\frac{\mu_v}{\rho_v} \right)_{av} \quad \text{if } p_{vf} > P_{\infty} \quad (6.4)$$

$$R_c = \infty \quad \text{if } p_{vf} \leq P_{\infty}$$

where μ_v and ρ_v are the vapor viscosity and density respectively evaluated as an average between the front and surface conditions; κ is the dry region permeability (m^2). Another expression for the surface mass flux is equation 4.9 expressed as:

$$N_v = \frac{\frac{y_{v\infty} - y_{vs}}{1 - y_{vs}}}{R_{D1}} \quad (6.5)$$

where R_{D1} is the surface diffusion resistance coefficient of the vapor through the boundary layer (m^2s/kg):

$$R_{D1} = \frac{1}{M_v \cdot K_y} \quad (6.6)$$

K_y is the mass transfer coefficient ($mole/m^2s$). When vapor diffusion is the main moisture transfer mechanism through the dried and boundary layers, equations 6.2 and 6.5 are equal and y_{vs} is the solution of the following equation:

$$\left(R_{D1} + \frac{R_{D2}}{2} \right) \cdot y_{vs}^2 - \left[R_{D1} \cdot (1 + y_{vt}) + R_{D2} \cdot \left(1 + \frac{y_{vs} - y_{vt}}{2} \right) \right] \cdot y_{vs} + R_{D1} \cdot y_{vt} + R_{D2} \cdot y_{vs} \cdot \left(1 - \frac{y_{vt}}{2} \right) = 0 \quad (6.5)$$

The drying rate can be expressed in terms of the wet zone moisture content (X_w) variation:

$$\frac{1}{A_s} \frac{dm_w}{dt} = \frac{d}{dt} [\rho_d X_w (b - x_f)] \quad (6.6)$$

where ρ_d is the dry material density and b the slab thickness. Expanding equation 6.6 yields:

$$\frac{1}{A_s} \frac{dm_w}{dt} = \rho_d (b - x_f) \frac{dX_w}{dt} - (\rho_d X_w) \frac{dx_f}{dt} \quad (6.7)$$

During the pendular regime, X_w is the same as X (average moisture content) and is greater than X_c , the front does not leave the surface ($x_f = 0$):

$$\frac{dx_f}{dt} = 0 \quad \text{if} \quad \frac{1}{b} \int_0^b X_w dx > X_c \quad (6.8)$$

As a result of combining equation 6.7 and 6.1 we have:

$$\frac{dX_w}{dt} = \frac{N_v}{\rho_d b} \quad (6.9)$$

During the funicular regime, the wet region moisture content X_w is uniform and does not change with time:

$$\frac{dX_w}{dt} = 0 \quad \text{if} \quad \frac{1}{b} \int_0^b X_w dx < X_c \quad (6.10)$$

The derivative of the front position is then evaluated from equation 6.7 and 6.1:

$$\frac{dx_f}{dt} = -\frac{N_v}{\rho_d X_w} \quad (6.11)$$

The assumption of a step shape for the moisture content distribution is not exact and results in a high rate of recession of the drying front within the material which gives a stronger attenuation of the drying rate than that observed experimentally (Schadler and Kast, 1987). At the front, the capillary liquid movement constrains the drying front spread. Experiments have shown that a more gradual transition of moisture content between the dry and wet regions occurs and increases the size of the wet region. Hence, it is necessary to correct the moisture distribution to evaluate the heat and mass transfer resistance throughout the dry zone. Schadler and Kast (1987) proposed a correction to modify x_f which was tested successfully in convective drying of cylinder and sphere at low temperatures ($d = 10-400 \mu\text{m}$, $D \sim 20 \text{ mm}$, $T_\infty^* = 30-70 \text{ }^\circ\text{C}$, $v_\infty^* \sim 0.23 \text{ m/s}$). This empirical correction to x_f gives x_f' as:

$$x_f' = x_f \left[1 - \frac{X}{X_c} \frac{(b - x_f)}{b} \right] \quad (6.12)$$

The appropriateness of such a correction will be tested for the case of high temperature convective drying and for combined convective-I.R. drying.

Equation 6.9 and 6.11 are first order differential equations which can be solved by the Runge-Kutta method as described in Appendix 10 once the temperatures at the front (and/or surface) are known from the solution of the energy conservation equation.

6.4 ENERGY CONSERVATION EQUATION

The solution of the temperature field in the presence of a drying front necessitates the use of a variable grid (with a constant number of nodes in the dry and wet zones). In order to take into account the effect of the grid displacement on the solution, it is necessary to derive the energy conservation equation with a moving control volume. Dostie (1992) has presented such a derivation which is summarized here.

Consider the control volume (Figure 6.1b) limited by surface a_f which is moving at speed \bar{V}_f . Assume that it contains n phases separated by interfaces a_{ki} moving at speed \bar{V}_{ki} . The variation of a quantity ψ_k characterizing the k phase is given as:

$$\begin{aligned} \frac{d}{dt} \int_{v_k} \rho_k \psi_k dv &= - \int_{a_a} \rho_k \psi_k (\bar{V}_k - \bar{V}_f) \cdot \bar{n}_f da - \sum_{i=1}^n \int_{a_{ki}} \rho_k \psi_k (\bar{V}_k - \bar{V}_{ki}) \cdot \bar{n}_{ki} da \\ &\quad - \int_{a_a} \bar{n}_f \cdot \bar{J} da - \sum_{i=1}^n \int_{a_{ki}} \bar{n}_{ki} \cdot \bar{J} da \\ &\quad + \int_{v_k} \phi_k dv \end{aligned} \quad (6.13)$$

where ρ_k is the k phase density; v_k the k phase volume; \bar{V}_k the k phase velocity; \bar{n} the normal to the surface; \bar{J} the flux term and ϕ_k the volumic source of ψ_k . The intrinsic phase average (Whitaker, 1977) of a quantity f is, by definition:

$$\langle f \rangle_3 = \frac{1}{v_k} \int_{v_k} f dv \quad (6.14)$$

Equation 6.13 can now be written:

$$\begin{aligned} \frac{d}{dt} v_k \langle \rho_k \psi_k \rangle_3 &= - \int_{a_k} \rho_k \psi_k (\bar{V}_k - \bar{V}_l) \cdot \bar{n}_l da - \sum_{\substack{l=1 \\ l \neq k}}^n \int_{a_k} \rho_k \psi_k (\bar{V}_k - \bar{V}_l) \cdot \bar{n}_l da \\ &- \int_{a_k} \bar{n}_l \cdot \bar{J} da - \sum_{\substack{l=1 \\ l \neq k}}^n \int_{a_k} \bar{n}_l \cdot \bar{J} da + \int_{v_k} \varphi_k dv \end{aligned} \quad (6.15)$$

A special case of this equation is for $\psi_k = h_k$, the enthalpy. In this case, if kinetic energies, compressional as well as viscous dissipation are neglected, \bar{J} is the heat flux \bar{q}_k :

$$\bar{q}_k = -k_k \bar{\nabla} T_k \quad (6.16)$$

where k_k is the k phase thermal conductivity, T_k its temperature and φ_k the volumic rate of enthalpy generation. The energy conservation equation becomes:

$$\begin{aligned} \frac{d}{dt} v_k \langle \rho_k h_k \rangle_3 &= - \int_{a_k} \rho_k h_k (\bar{V}_k - \bar{V}_l) \cdot \bar{n}_l da - \sum_{\substack{l=1 \\ l \neq k}}^n \int_{a_k} \rho_k h_k (\bar{V}_k - \bar{V}_l) \cdot \bar{n}_l da \\ &+ \int_{a_k} k_k \bar{\nabla} T_k \cdot \bar{n}_l da + \sum_{\substack{l=1 \\ l \neq k}}^n \int_{a_k} k_k \bar{\nabla} T_k \cdot \bar{n}_l da + \int_{v_k} \varphi_k dv \end{aligned} \quad (6.17)$$

The summation of equation 6.17 for all phases eliminates the interfacial transfer terms within the control volume and provides an equation valid for the mixture:

$$\begin{aligned} \sum_{k=1}^n \frac{d}{dt} v_k \langle \rho_k h_k \rangle_3 &= - \sum_{k=1}^n \int_{a_k} \rho_k h_k (\bar{V}_k - \bar{V}_l) \cdot \bar{n}_l da + \sum_{k=1}^n \int_{a_k} k_k \bar{\nabla} T_k \cdot \bar{n}_l da \\ &+ \sum_{k=1}^n \int_{v_k} \varphi_k dv \end{aligned} \quad (6.18)$$

where α_k is the volume fraction occupied by the k phase and v the overall volume. According to the nomenclature defined in Figure 6.1c, the spatial discretization of 6.18 for the sketched control volume is:

$$\begin{aligned} \frac{d}{dt} \left[(x_{cv,i} - x_{cv,i-1}) \sum_{k=1}^n \alpha_k \langle \rho_k h_k \rangle_3 \right] = \\ \sum_{k=1}^n \left[- \langle \beta_{k,i} \langle \rho_k h_k (V_k - V_i) \rangle_{2,i} - \beta_{k,i-1} \langle \rho_k h_k (V_k - V_i) \rangle_{2,i-1} \right. \\ \left. + \beta_{k,i} \left\langle k_k \frac{\partial T_k}{\partial x} \right\rangle_{2,i} - \beta_{k,i-1} \left\langle k_k \frac{\partial T_k}{\partial x} \right\rangle_{2,i-1} \right. \\ \left. + \langle \varphi_k \rangle_3 (x_{cv,i} - x_{cv,i-1}) \right] \end{aligned} \quad (6.19)$$

where $\langle \rangle_{2,i}$ is the control volume average on surface i . $\beta_{k,i}$ is the part of the surface a_f occupied by k phase at the i th boundary. The following hypothesis is made to simplify the evaluation of the volumic and surface averages in equation 6.19:

$$\langle f_1 f_2 \rangle_x = \langle f_1 \rangle_x \langle f_2 \rangle_x \quad (6.20)$$

This hypothesis has no theoretical justification but was used successfully in multiphase flow studies (Delhaye et al., 1981). Equation 6.19 becomes:

$$\begin{aligned} \frac{d}{dt} \left[(x_{cv,i} - x_{cv,i-1}) \sum_{k=1}^n \alpha_k \langle \rho_k \rangle_{3,i} \langle h_k \rangle_{3,i} \right] = \\ \sum_{k=1}^n \left[- \langle \beta_{k,i} \langle \rho_k \rangle_{2,i} \langle h_k \rangle_{2,i} (\langle V_k \rangle_{2,i} - \langle V_i \rangle_{2,i}) \right. \\ \left. - \beta_{k,i-1} \langle \rho_k \rangle_{2,i-1} \langle h_k \rangle_{2,i-1} (\langle V_k \rangle_{2,i-1} - \langle V_i \rangle_{2,i-1}) \right. \\ \left. + \beta_{k,i} \left\langle k_k \frac{\partial T_k}{\partial x} \right\rangle_{2,i} - \beta_{k,i-1} \left\langle k_k \frac{\partial T_k}{\partial x} \right\rangle_{2,i-1} \right. \\ \left. + \langle \varphi_k \rangle_{3,i} (x_{cv,i} - x_{cv,i-1}) \right] \end{aligned} \quad (6.21)$$

For an isotropic medium:

$$\alpha_k = \beta_k \quad (6.22)$$

The mass fluxes at the control volume boundaries can be written:

$$\begin{aligned} m_{k,l} &= \alpha_k \langle \rho_k \rangle_{2,l} \langle V_k \rangle_{2,l} \\ m_{1k,l} &= \alpha_k \langle \rho_k \rangle_{2,l} \langle V_1 \rangle_{2,l} \end{aligned} \quad (6.23)$$

If local thermal equilibrium is assumed between the phases, an approximation to the heat flux in the case of a three phase system (porous matrix, a liquid and its vapor in a gaseous mixture) can be written using an apparent thermal conductivity which includes the effect of evaporation-condensation at the pore level (Azizi et al., 1988):

$$\sum_{k=1}^n \alpha_{k,l} \left\langle k_k \frac{\partial T_k}{\partial x} \right\rangle_{2,l} = \langle k \rangle_{2,l} \left\langle \frac{\partial}{\partial x} \langle T \rangle_3 \right\rangle_{2,l} \quad (6.24)$$

The enthalpy conservation equation is now:

$$\begin{aligned} \frac{d}{dt} \left[(x_{cv,l} - x_{cv,l-1}) \sum_{k=1}^n \alpha_k \langle \rho_k \rangle_{3,l} \langle h_k \rangle_{3,l} \right] &= \sum_{k=1}^n \left[-((m_{k,l} - m_{1k,l}) \langle h_k \rangle_{2,l}) \right. \\ &\quad \left. + ((m_{k,l-1} - m_{1k,l-1}) \langle h_k \rangle_{2,l-1}) + \langle \varphi_k \rangle_{3,l} (x_{cv,l} - x_{cv,l-1}) \right] \\ &\quad + \langle k \rangle_{2,l} \frac{(\langle T \rangle_{3,l+1} - \langle T \rangle_{3,l})}{\Delta x_l} - \langle k \rangle_{2,l-1} \frac{(\langle T \rangle_{3,l} - \langle T \rangle_{3,l-1})}{\Delta x_{l-1}} \end{aligned} \quad (6.25)$$

If φ_k the volumic source in the k phase of enthalpy is zero, using a fully implicit discretization scheme the time integration of 6.25 provides the final linearized version of equation 6.18:

$$\begin{aligned}
\left(\frac{\delta x_1}{\Delta t} \sum_{k=1}^n \alpha_k \langle \rho_k \rangle_{3,l} \langle h_k \rangle_{3,l} \right)^1 - \left(\frac{\delta x_1}{\Delta t} \sum_{k=1}^n \alpha_k \langle \rho_k \rangle_{3,l} \langle h_k \rangle_{3,l} \right)^0 &= \sum_{k=1}^n \left[-((m_{k,l} - m_{rk,l}) \langle h_k \rangle_{2,l})^1 \right. \\
&\quad \left. + ((m_{k,l-1} - m_{rk,l-1}) \langle h_k \rangle_{2,l-1})^1 \right] \\
&\quad + \left(\langle k \rangle_{2,l} \frac{(\langle T \rangle_{3,l+1} - \langle T \rangle_{3,l})}{\Delta x_1} \right)^1 - \left(\langle k \rangle_{2,l-1} \frac{(\langle T \rangle_{3,l} - \langle T \rangle_{3,l-1})}{\Delta x_{l-1}} \right)^1
\end{aligned} \tag{6.26}$$

In this equation Δt is the time step, superscript ¹ indicates that this quantity is evaluated at time $t+\Delta t$ while superscript ⁰ indicates that this quantity is evaluated at time t .

Eleven nodes uniformly distributed in each zone (21 total number) were found necessary to obtain a grid independent solution for the temperature distribution in the range of thickness considered ($b < 20$ mm). One node is always located at the front which is moving at a velocity defined by equation 6.11. Half control volumes are located close to the surface (node 1) and the symmetry line (node 21); a grid point is positioned at each of these locations. From equation 6.18 the discretized equation at the surface can be written:

$$\begin{aligned}
\left(\frac{\delta x_1}{\Delta t} \sum_{k=1}^n \alpha_k \langle \rho_k \rangle_{3,1} \langle h_k \rangle_{3,1} \right)^1 - \left(\frac{\delta x_1}{\Delta t} \sum_{k=1}^n \alpha_k \langle \rho_k \rangle_{3,1} \langle h_k \rangle_{3,1} \right)^0 &= \\
&\quad \sum_{k=1}^n \left[-((m_{k,1} - m_{rk,1}) \langle h_k \rangle_{2,1})^1 \right] \\
&\quad + \left(\langle k \rangle_{2,1} \frac{(\langle T \rangle_{3,2} - \langle T \rangle_{3,1})}{\Delta x_1} \right)^1 \\
&\quad + h_c (T_\infty - \langle T \rangle_{3,1})^1 - E_s (\sigma \langle T \rangle_{3,1}^4 - q_b^1)
\end{aligned} \tag{6.27}$$

For the insulated side:

$$\left(\frac{\delta X_{21}}{\Delta t} \sum_{k=1}^n \alpha_k \langle \rho_k \rangle_{3,21} \langle h_k \rangle_{3,21}\right)^1 - \left(\frac{\delta X_{21}}{\Delta t} \sum_{k=1}^n \alpha_k \langle \rho_k \rangle_{3,21} \langle h_k \rangle_{3,21}\right)^0 = \sum_{k=1}^n \left[+((m_{k,20} - m_{lk,20}) \langle h_k \rangle_{2,20})^1 \right] - \left(\langle k \rangle_{2,20} \frac{(\langle T \rangle_{3,21} - \langle T \rangle_{3,20})}{\Delta X_{20}} \right)^1 \quad (6.28)$$

Equations 6.26 to 6.28 represent a tridiagonal system of equations which can be solved in terms of the mixture enthalpy defined as:

$$\langle h \rangle_{3,l} = \sum_{k=1}^n \alpha_k \langle \rho_k \rangle_{3,l} \langle h_k \rangle_{3,l} = \langle c_p \rangle_{3,l} \langle T \rangle_{3,l} \quad (6.29)$$

through use of the Thomas algorithm or the Tridiagonal Matrix Algorithm (TDMA). Details of the solution procedure can be found in Patankar (1980). The steps that must be followed at each time step are summarized below:

- a) Compute a first estimate of X or x_f derivatives (equations 6.9 or 6.11) to evaluate a first estimate of X or x_f (first step of a RK22 algorithm);
- b) Evaluate the enthalpy field through solution of the system of equations 6.26 to 6.28;
- c) Calculate a final estimate of X or x_f derivatives (average of the first and present estimate) to obtain the final value of X or x_f at $t+\Delta t$ (second step of RK22);
- d) Get the enthalpy field (and temperatures) at $t+\Delta t$ using the value of X or x_f obtained in c)
- e) Proceed to a) for the next time step.

In order to accept a solution at $t+\Delta t$, relative variations between t and $t+\Delta t$ of temperature at various locations (surface, front) or average moisture content are

also used to control the size of Δt . Under-relaxation (Patankar, 1980) of the predicted mass transfer coefficient (equation 6.37, 5.15 and 4.15) was necessary in order to avoid the numerical instabilities related to θ_K rate of change with ϕ_K at high mass flux.

The numerical coding of this problem was realized recently by Dostie (1992) who also presented additional details on the numerical solution methodology. All the reported simulations have been carried out with a Hewlett-Packard workstation Apollo Series 700 and each took less than 10 seconds (real time) to be completed.

6.5 DRYING FRONT PARAMETERS FOR SIMULATIONS

Most of the thermophysical properties describing the water vapor, air and the glass beads are reported in Appendix 4. Table 3.1 summarizes the values of b , ε and ρ_d . The bed surface emissivity (E_s) was measured to be 0.95 in convection drying and 0.80 in combined convective-I.R. drying; the test section wall emissivity (E_t) was 0.28 (Appendix 6) while the sample-to-test section area ratio (A_s/A_t) was $9.1 \cdot 10^{-3}$. The critical moisture content (X_c) values were taken from Table 4.4 (convection drying) and Table 5.9 (combined convection-I.R. drying).

The dry permeability κ was evaluated from a relation given by Kaviany (1991) for packed beds of spherical particles with a narrow range of distribution in size:

$$\kappa = \frac{\varepsilon^{5.5}}{5.6} d^2 \quad (6.30)$$

The apparent local bed thermal conductivity (W/mK) was computed as (Azizi et al., 1988):

$$k = k_{dw} + f k_{dif} \quad (6.31)$$

which incorporates the transfer of latent heat by vapor movement under the influence of a temperature gradient (k_{dif}) and where f is the diffusion

resistance factor. k_{dw} is the thermal conductivity of the solid and liquid phase and was correlated from k_{dw} vs. S curves at low temperatures ($\sim 5 - 20$ °C) presented by Azizi et al. (1988):

$$k_{dw} = k_d + S \cdot (3.947 - 16.980 \cdot S + 34.666 \cdot S^2 - 30.716 \cdot S^3 + 10.112 \cdot S^4) \quad (6.32)$$

Here, k_d the dry bed thermal conductivity, was linearly correlated to local T (°C) from the experimental results presented by Azizi et al. (1988) since the bed surface temperature can reach up to 300 °C in the combined process:

$$k_d = 0.183 + 8.33 \cdot 10^{-4} \cdot T \quad (6.33)$$

For $T = 20$ °C, 0.2 is the value predicted by equation 6.33 which is close to the measured value (0.174) reported in Appendix 4. k_{diff} is written as (Moyné, 1987; Azizi et al., 1988):

$$k_{diff} = \frac{D_{va}}{R \cdot T} \cdot \frac{dp_v}{dT} \cdot \Delta H_v \cdot \frac{M_a \cdot M_v}{M_g} \quad (6.34)$$

f could be correlated as a function of S (0.00 to 1.00) from experimental results reported by Azizi et al. (1988) for a glass bead bed ($\epsilon = 0.40$):

$$f = 13.31 \cdot S - 6180 \cdot S^2 + 12193 \cdot S^3 - 11120 \cdot S^4 + 37.76 \cdot S^5 \quad (6.35)$$

The effective mass diffusivity value has been discussed recently by Kaviany (1991) who presented a comparison of an expression derived by Neale and Nader (1973) (for the case of packed beds of impermeable spheres) and experimental results within the porosity range of interest in the present study. Since the agreement was excellent, the effective diffusion coefficient D_e was taken to be:

$$D_e = \frac{2 \cdot \epsilon}{3 - \epsilon} \cdot D_{va} \quad (6.36)$$

The convective and radiative heat and mass transfer external parameters T_{∞}^* , T_d^* , h^* (h_c^* , h_{cp}^* or h_{cBL}^*), K_y^* (K_{yBL}^*) and/or q_{is}^* were obtained from the Tables presented in Chapters IV and V. The heat and mass transfer coefficients were corrected when the effect of the high mass transfer rate had to be evaluated. However, in order to avoid the numerical instabilities related to the use of B_K when y_{vs} get close to 1, 5.13 and 5.14 (correlation 5.15) were used to correct the heat transfer coefficient (with h_{cBL}^* instead of h_{cc}^*) while according to Bird et al. (1960), ϕ_K can be written:

$$\phi_K = \frac{N_v^*}{K_{yBL}^*} \quad (6.37)$$

The mass transfer coefficient can then be corrected with 4.15 and 6.37 (correlation 5.15).

For the convective simulations (when h_c^* or h_{cBL}^* were used) the net radiative heat flux q_{ts}^* exchanged between the environment (test section) and the material surface was evaluated (equation 4.7) in the model with an imposed equivalent test section temperature T_t^* (Table 6.2) computed so that q_{ts}^* is the same as the one in Table 4.1 (during the P.C.D.R.P.).

When the drying front position is corrected this is indicated by the parameter cor taken to be 1 whereas when it is 0, $x_f^i = x_f$ in the simulations.

6.6 CONVECTIVE DRYING SIMULATIONS

Few quantitative comparisons between the prediction of drying front models and experimental convective drying results have been reported in the literature.

The second falling rate period was modeled by Szentgyörgyi et al. (1980) with a drying front model where the moisture distribution was assumed to have a step shape (equilibrium moisture content in the dry zone, critical moisture content in the wet zone). An energy balance equation was used in the dry and the wet zone. The drying front progression was responsible for the evaporation rate (from an energy balance at the front). Using an approximate solution for the front

position as a function of time, the temperature distribution as well as drying rate were predicted fairly well for drying of a gypsum-pearlite board ($b = 30$ mm, $T_{\infty}^* = 81$ °C, $v_{\infty}^* = 1.96$ m/s).

According to Schadler and Kast (1987), capillary moisture movement is the key transport phenomenon during the constant rate period. The moisture content distribution can thus be obtained and when S_s is equal to the irreducible saturation S_{ir} , the moisture distribution is averaged across the material thickness and the drying front is assumed to start receding (constant moisture content in the wet zone, 0 in the dry zone). This results in a *a priori* determination of X_c . During the constant drying rate period the material temperature is assumed to be uniform and determined as the wet bulb temperature while in the receding front period, temperature gradients exist only in the dry zone. Analytical expressions are presented for the front and surface temperature in the receding front period when the main moisture transport through the dry layer is assumed to be a diffusive one. An excellent prediction of the drying rate curve as well as surface temperature vs. X was obtained for samples made of non-hygroscopic crushed glass ($d = 10$ - 350 μ m, cylinder $D = 23$ mm, $T_{\infty}^* = 30$ - 70 °C, $v_{\infty}^* = 0.21$ - 0.35 m/s) and ceramic filterstones ($d = 400$ μ m, sphere $D = 20$ mm, $T_{\infty}^* = 30$ °C, $v_{\infty}^* = 0.22$ m/s). The samples were wetted with various liquid such as water, benzene, n-hexane, methanol and tetrachloromethane.

Chen and Pei (1989) considered the existence of a wet and a sorption region. Liquid transfer by capillarity and vapor diffusion were the moisture transport mechanisms in the wet zone while bound water movement and vapor diffusion were dominant in the sorption zone. The heat and mass transfer conservation equations in the wet and sorption zones were linked through heat and mass balance at the front where the moisture content was assumed to equal the maximum sorptive moisture (X_{ms}) content. The dry-wet zone front starts to recede when $X_s = X_{ms}$ and its velocity was determined by the magnitude of the liquid flux toward the front. The experimental X_c was an input to the model and h_c as well K_p were assumed to be functions of X , X_c and X_{ms} in the first falling rate period. The finite element method with Galerkin formulation and a continuous mesh deformation (to concentrate points close to the front) was used to solve numerically the system of equations. Very good predictions of the drying

curves as well as temperature and moisture distributions were obtained for the convective drying of wool (cylinder $D = 73.6$ mm, $T_{\infty}^* = 78.5$ °C, $v_{\infty}^* = 5.3$ m/s), brick (slab $b = 50$ mm, $T_{\infty}^* = 80.0$ °C, $v_{\infty}^* = 5.0$ m/s) and corn kernels (sphere $D = 8.2$ mm, $T_{\infty}^* = 21.0-71.0$ °C, $v_{\infty}^* = 2.33$ m/s).

Rogers and Kaviany (1991) used basically the same type of model as Chen and Pei (simplified for non-hygroscopic material) but with the addition of the gas pressure equation. However they did not use experimentally determined value of X_c ; instead they assumed that this point was reached when $S_s = S_{ir}$. The implicit finite difference control volume technique was used to discretize the system of equations while an adaptive technique allowed concentrations of nodes near the front. Their evaluation of t_c compared favorably with the one from convective drying of a bed of glass beads ($d = 100$ μ m, $b = 25.4$ mm, $T_{\infty}^* = 55.0$ °C, $h_c^* = 18.3$ W/m²K). For a short period of time after the drying front starts receding, the drying rate curve and the temperature distributions within the material agreed well with the experimental results. However, their computation was not completed because the computing time was too excessive. Up to t_c , the S and T distributions show only small gradients throughout the glass beads bed.

All these works show that the applicability of the drying front model has been validated for only a limited range of experimental conditions (b , T_{∞}^* , v_{∞}^* , T_d^*).

6.6.1 EXPERIMENTAL DRYING CURVE: CORRECTION FOR GEOMETRICAL EFFECTS

A comparison between the experimental (Run no. co4, sample data) and simulated drying curves (h_c^* , K_y^* , $\text{cor} = 1$, T_t^*) is presented in Figures 6.2a and b for the drying rate curve. Major experimental parameters are indicated within the figures as well as the expected error bars on the experimental drying curve. It is observed that although N_v (Figure 6.2b) is always (except at the very beginning) higher for the simulations than the experiment, the X vs. t curve in Figure 6.2a seems to show that the experimental N_v is higher than its simulated counterpart. Furthermore, during the P.C.D.R.P. a step (~ 0.003 to 0.015) in X separate the experimental and simulated X .

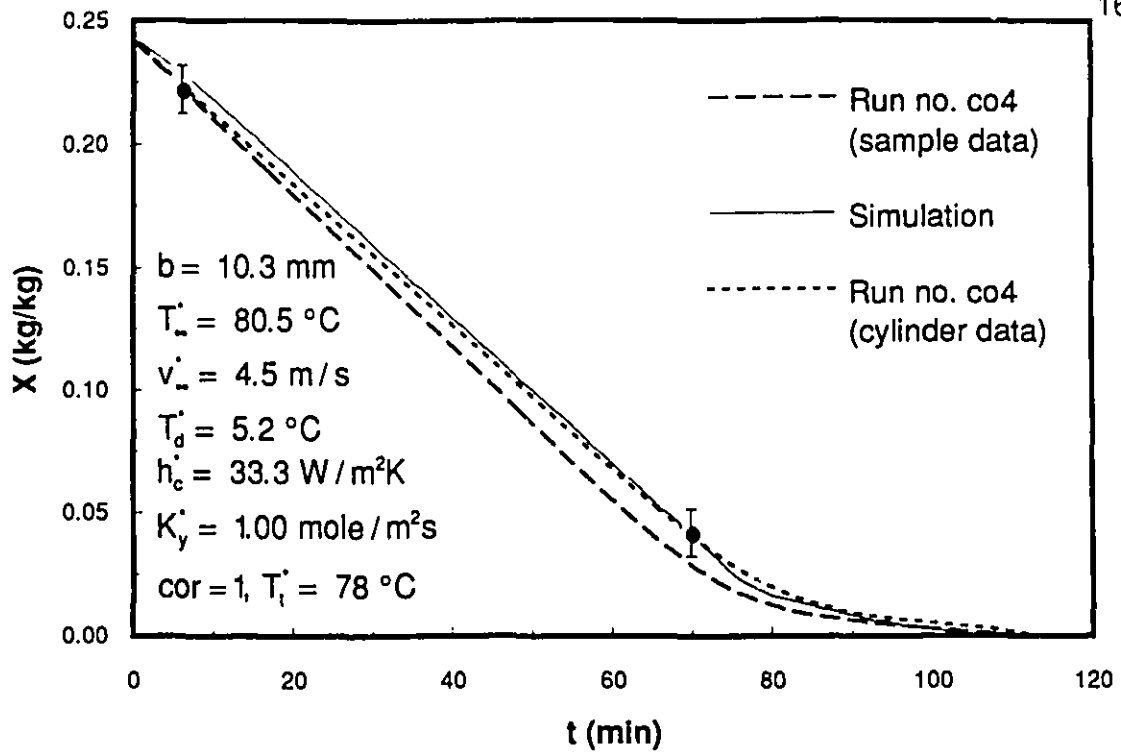


Figure 6.2a The drying curve for run no. co4

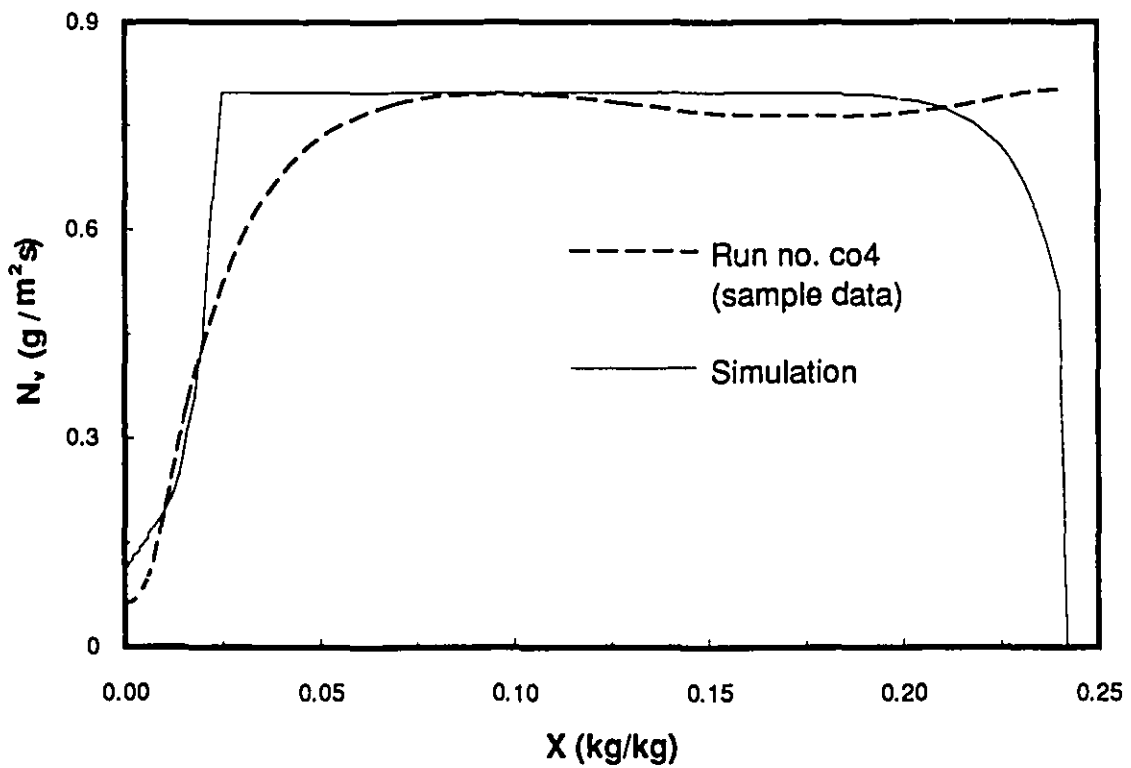


Figure 6.2b The drying rate curve for run no. co4

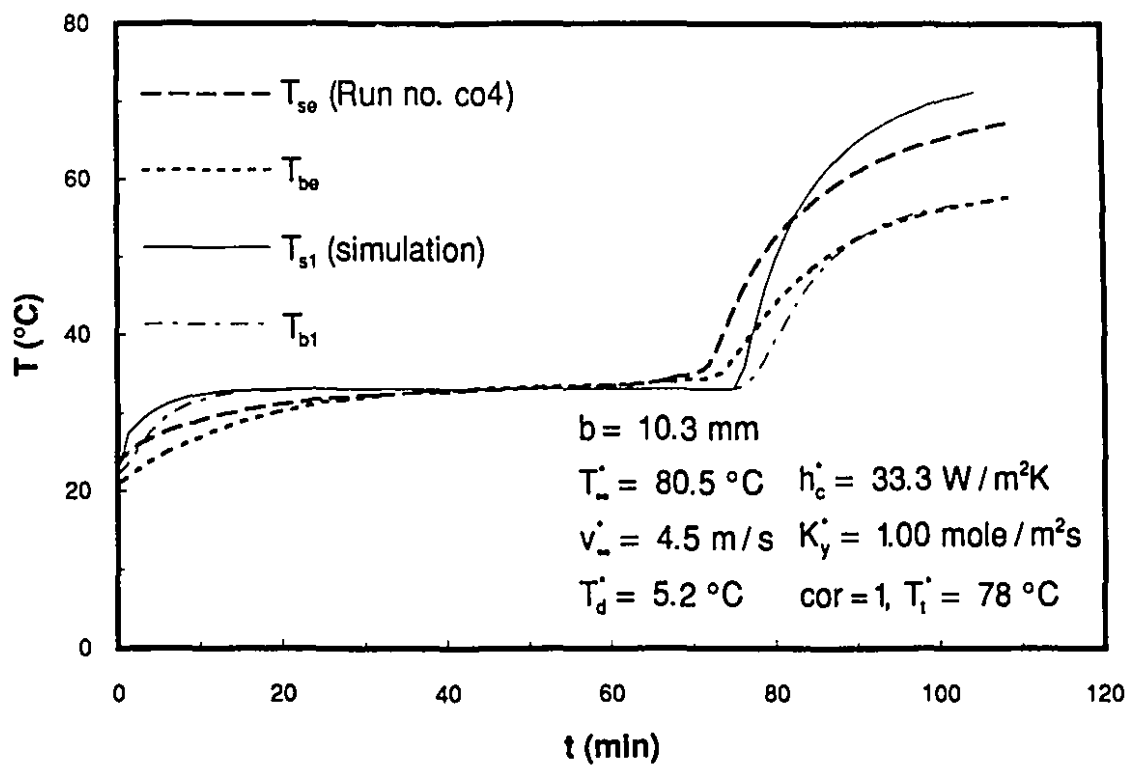


Figure 6.3 The surface and bottom temperatures for run no. co4

Such behavior results from differences in geometry; the sample is slightly conical (3° angle in Figures 3.4 and 3.8) while the simulated case correspond to an equivalent cylinder of thickness b with same surface area, cut into an infinite plane (one-dimensional drying). As one can see from Table 3.1, the cylinder volume V_{cy} (computed with b and D) is greater than V_t (the real measured sample overall volume). Thus for the same initial moisture content X_{in} , the initial mass of water m_{win} (per unit area) is higher in the simulation (for same b); similar N_v values (Figure 6.2b) result in the same amount of water evaporated at time t but m_w left is higher in the simulation which result in greater X , in agreement with results in Figure 6.2a.

The experimental drying curve was modified to represent the case of a cylinder with same b . Based on the assumption that the drying rate curve of a cylinder or a truncated cone are the same (valid for one-dimensional drying), the development of the necessary correction procedure is presented in Appendix 10.

In Figure 6.2a is displayed the modified drying curve (cylinder data) together with the results of simulation. The curves are in good agreement and the higher drying rates observable in Figure 6.2b for the numerical computation translate, as expected, into higher dX/dt (than the experiment) in Figure 6.2a. It is important to note that the higher drying rate in the simulation is a consequence of using the heat and mass transfer coefficients identified with N_v close to the highest experimental mass flux in Figure 6.2b. The experimental and predicted overall drying time t_o in Figure 6.2a differ by less than 7 %.

Although the measured (for a conical geometry) and predicted (for an equivalent cylindrical geometry) T vs. t curves are not strictly identical, they can be compared for the following reasons:

- a) For $t < t_c$, the difference in heat transfer between the two cases lay with the increase in the accumulated heat in the case of the cylinder since there is more water and material to heat. However, during most of that period, evaporation is the dominant heat transfer phenomenon which defines the temperature level within the material

as underlined by the very good agreement on T_s^* (Figure 6.3). Although t_c deduced from the experimental T vs. t curve is likely to be slightly underestimated when compared to the one derived from the simulations, X_c are the same for both conical and cylindrical geometries;

- b) For $t > t_c$, the drying front recession is faster for the reported experimental results because the front surface area decreases with increase in x_f . Thus the reported T_b within the material are expected to be slightly higher than their equivalent for the cylinder at same t.

Since the "experimental" t_c is smaller (by less than 4 %) the T vs. t curves in Figure 6.3 as compared to the ones deduced from the drying curve (for a cylinder) in Figure 6.2a, it is likely that the reported temperatures constitute a very good evaluation of temperature that could be measured if a perfect cylinder had been used in the experiments.

Figure 6.3, shows the evolution of T_s and T_b evolutions (Run no. co4). It may be observed that T_s^* is well reproduced (33.1 °C vs. 32.9 °C), the critical time t_c values are close (differences are less than 5 %) and the T_b evolution and level do not differ significantly since the observed differences are within the experimental uncertainty of the T_b measurement for most of the time. At the beginning of drying, the predicted T_s and T_b might be higher than measured due to a too high apparent local bed thermal conductivity used in the simulations (equation 6.34).

6.6.2 THE SURFACE TEMPERATURE MEASUREMENT BIAS IN CONVECTIVE DRYING

In Figure 6.3, a larger gradient exists between the surface and the bottom temperatures of the sample as predicted by the model in the receding front period. The lower measured gradient is a consequence of the surface thermocouple acting as a fin located between the sample bottom and surface. The magnitude of this effect can be quantified through evaluation of the two-dimensional temperature field close to the thermocouple at the end of drying with a commercial software FLUX2D under the following assumptions:

- a) The problem is axisymmetric and the geometry as defined in Figure 6.4;
- b) The measured T_{be} is the bottom boundary condition and convection is applied at the surface through h^* and T_∞^* ; the sides are adiabatic;
- c) The steady-state solution of the two dimensional temperature field is representative of the temperatures within the sample at the end of drying.

In Figure 6.4 are displayed the typical isotherm distortions which result from the thermocouple conducting heat from the surface to the bottom because of its much higher thermal conductivity (stainless steel ~ 17 W/mK vs. glass beads~ 0.26 W/mK). In Table 6.1 are reported the run identification number, the sample number, b , T_∞^* , h^* , T_{be} , T_{b1} , T_{se} , T_{c2D} , T_{s1} and T_{s2D} . T_{be} , T_{se} , T_{c2D} , T_{s2D} , T_{b1} and T_{s1} are the measured sample bottom and surface temperatures at the end of drying, the thermocouple and surface temperatures as evaluated with FLUX2D and the bottom as well as surface temperature predicted with the drying front model (at the end of drying, (h^* , K_y^* , $cor= 1$)) respectively. It is observed that:

- a) T_{be} and T_{b1} are close except for $b = 5.5$ mm;
- b) T_{se} and T_{c2D} are in good agreement, when the additional unknown thermal contact resistance between the thermocouple surface and the beads not included in the simulations with FLUX2D ($T_{se} \leq T_{c2D}$) as well as the uncertainty on the thermocouple measuring point location are taken into account;
- c) T_{s2D} and T_{s1} are in very good agreement since T_{s1} is determined when the material is such that $X < 2.5 \cdot 10^{-4}$ while T_{s2D} corresponds to a steady-state solution.

Figure 6.4 The isotherms within the dried sample close to the surface thermocouple for run no. 009

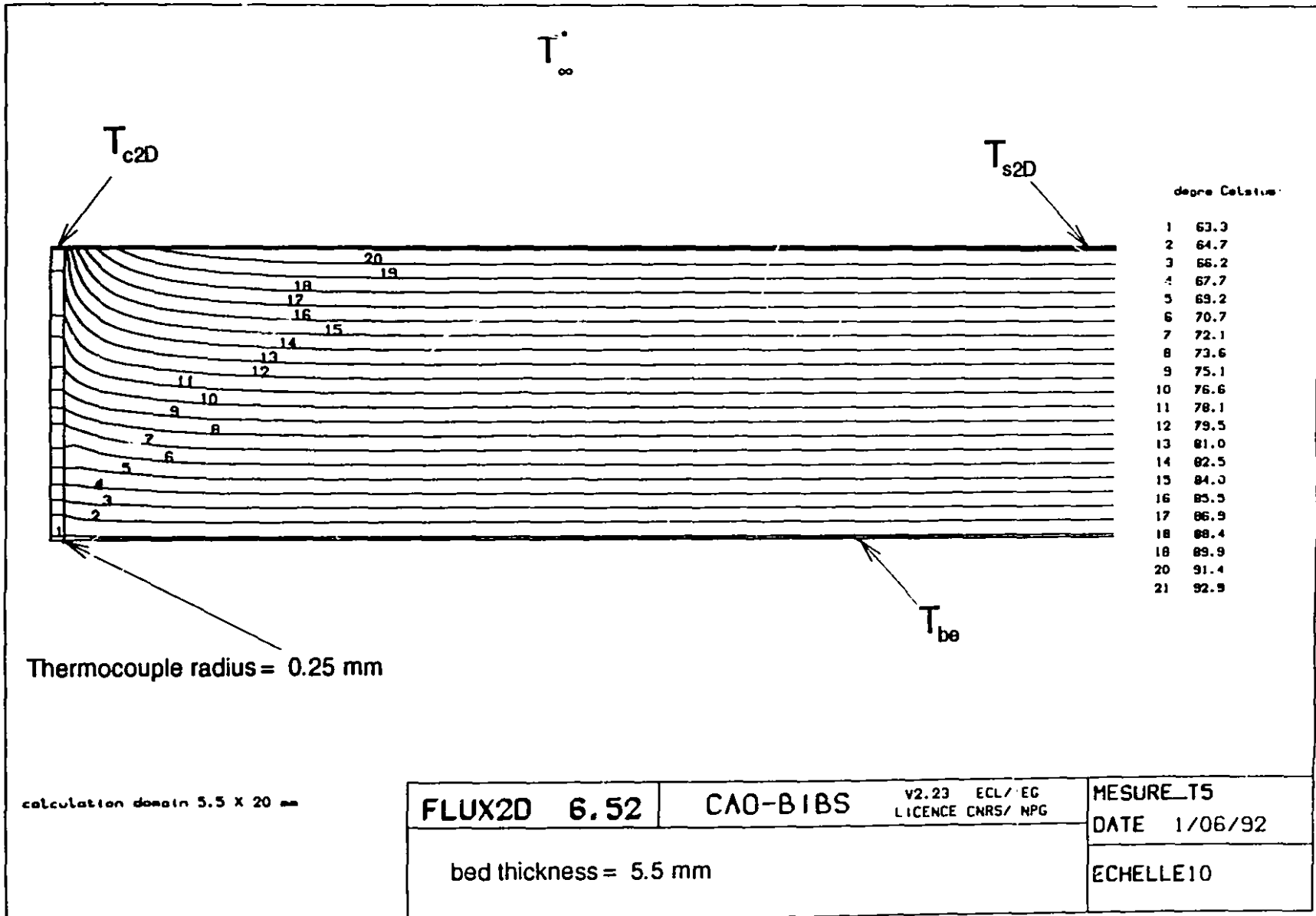


TABLE 6.1

MEASURED AND SIMULATED SURFACE TEMPERATURESFOR CONVECTIVE DRYING:EVALUATION OF THE EXPERIMENTAL BIAS AT THE END OF DRYING

Run No.	Sa. No.	b (mm)	T_{∞} (°C)	h^* (W/m ² K)	T_{be} (°C)	T_{b1} (°C)	T_{se} (°C)	T_{c2D} (°C)	T_{s1} (°C)	T_{s2D} (°C)
co2	X	10.3	79.9	27.1	52	55	60	63	68	67
re18	XII	19.9	79.8	29.0	57	58	67	69	73	73
co15	IX	5.5	80.2	40.0	50	54	57	58	66	64
co4	X	10.3	80.5	40.3	58	57	67	68	71	72
co3	XII	19.9	80.6	44.0	60	59	71	71	75	76
co7	X	10.3	130.6	26.1	67	66	89	91	95	99
co6	XII	19.9	130.7	26.8	72	71	97	103	108	111
co9	IX	5.5	130.4	38.4	63	65	81	81	91	93
co12	X	10.3	130.5	37.3	69	69	89	96	103	105
co8	XII	19.9	130.4	37.4	73	71	101	108	112	115
co11	X	10.3	180.5	27.5	76	73	104	117	121	123
co10	XII	19.9	180.6	27.6	82	76	125	138	139	148
re21	IX	5.5	180.0	40.4	66	72	89	98	115	119
re25	X	10.3	179.8	39.3	78	77	108	125	132	140
re6	XII	19.9	180.4	41.7	82	80	133	146	150	156

The phenomenon analyzed here is likely to be active as soon as temperature gradients exist within the bed (not during the P.C.D.R.P.) and the time dependent temperature differences appearing between T_{se} and T_{s1} are believed to be due to it; as was demonstrated at the end of drying.

For $b = 10.3$ or 19.9 mm, the measured T_b are not affected by such a problem because the bottom thermocouple wire is parallel to the isotherms within the sample and in good thermal contact with the bed bottom for a distance of about 45 mm. For $b = 5.5$ mm ($T_{be} < T_{b1}$), as the thermocouple wire was inserted within the low thermal conductivity foam (Figure 6.5) and goes through a region close to the cooled sample holder fin, the recorded T_b is lower than it should be.

It can be concluded that the drying front model (h^* , K_y^* , $cor = 1$) predicts very well T_b and T_s at the end of drying for most of the convective runs.

6.6.3 THE DRYING FRONT POSITION CORRECTION EFFECT IN CONVECTIVE DRYING

The effect of the correction to the drying front position has been quantified in Table 6.2 where the run identification number, T_∞^* , T_t^* , t_{oe} , t_{o1} , $\Delta t_{o1}\%$, t_{o0} , $\Delta t_{o0}\%$, T_{be} , T_{b1} , T_{b0} , T_{s1} , T_{s0} and T_{s2D} are reported. t_{oe} , t_{o1} and t_{o0} are the experimental and predicted overall drying times with the drying front model (h_c^* , K_y^* , T_t^*) when $cor=1$ or 0 respectively. $\Delta t_{o1}\%$ and $\Delta t_{o0}\%$ are the differences between t_{o1} and t_{oe} as well as t_{o0} and t_{oe} divided by their average values and expressed in percent. The T_b and T_s temperatures are taken from data at the end of drying from the experiments and when $cor = 1$ or 0 while T_{s2D} has been defined in the preceding section. These data show that:

- a) The average differences between the experimental and predicted t_o are 4.1 % ($cor = 1$, standard deviation = 4.1 %) and 1.5 % ($cor = 0$, standard deviation = 5.8 %). Thus on the average t_o is slightly underpredicted when the drying front correction is applied whereas it is slightly overestimated when it is not;
- b) T_{be} appears to be well predicted with or without the drying front correction;

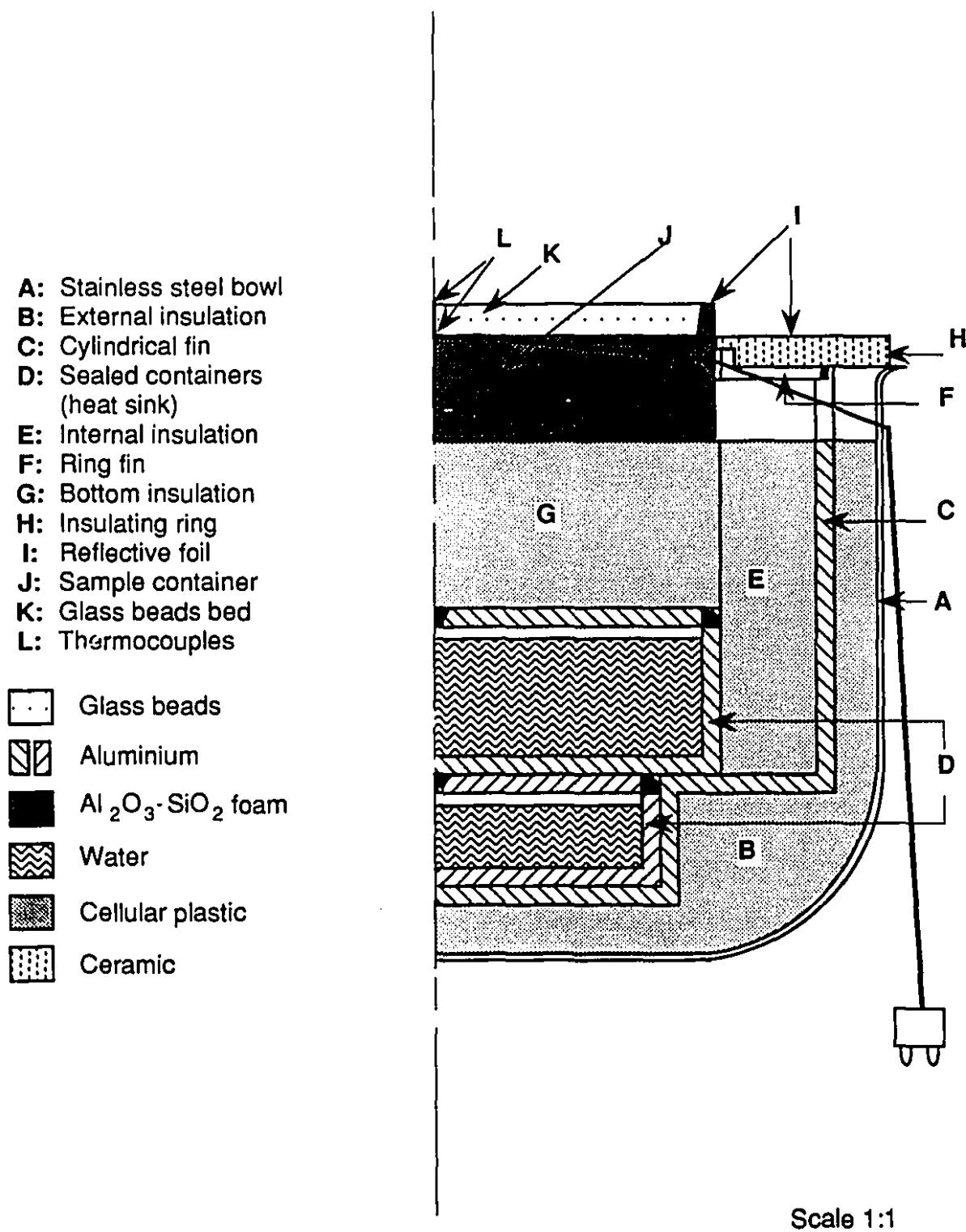


Figure 6.5 The 5.5 mm sample: cross sectional view

TABLE 6.2

MEASURED AND SIMULATED DRYING TIMES, BOTTOM AND SURFACE TEMPERATURES AT THE END OF DRYING WITH AND WITHOUT DRYING FRONT CORRECTION FOR CONVECTIVE DRYING

Run No.	T_{∞}^*	T_t^*	t_{oe}	t_{o1}	$\Delta t_{o1}\%$	t_{o0}	$\Delta t_{o0}\%$	T_{be}	T_{b1}	T_{b0}	T_{s1}	T_{so}	T_{s2D}
(.)	(°C)	(°C)	min.	min.	(.)	min.	(.)	(°C)	(°C)	(°C)	(°C)	(°C)	(°C)
co2	79.9	76	158.6	144.2	-9.1	153.4	-3.3	52	55	56	68	68	67
re18	79.8	76	272.5	283.9	4.2	311.0	13.2	57	57	59	72	73	73
co15	80.2	77	54.6	50.3	-7.9	53.3	-2.4	50	54	55	66	67	64
co4	80.5	78	112.6	104.8	-6.9	112.8	0.2	58	57	58	71	72	72
co3	80.6	78	205.0	205.1	0.0	227.9	10.6	60	59	60	75	76	76
co7	130.6	121	83.3	78.5	-5.8	81.3	-2.4	67	66	69	96	98	99
co6	130.7	121	163.0	164.7	1.0	174.8	7.0	72	71	74	107	109	111
co9	130.4	124	32.3	28.6	-11.5	29.5	-9.1	63	65	68	92	95	93
co12	130.5	125	60.0	58.9	-1.8	61.7	2.8	69	69	72	103	105	105
co8	130.4	125	127.1	121.9	-4.1	130.5	2.6	73	71	74	112	114	115
co11	180.5	164	54.5	51.7	-5.1	53.4	-2.0	76	74	77	122	126	123
co10	180.6	165	112.1	108.7	-3.0	114.0	1.7	82	76	80	139	142	148
re21	180.0	169	19.0	18.5	-6.1	19.0	-3.6	66	72	76	116	120	119
re25	179.8	170	39.4	38.4	-2.5	40.4	2.5	78	77	80	133	136	140
re6	180.4	170	77.8	75.5	-3.0	81.3	4.4	82	80	83	150	153	156
				Av.	-4.1		1.5						
				Stdev.	4.1		5.8						

- c) The differences between T_{s1} , T_{s0} and T_{s2D} are low considering the temperature level reached.

Figures 6.6 (6.7a) and 6.8 (6.7b) present a comparison between the experimental results (Run no. co7 and re6 respectively) and simulations with and without drying front correction (h_c^* , K_y^* , cor= 0 or 1, T_t^*) for the X vs. t, T vs. t and N_v vs. X curves, respectively. The X vs. t curves (Figures 6.6a and 6.8a) are well reproduced (within the experimental uncertainties of the experimental results) while the overall behavior of the T vs.t curves (Figures 6.6b and 6.8b) is followed accurately (not T_s after the critical point) with differences greater than experimental uncertainty at the beginning of drying. On the N_v vs. X curves (Figures 6.7a and b), the simulation with no drying front position correction (cor = 0) predicts a more abrupt fall of N_v as compared to the one with drying front position correction (cor = 1) which qualitatively suggests, when compared to the experimental results, that the correction of the drying front position to evaluate the mass transfer resistance is valid. In addition, for most of the receding front period, the predicted T_b is slightly closer to the experimentally measured T_b when cor = 1.

6.6.4 THE TRANSFER COEFFICIENT CORRECTIONS AND THE DRYING FRONT MODEL RESULTS IN CONVECTIVE DRYING

The effect of the heat and mass transfer coefficient correction procedure (boundary layer theory) can be quantified by reference to a typical simulation (Run no. co11, (h_{cBL}^* , K_{yBL}^* , cor = 1, T_t^*)) for which, according to section 4.3, θ_h (0.90) and θ_K (0.92) are among the lowest (as evaluated during the P.C.D.R.P.) and the transfer coefficients were modified as a function of the instantaneous value of N_v . A reference simulation was also carried out with h_{cBL}^* and K_{yBL}^* held constant. Figures 6.9a and b present X vs. t and T vs. t curves (experiments and simulations) while Figure 6.10a displays the N_v vs. X curve.

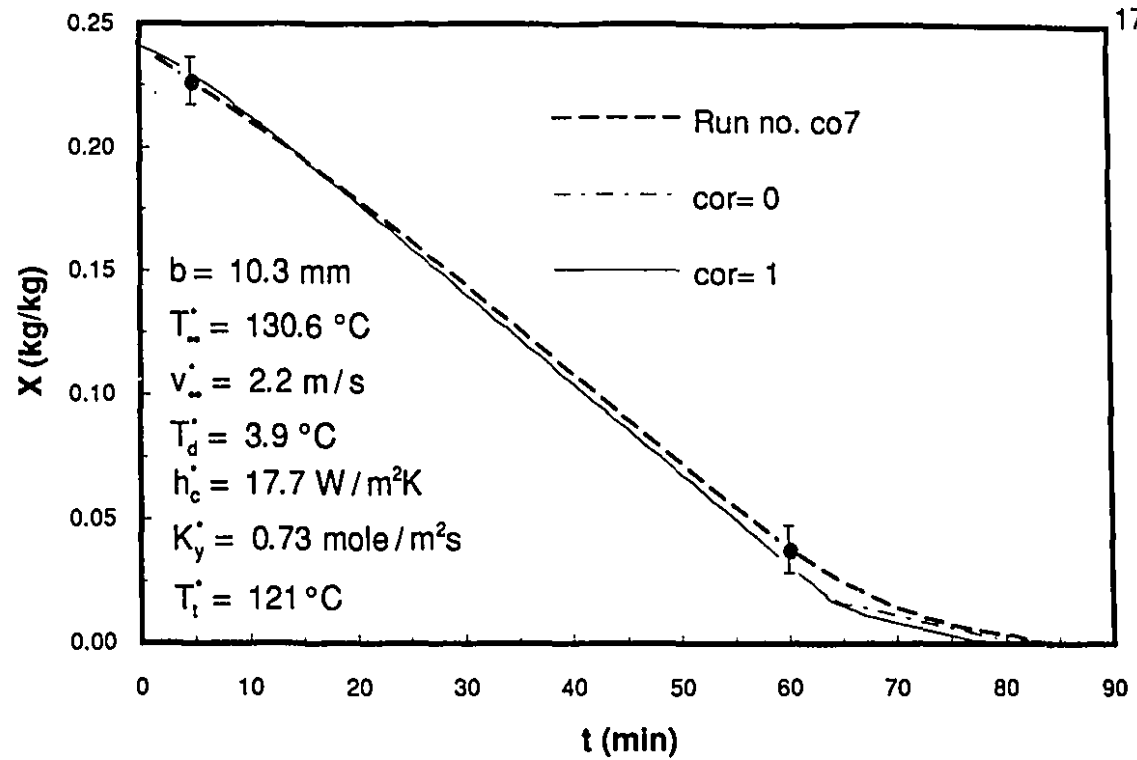


Figure 6.6a The drying curve for run no. co7: test of the drying front position correction

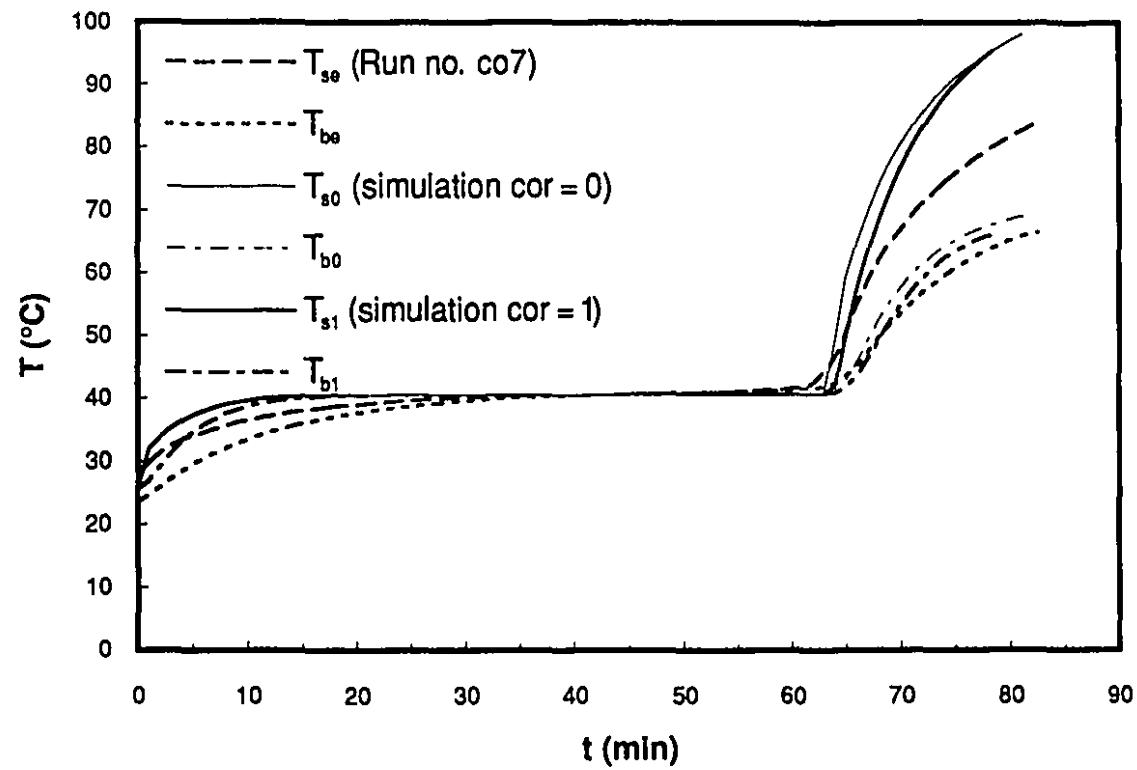


Figure 6.6b The surface and bottom temperatures for run no. co7: test of the drying front position correction

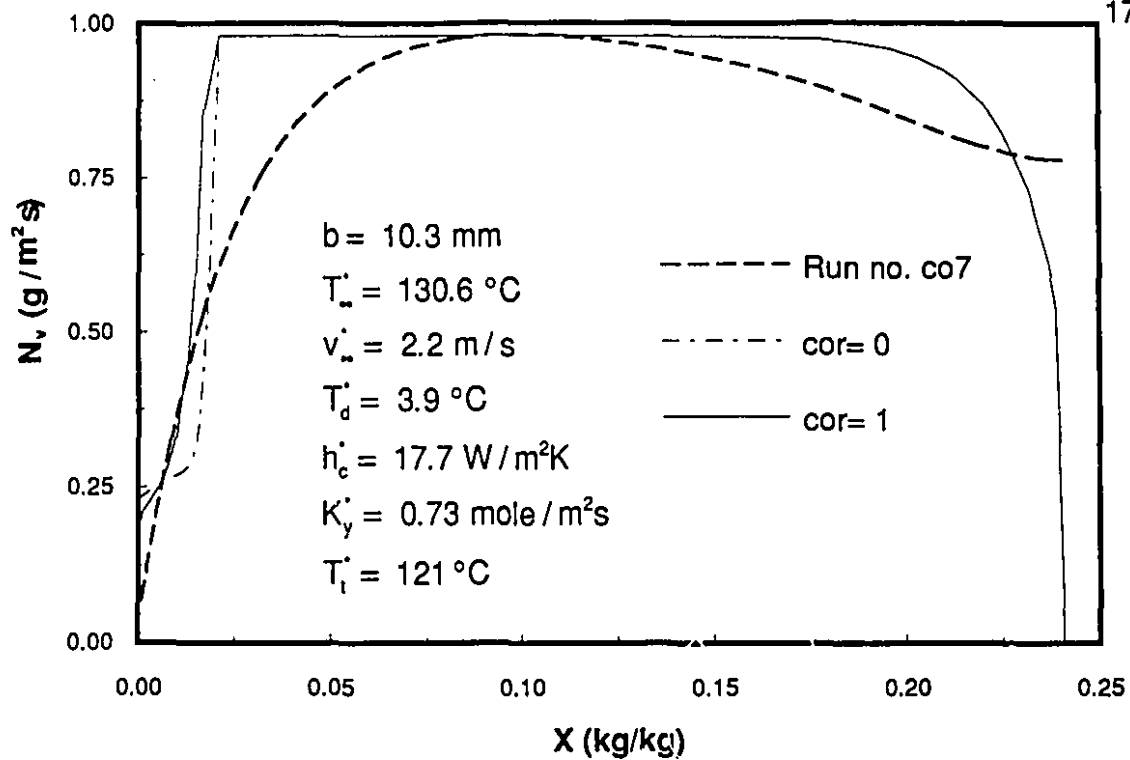


Figure 6.7a The drying rate curve for run no. co7: test of the drying front position correction

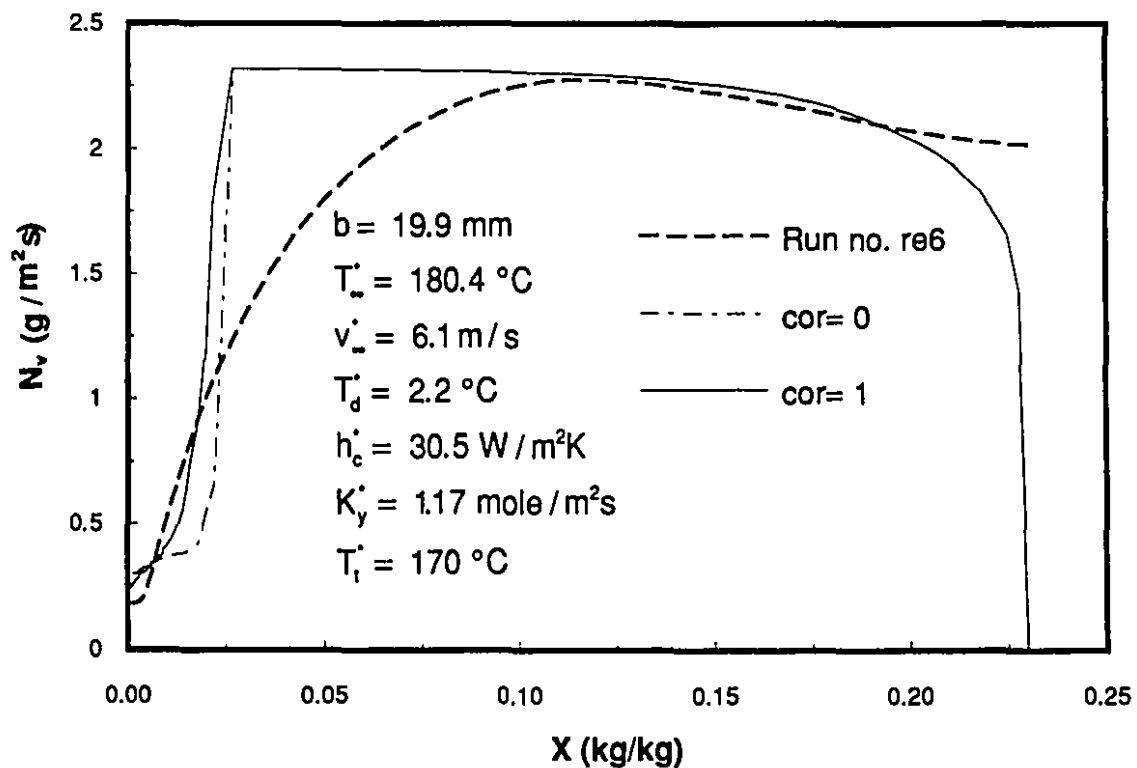


Figure 6.7b The drying rate curve for run no. re6: test of the drying front position correction

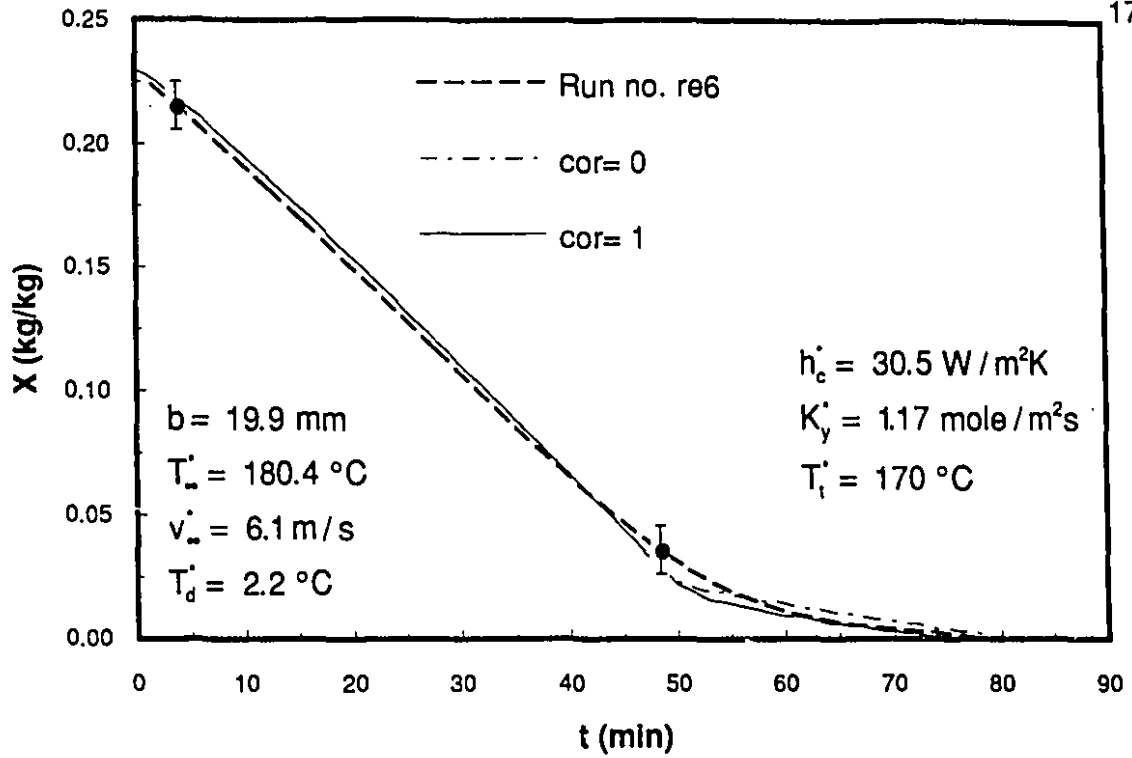


Figure 6.8a The drying curve for run no. re6: test of the drying front position correction

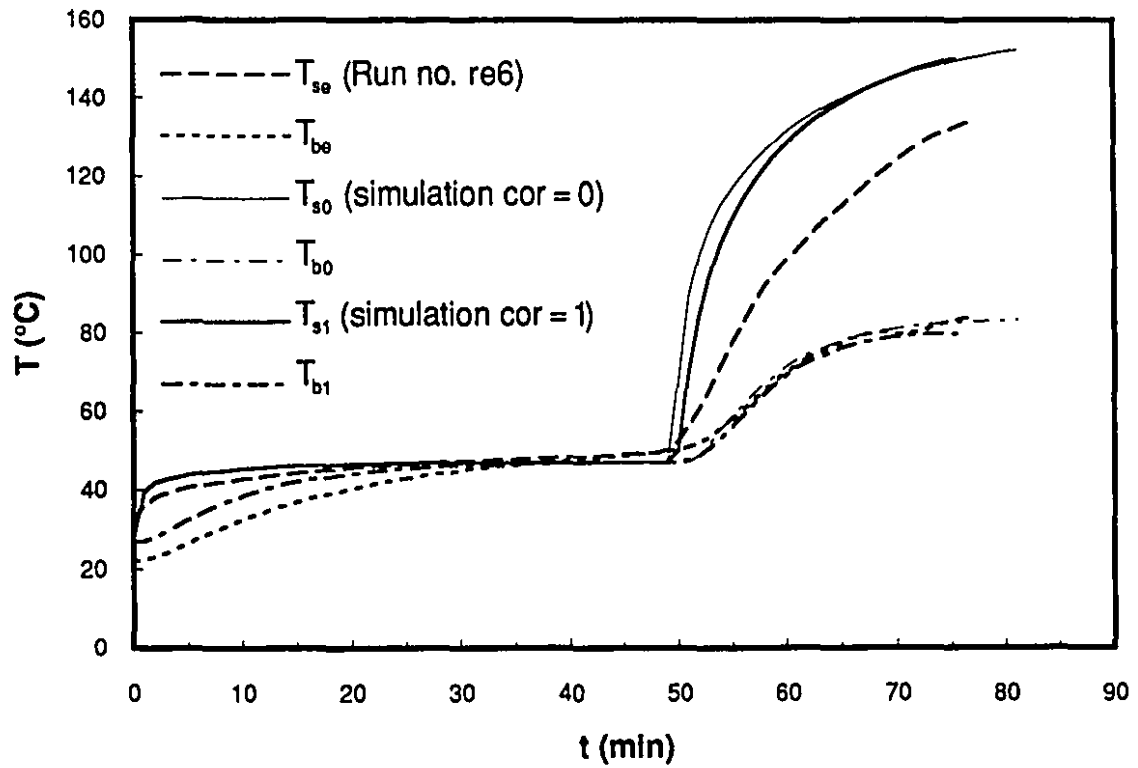


Figure 6.8b The surface and bottom temperatures for run no. re6: test of the drying front position correction

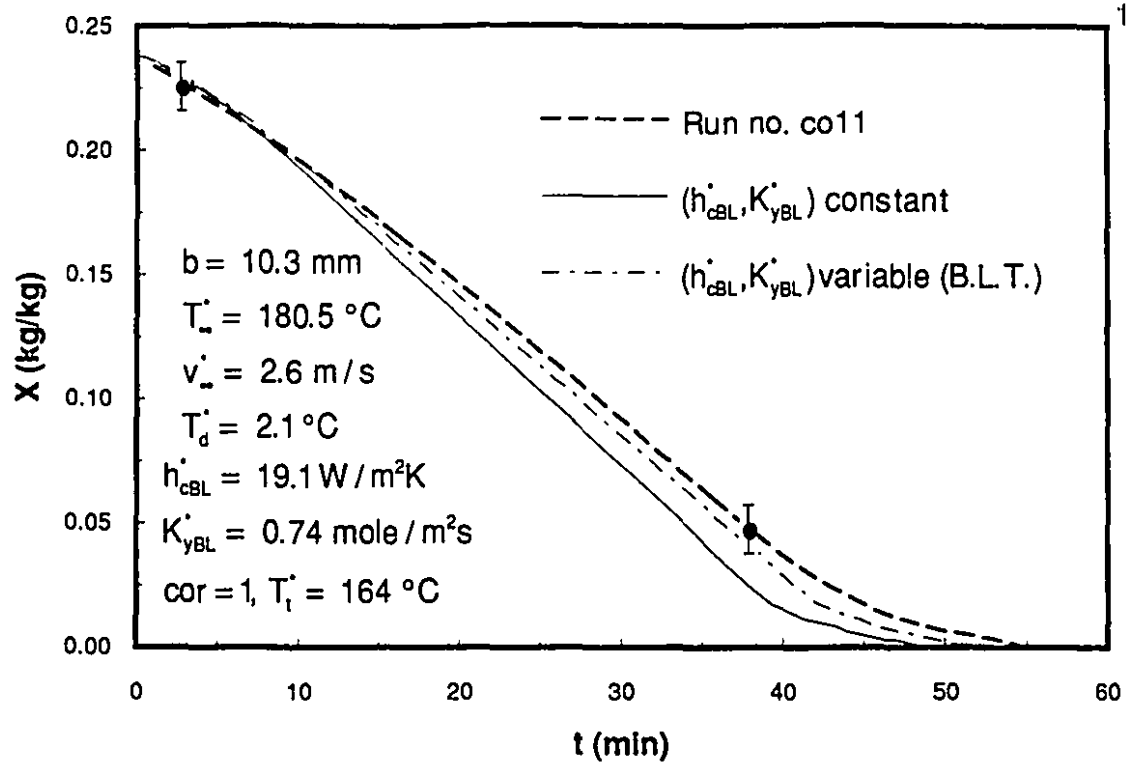


Figure 6.9a The drying curve for run no. co11: test of the transfer coefficient correction procedure (B.L.T.)

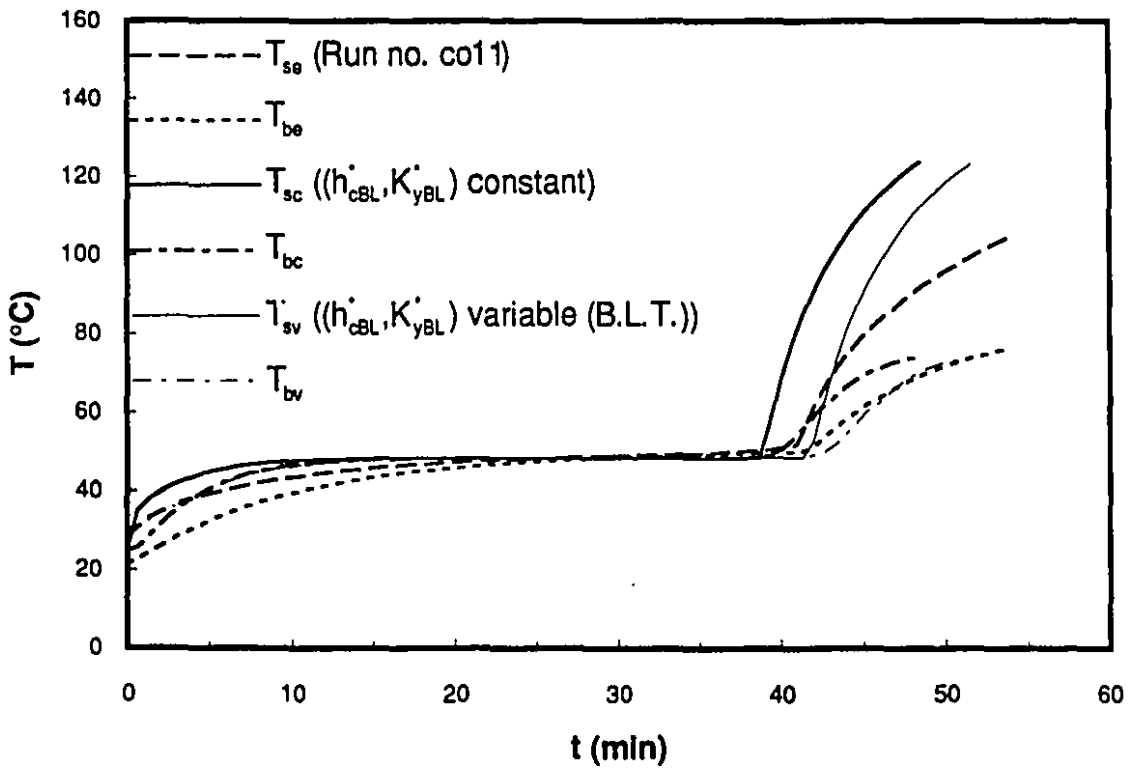


Figure 6.9b The surface and bottom temperatures for run no. co11: test of the transfer coefficient correction procedure (B.L.T.)

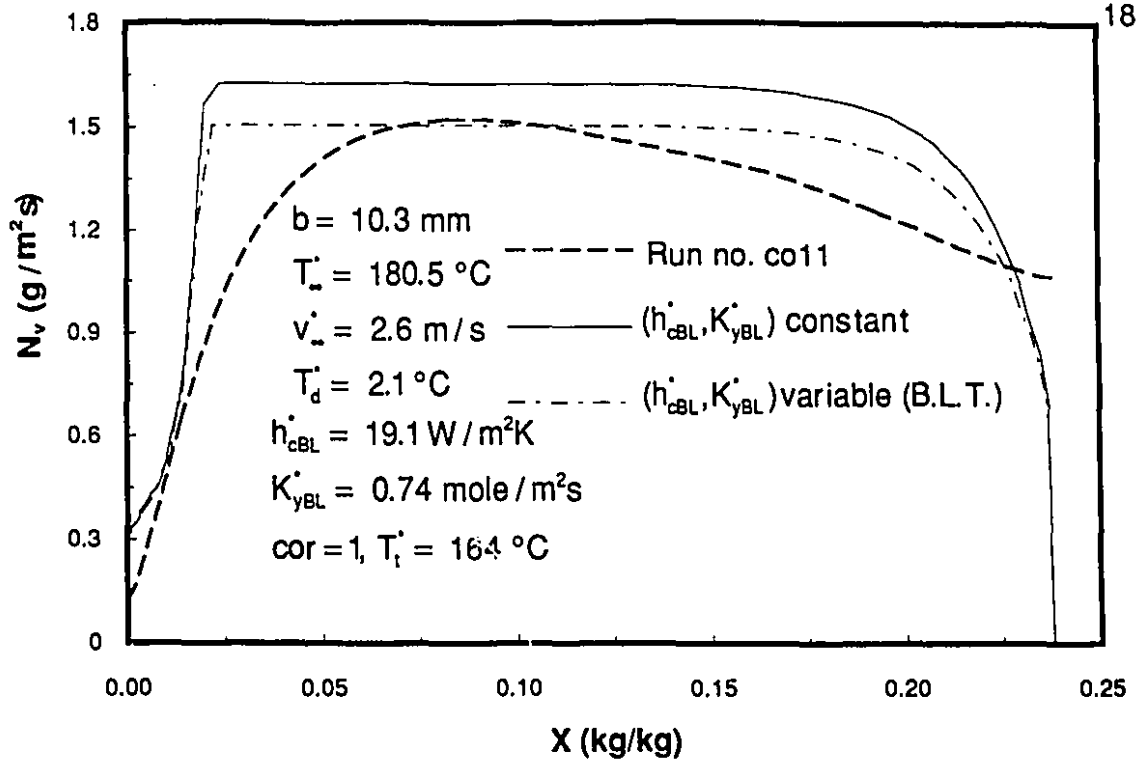


Figure 6.10a The drying rate curve for run no. co11: test of the transfer coefficient correction procedure (B.L.T.)

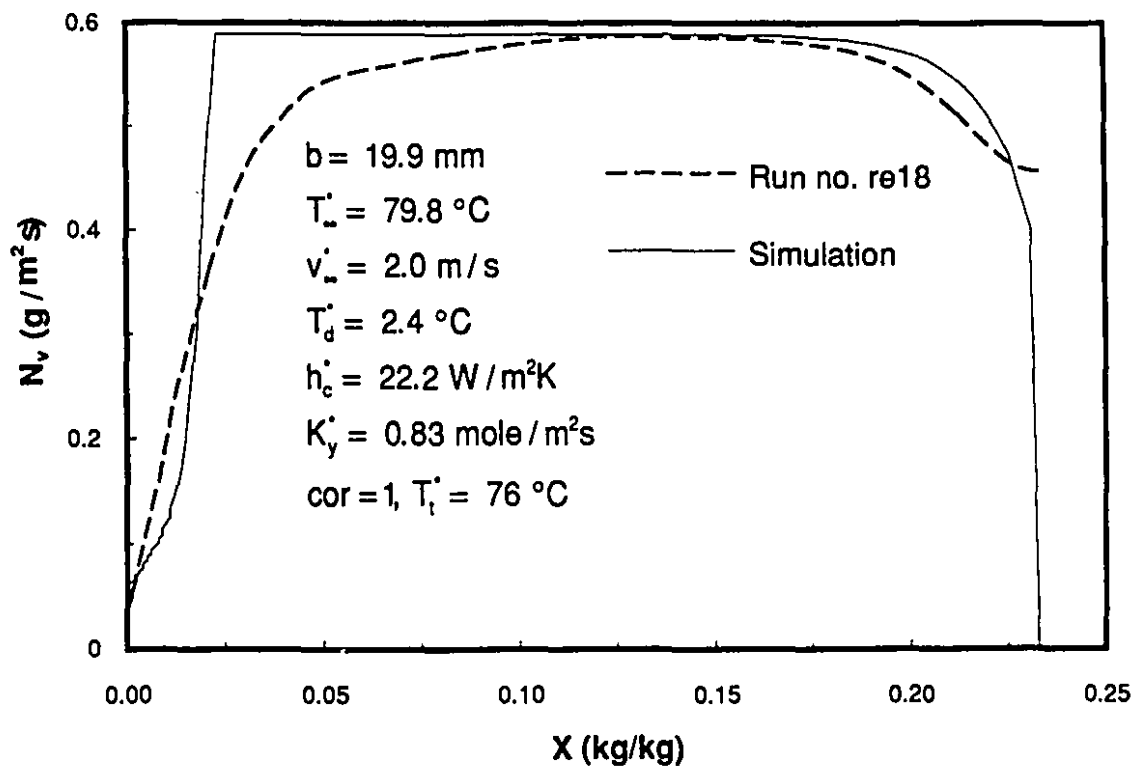


Figure 6.10b The drying rate curve for run no. re18

It is observed that:

- a) The use of constant heat and mass transfer coefficients (h_{cBL}^* , K_{yBL}^*) - valid under low mass flux condition- leads to a higher drying rate (8 %) and a shorter drying time (5 %) as compared to the simulated results when the coefficients are variable;
- b) The variation of the transfer coefficients as predicted by the boundary layer theory provides a better prediction of the experimental drying curve (within experimental uncertainty);
- c) Since X_c is reached earlier when the transfer coefficients are constant the T_s and T_b rise earlier than the experimental ones or when the transfer coefficients vary. As the transfer coefficient ratios 4.10 and 4.22 are the same, T_s^* is unchanged for both simulations.

This result suggests that the heat and mass transfer coefficients determined under low mass flux conditions (or from heat transfer correlations) should be corrected for the effect of the diffusion mass flux when air temperatures as high as 180 °C are considered. It is important to note that in the range of θ_K and θ_h reached in case of convective drying, the application of the boundary layer, penetration or film theories gives the same correction (within 1 to 2 %) of the transfer coefficient. Thus, in case of convective drying, the mass transfer rate reduction can be taken into account by using the result of any of these correction procedures.

6.6.5 COMPARISON BETWEEN THE CONVECTIVE DRYING RUNS AND THE DRYING FRONT MODEL

Results of the X vs. t , T vs. t and N_y vs. X curves from simulations (h_c^* , K_y^* , $cor = 1$, T_t^*) for experiments no. re18, co8 and re21 are displayed in Figures 6.11 (6.10b), 6.12 (6.13a) and 6.14 (6.13b) respectively. These runs were chosen to cover the spectrum of parameters for which no detailed data have been presented previously.

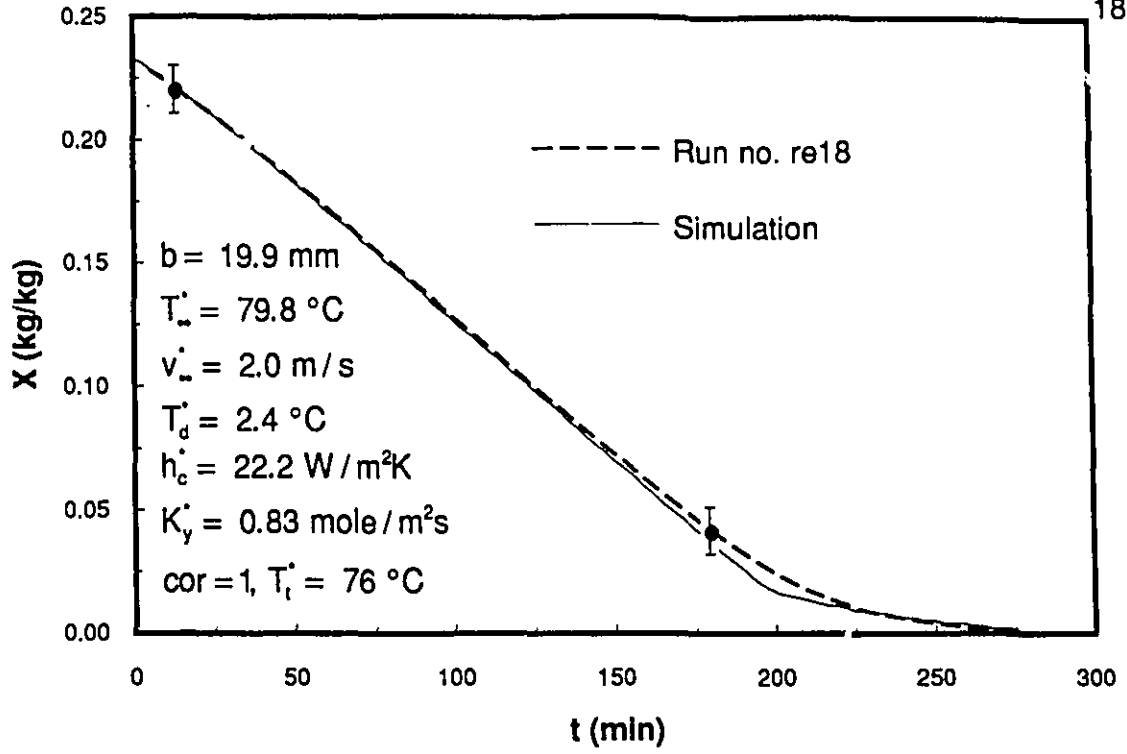


Figure 6.11a The drying curve for run no. re18

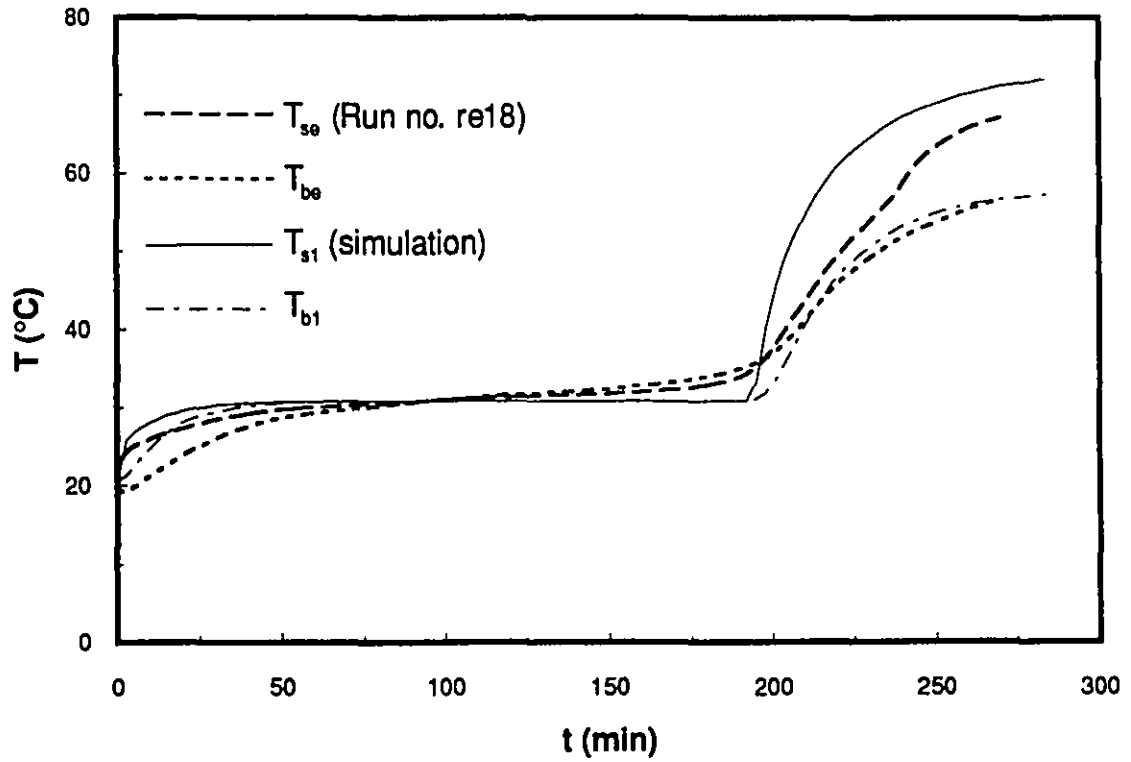


Figure 6.11b The surface and bottom temperatures for run no. re18

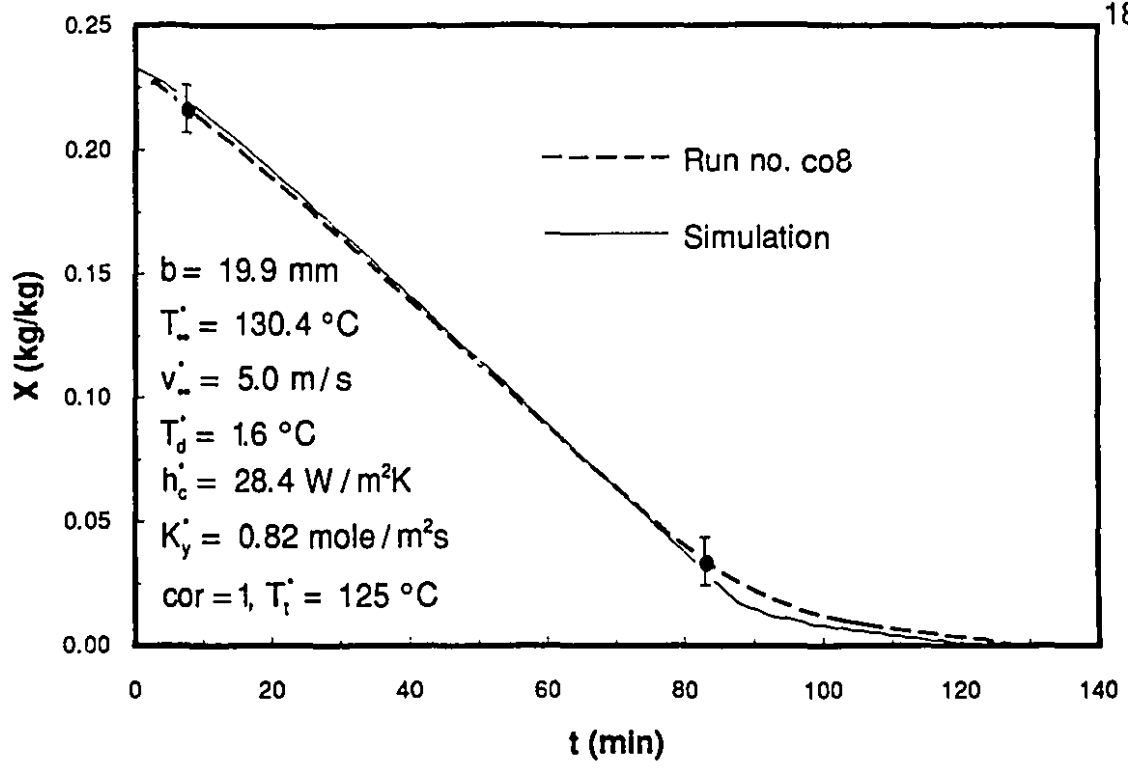


Figure 6.12a The drying curve for run no. co8

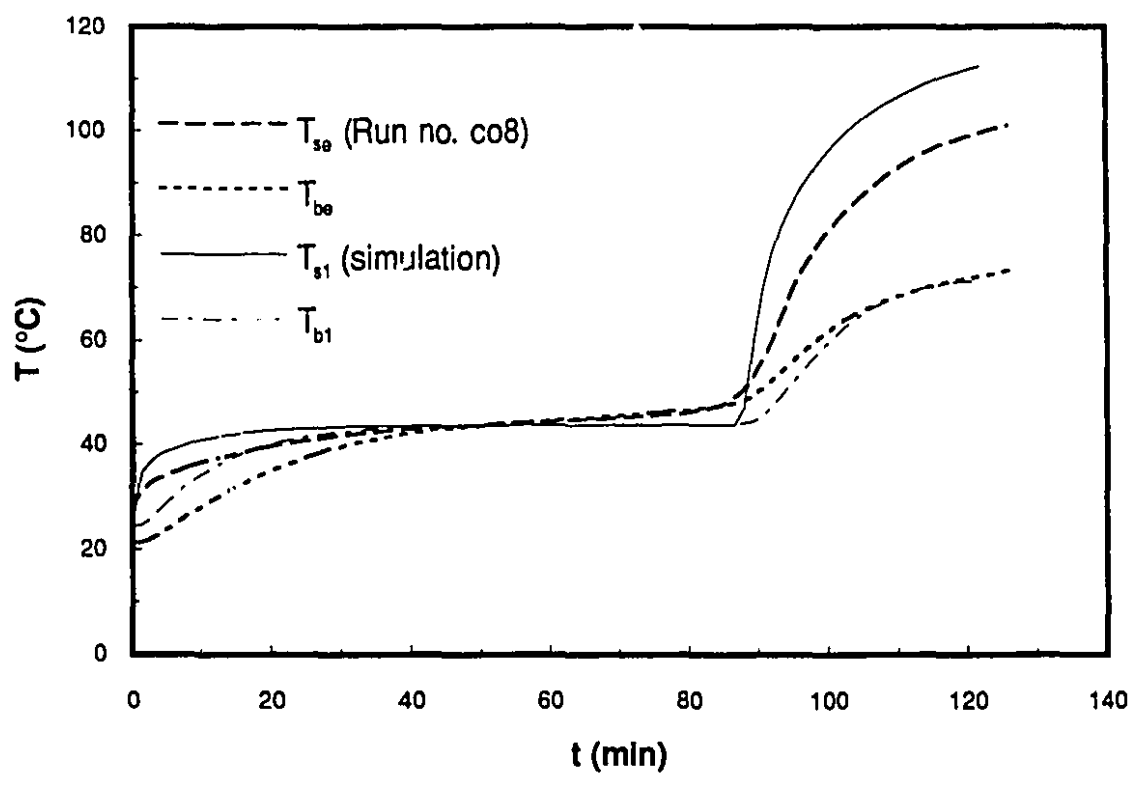


Figure 6.12b The surface and bottom temperatures for run no. co8

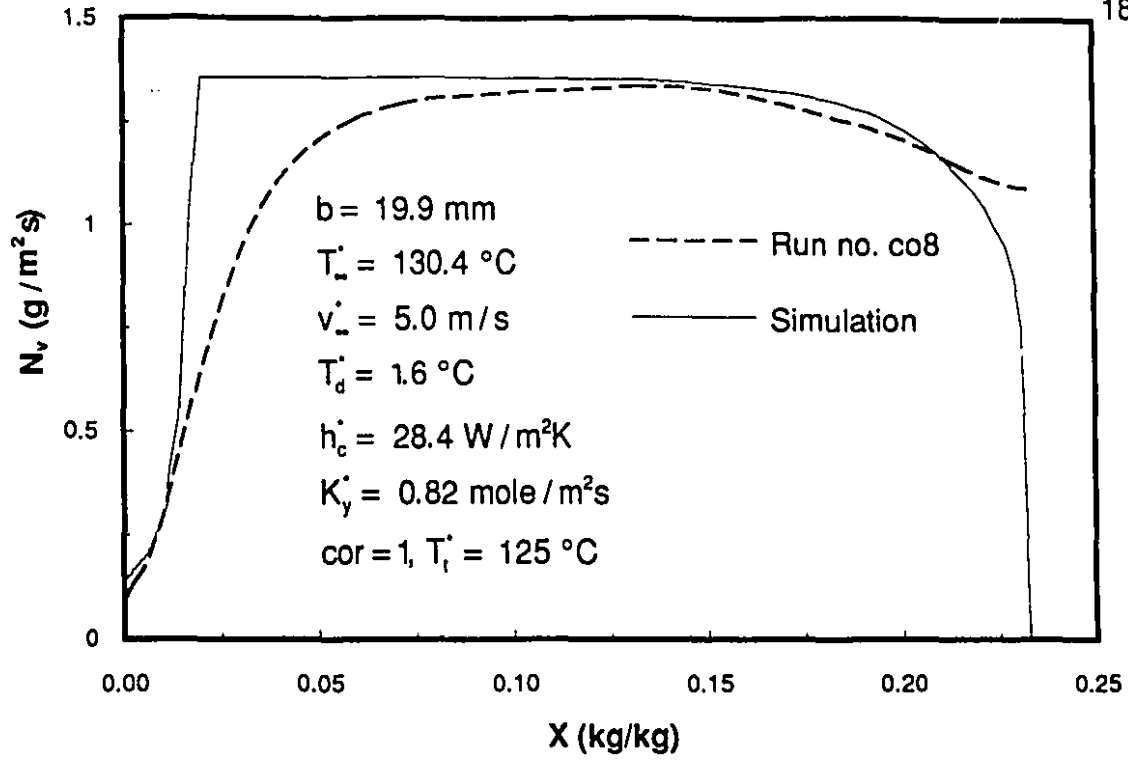


Figure 6.13a The drying rate curve for run no. co8

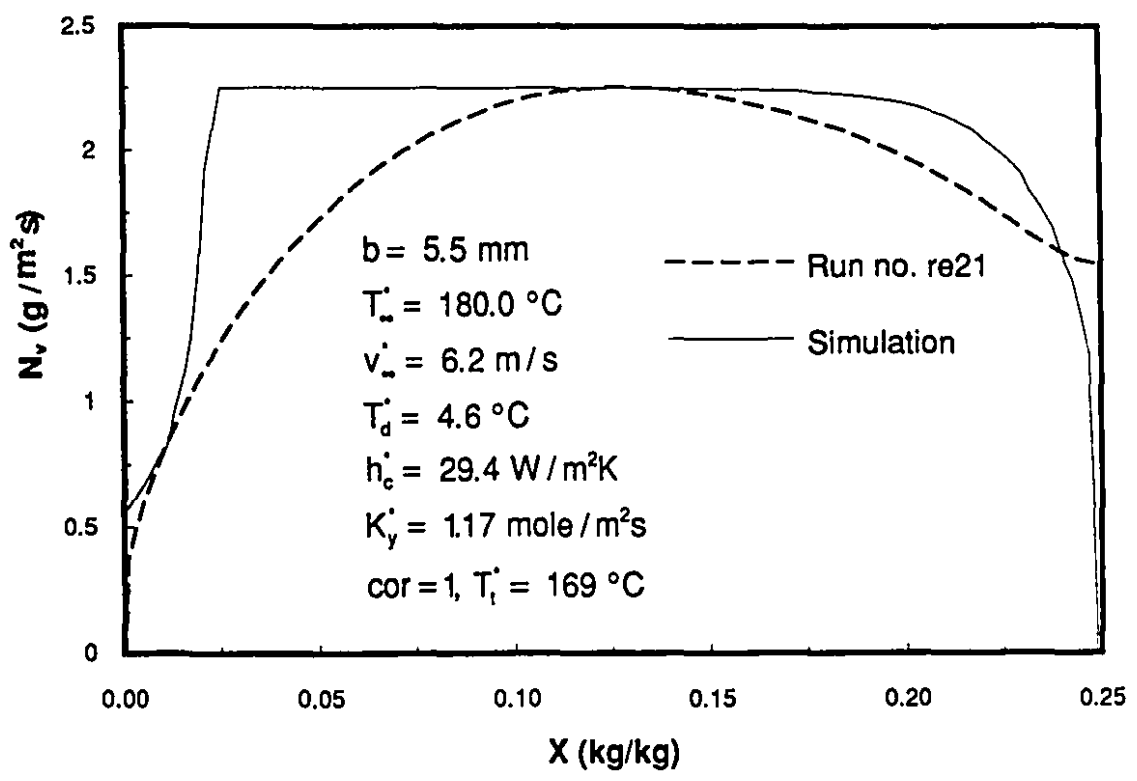


Figure 6.13b The drying rate curve for run no. re21

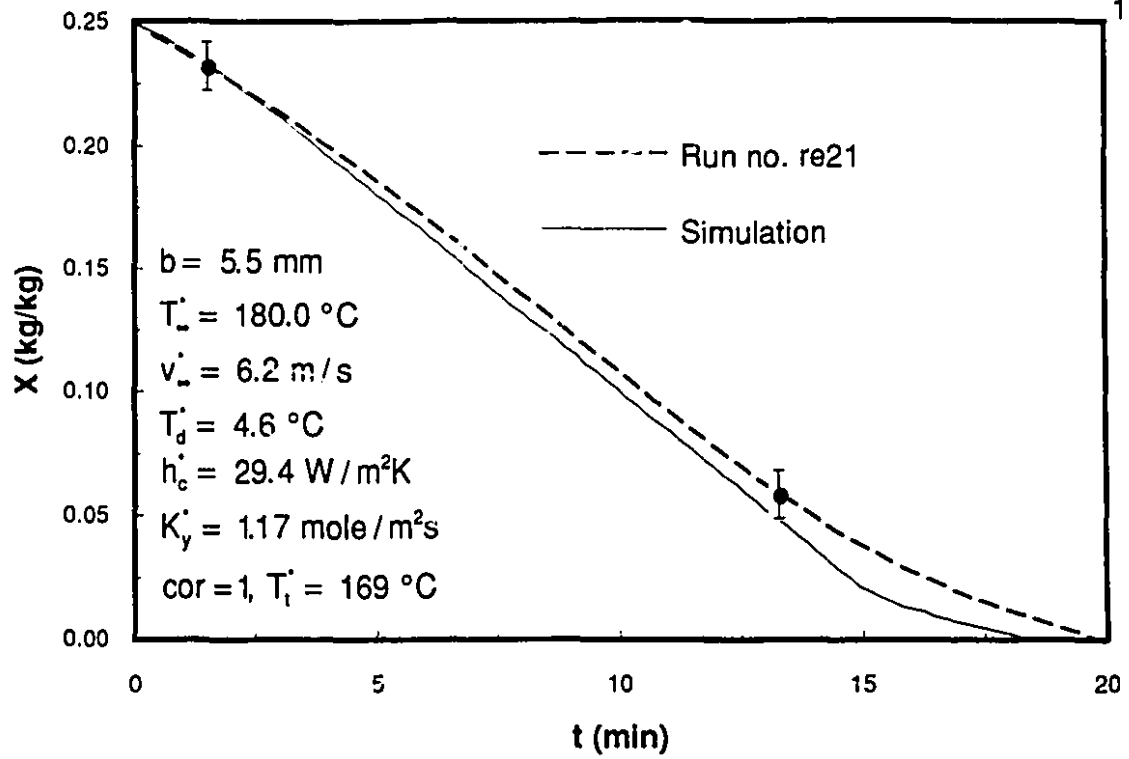


Figure 6.14a The drying curve for run no. re21

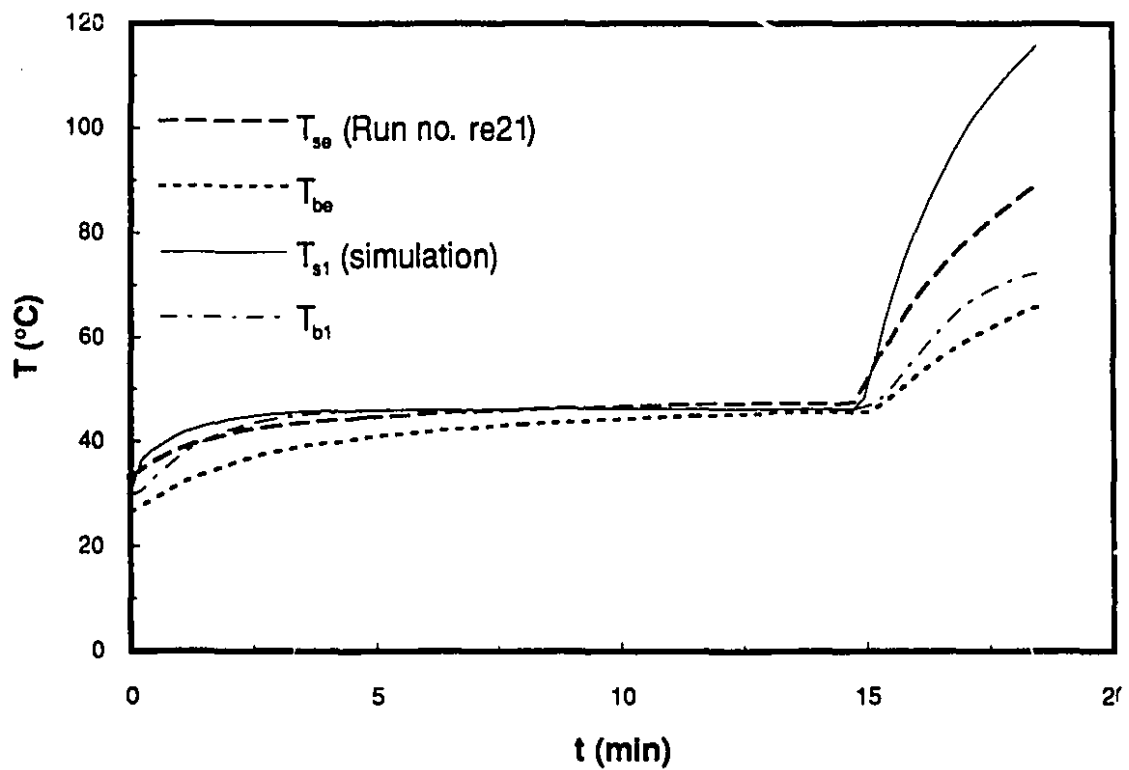


Figure 6.14b The surface and bottom temperatures for run no. re21

All the experimental N_v vs. X curves presented show no extensive constant drying rate period in agreement with the doubts raised by Keey (1972) and van Brakel (1980) about the systematic representation of "strict" constant drying rate periods even for the case of a capillary porous medium. In Figures 6.11b and 6.12b, T_s is slightly lower than T_b at the end of the P.C.D.R.P.; this indicates that two-dimensional heat transfer effects affect at least partially the shape of the drying rate curve. Since during the experiments, the data acquisition was not started as soon as the sample was introduced in the test section and as the surface temperature is underestimated when temperature gradients are present, the experimental drying rate is higher than the simulated one at the beginning of drying.

The comparison of the experimental results from runs no. re18, co4, co7 co8, co11, re21 and re6 with the drying front model (Dostie, 1991) predictions demonstrate its ability (in the parameter range investigated) to evaluate satisfactorily:

- a) The drying curve (X vs. t) and t_0 ;
- b) The T_b vs. t curve and T_s level at the end of drying. The experimental bias on the T_s measurement did not allowed us to verify directly the drying front prediction of the T_s vs. t curve when $X < X_c$;
- c) The overall behavior of N_v on the drying rate curve is rather well reproduced.

6.7 COMBINED CONVECTIVE AND I.R. DRYING SIMULATIONS

6.7.1 THE SURFACE TEMPERATURE MEASUREMENT BIAS IN THE COMBINED CONVECTIVE-I.R. DRYING PROCESS

In order to quantify the effect of the surface thermocouple on the T_s measurement in case of combined convective-I.R. drying, the same study as in 6.6.2 was carried out. However, here the already defined temperatures are presented as a function of the absorbed (q_{ab}) heat flux at the surface.

In FLUX2D, q_{ab} was specified through variation of h^* and T_∞^* while for T_{be} , T_{b1} , T_{se} , T_{s1} , it was evaluated from an energy balance at the surface with T_{s1} as the surface temperature.

Figure 6.15 displays T_{be} , T_{b1} , T_{se} , T_{s1} , T_{c2D} and T_{s2D} . It is observed that:

- a) T_{be} and T_{b1} are close for the 5.5 and 10.3 mm samples;
- b) T_{se} and T_{s1} increase almost linearly with q_{ab} . The same phenomenon occurs for T_{s2D} and T_{c2D} ;
- c) For a given q_{ab} , the difference between T_{se} and T_{s1} is comparable to the difference between T_{s2D} and T_{c2D} especially if one account for the unknown additional thermal contact resistance between the thermocouple and the beads as well as the uncertainty on the exact location of the thermocouple measuring point;
- d) T_{s2D} is greater than T_{s1} which is not the solution, at the surface, of the steady state two dimensional temperature field (within the sample) since the rate of variation of T_{s1} as a function of time is probably too high (see T vs. t curves).

Although temperature gradients exist during the P.C.D.R.P. of the combined convective-I.R. drying runs, the much higher bed thermal conductivity ($k \sim 1.2$ - 1.6 W/mK) and lower temperature gradients ($T_{se}-T_{be} \sim 20$ °C) do limit the fin effect (between 2 to 4 °C) on the T_s measurement. A significant fraction of the difference between T_{se} and T_{s1} might also be due to possible variations of E_s with the surface moisture content. Such effect on E_s has been quantified by Navarri (1991) for sea sand ($d = 200$ - 250 μ m); E_s was 0.77, from an energy balance during the constant drying rate period while it was 0.55, from an energy balance with dry sand on a controlled heat sink.

It can be concluded that the drying front model (h_c^* , K_y^* , $cor = 1$, q_{is}^*) predicts T_b quite well at the end of drying for most of the combined convective and I.R. drying runs.

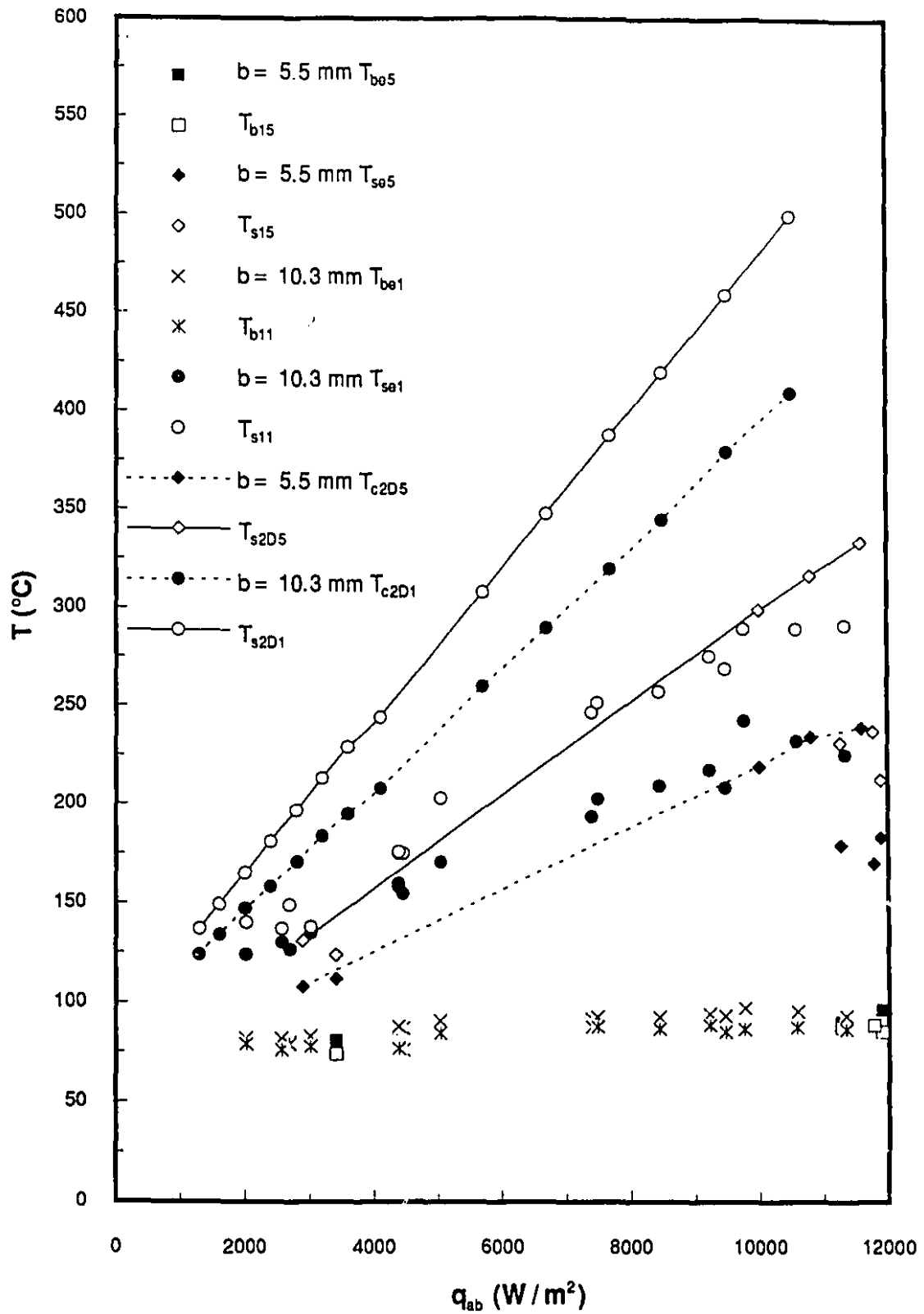


Figure 6.15 An evaluation of the experimental surface temperature measurement bias for the combined convective and IR. drying runs

6.7.2 THE DRYING FRONT POSITION CORRECTION EFFECT IN THE COMBINED CONVECTIVE-I.R. DRYING PROCESS

The effect of the correction to the drying front position for the combined convective-I.R. drying runs is quantified in Table 6.3 where the run identification number, T_{∞}^* , q_{is}^* , t_{oe} , t_{o1} , $\Delta t_{o1}\%$, t_{o0} , $\Delta t_{o0}\%$, T_{be} , T_{b1} , T_{b0} , T_{s1} and T_{s0} are reported. t_{oe} , t_{o1} and t_{o0} are the experimental and predicted overall drying times with the drying front model (h_c^* , K_y^* , q_{is}^*) when $cor=1$ or 0 respectively. These data show that:

- a) The average differences between the experimental and predicted t_o are 2.9 % ($cor = 1$, standard deviation = 3.6 %) and 0.3 % ($cor = 0$, standard deviation = 3.9 %); thus on the average t_o is slightly underpredicted when the drying front correction is applied; the prediction is closer without correction;
- b) T_{be} is, for most cases, closer to T_{b0} than to T_{b1} ($T_{b1} \leq T_{b0} \leq T_{be}$). This suggests that the diffusion resistance of the dried layer is adequately taken into account when no drying front correction is applied;
- c) The differences between T_{s1} and T_{s0} are low considering the temperature level reached.

While t_o is predicted equally well when cor is equal to 1 or 0, the improved prediction of T_b at the end of drying suggests that it might not be justified to apply the drying front position correction to evaluate the mass transfer resistance. Figures 6.16 (6.17a) and 6.18 (6.17b) present comparison between the experimental results (Run no. ir1 and ir4 respectively) and simulations with and without drying front correction (h_c^* or h_{cp}^* , K_y^* , $cor = 0$ or 1 , q_{is}^*) for the X vs. t , T vs. t and N_v vs. X . The simulated X vs. t curves (Figures 6.16a and 6.18a) are within $\pm 4\%$ (with respect to X_{in}) of the experimental one.

TABLE 6.3

MEASURED AND SIMULATED DRYING TIMES AND BOTTOM
TEMPERATURES AT THE END OF DRYING WITH AND
WITHOUT DRYING FRONT CORRECTION FOR
COMBINED CONVECTIVE AND I.R. DRYING

Run No.	T_{∞}^*	q_{is}^*	t_{oe}	t_{o1}	$\Delta t_{o1}\%$	t_{o0}	$\Delta t_{o0}\%$	T_{be}	T_{b1}	T_{b0}	T_{s1}	T_{s0}
(.)	(°C)	(°C)	min.	min.	(.)	min.	(.)	(°C)	(°C)	(°C)	(°C)	(°C)
ir17	79.2	6810	20.3	18.4	-9.8	18.8	-8.1	81	74	78	124	129
ir18	86.1	20340	7.7	6.9	-11.0	7.1	-8.6	97	86	91	213	221
i85h	145.0	20740	6.7	6.6	-1.5	6.7	0.0	89	89	93	238	253
i83h	141.7	20770	6.7	6.7	0.0	6.9	2.9	91	88	93	232	242
ir2	81.1	12110	22.4	22.1	-1.3	22.8	1.8	91	85	89	203	210
ir3	83.1	16980	17.0	16.3	-4.2	16.8	-1.2	92	88	93	247	256
ir1	80.0	6930	35.5	36.0	1.4	37.2	4.6	80	79	83	149	153
ir5	79.9	6890	36.2	36.1	-0.3	36.7	1.4	83	78	80	138	141
ir7	79.8	6860	35.5	35.5	0.0	36.7	3.3	82	76	80	137	141
ir9	79.8	6840	36.7	36.9	0.5	38.4	4.5	82	79	82	140	143
ir4	86.7	20520	14.0	13.6	-2.9	14.1	0.7	95	89	94	276	286
ir6	85.6	20510	14.7	13.3	-10.0	13.8	-6.6	94	86	91	270	281
ir8	83.0	20490	13.7	13.6	-0.7	14.0	2.2	93	87	92	258	267
ir10	83.7	20510	14.0	13.7	-2.2	14.3	2.1	93	88	93	252	259
ir11	180.0	7660	24.7	24.0	-2.9	24.6	-0.4	87	77	83	175	182
ir13	180.0	7710	22.9	21.8	-4.9	22.4	-2.3	87	76	82	175	182
ir15	179.8	7660	22.4	21.7	-3.2	22.8	1.8	88	77	83	176	183
ir12	183.3	21370	11.8	11.8	0.0	12.3	4.1	94	87	93	292	303
ir14	181.1	21370	11.6	11.6	0.0	12.0	3.4	96	88	93	290	300
ir16	180.1	21380	12.1	11.6	-4.2	12.1	0.0	98	87	92	290	301
				Av.	-2.9		0.3					
				Stdev.	3.6		3.9					

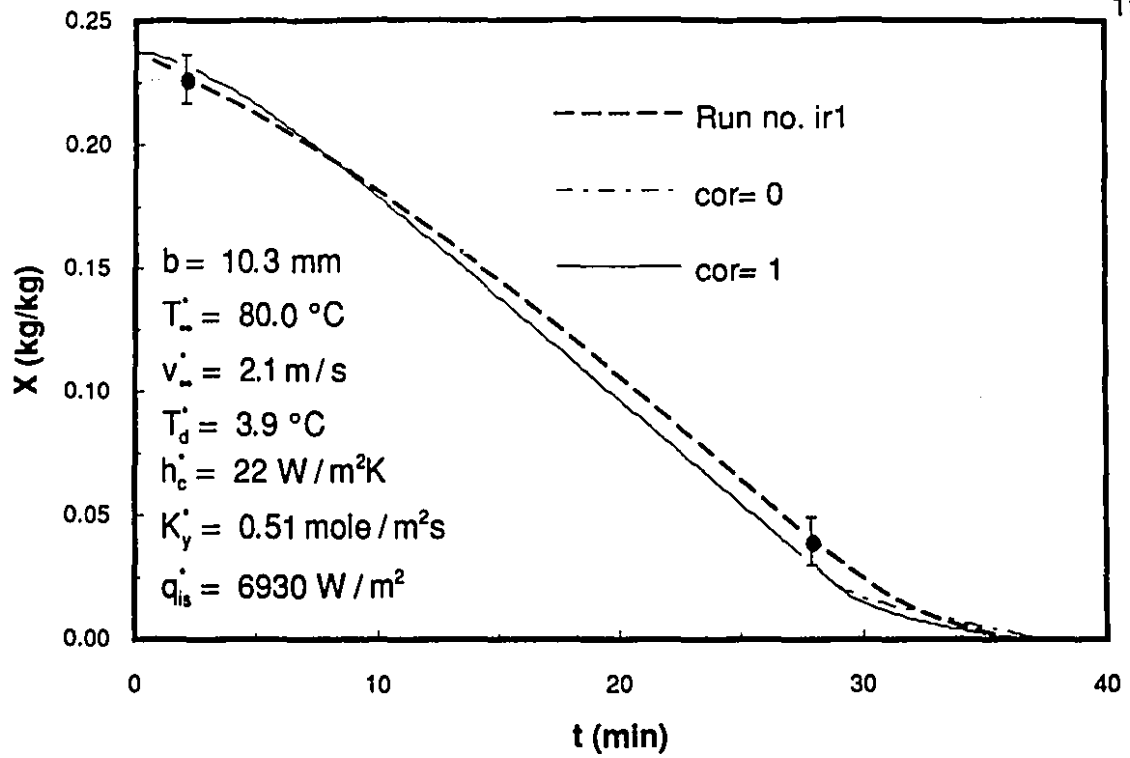


Figure 6.16a The drying curve for run no. ir1: test of the front position correction

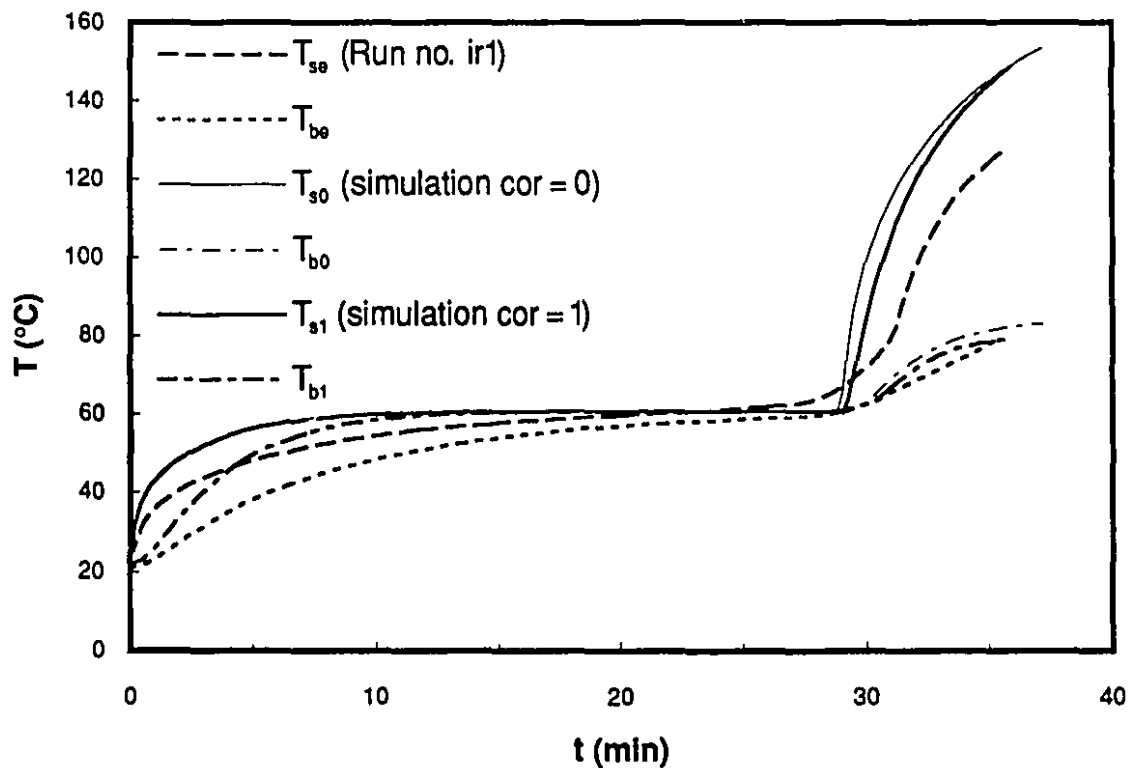


Figure 6.16b The surface and bottom temperatures for run no. ir1: test of the front position correction

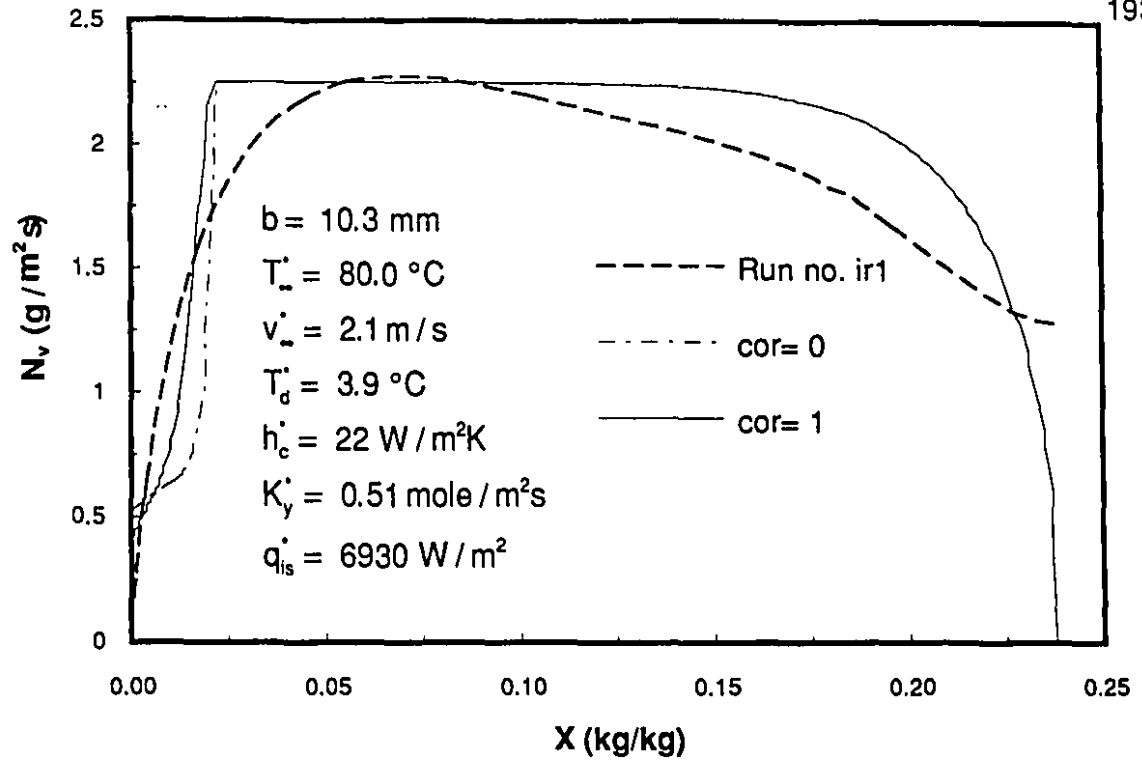


Figure 6.17a The drying rate curve for run no. ir1: test of the front position correction

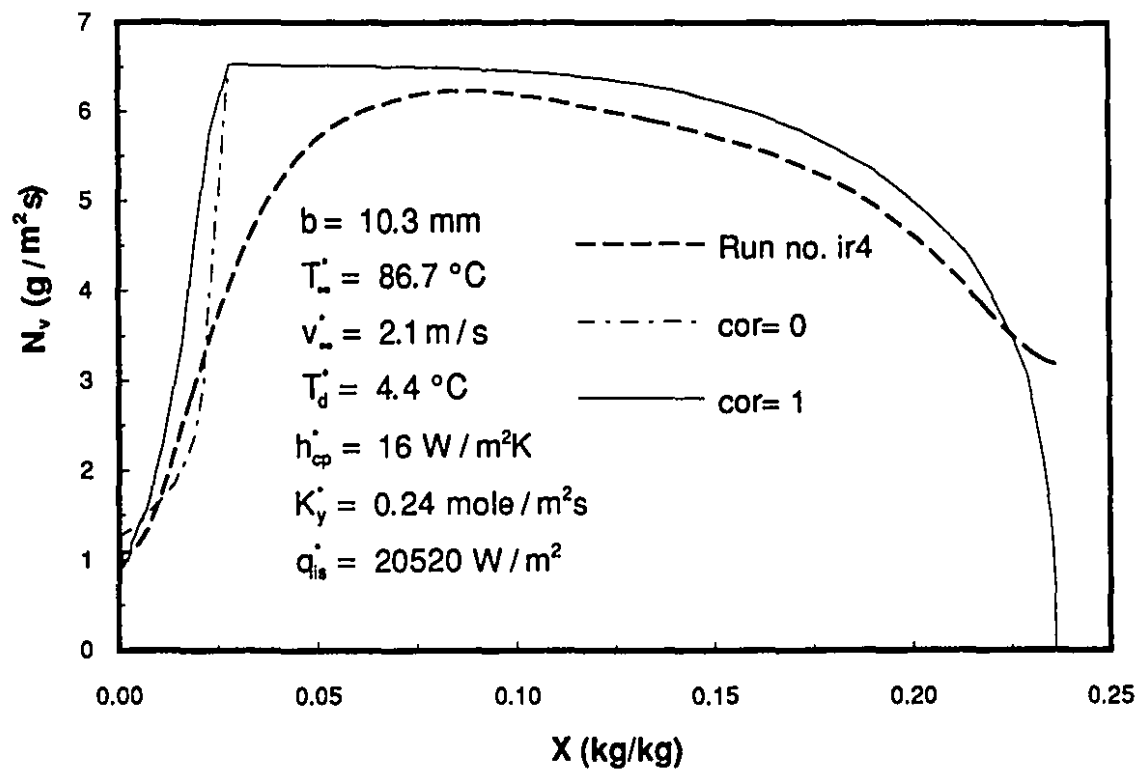


Figure 6.17b The drying rate curve for run no. ir4: test of the front position correction

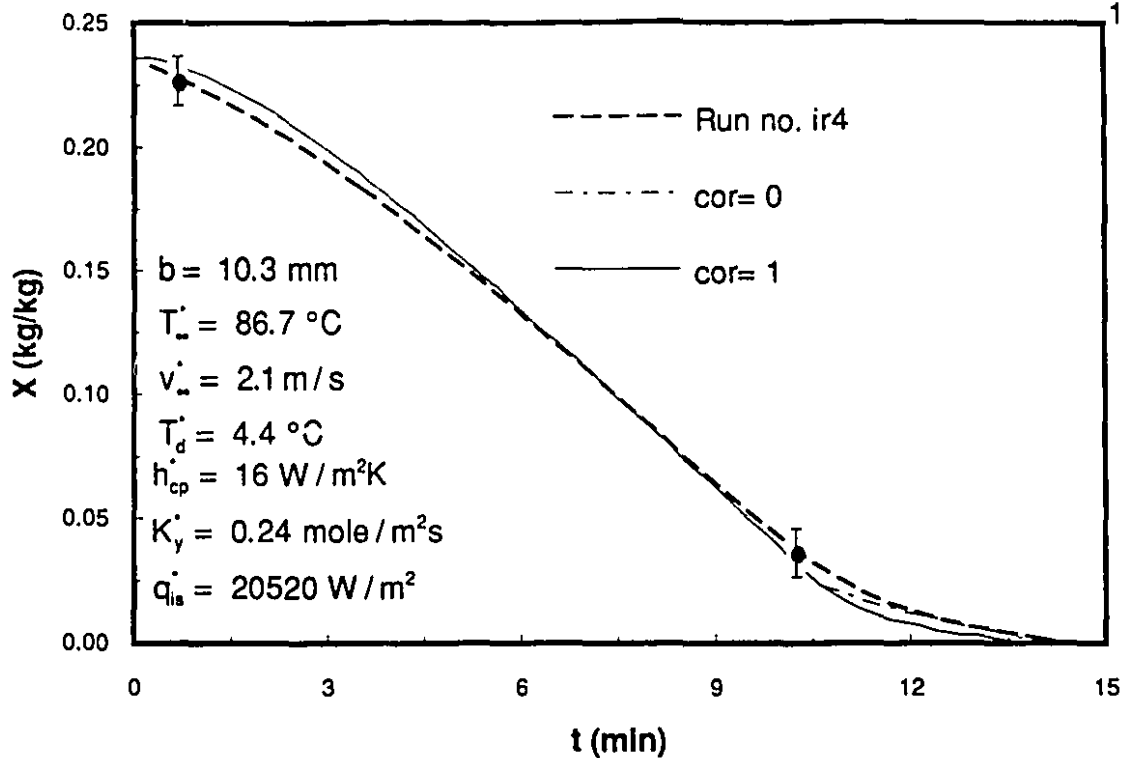


Figure 6.18a The drying curve for run no. ir4: test of the front position correction

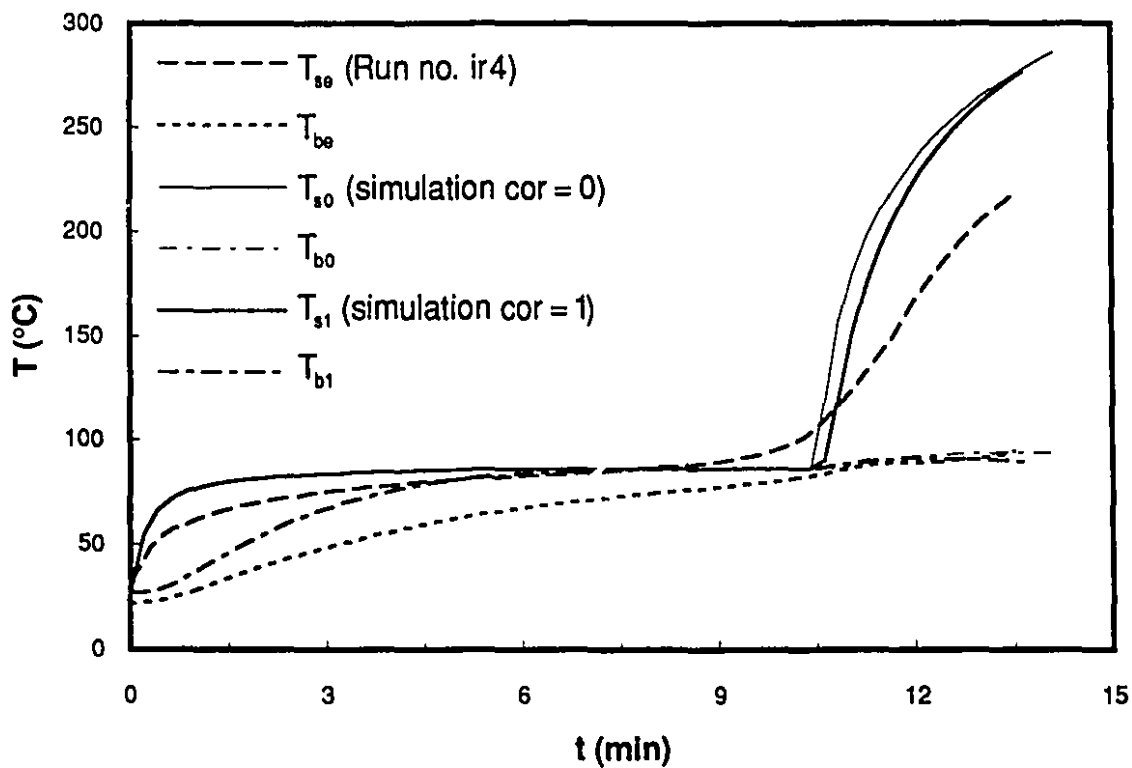


Figure 6.18b The surface and bottom temperatures for run no. ir4: test of the front position correction

For $t < t_c$, the simulated T_s and T_b vs. t curves are higher than the experimental ones though the difference decreases as t get closer to t_c . For T_s , a fraction of this difference is due to the bias discussed in 6.7.2 and 3.8.2. For $t > t_c$, T_{se} is biased while simulated T_b are higher than T_{be} by a maximum of 6 °C.

The simulation with no drying front position correction ($cor = 0$) predict a more abrupt fall of N_v (Figures 6.17a and b), as compared to the one with drying front position correction ($cor = 1$). The highest rate (~ 4 %) observed with the numerical results (Run no. ir4) is a mainly a consequence of using h_{cp}^* determined with h_{cc}^* and the boundary layer theory. However, both simulations ($cor = 0$ or 1) approximate quite well the overall behavior of the N_v vs. X curve.

6.7.3 THE TRANSFER COEFFICIENTS CORRECTION AND THE DRYING FRONT MODEL RESULTS IN THE COMBINED CONVECTIVE-I.R. DRYING PROCESS

An upper bound on the effect of the transfer coefficient correction procedure on the combined process is provided by run no. ir15 for which the convective heat transfer represents about 40 % of the overall heat transfer to the sample during the P.C.D.R.P..

Figures 6.19 (a,b) and 6.20a show a comparison between the experimental results (Run no. ir15) and simulations with and without correction of the transfer coefficient (h_{cBL}^* , K_{yBL}^* , $cor = 1$, q_{is}^*) for X vs. t , T vs. t and N_v vs. X , respectively. It is observed that the drying curve (Figure 6.19a) is predicted within experimental uncertainty when the transfer coefficient are varied; this is linked to a more accurate prediction of the T_s (Figure 6.19b) level during the P.C.D.R.P. (when K_{yBL}^* is not corrected, T_s^* is smaller by 4 °C). When h_{cBL}^* and K_{yBL}^* are kept constant, X_c is reached earlier which leads to a predicted t_o , 15 % lower than the experimental one (as compared to 3 % lower when h_{cBL}^* and K_{yBL}^* are varied). The reduction of the mass transfer rate as a result of the surface diffusion mass flux represents (within the parameter range investigated) 8 % of the experimental one (Figure 6.20a) during the P.C.D.R.P. in the combined convective-I.R. drying process.

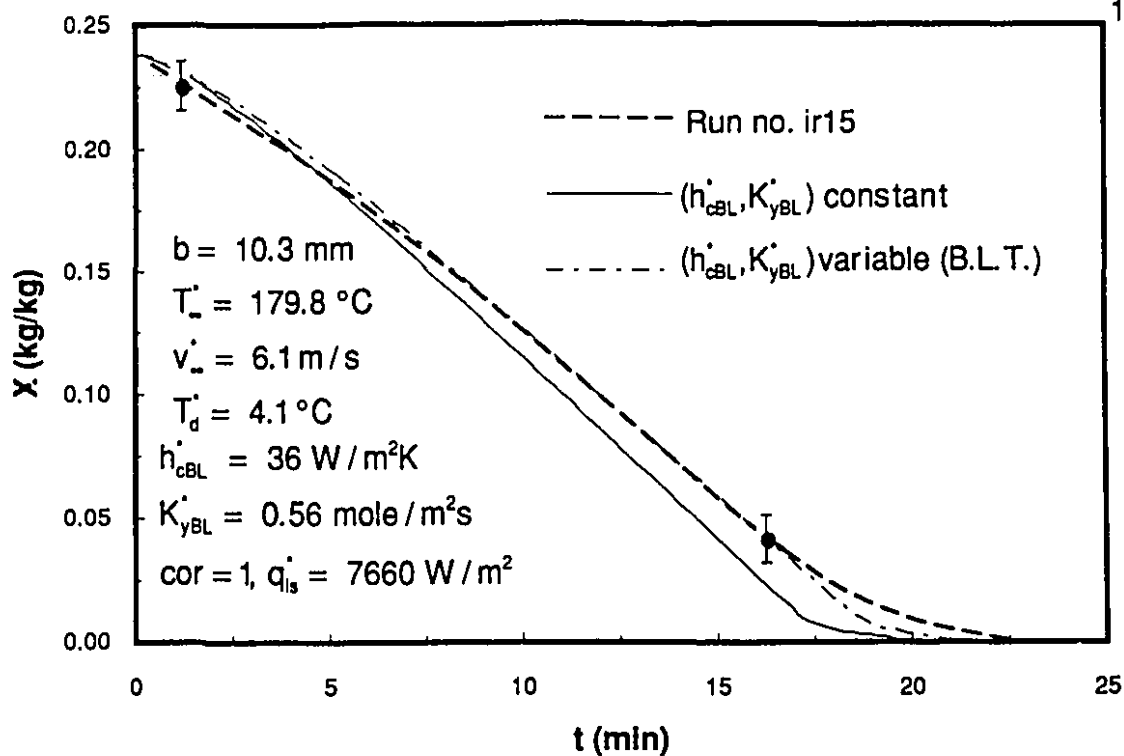


Figure 6.19a The drying curve for run no. ir15: test of the transfer coefficient correction procedure (B.L.T.)

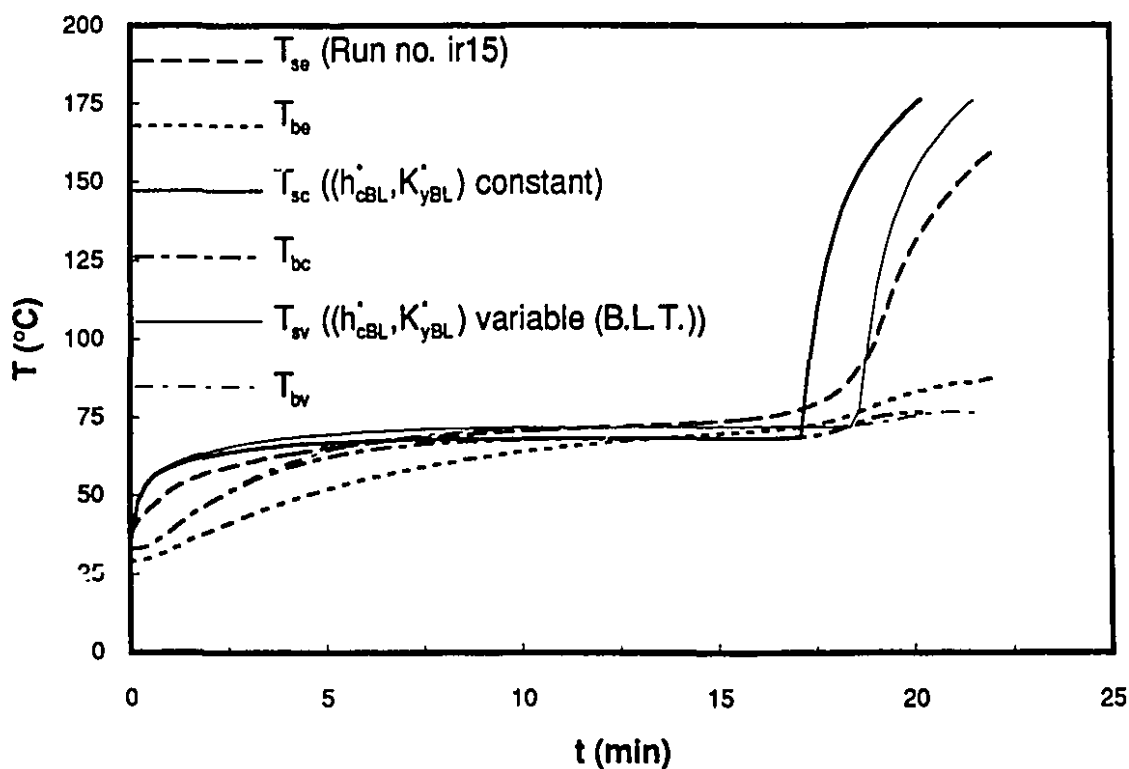


Figure 6.19b The surface and bottom temperatures for run no. ir15: test of the transfer coefficient correction procedure (B.L.T.)

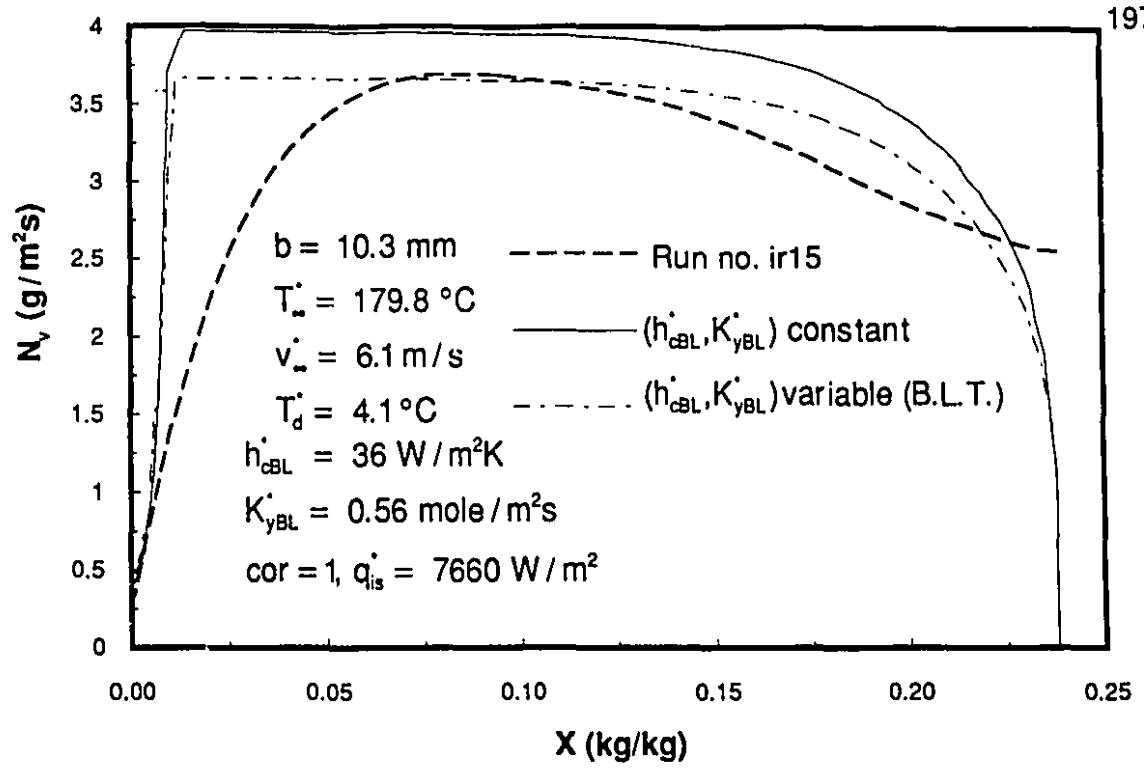


Figure 6.20a The drying rate curve for run no. ir15: test of the transfer coefficient correction procedure (B.L.T.)

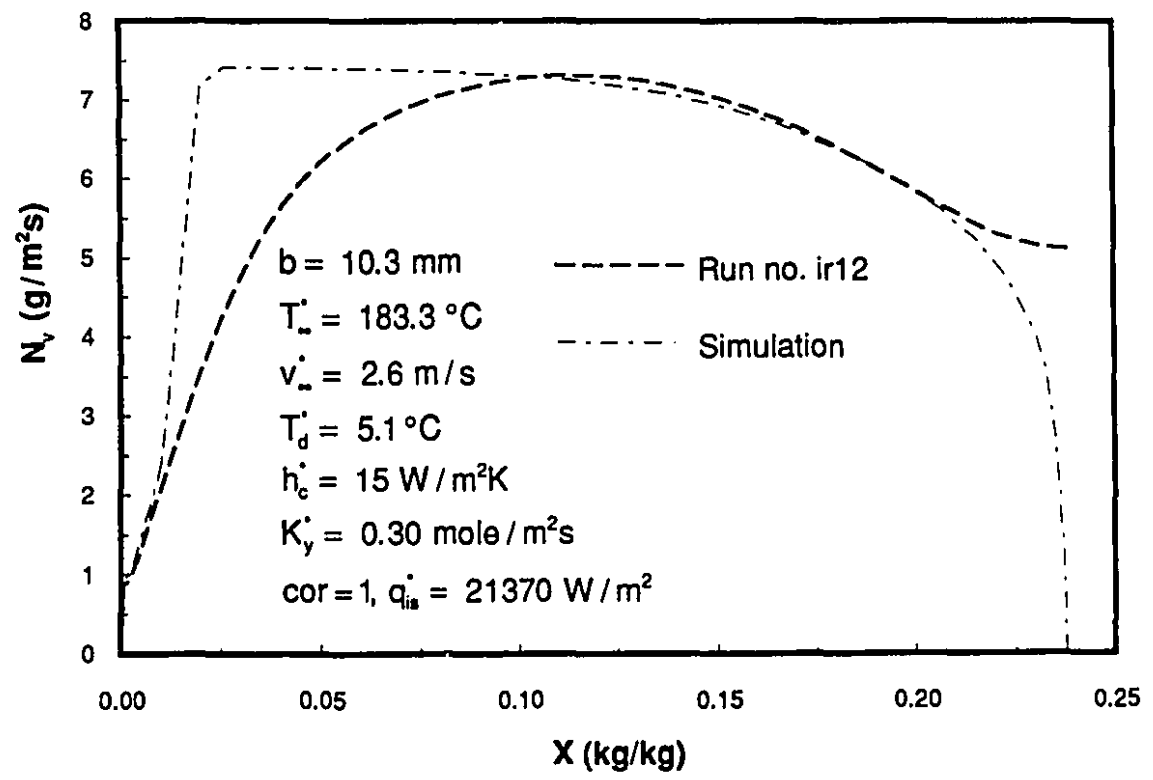


Figure 6.20b The drying rate curve for run no. ir12

6.7.4 COMPARISON BETWEEN EXPERIMENTAL COMBINED CONVECTIVE-I.R. DRYING DATA AND THE DRYING FRONT MODEL PREDICTIONS

Results for X vs. t , T vs. t and N_V vs. X curves from simulations (h_c^* or h_{cp}^* , K_y^* , $cor = 1$, q_{is}^*) for run no. ir12, ir2 and i85h are drawn in Figure 6.21 (6.20b), 6.22 (6.23a) and 6.24 (6.23b) respectively. These runs were chosen to cover the spectrum of parameters for which no detailed data have been previously presented.

Run no. ir12 is a typical case of the highest mass flux recorded. In Figure 6.21a, the differences appearing on the X vs. t curve result from a lower simulated N_V from X_{in} to 0.2 as observed in Figure 6.20b. However, simulated results stays within the experimental uncertainty on the drying curve. The t_c time lag (7 %) in Figure 6.21b has the same origin.

Run no. ir2 represents an intermediate heat flux case ($q_{is}^* = 12110 \text{ W/m}^2$) for which it was not possible to evaluate h_c^* (h_{cp}^* was used). The agreement in Figures 6.22 and 6.23a between the simulations and experimental results is comparable to the one found for the other simulated cases and suggests (see also simulation for run no. ir4) that it is possible to use correlated heat transfer coefficient (h_{cc}^*) corrected for high mass transfer rate effect (h_{cp}^*).

Run no. i85h was carried out with a 5.5 mm sample. The drying rate curve (Figure 6.23b) is similar in shape to the one already presented in Figure 6.13b for the 5.5 mm sample. The drying curve is closely reproduced within less than 4 %.

Results for the X vs. t , T vs. t and N_V vs. X curves from simulations (h_{cBL}^* , K_{yBL}^* , $cor = 1$, $q_{is}^* = 7920$ or 22020 W/m^2) for experiments no. i38h and i76h ($b = 19.9 \text{ mm}$) are drawn in Figures 6.25 (6.26a) and 6.27 (6.26b) respectively. Since in the experiments the surface temperature was controlled to within $\pm 5 \text{ }^\circ\text{C}$ approximately at $140 \text{ }^\circ\text{C}$ (Run no. i38h) and $180 \text{ }^\circ\text{C}$ (Run no. i76h) using the sliding plate (Figure 3.3a), in the simulation q_{is}^* was 0 or q_{is}^* so that the

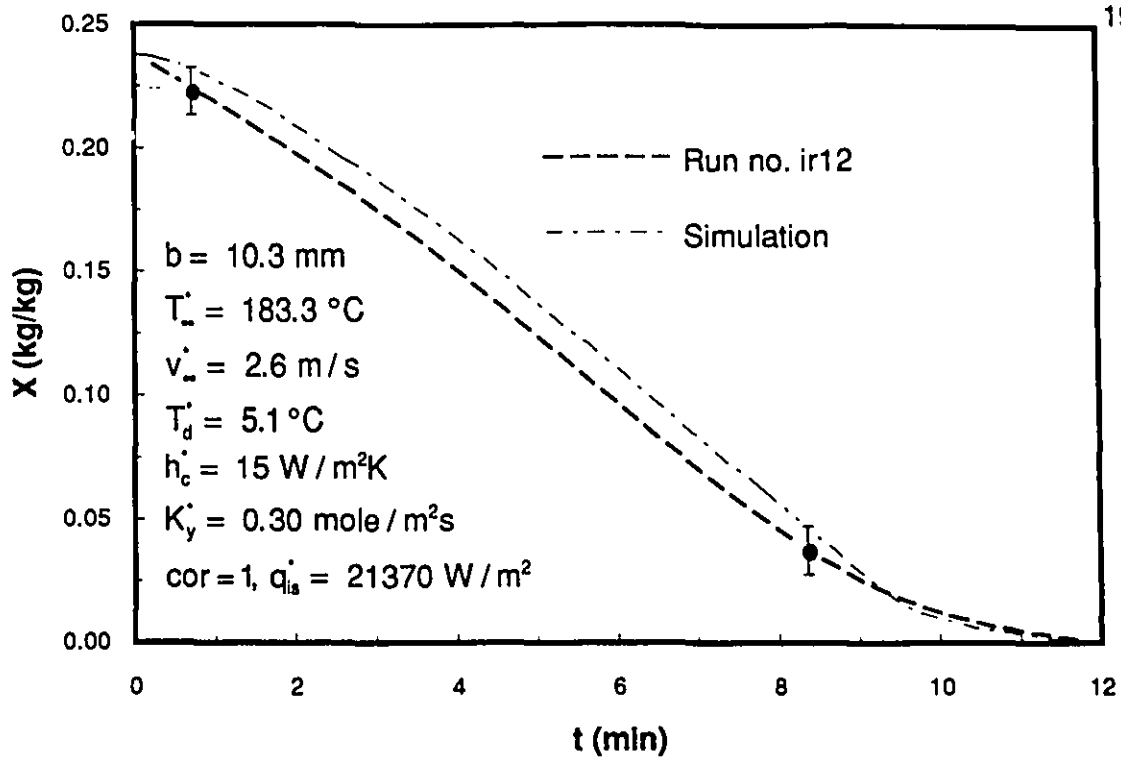


Figure 6.21a The drying curve for run no. ir12

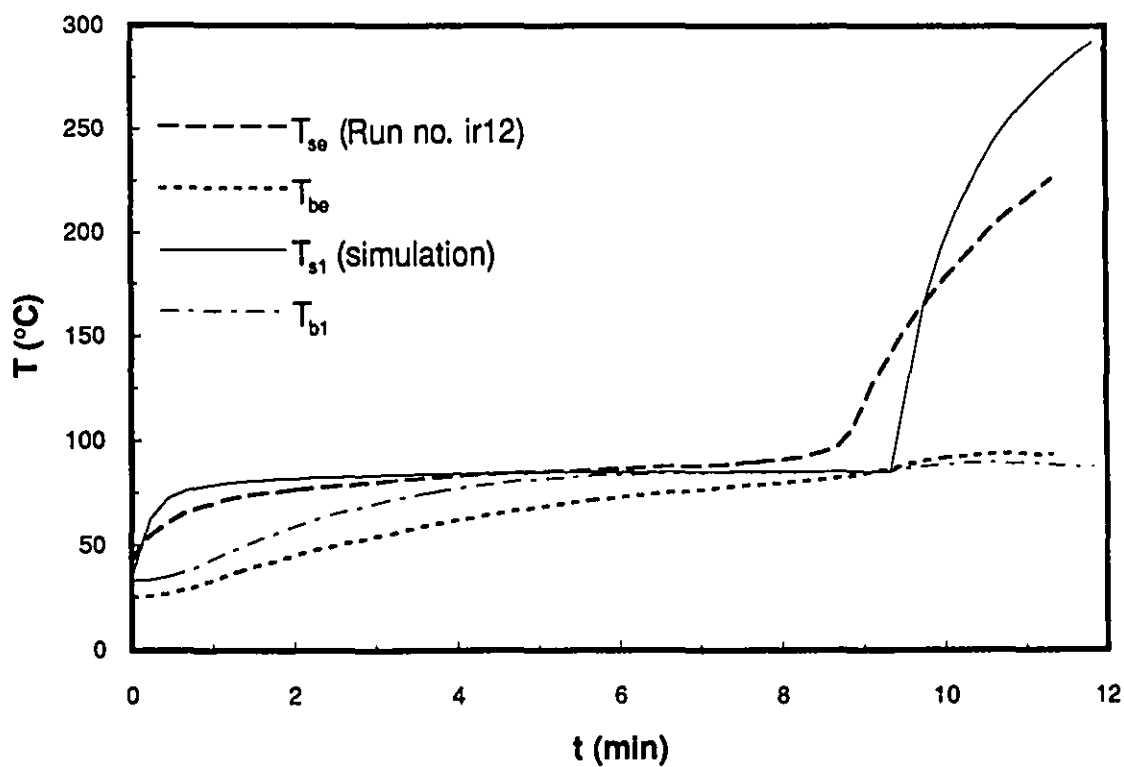


Figure 6.21b The surface and bottom temperatures for run no. ir12

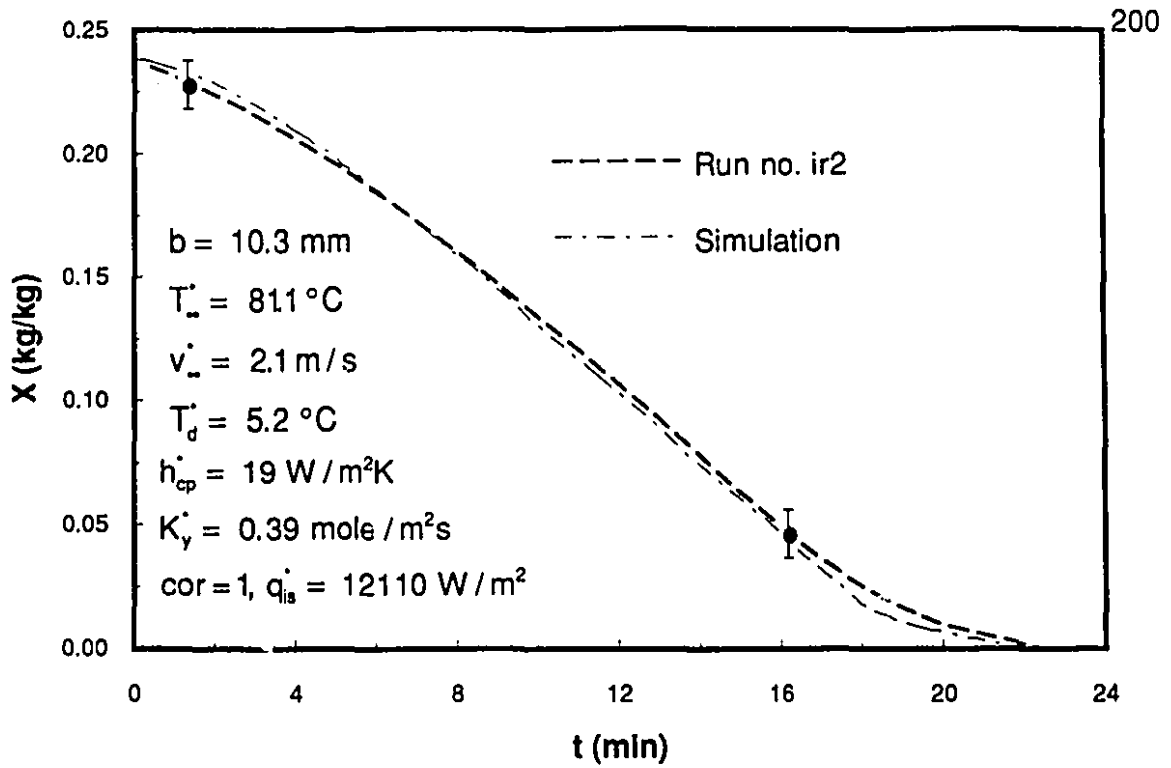


Figure 6.22a The drying curve for run no. ir2

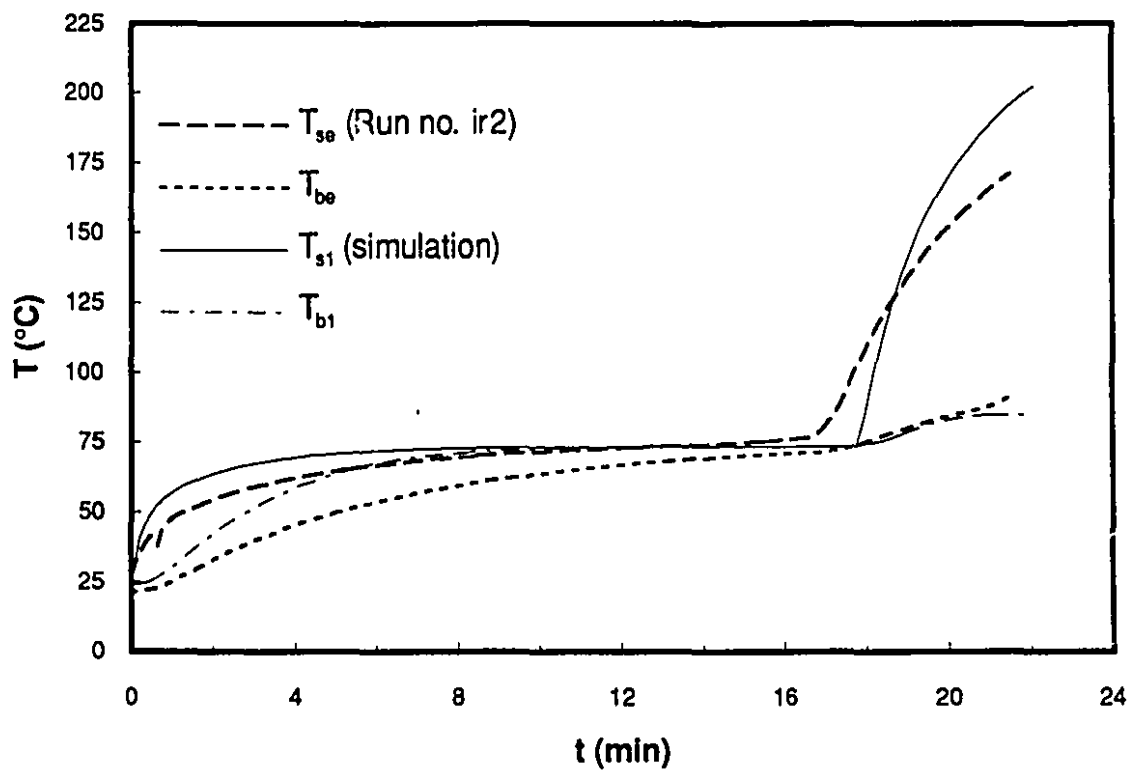


Figure 6.22b The surface and bottom temperatures for run no. ir2

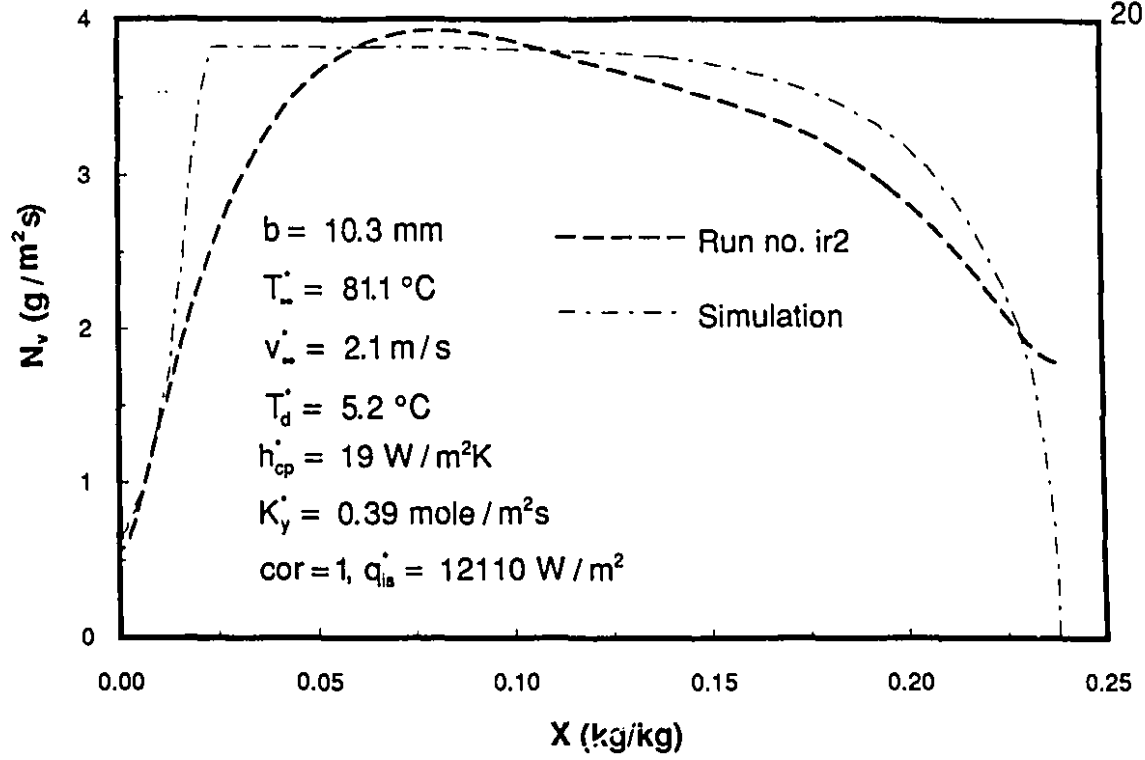


Figure 6.23a The drying rate curve for run no. ir2

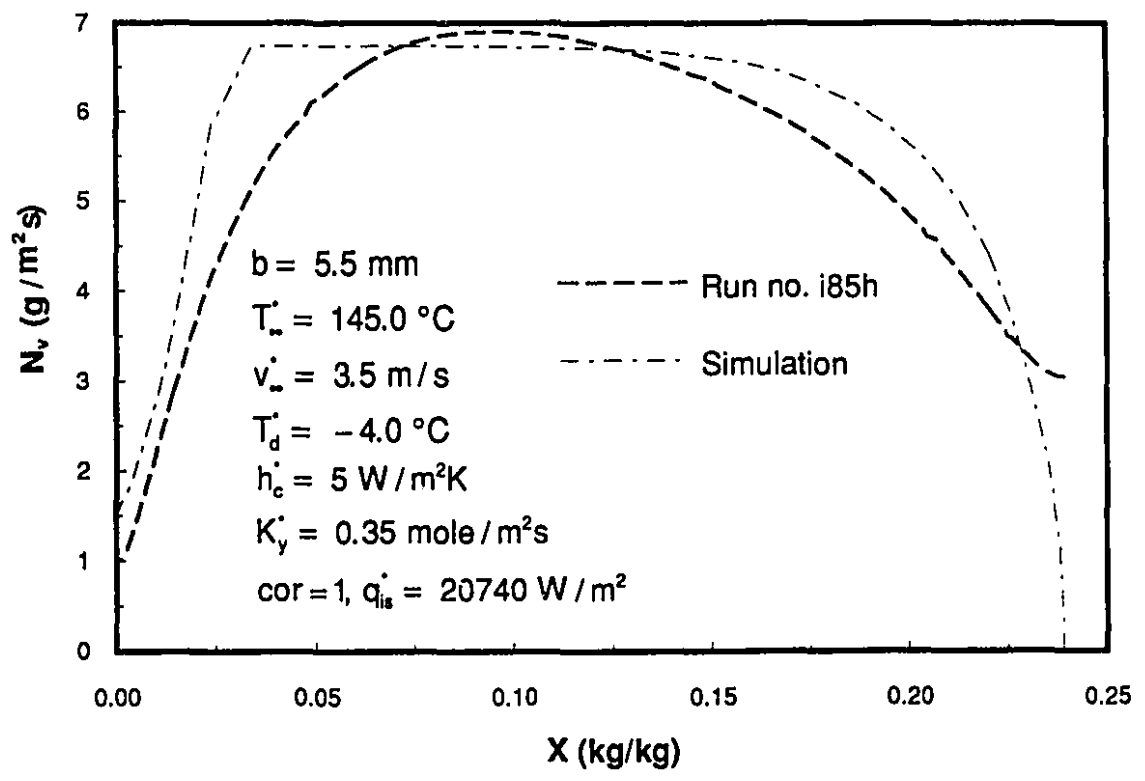


Figure 6.23b The drying rate curve for run no. i85h

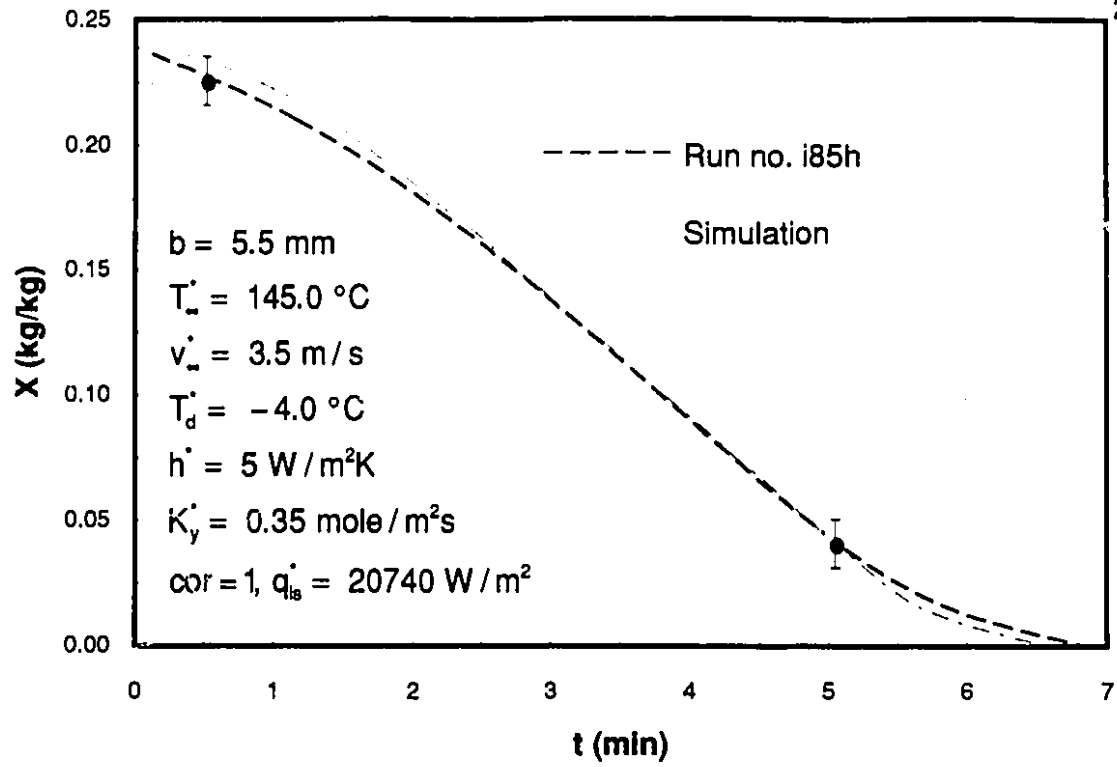
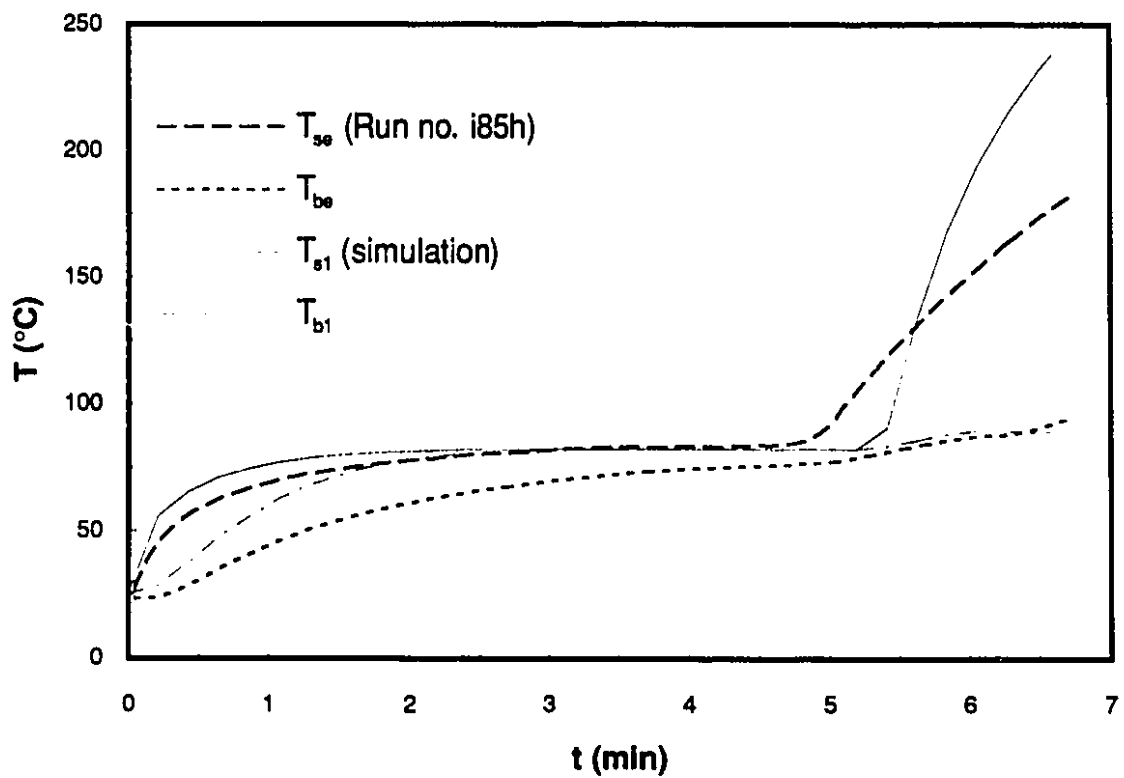


Figure 6.24a The drying curve for run no. i85h



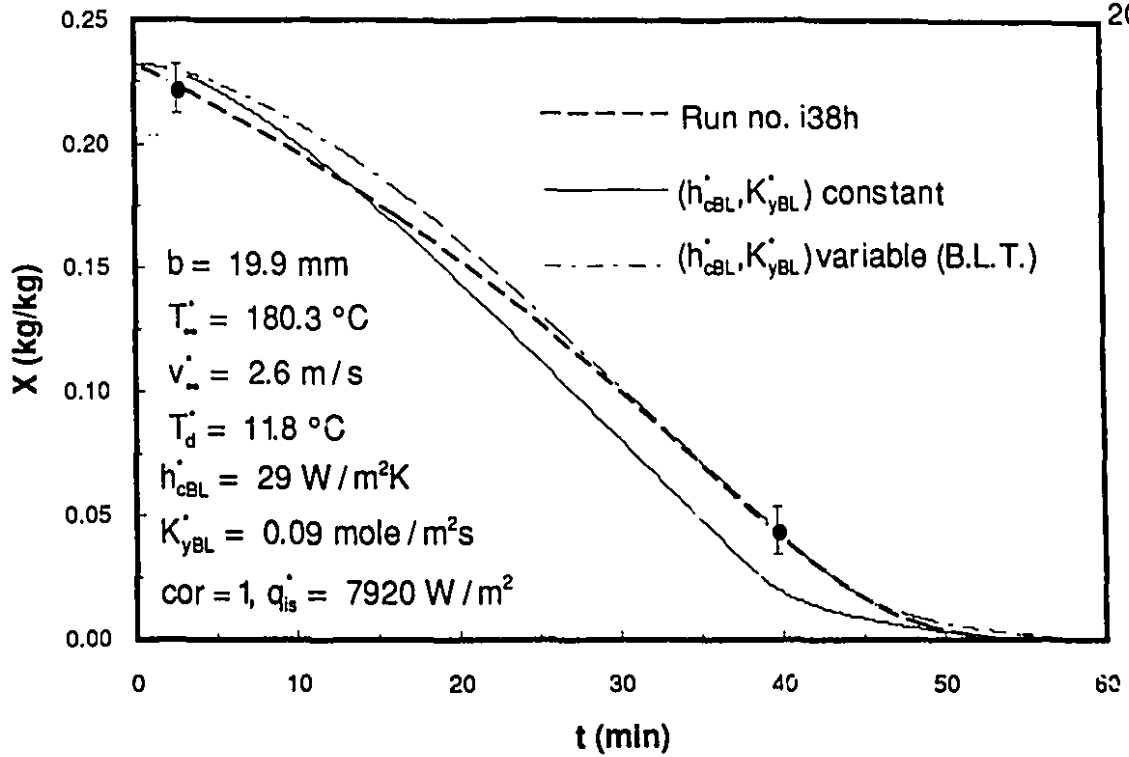


Figure 6.25a The drying curve for run no. i38h: The transition to the boiling point temperature at low radiative heat flux ($q'_{is} = 7920 \text{ W/m}^2$)

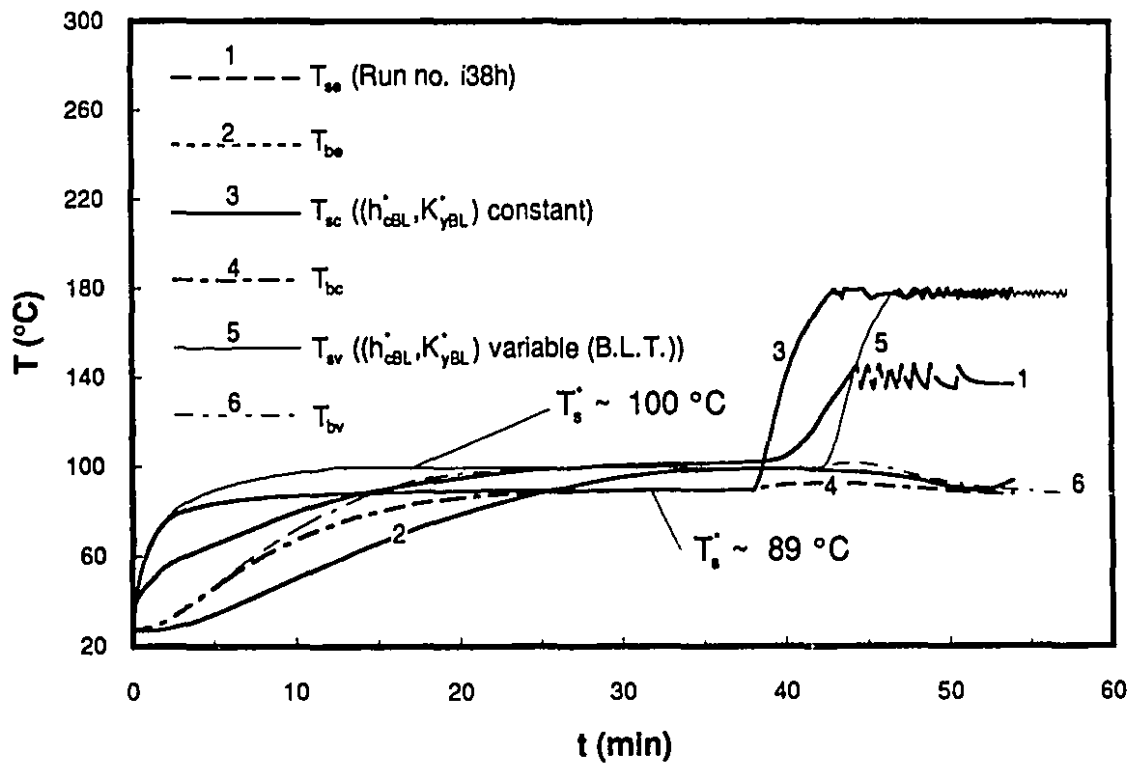


Figure 6.25b The surface and bottom temperatures for run no. i38h: The transition to the boiling point temperature at low radiative heat flux ($q'_{is} = 7920 \text{ W/m}^2$)

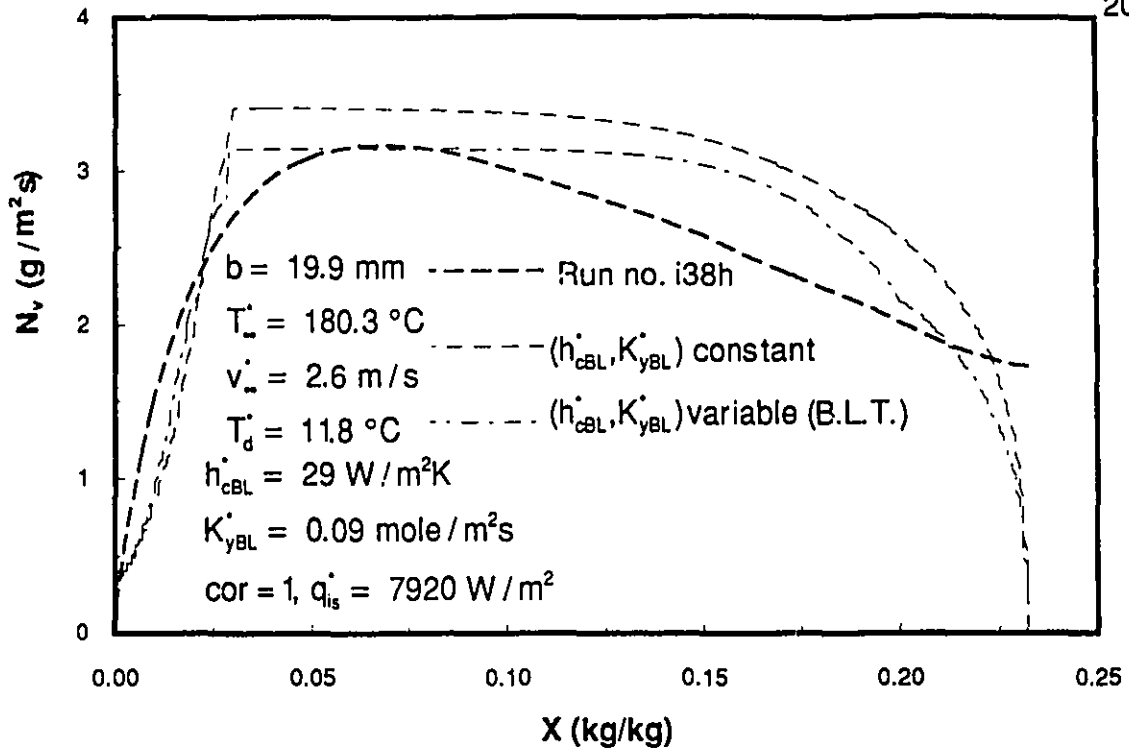


Figure 6.26a The drying rate curve for run no. i38h: The transition to the boiling point temperature at low radiative heat flux ($q_{is} = 7920 \text{ W/m}^2$)

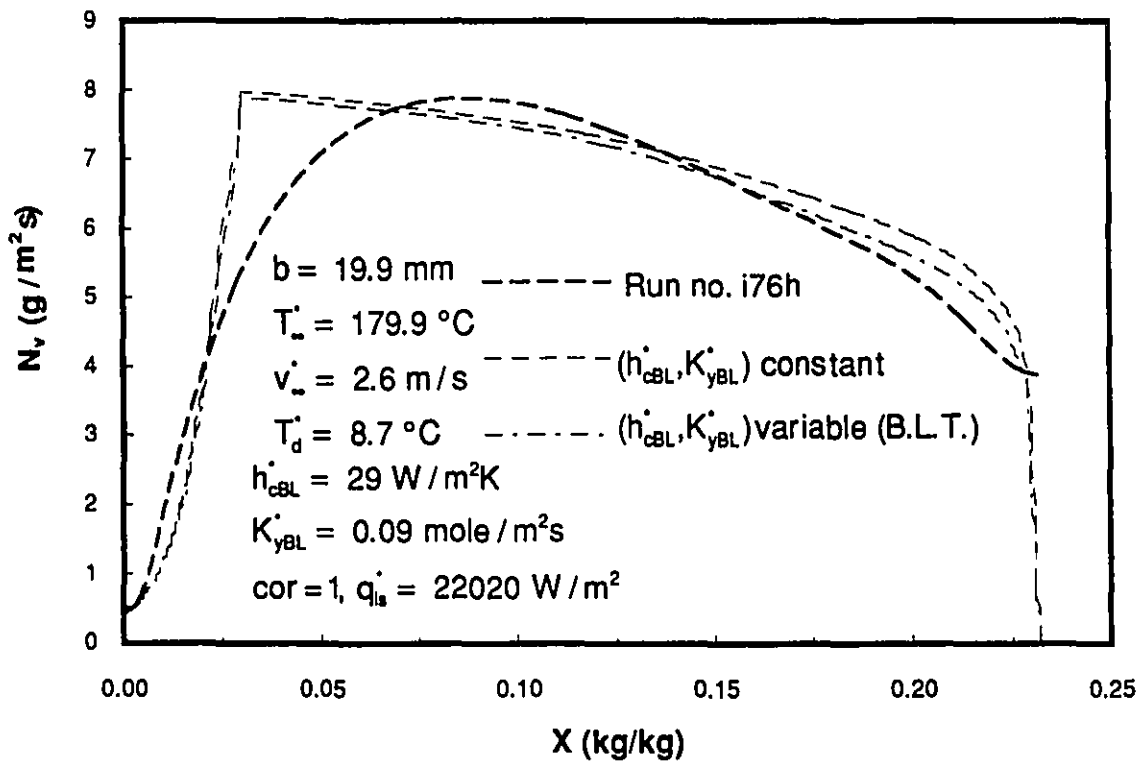


Figure 6.26b The drying rate curve for run no. i76h: The transition to the boiling point temperature at high radiative heat flux ($q_{is} = 22020 \text{ W/m}^2$)

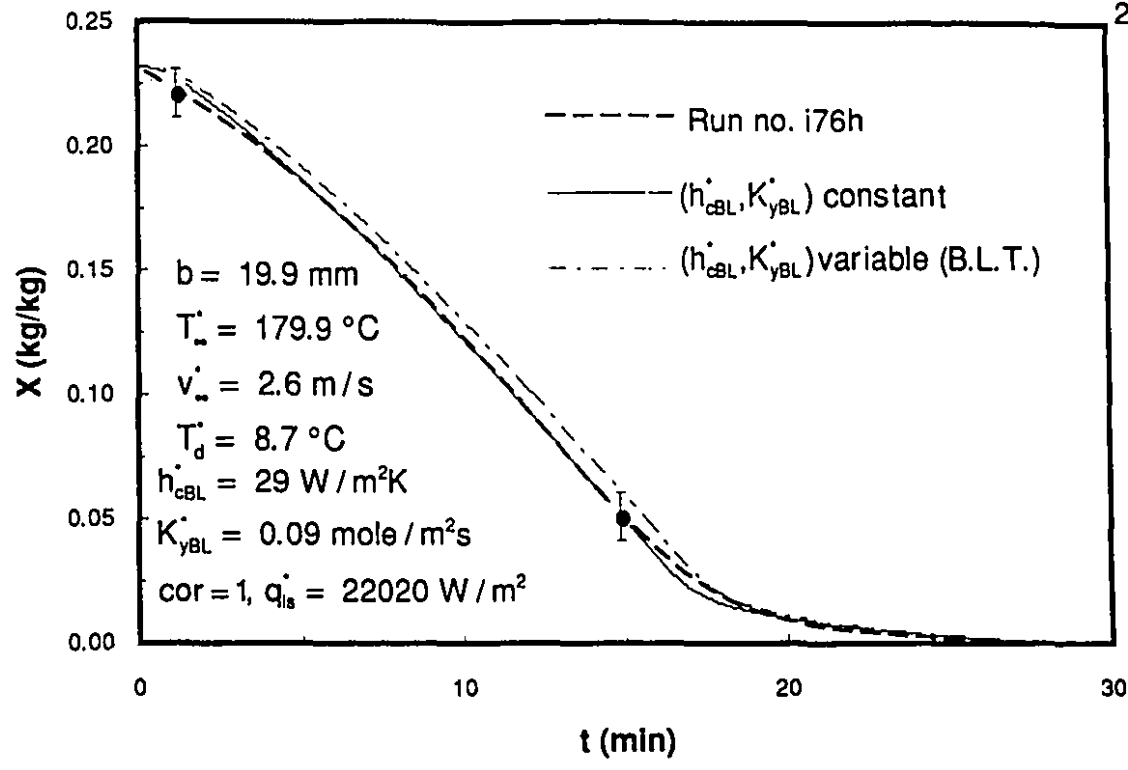


Figure 6.27a The drying curve for run no. i76h: The transition to the boiling point temperature at high radiative heat flux ($q'_{is} = 22020 \text{ W/m}^2$)

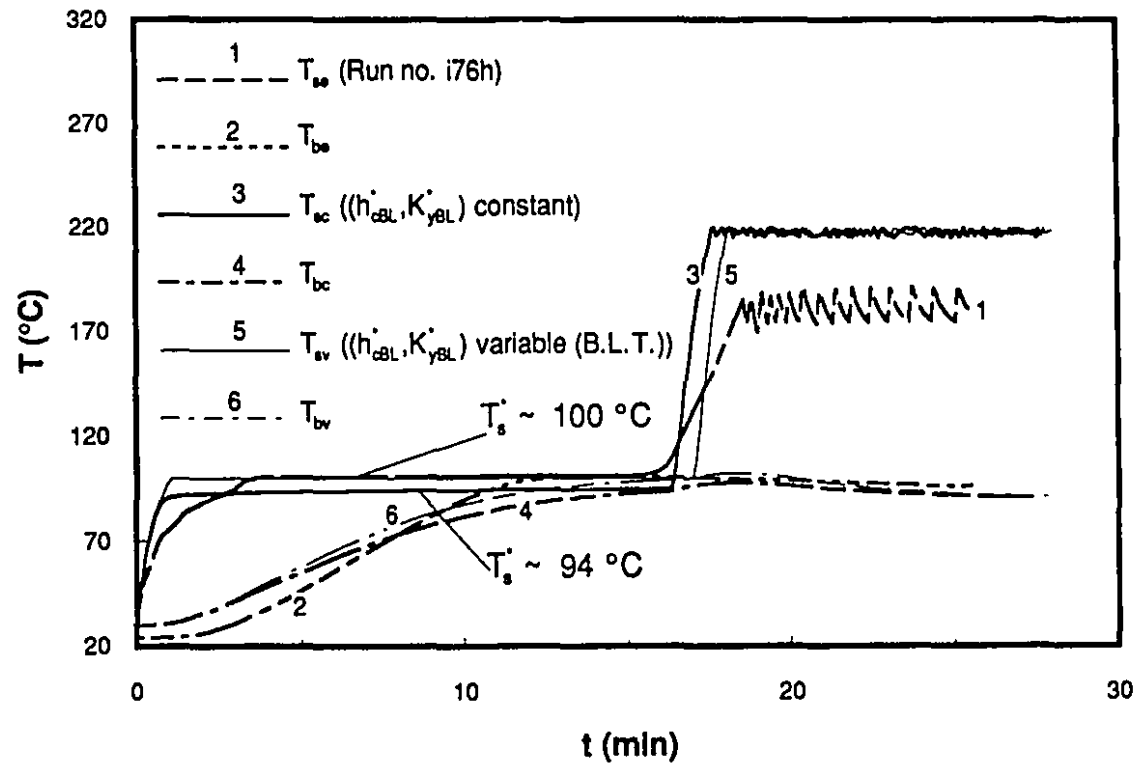


Figure 6.27b The surface and bottom temperatures for run no. i76h: The transition to the boiling point temperature at high radiative heat flux ($q'_{is} = 22020 \text{ W/m}^2$)

surface temperatures were 180 °C and 220 °C (within ± 5 °C) respectively. These higher temperatures were used as they represent more closely the real temperatures existing at the surface when the measured (biased) temperature was chosen for the control during the experiments.

h_{cBL}^* (29 W/m²K) was obtained from the experimental h_c^* (23 W/m²K, Table 5.4b) corrected with the boundary layer theory while K_{yBL}^* (0.09 mole/m²s) is given in Table 5.5 for sample No. XII ($K_{yBL}^* = 0.10$ mole/m²s when H_c is taken into account). Constant and variable h_{cBL}^* and K_{yBL}^* were used in the computation of results presented in these figures.

When the transfer coefficients are kept constant, T_s^* stabilizes to a value lower than the boiling point (89 °C, $q_{is}^* = 7920$ W/m²; 94 °C, $q_{is}^* = 22020$ W/m²). These values are comparable to T_s^* found for run no. i79h (b = 10.3 mm, $T_s^* \sim 85$ °C, $q_{is}^* = 6760$ W/m²) and run no. i80h (b = 10.3 mm, $T_s^* \sim 96$ °C, $q_{is}^* = 20460$ W/m²) in free convection-I.R. drying (Table 5.2) for which it is possible to identify K_y^* to be of the same order as K_{yBL}^* : 0.09 (Run no. i79h) and 0.05 (Run no. i80h).

When the transfer coefficients are varied according to the boundary layer theory predictions, the initially small value of K_{yBL}^* and its lowering lead to an increase of T_s^* up to the boiling point temperature. At this point, in the model bulk flow of vapor at the surface is possible since a convective term is included in equation 6.2. The good quantitative agreement in terms of drying curve and the good qualitative prediction of T_s and T_b evolution with time, at low and high heat fluxes in Figures 6.25 to 6.27 between the experimental and numerical results with variable heat and mass transfer coefficients suggest that the reduction of the mass transfer coefficient constitute an appropriate explanation to clarify why the observed T_s reach the boiling point temperature in case a small equivalent mass transfer coefficient can be identified to link the internal (within the material) and external mass transport.

6.8 CONCLUSIONS

Comparison between the convective as well as combined convective-I.R. drying results and simulations with the drying front model have shown that the following parameters are quite well reproduced by the model presented:

- (a) The drying curve and drying time.
- (b) The bottom temperature evolution with time.
- (c) The surface temperature evolution up to the critical point and the surface temperature at the end of drying (convection).
- (d) The overall shape of the drying rate curve.

Results from the simulations have also demonstrated that:

- (e) The experimentally measured surface temperature during the receding front period was lower than expected due to a bias generated by the surface thermocouple.
- (f) As a result of experimental uncertainties (on the X vs. t and T vs. t curves) and the low average critical moisture content ($X_c \sim 0.024$), it is not possible to decide if a correction of the drying front position to evaluate the mass transfer resistance within the materials is appropriate. However, better qualitative agreement was found for the N_v vs. X curve when the drying front empirical correction is used in the receding front period.

- (g) Within the parameter range investigated, the effect of the diffusion mass flux on the heat and mass transfer coefficients leads to a decrease of the evaporation rate by a maximum of 8 % for both the purely convective and combined processes.

- (h) The mass transfer coefficient decrease as a result of the high mass transfer flux effect at the surface level was evaluated as a plausible explanation to clarify why the evaporation temperature of the surface contaminated 19.9 mm sample (chapter V) reach the boiling point.

Finally, it can be concluded that the proposed drying front model (Dostie; 1991, 1992) is a very efficient tool to predict the key features of the drying process (convective and combined convective-I.R.) within the parameter range investigated (glass beads, $d=90-105 \mu\text{m}$, $b= 5.5-19.9 \text{ mm}$, $T_{\infty}^* \sim 80-180 \text{ }^{\circ}\text{C}$, $v_{\infty}^* = 2.0-5.2 \text{ m/s}$, $T_d^* = -10.6-+17.9 \text{ }^{\circ}\text{C}$, with or without $q_{is}^* = 6810-22020 \text{ W/m}^2$).

CHAPTER VII - CONCLUSIONS

7.1 SUMMARY

This research has resulted in the design and development of an experimental facility to study the combined convective-I.R. drying process.

First, the convective drying of a capillary porous material (glass beads, $d = 90-105 \mu\text{m}$) was studied in high temperature flow conditions ($b = 5.5-20 \text{ mm}$, $T_{\infty}^* \sim 80-180 \text{ }^{\circ}\text{C}$, $v_{\infty}^* \sim 2.0-6.3 \text{ m/s}$, $T_d^* \sim -1.8 - +7.8 \text{ }^{\circ}\text{C}$). The experimental results were found to be in good agreement with the classical results for analogy between the transfer of heat and mass expressed in terms of average heat and mass transfer coefficient ratios (Bird et al., 1960). This conclusion was found to apply (within experimental uncertainty) whether the transfer coefficients are corrected or not to account for the effect of the surface diffusion mass flux and/or density variation. It was also observed that the critical moisture content is independent of the convective drying parameters and sample thickness.

Second, combined convective-I.R. drying of a capillary porous material (glass beads, $d = 90-105 \mu\text{m}$) was examined experimentally ($b = 5.5-19.9 \text{ mm}$, $T_{\infty}^* \sim 80-180^{\circ}\text{C}$, $v_{\infty}^* = 2.0-6.2 \text{ m/s}$, $T_d^* = -10.6 - +17.9 \text{ }^{\circ}\text{C}$, $q_{is}^* = 6810-22020 \text{ W/m}^2$). It was observed that there is a link between the evaporation temperature and crust formation on the surface. An increase in the heat transfer coefficient was observed to occur when the surface reaches the boiling point and is higher than that of the flowing air. The necessity to take into account the effect of high mass transfer flux on the heat transfer coefficient (when convection is combined with I.R. heating) has been demonstrated. Further, the analogy between the transfer of heat and mass (expressed in terms of average heat and mass transfer coefficient ratios) was found to be verified quite well when the mass transfer resistance is mainly determined by the external boundary layer whereas it is not when the mass transfer coefficient is reduced as a result of crust formation. Lastly, It was observed that the critical moisture content is independent of the convective drying parameters, sample thickness, the overall incident heat flux and surface contamination.

Third, a drying front model developed by Dostie (1991, 1992) was discussed and tested. Comparison, within the whole experimental range, between the drying front model predictions and the experimental results of this study in convection drying and for the combined process have shown that the drying time, the bottom temperature evolution, the surface temperature evolution up to the critical point and the overall shape of the drying rate curve were quite well reproduced by the model. Simulations have also shown that, within experimental range, the effect of the diffusion mass flux on the heat and mass transfer coefficients leads to a decrease of the evaporation rate by a maximum of 8 % for both the purely convective and combined processes. The mass transfer coefficient reduction was evaluated as a plausible explanation to clarify why the evaporation temperature of a surface contaminated 19.9 mm sample (chapter V) reaches the boiling point temperature.

7.2 CONTRIBUTIONS TO KNOWLEDGE

The following are the original contributions of this thesis:

- a) In the combined high temperature convective-I.R drying process, the heat and mass transfer analogy (as expressed in terms of heat and mass transfer coefficients ratios) was found to be verified when the mass transfer resistance is mainly determined by the external boundary layer whereas it is not when the mass transfer coefficient is diminished as a result of crust formation.
- b) A convective heat transfer coefficient increase has been experimentally demonstrated to exist when the surface temperature has reached the boiling point and the gas temperature is lower than the surface temperature. This effect decreases the drying rate and leads to a lower efficiency of the I.R. heating process.
- c) The necessity to take into account the effect of high mass transfer flux on the heat transfer coefficient (when convection is combined with I.R. heating) has been demonstrated.
- d) The critical moisture content is the same for both the convective drying and the combined high temperature convective-I.R. drying processes.
- e) It was demonstrated that the combined convective-I.R. drying process of a non-hygroscopic material proved to be well predicted with a drying front model.

7.3 RECOMMENDATIONS FOR FUTURE WORK

- a) Develop a reliable calibration and on-line measurement procedure to evaluate the incident I.R. heat flux under combined convective-I.R. heating.
- a) Develop an efficient surface temperature measurement technique not sensitive to the I.R. heat flux (over the whole useful wavelength range).
- c) Further experimentation should be carried out to determine the detailed temperature field within the test sample for closer comparison with predictions of the drying front model or other drying models.
- d) Carried out an experimental study of the phenomenon related to the observed increase of the convective heat transfer coefficient.
- e) Study experimentally continuous and intermittent combined convective-I.R. drying of hygroscopic and/or semi-transparent materials.
- f) Evaluate the appropriateness of the drying front correction for the cases of materials with much higher critical moisture contents and/or much lower thermal conductivity ($k_d \sim 0.03 \text{ W/mK}$). For example, very fine sand ($d < 50 \mu\text{m}$) or acoustic tiles (Dostie et al., 1988).
- g) Extend the applicability of the drying front model for hygroscopic materials and other combined heating modes (microwave, high-frequency).
- h) Verify the applicability of the high mass transfer rate correction procedures and analogy to the case of combined convective and microwave or high-frequency drying.

REFERENCES

- Adrie, F., Jacobs, G. and Welgraven, D., 1988. A simple model to calculate the Sherwood and Nusselt number for discs of various shape, *Int. J. Heat Mass Transfer*, Vol. 31, No. 1, pp. 119-127.
- American Society of Heating Refrigerating and Air-Conditioning Engineers Inc., 1977. *Ashrae Handbook 1977 Fundamentals*, New-York.
- Arai, N., Takahashi, S., Hasatani, M. and Sugiyama, S., 1979 a. Simultaneous heat and mass transfer on the surface of an optically thick semitransparent liquid heated by a radiant heat source, *Heat Transfer Japanese Res.*, Vol. 8, pp. 1-9.
- Arai, N., Takahashi, S. and Sugiyama, S., 1979 b. Natural-convection heat and mass transfer from a horizontal upward-facing plane surface to air -experimental study on a plane surface heated by radiation, *Heat Transfer Japanese Res.*, Vol. 8, pp. 94-101.
- Audet, D., Boucher, C. Caumartin A. and Skeene, C., 1986. *Probabilités et statistiques*, Gaëtan Morin éditeur, Chicoutimi.
- Azizi, S., Moyne, C. and Degiovanni, A., 1988. Approche expérimentale et théorique de la conductivité thermique des milieux poreux humides, *Int. J. Heat Mass Transfer*, Vol. 31, No. 11, pp. 2305-2317.
- Baines, D. J., 1970. A comparative theoretical evaluation of five commonly used types of unsteady heat flux sensor, report HSA 27, Australian Defence Scientific Service, Weapons Research establishment.
- Basilico, C. and Martin, M., 1983. Approche expérimentale des mécanismes de transfert au cours du séchage à haute température d'un bois résineux, *Int. J. Heat Mass Transfer*, Vol. 27, No. 5, pp. 657-668.

Bédard, N., 1985. Présentation d'un programme caractérisant l'échange radiatif à l'intérieur d'une enceinte, Rapport interne IREQ 8RT-3454-G, Varennes, Québec, Canada.

Ben Nasrallah, S. and Arnaud, G., 1986. Séchage d'un milieu poreux contenant une faible teneur en eau, *Int. J. Heat Mass Transfer*, Vol. 29, No. 9, pp. 1443-1449.

Berger, D. and Pei, D.C.T., 1973. Drying of hygroscopic capillary porous solids- A theoretical approach, *Int. J. Heat Mass Transfer*, Vol. 16, pp. 293-302.

Bird, R. B. and Stewart, W. E. and Lightfoot, E. N., 1960. *Transport Phenomena*, John Wiley & Sons, New-York.

Birkebak, R. C., 1972. A technique for measuring spectral emittance, *The Review of Scientific Instruments*, Vol. 43, No. 37, pp. 1027-1030.

Bories, S., 1988. Recent advances in modelisation of coupled heat and mass transfer in capillary-porous bodies, *Drying'89*, A. S. Mujumdar Ed., Hemisphere Pub. Corp., pp. KL.47-KL.61.

Bragg, G. M., 1974. *Principles of experimentation and Measurement*, Prentice-Hall Inc., Englewood Cliffs, New Jersey.

Buckingham, E. A., 1907. Studies on the movement of soil moisture, U. S. Dept. Agr. Bull., No. 38.

Ceaglske, N. H. and Hougen, O. A., 1937. The drying of granular solids, *Trans. A.I.Ch.E.*, Vol. 30, pp. 283-314.

Charlaix, E., Hulin, J. P. and Plona, T. J., 1987. Experimental study of tracer dispersion in sintered glass porous materials of variable compaction, *Phys. Fluids*, Vol. 30, No. 6, pp. 1690-1698.

Chen, P., 1986. Mathematical modelling of drying and freezing processes in food industry, Ph.D. Thesis, Department of Chemical Engineering, University of Waterloo.

Chen, P. and Pei, D. C.T., 1989. A mathematical model of drying processes, Int. J. Heat Mass Transfer, Vol. 32, No. 2, pp. 297-310.

Chiang, W. C., 1987. Analysis of temperature and moisture profiles during apple drying, Ph.D. Thesis, Department of Chemical Engineering, Washington State University.

Chilton, T. H. and Colburn, A. P., 1934. Mass transfer (absorption) Coefficients, Ind. Eng. Chem., Vol. 26, No. 11, pp. 1183-1187.

Collignan, A. 1990, personal communication.

Comings, E.W. and Sherwood, T. K., 1934. The drying of solids -VII Moisture movement by capillarity in drying granular materials, Ind. Chem. Eng., Vol. 26, No. 10, pp. 1096-1097.

Corben, R. W. and Newitt, M. C., 1955. The mechanism of the drying of solids Part VI: The drying characteristics of porous granular material, Trans. Instn Chem. Engrs, Vol. 33, pp. 52-63.

Crausse, P., 1983. Etude fondamentale des transferts couplés de chaleur et d'humidité en milieu poreux non saturé. Thèse d'État, Institut National Polytechnique de Toulouse, Toulouse.

Cunningham, R. M. and Kelly, J. J., 1980. Moisture concentration profiles in drying packed beds, Drying'82, A. S. Mujumdar Ed., Hemisphere Pub. Corp., pp. 178-189.

Dayan, A. and Gluekler, E. L., 1982. Heat and mass transfer within an intensely heated concrete slab, Int. J. Heat Mass Transfer, Vol. 25, No. 10, pp. 1469-1476.

Delhaye, J. M., 1981. Thermohydraulics of two-phase systems for industrial design and nuclear engineering, McGraw-Hill Series in Thermal and Fluids Engineering, New-York.

De Vriendt, A. B., 1984. La transmission de la chaleur: Volume 2 Introduction au rayonnement thermique, Gaëtan Morin Ed., Chicoutimi, Québec, Canada.

Dinulescu, H. A. and Eckert , E. R. G., 1980. Analysis of the one dimensional moisture migration caused by temperature gradients in porous medium, Int. J. Heat Mass Transfer, Vol. 23, pp . 1069-1077.

Dostie, M., 1991. SELECT 2.3: Description du logiciel et état de développement, Rapport interne LTEE-90-1-011-71, Shawinigan, Québec, Canada.

Dostie, M., 1992. SELECT 3.0: Description du logiciel et état de développement, Rapport interne LTEE-92, Shawinigan, Québec, Canada.

Eckert , E. R. G. and Drake, R. M., 1972. Analysis of Heat and Mass Transfer, McGraw-Hill Series in Mechanical Engineering, New-York.

Eckert , E. R. G. and Faghri, M., 1980. A general analysis of moisture migration caused by temperature differences in an unsaturated porous medium, Int. J. Heat Mass Transfer, Vol. 22, pp . 1613-1623.

Endo, A , Shishido, I., Suzuki, M. and Ohtani, S., 1977. Estimation of critical moisture content, A.I.Ch. E. Symposium Series, Vol. 73, No. 163, pp. 57-62.

Enoch, I. E., 1984. Combined heat transfer inside fibrous material with external short wavelength radiation, Ph.D. Thesis, Department of Mechanical Engineering, University of Kentucky.

Franzen, K., Liang, H., Litchfield, B., Murakami, E., Nichols, C., Waananen, K., Miles, G. and Okos, M., 1987. Design and control of energy efficient drying processes with specific reference to foods: Volume 1 -Literature Review, Report No. DOE/ID/12608-2(Vol.1), Purdue University, West Lafayette, Indiana.

Gardner, W., 1920. The movement of moisture in soil by capillarity, *Soil Sci.*, Vol. 7, pp. 313-317.

Greiner, M. and Winter, E. R. F., 1978. Forced flow evaporation at high mass transfer rates, *Ger. Chem. Eng.*, Vol. 1, pp. 352-360.

Guyon, E., Oger, L. and Plona, T. J., 1987. Transport properties in sintered porous media composed of two particles sizes, *J. Phys. D: Appl. Phys.*, Vol. 20, pp. 1637-1644.

Hadley, G. R., 1984. Numerical modelling of the drying of porous material, *Proc. fourth Int. Drying Symp.*, Kyoto, Japan, pp.151-158.

Hanna, O T., 1962. Isothermal diffusion with a variable density, *A.I.Ch.E. J.*, Vol. 8, No. 2, pp. 278-279.

Harmathy, T. Z., 1969. Simultaneous moisture and heat transfer in porous systems with particular reference to drying, *I. & E. C. Fund.*, Vol. 8, No. 1, pp. 92-103.

Hasan, M., 1988. Cyclic phase change: Energy storage and recovery, Ph.D. Thesis, Chemical Engineering Department, McGill University, Montréal.

Hasatani, M., Arai, N., Itaya, Y. and Onoda, N., 1983. Drying of optically semitransparent materials by combined radiative-convective heating, *Drying Technology*, Vol. 1, No. 2, pp. 193-214.

Hasatani, M., Itaya, Y. and Miura, K., 1988. Hybrid drying of granular materials by combined radiative and convective heating, *Drying Technology*, Vol. 6, No. 1, pp. 43-67.

Haughey, D. P. and Beveridge, G. S. G., 1969. Structural properties of packed beds- A review, *Can. J. Chem. Eng.*, Vol. 47, pp. 130-140.

Heertjes, P. M. and Ringens, W. P., 1956. The J_H and J_D factor of air use for drying, Chem. Eng. Sci., Vol. 5, pp. 226-231.

Holman, J. P., 1981. *Heat Transfer*, McGraw-Hill Book Comp., New-York.

Holman, J. P., 1984. *Experimental Methods for Engineers*, McGraw-Hill Book Comp., New-York.

Huang, C. L. D., 1979. Multi phase moisture transfer in porous media subjected to temperature gradient, Int. J. Heat Mass Transfer, Vol. 22, pp. 1295-1307.

Hulin, J. P., Charlaix, E., Plona, T. J., Oger, L. and Guyon, E., 1988. Tracer dispersion in sintered glass beads with a bidisperse size distribution, A.I.Ch.E. J., Vol. 30, No. 4, pp. 610-617.

Illic, M. and Turner, I. W., 1989. Convective drying of a consolidated slab of wet porous material, Int. J. Heat Mass Transfer, Vol. 32, pp. 2351-2362.

Incropera F. P. and DeWitt, D. P., 1985. *Fundamentals of Heat and Mass Transfer*, John Wiley & Sons, New-York.

Kast, W., 1982. Coefficients for the combined heat and momentum transfer in laminar and turbulent boundary layers, Proc. 7 th. Int. Heat Tranf. Conf., Munich, Germany, Vol. 3, pp. 263-268.

Kast, W., 1984. Variation of heat and mass transfer coefficients for simultaneous heat and mass transfer, Int. Chem. Eng., Vol. 24, No. 8, pp. 23-28.

Kaviany, M. and Mittal, M., 1987. Funicular state in drying of a porous slab, Int. J. Heat Mass Transfer, Vol. 30, No. 7, pp. 1407-1418.

Kaviany, M., 1991. *Principles of Heat Transfer in Porous Media*, Springer-Verlag, New-York.

Kays, W. M. and Crawford, M. E., 1980. Convective Heat and Mass Transfer, McGraw-Hill Series in Mechanical Engineering, New-York.

Keey, R. B., 1972. Drying Principles and Practice, Pergamon Press, New-York.

Keey, R. B., 1978. Introduction to industrial drying operations, Pergamon Press, New-York.

Kline, S. J. and McClintock, F. A., 1953. Describing uncertainties in single-sample experiment, Mechanical Engineering, pp. 3-8.

Kobari, M., Shimizu, Y. and Endo, M., 1985. Contact drying of fibrous sheet material, Ind. Eng. Chem. Process Des. Dev., Vol. 24, pp. 188-194.

Krischer, O., 1963. Die Wissenschaftlichen Grundlagen der Trocknungstechnik, Vol. 1, 2nd. ed., Springer-Verlag, Berlin/Göttingen/Heidelberg.

Lewis, W. K., 1921. The rate of drying of solids materials, J. Ind. Eng. Chem., Vol. 13, No. 5, pp. 427-438.

Loughlin, K. F., Hadley-Coates, L. and Halhouli, K., 1985. High mass flux evaporation, Chem. Eng. Sci., Vol. 40, No. 7, pp. 1263-1272.

Luikov, A. V., 1966. Heat and mass transfer in capillary porous bodies, First Edition, Pergamon Press.

Maneval, J. E., McCarthy, M. J. and Whitaker, S., 1991. Studies of the drying process by NMR imaging, Drying'91, A. S. Mujumdar Ed., Hemisphere Pub. Corp.

Marseille, T. J., Schliesing J. S., Bell, D. M. and Johnson, B. M., 1991. Extending cooling tower thermal performance prediction using a liquid-side film resistance model, Heat Transfer Engineering, Vol. 12, No. 3, pp. 19-30.

Mendelson, H. and Yerazunis, S., 1965. Mass transfer at high mass fluxes: Part I Evaporation at the stagnation point of a cylinder, A.I.Ch.E. J., Vol. 11, No. 5, pp. 834-840.

McCormick, D. and Roach, A., 1980. *Measurement, Statistics and Computation*, Chapman N. B. Ed., John Wiley & Sons, New-York.

Min, K. and Emmons, H. 1972, The drying of porous media, Proc. Heat Transfer and Fluid Mech. Inst., Northridge, California, pp 1-18.

Moffat, R. J., 1988. Describing the uncertainties in experimental results, Experimental Thermal and Fluids Science, Vol. 1, pp. 3-17.

Morgan, R. P. and Yerazunis, S., 1967. Heat and mass transfer during liquid evaporation from porous materials, Chem. Eng. Prog. Symp. Ser., Vol. 63, No. 79, pp. 1-13.

Moyne, C., 1987. Transferts couplés chaleur masse lors du séchage: prise en compte du mouvement de la phase gazeuse. Thèse d'état, Institut National Polytechnique de Lorraine, Nancy.

Murray, W. D. and Landis, F., 1959. Numerical and machine solution of transient heat conduction problems involving melting or freezing, Trans. A.S.M.E., J. Heat Transfer, Vol. 81C, No. 2, pp. 106-112.

Navarri, P., 1990. Étude du séchage mixte par infra-rouge et convection, Rapport interne CETIAT NTV 90 074, Villeurbanne, France.

Navarri, P., 1991. Étude du séchage mixte par infra-rouge et convection d'un produit granulaire non hygroscopique, Rapport interne CETIAT NTV 901 116, Villeurbanne, France.

Neale, G. H. and Nader, W. K., 1973. Prediction of transport processes within porous media: diffusive flow processes within homogeneous swarm of spherical particles, A.I.Ch.E. J., Vol. 19, pp. 112-119.

Nienow, A. W., 1967. Transfer processes with a high mass flux, Brit. Chem. Eng., Vol. 12, No. 11, pp. 1737-1743.

Nienow, A. W., Unahabhokha R. and Mullin, J. W., 1969. The mass transfer driving force for high mass flux, Chem. Eng. Sci., Vol. 24, pp. 1655-1660.

Nissan, A. H., Kaye, W. G. and Bell, J. R., 1959. Mechanism of drying thick porous bodies during the falling rate period, A.I.Ch.E. J., Vol. 5, P. 103-110.

Obot, N. T. and Trabold, T. A., 1992. On the rate balance between impingement water evaporation and heat transfer, Int. Comm. Heat Mass Transfer, Vol. 19, No. 1, pp. 51-58.

Orfeuil, M., 1987. Electric Process Heating: Technologies / Equipment / Applications. Battelle Press, Columbus, Richland.

Patankar, S. V., 1980. Numerical Heat Transfer and Fluid Flow. Series in Computational Methods in Mechanics and Thermal Sciences, McGraw-Hill Book Comp., New-York.

Peck, R. E., Vyas, K. C. and Toei, R., 1977. Capillary theory applied to drying, A.I.Ch.E. Symp. Ser., Vol. 73, No. 163, pp. 63-70.

Pépin, T., 1989. Développement d'une sonde mesurant la température de l'air sous un fort rayonnement: évaluation théorique de ladite sonde, Rapport interne LTEE, Shawinigan, Québec, Canada.

Perré, P., 1987. Le séchage convectif de bois résineux: choix, validation et utilisation d'un modèle. Thèse de docteur de l'Université Paris VII, Paris.

Perrin, B. and Darolles, D., 1988. Couplage entre transferts de chaleur et de masse à la surface de matériaux poreux utilisés en génie civil, Rev. Gén. Therm. Fr., No. 323, pp. 585-590.

Perrin, B. and Foures, J. C., 1991. Détermination expérimentale du coefficient d'échange de masse en écoulement turbulent: prévision de la cinétique de séchage, Rev. Gén. Therm. Fr., No. 349, pp. 39-45.

Philip, J. R. and De Vries, D. A., 1957. Moisture movement in porous material under temperature gradient, Trans. Am. Geo. Union, Vol. 38, No. 2, pp. 222-232.

Pilitsis, S., 1986. A computational analysis of heat and mass transfer during the drying of granular porous media. M.Sc., Chemical Engineering Department, University of California, Davis.

Plumb, O. A., Spolek, G. E. and Olmstead, B. A., 1985. Heat and mass transfer in wood during drying, Int. J. Heat Mass Transfer, Vol. 28, pp. 1669-1678.

Prat, M., 1986 a. Analysis of experiments of moisture migration caused by temperature differences in unsaturated porous medium by means of two-dimensional numerical simulation, Int. J. Heat Mass Transfer, Vol. 29, No. 7, pp. 1033-1039.

Prat, M., 1986 b. Heat and mass transfer predetermination between a drying material and an external flow, Drying'86, A. S. Mujumdar Ed., Hemisphere Pub. Corp., pp. 105-111.

Prat, M., 1991. 2D Modelling of drying of porous media: influence of edge effects at the interface, Drying technology, Vol. 9, No. 5, pp. 1181-1208.

Puiggali, J. R., 1987. Séchage de produits naturels: du processus au procédé, Doctorat d'État, Université de Bordeaux I.

Reinsch, C. H., 1967. Smoothing by spline function, Numerische Mathematik, Vol. 10, pp. 177-183.

Ridgway, K. and Tarbuck, K. J., 1968. Voidage fluctuations in randomly-packed beds of spheres adjacent to a containing wall, Chem. Eng. Sci., Vol. 23, pp. 1147-1155.

- Rogers, J. A. and Kaviany, M., 1990. Variation of heat and mass transfer coefficients during drying of granular beds, J. Heat Transfer, Trans. A.S.M.E., Vol. 112, , No. 3, pp. 668-674.
- Rogers, J. A. and Kaviany, M., 1991. Funicular and evaporation front regimes in drying of ceramic beds, Int. J. Heat Mass Transfer, to appear (ref. Kaviany M., 1991).
- Sala, A., 1986. Radiant Properties of Materials: tables of radiant values for black body and real materials, Physical Sciences Data 21, Elsevier, New-York.
- Schadler, N. and Kast, W., 1987. A complete model of the drying curve for porous bodies - experimental and theoretical studies, Int. J. Heat Mass Transfer, Vol. 30, No. 10, pp. 2031-2044.
- Schajer, G. S., Stanish, M. A. and Kayihan, F., 1984. A computationally efficient fundamental approach to drying hygroscopic and non-hygroscopic porous material, Trans. A.S.M.E., 84-WA-HT-13.
- Schornhorst, J. R. and Viskanta, R., 1968. An experimental examination of the validity of the commonly used methods of radiant heat transfer analysis, J. Heat Transfer, Vol. 90, No. 4, pp. 429-436.
- Seki, N., Fukusako S. and Tanaka, M., 1977. Drying phenomena of a horizontal wetted porous layer under high heat flux, Bulletin of the J.S.M.E., Vol. 20, No. 149, pp. 1484-1491.
- Sherwood, T. K., 1929. The drying of solids -I, J. Ind. Chem. Eng., Vol. 21, No. 1, pp. 12-16.
- Sherwood, T. K., 1937. The air drying of solids, Trans. A.I.Ch.E., Vol. 32, pp. 150-168.

Sherwood, T. K. and Comings, E.W., 1933. The drying of solids -V Mechanism of drying of clays, J. Ind. Chem. Eng., Vol. 25, No. 3, pp. 311-316.

Shimizu, M., Hashimoto A., Hirota K., Honda T. and Watanabe, M., 1990. Infrared radiation drying of granular materials in constant rate period, CHISA 10th International Congress of Chemical Engineering, Praha, Czechoslovakia, august 26-31 1990, paper No. F6.3.

Siegel, R. and Howell, J. R., 1981. *Thermal Radiation Heat Transfer*. McGraw-Hill Series in Thermal and Fluids Engineering, New-York.

Smolsky, B. M. and Sergeyev, G. T., 1962. Heat and mass transfer with liquid evaporation, Int. J. Heat Mass Transfer, Vol. 5, pp. 1011-1021.

Szentgyörgyi, S., Molnar, K. and Ôrvös, M., 1980. Modelling and calculation of the drying process of capillary porous materials, Drying'80, A. S. Mujumdar Ed., Hemisphere Pub. Corp, pp. 29-35.

Toei, R., Hayashi, S., Hasegawa, J., Kai, T. and Tanaka, S., 1964. The mechanism of drying of a bed of granular and powdered materials during the second falling rate period, Kagaku Kogaku (Chemical Engineering, Japan), Vol. 28, No. 6, pp. 458-467.

Van Brakel, J. and Heertjes, P. M., 1974. Homogeneous particle packings and porous masses. Some experimental techniques, Powder Technology, Vol. 9, pp. 263-271.

Van Brakel, J., 1980. Mass transfer in convective drying, Advances in Drying, A. S. Mujumdar Ed., Hemisphere Pub. Corp, Vol. 1, pp. 217-267.

Van Wylen, G. J., Sonntag, R. E. and Desrochers, P., 1981. *Thermodynamique Appliquée*, 2^o édition, Édition du Renouveau Pédagogique, Montréal, Canada.

Wade, R. W. and Wayne S. S., 1962. Measurement of total emittance of several refractory oxides, cermets, and ceramics for temperatures from 600 °F to 2000 °F, NASA Technical Note D-998.

Weast, R. C., Astle, M. J. and Beyer, W. H., 1989. CRC Handbook of Chemistry and Physics, 69th Edition, CRC Press Inc., Boca Raton, Florida.

Webb, R. L., 1990. Standard nomenclature for mass transfer processes, Int. Comm. Heat Mass Transfer, Vol. 17, pp. 529-535.

Wei, C. K., 1984. Heat and mass transfer in porous media in convective heating and/or microwave heating. Ph.D. Thesis, University of Minnesota, Montréal.

Whitaker, S., 1977. Simultaneous heat, mass and momentum transfer in porous media: a theory of drying, Advances in Heat Transfer, Academic Press, New-York, Vol. 13, pp. 119-205.

Wisniak, J., Fertilio, A. and Freed C., 1967. Critical moisture of sand and its properties, British Chem. Eng., Vol. 12, pp. 1590-1592.

Wong, P. Z., Koplik, J. and Tomanic, J. P., 1984. Conductivity and permeability of rocks, Phys. Rev. B, Vol. 30, No. 11, pp. 6606-6614.

Yagi, S., Kunii, D., Okada S. and Toyabe, R., 1957. Studies on the infrared drying of powdery and granular solids in falling rate period, Kagaku Kogaku, Vol. 21, No. 8, pp. 486-491.

APPENDIX 1
THE EXPERIMENTAL SET-UP ACCESSORIES OR EQUIPMENTS

USE WITHIN THE EXPERIMENTAL FACILITY	ACCESSORY OR EQUIPMENT	BRAND	MODEL NO. OR DENOMINATION	TECHNICAL SPECIFICATIONS
To provide a mechanical support and a thermally stable environment	Batch oven	Pyradia	BT 242436 HCE	9 tubular type heaters, $T_{max} = 400\text{ }^{\circ}\text{C}$, $P = 18\text{ kW}$, $U = 600\text{ V}$, Rockwool insulation thickness = 150 mm, Vol. = 337824 cm^3
To allow selection and control of the air temperature	Oven Temperature controller	Barber Colman Comp.	BC-560	PID controller with on-off capability
To supply the oven airflow	Oven fan	Pyradia	na	Squirrel cage, $\sigma = 312\text{ mm}$, output = 1700 cfm
To supply the necessary oven fan rpm.	DC motor	Leroy Somer	FE-65FJ5V	max. rpm = 1750, $P = 1750\text{ W}$, $U = 180\text{ V}$
To allow selection and control the stability of the DC motor rpm.	Solid state DC motor speed controller	Leroy Somer	LStronics	Load and line regulation = 1 % and 0.5 % respectively
To cool the bottom cavity	Fan	Dayton Electric Mfg.	2C915A	Squirrel cage type with output limited by a shutter, $P = 125\text{ W}$
To cool the I.R. source and to renew air in the oven	Fan	Electrohome	EB-4	Squirrel cage type with variable speed, $P = 96\text{ W}$
To renew air in the oven	Fan	Reznor Venter	LV-301	Squirrel cage type, admission limited by a shutter, $P = 161\text{ W}$
To supply the I.R. heat flux	I.R. source	Glenro Inc.	Radplane Heater Series 80	$P = 4.3\text{ kW}$, $U = 240\text{ V}$, size = 457 X 356 mm
To allow the choice of the I.R. source temperature	Manual variable transformer	The Superior Electric Co.	11560D0-2S	U range = 0-280 V, $P = 14\text{ kW}$
To guard against air heat losses to the bottom cavity upstream of the sample	Flexible heaters	Watlow Corp.	Silicone rubber rectangles, etched-foil construction	1 (300 W; 152 X 126 mm) + 1 (150 W; 128 X 77 mm) + 2 (50 W; 125 X 25 mm), Thickness = 0.5 mm
To maintain the lower test section wall temperature close to the sample	Temperature controller	Partlow Corp.	MIC 2000	PID controller with on-off capability
To allow selection and control of the lower test section wall temperature on the bottom of the flow mixer	Temperature controller	RKC Inst. Inc.	REX-C10	Auto-tune PID controller with on-off capability
To Reduce the inlet flow turbulence scale and to improve the velocity uniformity	Flow mixer	Perforated grids assembly with 2 sets of plates. Each set has 3 plates with 33 %, 40 % and 51 % open area with 5 mm gap in between. 3 wire mesh of 100 mesh with 40 S.W.G wire. A 5 mm gap in between wire mesh was left. Size = 60 X 500 X 100 mm		
To compact the glass beads bed	Vertical vibrator	Ray Foster Dental Equipment	34	$U = 115\text{ V}$, $f = 60\text{ Hz}$
To consolidate the glass beads bed	High temperature batch oven	Pyradia	F6P141418SVF	12 spiral type heaters, $T_{max} = 1260\text{ }^{\circ}\text{C}$, $P = 10\text{ kW}$, $U = 600\text{ V}$, Ceramic insulation thickness = 200 mm, Vol. = 66938 cm^3

na : not available

APPENDIX 2
THE SPATIAL LOCATION OF THE MEASURING POINTS
WITH RESPECT TO Oxyz

Measuring point	x (mm)	y (mm)	z (mm)
T_{∞}	120	0	50
v_{∞}	-125	-190	50
T_d	0	-60	40
T_{sir}	-30	-125	295
T_{t1}	0	205	100
T_{t2}	80	0	100
T_{t3}	165	0	100
T_{t4}	0	-125	100
T_{t5}	-85	-125	100
T_{t6}	-250	0	50
$T_{\infty 1}$	0	205	50
$T_{\infty 2}$	0	205	0
$T_{\infty 3}$	0	60	3
$T_{\infty 4}$	0	0	15
$T_{\infty 5}$	0	0	50
T_{p1}	0	223	-1
T_{p2}	0	50	-1
T_{p3}	-50	0	-1
T_{p4}	50	0	-1

See Figures 3.3 or A5.1 for Oxyz location.

APPENDIX 3
MEASUREMENT DEVICES AND/OR SENSORS

VARIABLES	MEASURING APPARATUS AND/OR SENSORS	BRAND	MODEL	RANGE	ACCURACY	RESOLUTION	REPEATABILITY	RESPONSE TIME OR RATE
T_d	Condensation dew point hygrometer	General Eastern Instrument Corp.	1211 sensor 1100DP indicator unit 1220 thermostated NEMA enclosure	- 40 °C - + 80 °C	± 0.3 °C	0.1 °C	na	2 °C/s
v_{∞}	Air velocity meter	Sierra Instruments	615 MHTV	0 - 6 m/s	± 0.24 m/s	0.01 m/s	± 0.012 m/s	0.01 s
P_{∞}	Mercury barometer	Fisher Scientific Instrument	National Weather Service Type 02-380	647-805 mm	0.2 mm	0.1 mm	na	na
m	Balance	Mettler Instrumente AG	PM 4000	0 - 4100 g	± 0.02 g	0.01 g	± 0.01 g	2 s
P_i	Wattmeter	Westinghouse	VP4-846	0 - 5 kW	± 0.6%	1 W	na	0.4 s
$T_{\infty}, T_{\infty i}$ (i = 3,5)	Thermocouple	Omega	30 gage type J or K, Kapton insulation	0 °C - + 316 °C	± 0.5 °C	0.01 °C	na	~ 3 s
T_{sir}, T_{pi} (i = 1,4)	Thermocouple	Omega	30 gage type K, glass braid insulation	- 73 °C - + 482 °C	± 1.1 °C	0.01 °C	na	< 3 s
T_s T_b	Thermocouple	Thermo-kinetics	0.5 mm ø type K, MgO insulation and stainless steel sheats	- 200 °C - + 927 °C	± 0.5 °C	0.01 °C	na	< 2 s
$T_{ti}, T_{\infty i}$ (i = 1,2)	Thermocouple	Omega	24 gage type K, Kapton insulation	0 °C - + 16 °C	± 1.1 °C	0.01 °C	na	~ 6 s
q_{js}	Heat Flux Transducer	Medtherm Corp.	64-2-18-K Schmidt-Boelter	0 to 23 kW/m ²	± 3 %	1 W	± 0.5 %	0.29 s
E	Infrared Pyrometer	Raytek, Inc.	Raynger II R2LT 8 to 14 µm spectral range	- 30 °C - 1400 °C	± 1 % reading (T)	1 °C 0.01 in E	± 0.5 % reading (T)	0.25 s
ΔP_{∞}	Differential Pressure meter	AIR LTD.	MP 20-2A	0 ± 20 in.H ₂ O	± 1.5 % reading (ΔP)	na	na	na

na : not available

APPENDIX 4

**THE THERMOPHYSICAL PROPERTIES OF WATER, WATER VAPOR,
AIR AND THE GLASS BEADS**

The water vapor thermal conductivity (W/mK) was reported by Chiang (1987):

(T; K)

$$k_v = 10^3 \cdot [7.33746 \cdot 10^{-6} - 1.01321 \cdot 10^{-8} \cdot T + 1.80034 \cdot 10^{-10} \cdot T^2 - 9.09792 \cdot 10^{-14} \cdot T^3] \quad (\text{A4.1})$$

The air thermal conductivity (W/mK) was correlated by Irvine and Liley (1984):

250 K ≤ T < 1050 K

$$k_a = -2.276501 \cdot 10^{-3} + 1.2598485 \cdot 10^{-4} \cdot T - 1.4815235 \cdot 10^{-7} \cdot T^2 + 1.73550646 \cdot 10^{-10} \cdot T^3 - 1.066657 \cdot 10^{-13} \cdot T^4 + 2.47663035 \cdot 10^{-17} \cdot T^5 \quad (\text{A4.2})$$

The thermal conductivity (W/mK) of the gas mixture can be evaluated from the relation given by Chiang (1987):

$$k_g = \frac{y_v k_v (M_v)^{\frac{1}{3}} + y_a k_a (M_a)^{\frac{1}{3}}}{y_v (M_v)^{\frac{1}{3}} + y_a (M_a)^{\frac{1}{3}}} \quad (\text{A4.3})$$

The vapor specific heat (J/kgK) has been given by Van Wylen et al. (1981):

300 K < T < 3500 K

$$\theta = \frac{T}{100}$$

$$c_{pv} = 143.05 - 183.54 \cdot \theta^{0.25} + 82.751 \cdot \theta^{0.5} - 3.6989 \cdot \theta \quad (\text{A4.4})$$

The air specific heat (J/kgK) was correlated by Irvine and Liley (1984):

$$250 \text{ K} \leq T < 2000 \text{ K}$$

$$c_{pa} = 10^3 \cdot [1.03409 - 0.2848870 \cdot 10^{-3} \cdot T + 0.7816818 \cdot 10^{-6} \cdot T^2 - 0.4970786 \cdot 10^{-9} \cdot T^3 + 0.1077024 \cdot 10^{-12} \cdot T^4] \quad (\text{A4.5})$$

The heat capacity (J/kgK) of the moist air mixture can be computed from a formula reported by Eckert and Drake (1972):

$$c_{pg} = \omega_v c_{pv} + (1 - \omega_v) c_{pa} \quad (\text{A4.6})$$

where ω_v is the mass fraction of water vapor.

The liquid water specific heat (J/kgK) was taken to be a constant (Incropera, 1984) because the variation with T were lower than 0.5 % in the range (273.15 K - 373.15 K):

$$c_{pw} = 4180 \quad (\text{A4.7})$$

The vapor viscosity (kg/ms) is given as (Chiang, 1987):

(T; K)

$$\mu_v = -3.189 \cdot 10^{-6} + 4.145 \cdot 10^{-8} \cdot T - 8.272 \cdot 10^{-13} \cdot T^2 \quad (\text{A4.8})$$

The air viscosity (kg/ms) was calculated from (Irvine and Liley, 1984):

$$250 \text{ K} \leq T < 600 \text{ K}$$

$$\mu_a = 10^{-6} \cdot [-0.98601 + 9.080125 \cdot 10^{-2} \cdot T - 1.17635375 \cdot 10^{-4} \cdot T^2 + 1.2349703 \cdot 10^{-7} \cdot T^3 - 5.7971299 \cdot 10^{-11} \cdot T^4] \quad (\text{A4.9})$$

The viscosity (kg/ms) of a low-pressure moist air mixture may be simply calculated from the component viscosities (Chiang, 1987):

$$\mu_g = \frac{y_v \mu_v M_v^{\frac{1}{2}} + (1 - y_v) \mu_a M_a^{\frac{1}{2}}}{y_v M_v^{\frac{1}{2}} + (1 - y_v) M_a^{\frac{1}{2}}} \quad (\text{A4.10})$$

The latent heat of evaporation (J/kg) was evaluated with (Irvine and Liley, 1984):

$$273.15 \text{ K} \leq T \leq 647.3 \text{ K}$$

$$\Delta H_v = 2.5009 \cdot 10^6 \cdot \left[0.779221 \cdot T^{\frac{1}{3}} + 4.62668 \cdot T^{\frac{5}{6}} - 1.07931 \cdot T^{\frac{7}{6}} - 3.87446 \cdot T + 2.94553 \cdot T^2 - 8.06395 \cdot T^3 + 11.5633 \cdot T^4 - 6.02884 \cdot T^5 \right] \quad (\text{A4.11})$$

The vapor saturation pressure (Pa) was computed with (ASHRAE, 1977):

$$273.15 \text{ K} \leq T \leq 647.3 \text{ K}$$

$$\theta = 0.65 - 0.01 \cdot (T - 273.15)$$

$$\ln\left(\frac{p_v}{217.99}\right) = \left(\frac{101325 \cdot 0.01}{T}\right) \cdot (374.136 - (T - 273.15)) \cdot \left[\begin{array}{l} -741.9242 - 29.721 \cdot \theta - 11.55286 \cdot \theta^2 \\ -0.8685635 \cdot \theta^3 + 0.1094098 \cdot \theta^4 \\ + 0.439993 \cdot \theta^5 + 0.2520658 \cdot \theta^6 \\ + 0.05218684 \cdot \theta^7 \end{array} \right] \quad (\text{A4.12})$$

and $173.15 \text{ K} < T < 273.15 \text{ K}$

$$\theta = \frac{273.16}{T}$$

$$\log_{10}(p_v) = 101325 \cdot \left[\begin{array}{l} -9.096936 \cdot (\theta - 1) - 3.56654 \cdot \log_{10}(\theta) \\ +0.876817 \cdot \left(1 - \frac{1}{\theta}\right) - 2.2195983 \end{array} \right] \quad (\text{A4.13})$$

The vapor diffusion coefficient in air (m^2/s) was deduced from the relation given by Bird et al. (1960) for the mass diffusivity of a binary system at low pressure:

(T; K)

$$D_{va} = \frac{0.000004455 \cdot T^{2.334}}{P_-} \quad (\text{A4.14})$$

The consolidated glass beads bed thermal conductivity ($\text{W}/\text{m}^2\text{K}$) has been measured by Collignan (1990) for the dry bed at ambient temperature ($d = 90\text{--}105 \mu\text{m}$, $\varepsilon = 0.37$, $T_{\text{amb}} = 21 \text{ }^\circ\text{C}$):

$$k_d = 0.174 \pm 4 \% \quad (\text{A4.15})$$

This value is close to the one for non consolidated beds ($0.2 \text{ W}/\text{mK}$; $\varepsilon = 0.40$, $T_{\text{amb}} = 20 \text{ }^\circ\text{C}$) reported by Azizi et al. (1988) and by ($0.167 \text{ W}/\text{mK}$; $d = 485 \mu\text{m}$, $\varepsilon = 0.36$) Pilitsis (1986). The specific heat (J/kgK) of the glass beads is (Collignan, 1990):

$$c_{pb} = 893 \pm 7 \% \quad (\text{A4.16})$$

A similar value ($920 \text{ J}/\text{kg}$) has been measured by Azizi et al. (1988) for glass beads.

APPENDIX 5**THE RADIATIVE HEAT EXCHANGE IN THE TEST SECTION:
THE HYPOTHESES, SURFACES,
SYSTEM OF EQUATIONS AND SOLUTION****A HYPOTHESES**

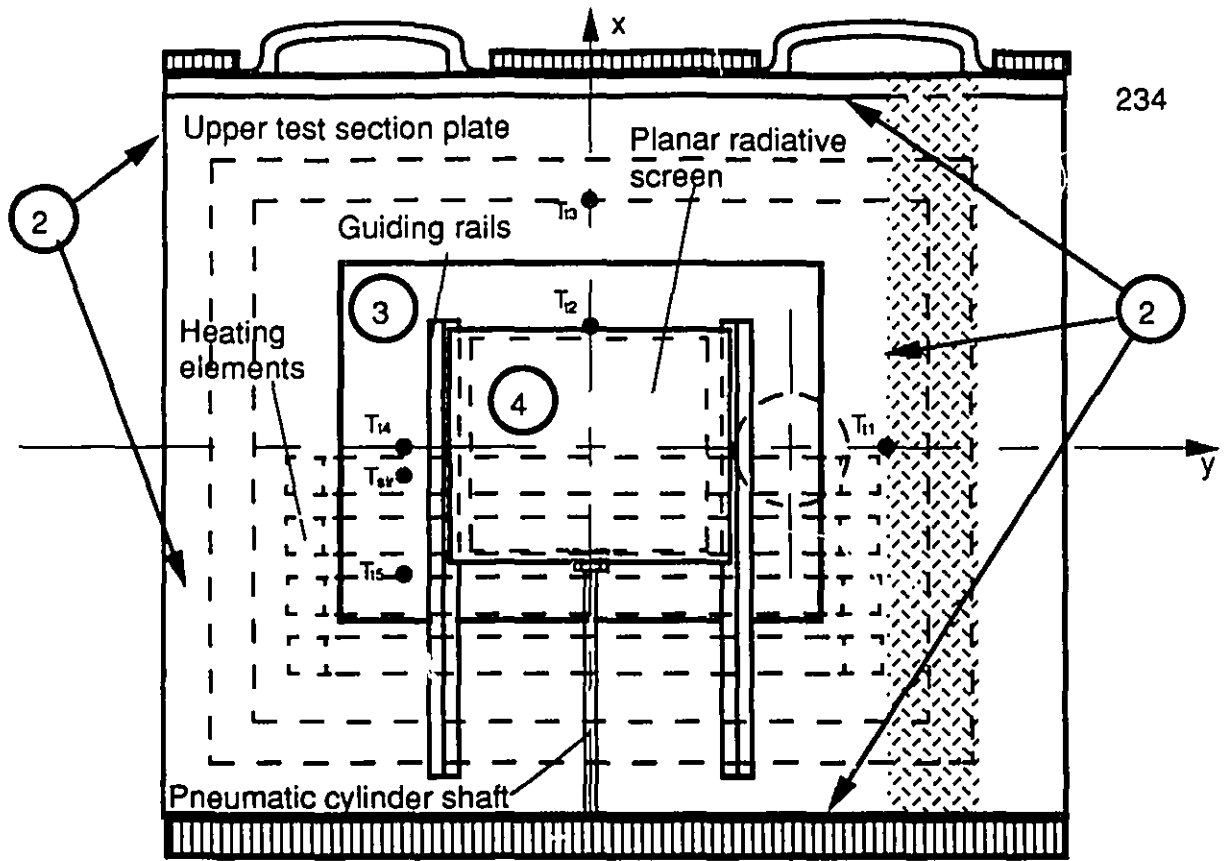
The application of the theory of radiation exchange in an enclosure of diffuse gray surfaces (Siegel and Howell, 1981) is subject to the following restrictions (over each surface area):

- a) The temperature is uniform;
- b) The directional and spectral emissivity, absorptivity and reflectivity are independent of wavelength and direction;
- c) All energy is emitted and reflected diffusely;
- d) The incident and hence reflected energy flux is uniform over each individual area.

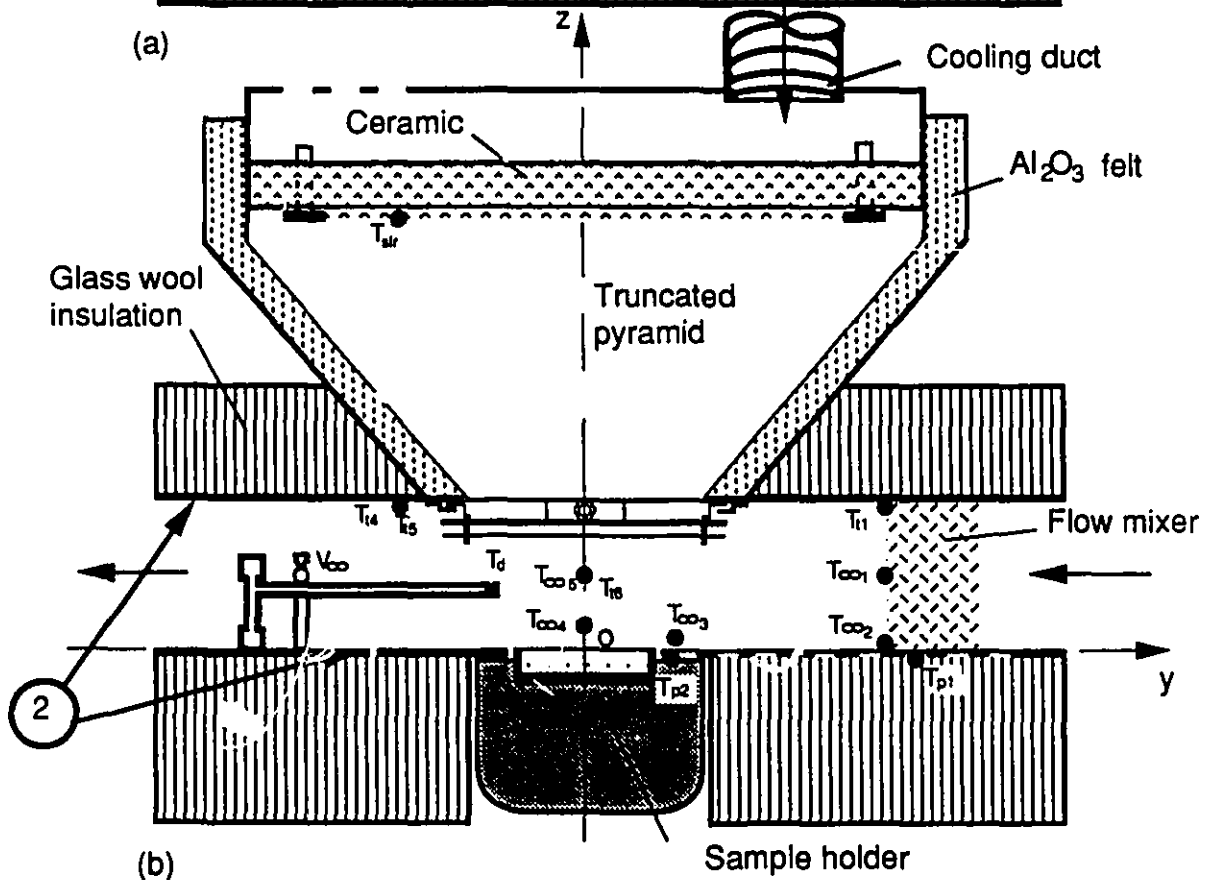
B SURFACES LOCATION, SIZE AND SHAPE FACTORS

The locations of the 4 surfaces used to evaluate the radiative heat exchange within the test section are displayed in Figure A5.1. The surfaces number are the following:

- a) Surface number 1 is the sample;



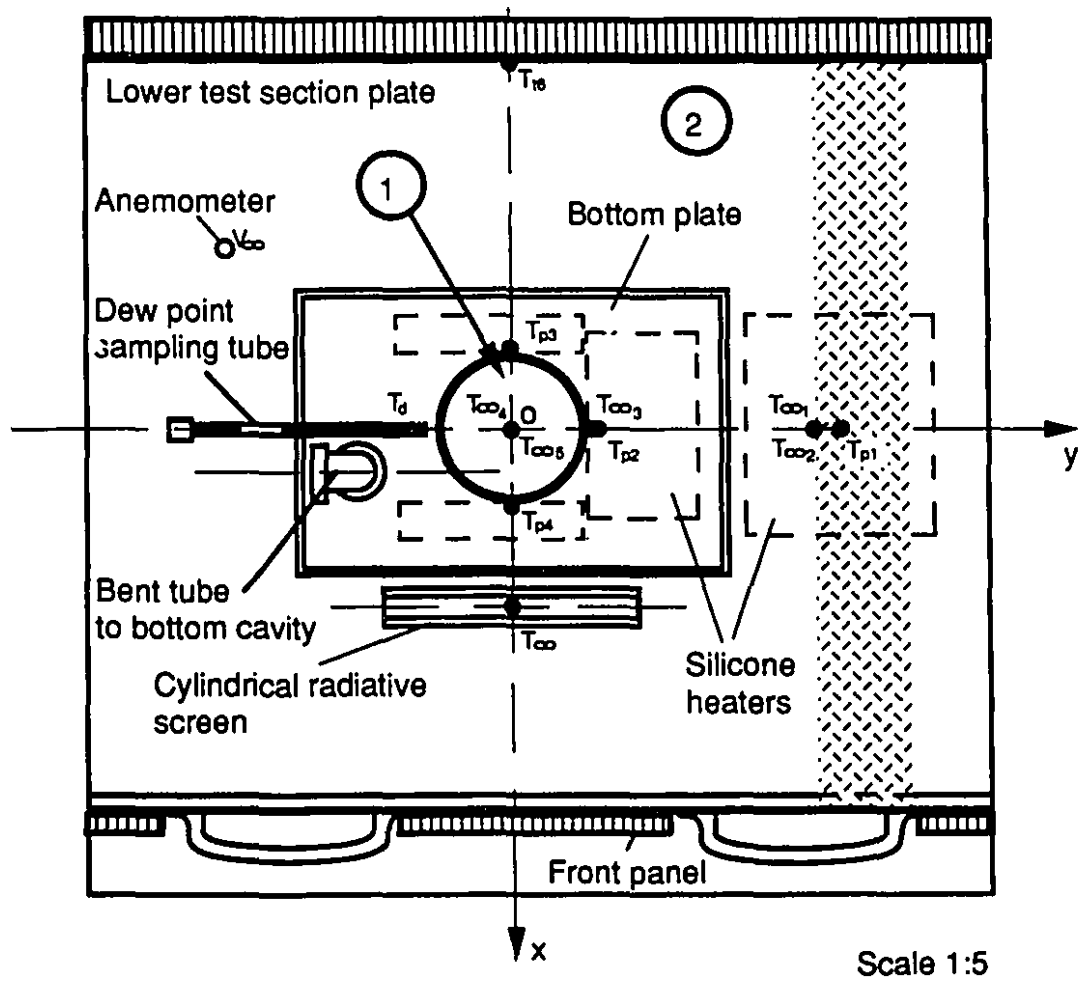
(a)



(b)

Figure A5.1a Test section: bottom view

b Test section: cross sectional view



(c)

Figure A5.1c Test section: top view

- b) Surface number 2 is composed of:
- i) The test section side surfaces (front panel, rear panel, flow mixer exit, test section flow exit);
 - ii) The test section bottom plate;
 - iii) The test section upper plate without the aperture for I.R. heating and surface 3 (drawn in Figure A5.1).
- c) Surface number 3 is located on the upper test section plate; it is symmetrically positioned with respect to the I.R. aperture and corresponds to a plate that was cut on the upper test section plate. The limiting line located in between T_{12} and T_{13} does cross the T_{12} - T_{13} line in the middle; the thermocouple T_{14} is located midway between the downstream I.R. aperture side and the downstream line which delimits surface 3;
- d) Surface 4 is the I.R. source aperture.

The actual surface areas of the four surfaces are:

$$A_1 = 0.0062 \text{ m}^2$$

$$A_2 = 0.6009 \text{ m}^2$$

$$A_3 = 0.0580 \text{ m}^2$$

$$A_4 = 0.0229 \text{ m}^2$$

The shape factors were computed with FACTIJ (Bédard, 1985) a software using a line integration algorithm. The accuracy of the shape factor determination was ascertained by Bédard (1985) for 31 simple cases for which an analytical solution exists (Siegel and Howell, 1981). Making use of the reciprocity relations and the sum rule (Incropera, 1985), only F_{14} (0.3894) and $F_{1(3+4)}$ (0.6935) had to be computed. The following values were found for the necessary shape factors:

$$F_{11} = 0.0000, F_{12} = 0.3065, F_{13} = 0.3041, F_{14} = 0.3894$$

$$F_{21} = 0.0032, F_{22} = 0.8693, F_{23} = 0.0934, F_{24} = 0.0341$$

$$F_{31} = 0.0325, F_{32} = 0.9675, F_{33} = 0.0000, F_{34} = 0.0000$$

$$F_{41} = 0.1054, F_{42} = 0.8946, F_{43} = 0.0000, F_{44} = 0.0000$$

C THE SYSTEM OF EQUATIONS AND SOLUTION TECHNIQUE

Given the surface temperature the system of equation to be solved has been summarized by Siegel and Howell (1981) as follows for the k^{th} equation ($k=1,4$):

$$\sum_{j=1}^4 \left(\frac{\delta_{kj}}{E_j} - F_{kj} \frac{1-E_j}{E_j} \right) \cdot \frac{Q_j}{A_j} = \sum_{j=1}^4 (\delta_{kj} - F_{kj}) \cdot \sigma \cdot T_j^4 \quad (\text{A5.1})$$

where δ_{kj} is the Kronecker delta defined as:

$$\delta_{kj} = \begin{cases} 1 & \text{when } k=j \\ 0 & \text{when } k \neq j \end{cases} \quad (\text{A5.2})$$

Q_j is the rate (W) of heat input to the surface or output of the surface j . The right-hand side of equation A5.1 can be computed for each surface when their surface temperature is known (here measured or evaluated). Each factor of Q_j on the left-hand side, can be evaluated and assembled in a matrix which can be inverted. The solution of the resulting system of linear equation is obtained simply by multiplying the inverted matrix and the left-hand side vector.

Finally the relation which link Q_1 to q_{is} (the overall incident radiative heat flux on the sample surface) is the following (Siegel and Howell, 1981):

$$Q_1 = A_s \cdot E_s \cdot (\sigma T_s^4 - q_{is}) \quad (\text{A5.3})$$

For the convective heating results, we have:

$$q_{is} = \frac{Q_1}{A_s} \quad (\text{A5.4})$$

APPENDIX 6

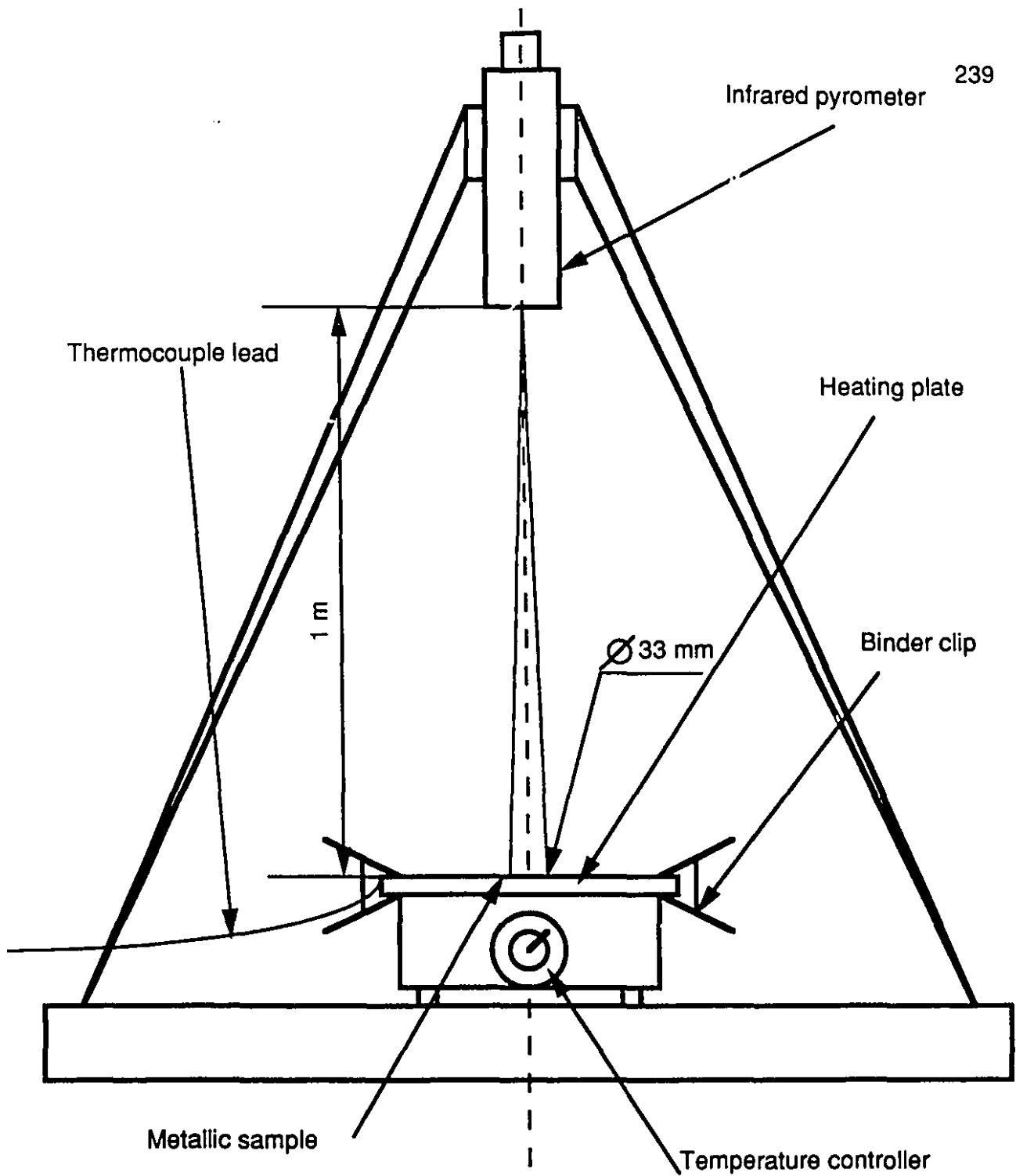
EMISSIVITY MEASUREMENT

A METALLIC SURFACE EMISSIVITY MEASUREMENT

The measurements were different for the metallic surfaces and the sample. As shown in Figure A6.1 the metallic surface was put in good contact with a heating plate with controllable surface temperature. For the test section plate a type K (30 gage) thermocouple was spot-welded in the center of the plate. For the stainless steel plate, a type K (butt bonded junction, 0.005" thickness) Omega co1 thermocouple was glued in the plate center. The instrumentation and heated plate were within a large room at ambient temperature (~ 21 °C).

The infrared pyrometer was located 1 m above the sample and the measurement area was about 33 mm \varnothing located in the metal plate center.

Before the final measurements could be made the metal plate was heated to the highest temperature for which a measurement was realized. It was left for a two hour period at this temperature. Such initial step was mandatory since it was observed that the emissivity measurement was not reproducible if the surface was not previously "aged". This step is quite commonly performed (Wade and Slomp, 1962) when measurements of emissivity are carried-out. Furthermore, such an "aged" surface corresponds more closely to the state of the metallic surfaces within the test section.



I

Figure A6.1 The emissivity measurement set-up

The procedure followed to take the reported measurement is:

- a) Adjust the plate controller to the needed plate temperature;
- b) Wait for a stable temperature reading with the surface thermocouple;
- c) Adjust the emissivity of the infrared pyrometer so that the pyrometer temperature reading and the thermocouple reading are the same;
- d) Record the emissivity and temperature.

This procedure was repeated for consistency at the same temperature and the results are presented in Figure A6.2a for the aluminized silicone paint on steel background and in Figure A6.2b for the polished stainless steel plate. The reproducibility of the measurement was evaluated to be within ± 0.01 in both cases. Furthermore, it can be observed that all the data are within ± 0.03 and ± 0.02 of the reported emissivity for the aluminized paint ($E_t = 0.28$) and the stainless steel plate ($E_{sc} = 0.13$) respectively. The emissivity increase slightly with temperature; this is the usual behavior of most metallic surfaces (Siegel and Howell, 1981). For the aluminized silicone paint it increase by 0.05 when the temperature goes from 50 °C to 270 °C. For the stainless steel plate, the emissivity increase by 0.04 when the temperature goes from 80 °C to 180 °C.

Values for the emissivity of an aluminized silicone paint has been reported by Siegel and Howell (1981) to vary in a range from 0.20 to 0.60 within which all the present value were measured. Sala (1986) reported a value between 0.10 and 0.15 for the same temperature range for stainless steel type 304.

B THE SAMPLE EMISSIVITY MEASUREMENT

The sample emissivity measurements were carried with a wet and a dry surface. The sample was introduced in a batch oven close to an aperture on the oven ceiling through which the sample surface could be focused with the pyrometer.

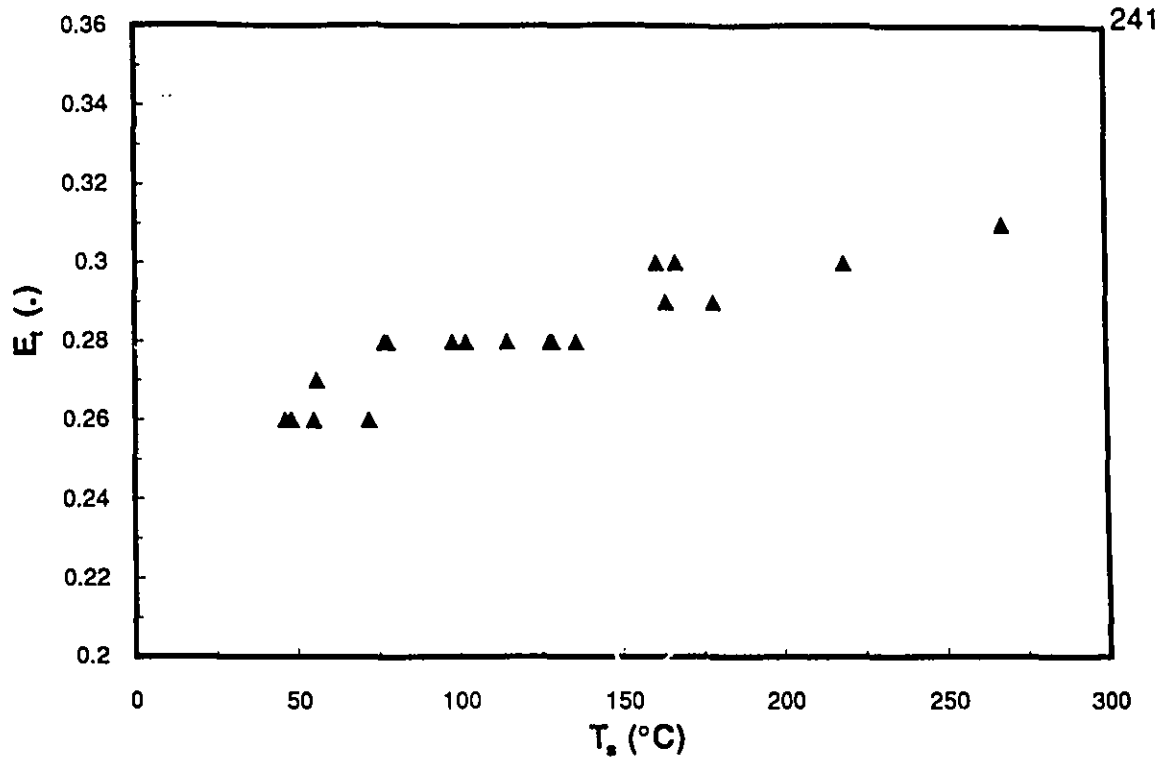


Figure A6.2a The emissivity of the test section walls: E_f

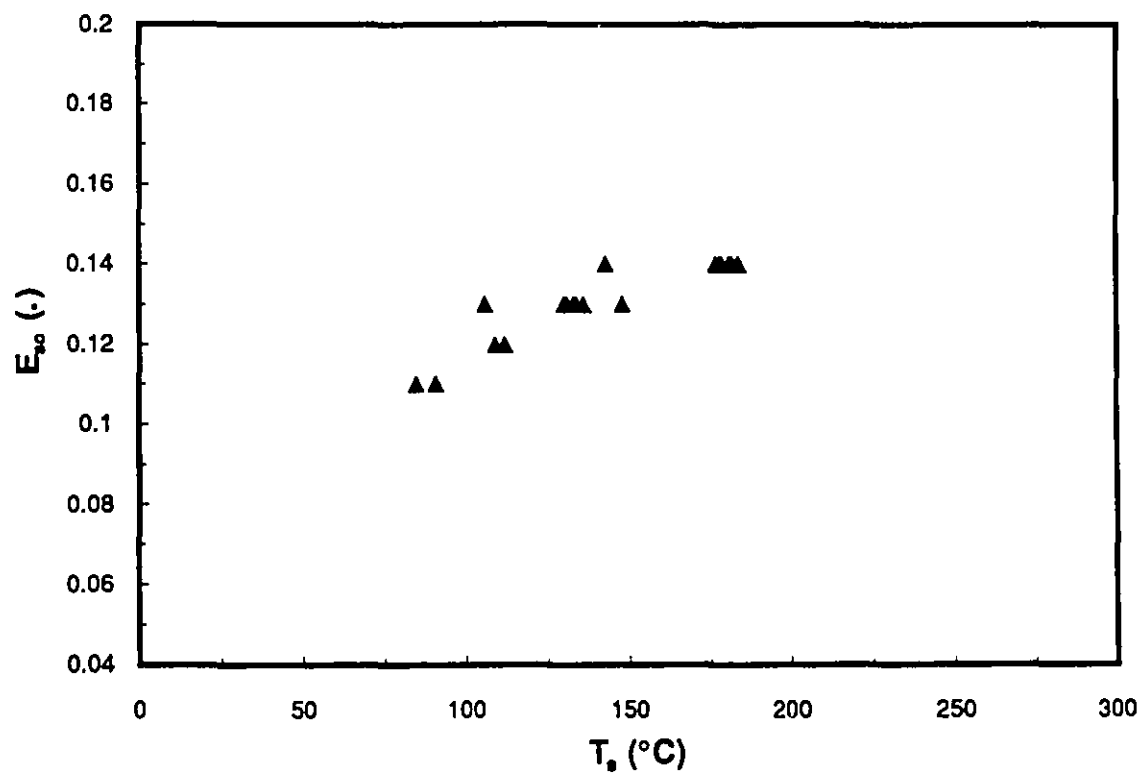


Figure A6.2b The emissivity of the stainless steel shield: E_{ss}

The results are displayed in Figure A6.3. When the sample surface is wet it was not possible to observe any temperature reading difference (thermocouple vs. pyrometer) as the emissivity varied in between 0.95 and 1.0. When the sample surface is dried, the sample surface emissivity is 0.91 within ± 0.01 . E_s was taken to equal 0.95 because:

- a) The sample surface is likely to be wet during the P.C.D.R.P.;
- b) Water emissivity is 0.96;
- c) It is likely that such a measurement is affected by the presence of the oven and the walls of the aperture since a portion of the reflected energy by the sample does contribute to increase the sample surface emissivity.

Nevertheless the magnitude of the latter effect cannot be evaluated with certainty.

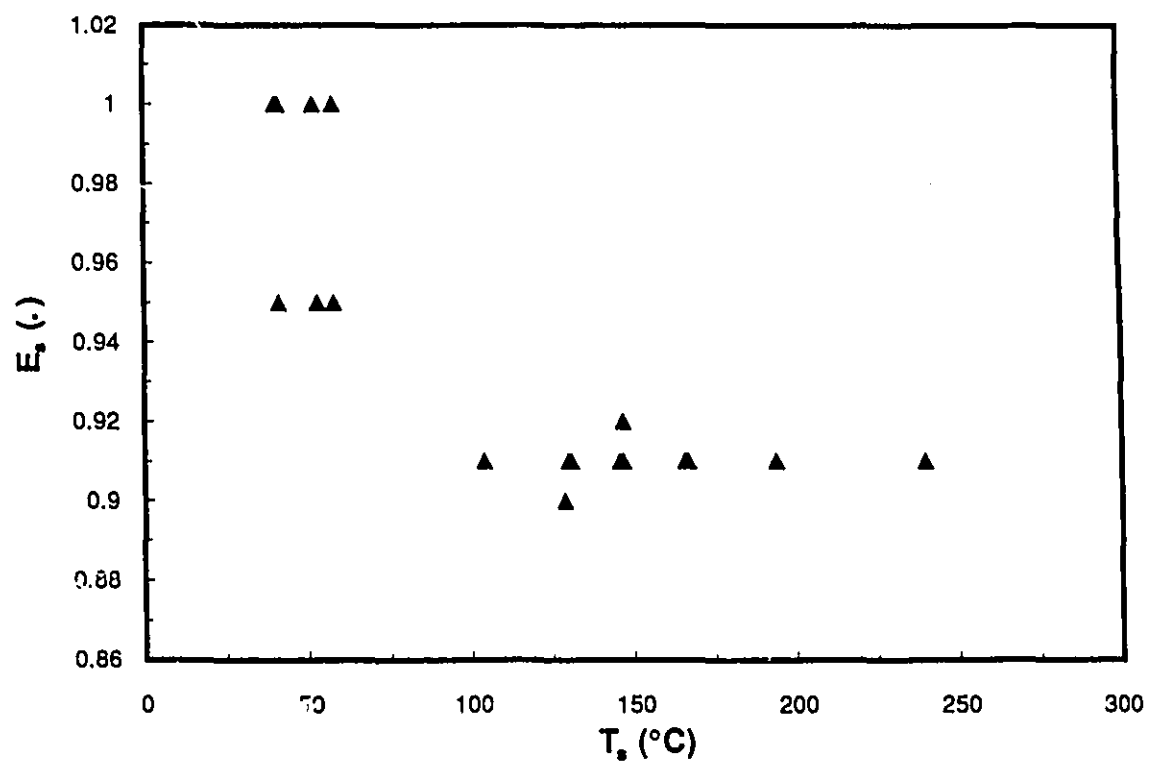


Figure A6.3 The emissivity of the glass bead sample: ϵ_s

APPENDIX 7

HEAT TRANSFER COEFFICIENT CORRELATION

An expression for the Nusselt number applicable to evaluate the convective heat transfer coefficient (h_{cBL}) in this study was developed to account for the effect of the significant temperature gradient existing between the sample surface and the test section flow. Kays and Crawford (1980) suggest that temperature variation effects be taken into account through the use of a temperature ratio. The Nusselt number was evaluated according to:

$$Nu' = \left(\frac{h_{cBL} \cdot D}{k_g} \right) \quad (A7.1)$$

where the thermal conductivity k_g was evaluated with the test section temperature T_{∞} and D , the sample diameter is given in Table 3.1. The following expression was found to give the highest correlation coefficient (0.96) with the experimental results:

$$Nu' = 0.27 \cdot Re'^{0.622} \cdot \left(\frac{T_s}{T_{\infty}} \right)^{1.12} \quad (A7.2)$$

where T_s is the sample surface temperature (K), T_{∞} the air temperature in the test section (K).

The Reynolds number is written as :

$$Re' = \left(\frac{\rho_g v_{\infty} D}{\mu_g} \right) \quad (A7.3)$$

ρ_g and μ_g are the test section air density and viscosity evaluated at T_{∞} , v_{∞} is the test section flow velocity. In Figure A7.1 a comparison of the experimental

Nusselt number computed with h_{cBL}^* (convective results, Table 4.2) and the expression A7.2 is presented. For most of the 26 convective cases represented the agreement is good. Quantitatively, the heat transfer coefficients deduced from equations A7.1 to A7.3 always differ by less than 12 % when compared to h_{cBL}^* given in Table 4.2. Unaffected heat transfer coefficients computed with the film or penetration theory are within 2 % to 3 % of unaffected heat transfer coefficient (h_{cBL}^*) reported in Table 4.2.

The exponent of the Reynolds number in the present expression A7.2 is bounded by the exponents (Incropera and DeWitt, 1985) used for the case of laminar flow over a flat plate and turbulent flow over a flat plate (0.5 (lam.) $< 0.622 < 0.8$ (turb.)). The same is true for the constant in equation A7.2 (0.037 (turb.) $< 0.270 < 0.664$ (lam.)).

Equation A7.2 is representative only of the experimental results found with the specific apparatus developed in this study and should be used only to predict heat transfer coefficients applicable in this equipment as long as the mass transfer rates are low (as is the case for the convective drying runs presented in Table 4.1) or for surfaces in the test section when there is no mass transfer.

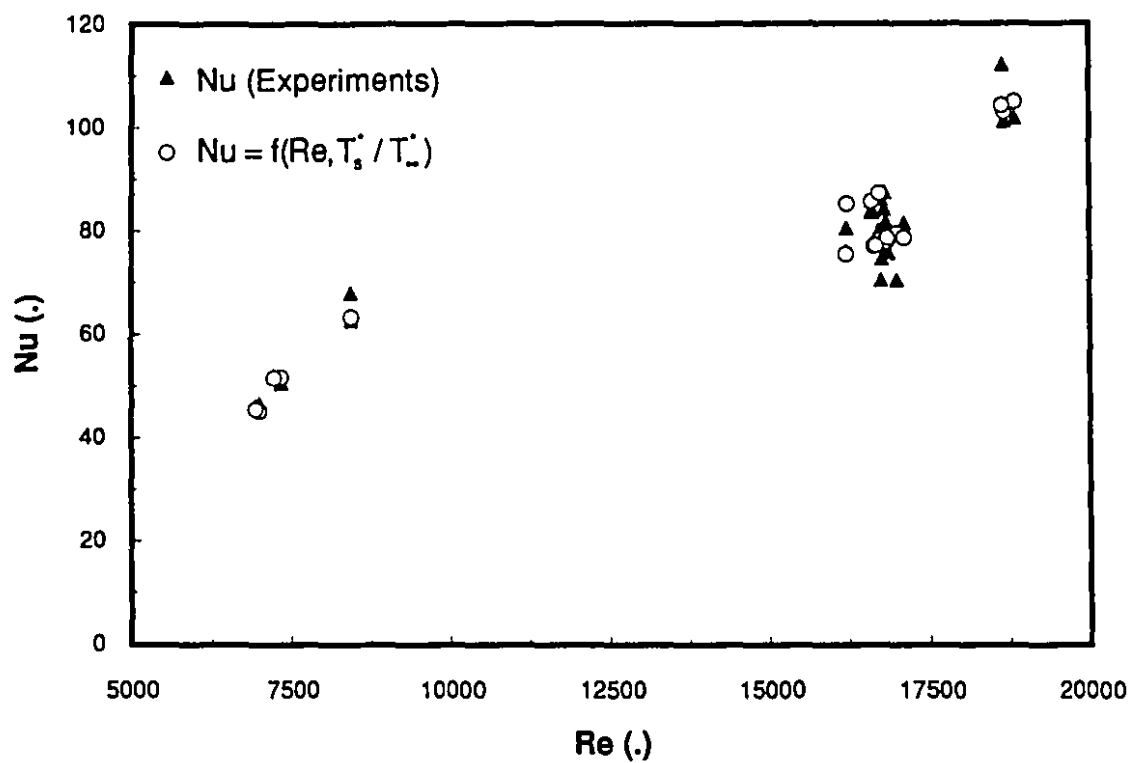


Figure A7.1 The Nu vs. Re curve: experiments and correlation (A7.2)

APPENDIX 8

EVALUATION OF THE HEAT TRANSFER LOSS OR GAIN DURING THE FREE CONVECTION-I.R. WATER EVAPORATION EXPERIMENTS

A HYPOTHESES

An evaluation of the heat losses or gain from the vessel side could be made under the following assumptions:

- a) The heat fluxes are one-dimensional;
- b) The cylindrical fin temperature (Figure A8.1) stays at room temperature;
- c) The vessel temperature is the same as the water temperature (T_w);
- d) The heat exchanged by convection on the vessel rim is negligible.

The heat loss by radiation and convection as the water recedes on the vessel internal side was not evaluated due to the unknown location of the water level as a function of time.

B HEAT TRANSFER RATE EVALUATIONS

Figure A8.1 displays the various heat transfer rates computed to account for the heat losses or gain on the vessel sides. The following relations were used (Holman, 1981):

$$Q_1 = k_T \cdot \frac{\Delta T_1}{\Delta x_1} \cdot S_1 = 0.02 \cdot \frac{(T_w - 20)}{55 \cdot 10^{-3}} \cdot \frac{\pi \cdot (93.5 \cdot 10^{-3})^2}{4} \quad (\text{A8.1})$$

- A: Stainless steel bowl
- B: External insulation
- C: Cylindrical fin
- D: Sealed container (heat sink)
- E: Internal insulation
- F: Ring fin
- G: Bottom insulation
- H: Insulating ring
- I: Reflective foil
- J: Pyrex vessel
- K: Water
- L: Thermocouple

-  Water
-  Aluminium
-  Pyrex
-  Cellular plastic
-  Ceramic

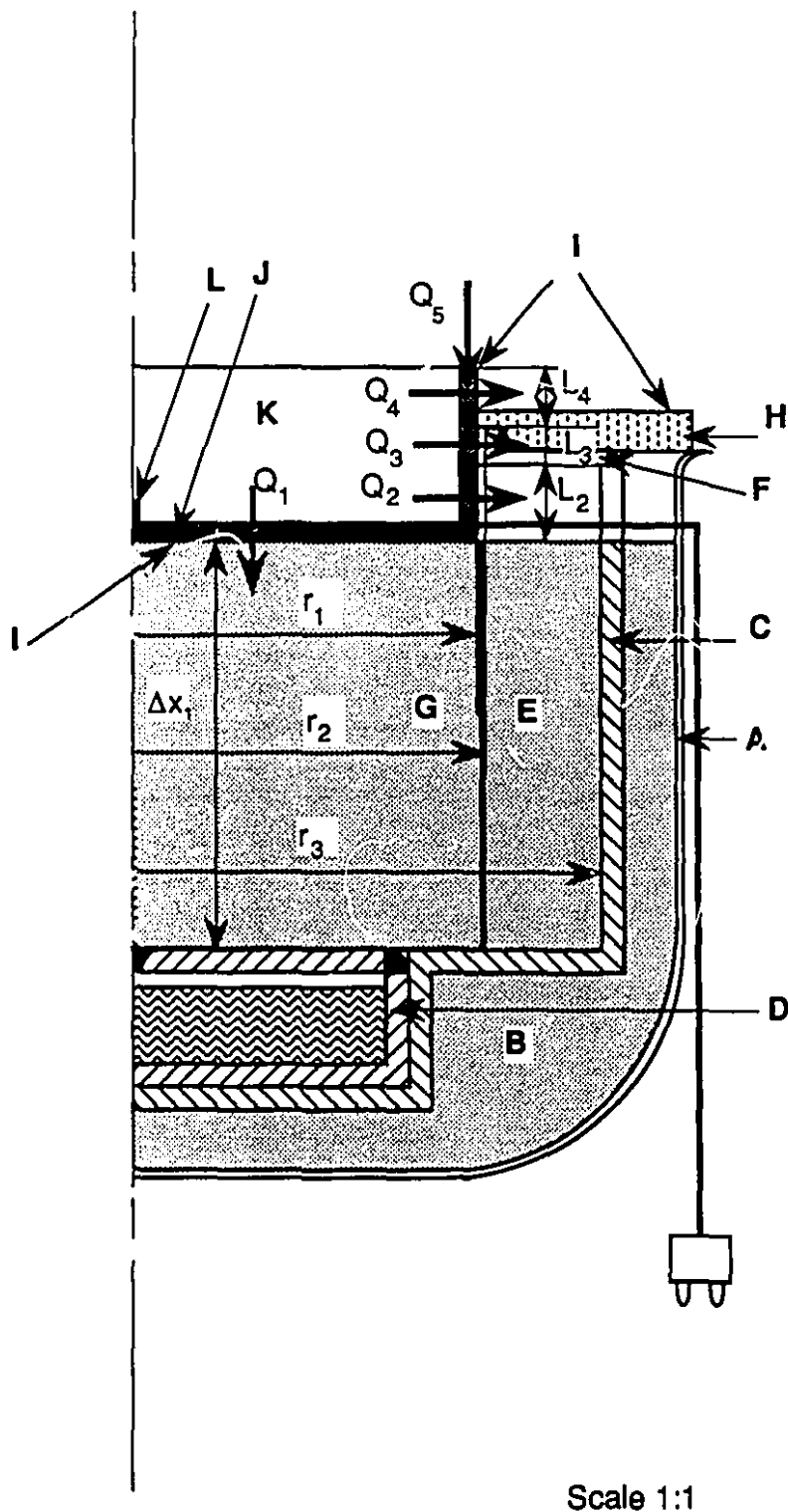


Figure A8.1 The heat transfer rates on the vertical side

$$Q_2 = \frac{2 \cdot \pi \cdot k_T \cdot L_2 \cdot \Delta T_2}{\ln\left(\frac{r_3}{r_1}\right)} = \frac{2 \cdot \pi \cdot 0.02 \cdot 10^{-2} \cdot (T_w - 20)}{\ln\left(\frac{6.3 \cdot 10^{-2}}{4.7 \cdot 10^{-2}}\right)} \quad (\text{A8.2})$$

$$Q_3 = \frac{2 \cdot \pi \cdot k_a \cdot L_3 \cdot \Delta T_3}{\ln\left(\frac{r_2}{r_1}\right)} = \frac{2 \cdot \pi \cdot 0.026 \cdot 5 \cdot 10^{-3} \cdot (T_w - 20)}{\ln\left(\frac{4.8 \cdot 10^{-2}}{4.7 \cdot 10^{-2}}\right)} \quad (\text{A8.3})$$

$$Q_4 = \frac{2 \cdot \pi \cdot k_a \cdot L_4 \cdot \Delta T_4}{\ln\left(\frac{r_2}{r_1}\right)} = \frac{2 \cdot \pi \cdot 0.026 \cdot 6.5 \cdot 10^{-3} \cdot (T_w - T_{pav})}{\ln\left(\frac{4.8 \cdot 10^{-2}}{4.7 \cdot 10^{-2}}\right)} \quad (\text{A8.4})$$

$$\begin{aligned} Q_5 &= -E_a (q_{is}^* - \sigma \cdot (T_w + 273.15)^4) \cdot S_5 \\ &= -0.06 (q_{is}^* - 5.67 \cdot 10^{-8} \cdot (T_w + 273.15)^4) \\ &\quad \cdot \frac{\pi((93.5 \cdot 10^{-3})^2 - (88.5 \cdot 10^{-3})^2)}{4} \end{aligned} \quad (\text{A8.5})$$

In these expressions the distances were taken from the vessel size and the sample holder dimensions represented in Figure A8.1. T_{pav} is the average bottom plate temperature close to the vessel upper side calculated as the average of T_{p2} , T_{p3} and T_{p4} (Figure 3.3). k_T is the Trymer 9501 thermal conductivity as given by the manufacturer (Dow Chemical Corp.) and k_a is the air thermal conductivity at 30 °C. Heat losses are affected by a plus sign in these relations.

A first evaluation of q_{is}^* was made without taking into account the lateral heat losses and then equations A8.1 to A8.5 were used to correct this evaluation.

APPENDIX 9

**EVALUATION OF THE MAXIMAL FRACTION OF THE EMITTED I.R.
HEAT FLUX ABSORBED BY THE AIR LAYER BETWEEN
THE SOURCE AND THE SAMPLE**

**A INFLUENCE OF CO₂ ON THE MEAN TOTAL ABSORPTIVITY OF THE GAS IN
THE TEST SECTION**

The mean beam length (De Vriendt, 1984) can be approximated by the one defined for the case of two parallel planes. The first plane is the test section bottom cavity and the second plane is the I.R. source emitting surface (the distance between the surfaces is 0.3 m). Thus the computation of the mean beam length gives (De Vriendt, 1984):

$$L_e = 2 \cdot 0.3 = 0.6 \text{ m} \quad (\text{A9.1})$$

The CO₂ partial pressure of dry air at atmospheric pressure is given by Weast et al. (1989):

$$p_{\text{CO}_2} = 33.4 \text{ Pa} = 0.00033 \text{ atm} \quad (\text{A9.2})$$

The emitting surface temperature is T_{sir} (850 °C) and the mean gas temperature is taken to be the average between the I.R. source temperature and the sample surface temperature:

$$T_g = (T_{\text{sir}} + T_s^*)/2 \quad (\text{A9.3})$$

Data to evaluate T_g are taken from run i79h (section 5.4, Table 5.2) because it corresponds to the highest dew point conditions (highest vapor concentration in air) encountered in all experimental runs ($T_d^* = 19.3$ °C and $T_s^* = 84$ °C). As a result the gas temperature is:

$$T_g = 467.7 \text{ °C} = 740.9 \text{ K} \quad (\text{A9.4})$$

The parameter to be evaluated to obtain the emissivity of CO₂ (E_{CO_2}) is (De Vriendt, 1984):

$$p_{CO_2} * L_e * T_{sir} / T_g = 0.00033 * 0.6 * 1123.15 / 740.9 = 0.003 \quad (A9.5)$$

This value and the diagram (De Vriendt, 1984) which link T_{sir} and E_{CO_2} gives E_{CO_2} :

$$E_{CO_2} = 0.008 \quad (A9.6)$$

Then the mean total absorptivity of CO₂ is (De Vriendt, 1984):

$$A_{CO_2} = (T_g / T_{sir})^{0.45} * E_{CO_2} = 0.007 \quad (A9.7)$$

B INFLUENCE OF H₂O ON THE MEAN TOTAL ABSORPTIVITY OF THE GAS IN THE TEST SECTION

L_e , T_{sir} , T_g are the same as in section A.

The H₂O partial pressure ($T_d = 19.3$ °C) of air in the test section is (Appendix 4):

$$p_{H_2O} = 2250 \text{ Pa} = 0.0222 \text{ atm} \quad (A9.10)$$

The parameter to be evaluated to compute the emissivity of water vapor E_{H_2O} in the gas layer is (De Vriendt, 1984):

$$p_{H_2O} * L_e * T_{sir} / T_g = 0.0222 * 0.6 * 1123.15 / 740.95 = 0.020 \quad (A9.11)$$

This value and the diagram (De Vriendt, 1984) which link T_{sir} and E_{H_2O} gives E_{H_2O} :

$$E_{H_2O} = 0.038 \quad (A9.12)$$

Then the mean total absorptivity of H₂O is (De Vriendt, 1984):

$$A_{\text{H}_2\text{O}} = (T_g/T_{\text{sir}})^{0.45} E_{\text{H}_2\text{O}} = 0.032 \quad (\text{A9.13})$$

C THE MEAN TOTAL ABSORPTIVITY OF THE GAS IN THE TEST SECTION

CO₂ and H₂O are the only gaseous species to participate to the absorption of I.R. radiation (De Vriendt, 1984), other species such as nonpolar gas (N₂, O₂) do not interact significantly with I.R. radiation. The absorptivity of the gaseous mixture is (De Vriendt, 1984):

$$A_g = A_{\text{CO}_2} + A_{\text{H}_2\text{O}} - \Delta A = 0.007 + 0.032 - 0.000 = 0.039 \quad (\text{A9.14})$$

ΔA is an absorptivity correction which result from the overlapping of the absorbing band of each gaseous species.

It can be concluded that for all runs less than 4% of the emitted heat flux is absorbed before reaching the bottom cavity of the test section. Furthermore, it can be noted that there is no systematic bias on the reported values of q_{is} in Figure 5.2 which might result from a difference in absorption although important variation of T_d^* do occur for runs with same number of heating elements. (~ 10 °C in T_d^* differences). Since the computation of q_{is} (equation 5.3) did not take into account such absorption effect, if it was important, it should reflect in data presented in Figure 5.2.

APPENDIX 10

CORRECTION TO THE EXPERIMENTAL DRYING CURVE OF A TRUNCATED CONE TO OBTAIN THE CORRESPONDING DRYING CURVE FOR A CYLINDER

A HYPOTHESES AND PROCEDURE

If one assumes that the drying rate curves for a cylinder and a truncated cone are the same the cylinder moisture content vs. t curves is obtained as follows:

- a) Obtain an expression for the cylinder moisture content;
- b) Mass flux correction to obtain the corresponding cylinder drying rate:
 - (i). Evaluation of the drying front position;
 - (ii). Correction of the cone drying rate as a result of the evaporation surface reduction;
 - (iii). Correction of the drying rate to account for the effect of the additional diffusion resistance for the cylinder;
 - (iv). Evaluation of the drying rate vs. moisture content curve for the cylinder;
- c) Computation of the moisture content evolution for the cylinder.

B COMPUTATION OF THE DRYING CURVE

When $X > X_c$ (critical moisture content):

Evaporation is considered as a surface phenomenon and the evaporation rate of a cone at a specific moisture content is the same as the one for a cylinder. Then the development according to the steps already defined is the following:

- a) The moisture contents are the same for the cylinder (X_{cy}) and the truncated cone (X_{co}) for the same drying rate:

$$X_{cy} = X_{co} \quad (\text{A10.1})$$

- b) There is no correction applicable:

- (i) The drying front is at the surface (x_f drying front position from the surface):

$$x_f = 0 \quad (\text{A10.2})$$

- (ii) No correction;

- (iii) No correction;

- (iv) The drying rate of the cylinder (N_{vcy}) and the truncated cone (N_{vco}) are the same:

$$N_{vcy} = N_{vco} \quad (\text{A10.3})$$

When $X < X_c$:

If one assumes that the moisture content distribution is uniform in the wet zone. The development according to the steps already defined is the following:

- a) The expression for the cylinder moisture content is:

$$X_{cy} = \left(i - \frac{x_f}{b} \right) * X_c \quad (\text{A10.4})$$

- (i) The cone moisture content is:

$$X_{co} = \frac{V_w}{V_{co}} * X_c \quad (\text{A10.5})$$

where V_w is the volume of the wet zone and V_{co} the overall truncated cone volume. V_{co} is:

$$V_{co} = \frac{\pi \cdot b}{3} \cdot (R_1^2 + R_2^2 + R_1 \cdot R_2) \quad (A10.6)$$

where R_1 is the evaporation surface radius (Table 3.1) and R_2 is the truncated cone bottom radius. V_w is:

$$V_w = V_{co} - \frac{\pi \cdot x_f}{3} \cdot (R_f^2 + R_1^2 + R_f \cdot R_1) \quad (A10.7)$$

where R_f is the evaporation front surface radius. R_f is:

$$R_f = R_1 - x_f \cdot \text{tg}(\alpha) \quad (A10.8)$$

where α is the cone angle (3°). A similar expression is valid for R_2 with b instead of x_f .

The final expression (deduced from A10.5 to A 10.8) which links x_f to the other variables is:

$$\begin{aligned} & (\text{tg}(\alpha))^2 \cdot x_f^3 - 3 \cdot \text{tg}(\alpha) \cdot R_1 \cdot x_f^2 + 3 \cdot R_1^2 \cdot x_f \\ & + b \cdot (R_1^2 + R_2^2 + R_1 \cdot R_2) \cdot \left(\frac{X_\infty}{X_c} - 1 \right) = 0 \end{aligned} \quad (A10.9)$$

- (ii) The correction of the truncated cone drying rate for the effect of a reduced evaporation surface gives (equality of mass transfer rate):

$$N_{vcy} = \frac{R_1^2}{(R_1 - x_f \cdot \text{tg}(\alpha))^2} \cdot N_{vco} \quad (A10.10)$$

- (iii) The correction of the cylinder drying rate for the effect of increase diffusion resistance is approximated by A10.10

corrected by a factor corresponding to an evaporation surface area reduction:

$$N_{vcy} = \frac{R_1^2}{(R_1 - x_1 \cdot \text{tg}(\alpha))^2} \cdot \frac{(R_1 - x_1 \cdot \text{tg}(\alpha/2))^2}{R_1^2} \cdot N_{vco} \quad (\text{A10.11})$$

(vi) Equations A10.4 and A10.11 define the drying rate curve during the falling rate period of the cylinder.

Step (c) is the same whatever X. The expression for the derivative of the cylinder moisture content is:

$$\frac{dX_{cy}}{dt} = -\frac{N_{vcy}}{V_{cy} \cdot \rho_d} \cdot A_{cy} = -\frac{N_{vcy}}{b \cdot \rho_d} \quad (\text{A10.12})$$

Where V_{cy} and A_{cy} are the cylinder volume and drying surface respectively.

The computation starts from equation A10.12 for which the Runge-Kutta method (RK22) was used to obtain a numerical solution. A first evaluation $(X_{cy})_1$ of X_{cy} ($t + dt$) is made with $(N_{vcy})_1$ evaluated from the drying rate curve and $X_{cy}(t)$:

$$(X_{cy})_1 = X_{cy}(t) + \left(\frac{N_{vcy}}{b \cdot \rho_d} \right)_1 \cdot dt \quad (\text{A10.13})$$

Then $(X_{cy})_1$ is used to obtain an approximation to the drying rate $(N_{vcy})_2$. Finally, the expression of $X_{cy}(t+dt)$ is:

$$X_{cy}(t + dt) = X_{cy}(t) + \frac{\left[\left(\frac{N_{vcy}}{b \cdot \rho_d} \right)_1 + \left(\frac{N_{vcy}}{b \cdot \rho_d} \right)_2 \right]}{2} \cdot dt \quad (\text{A10.14})$$

The procedure is continued until X_{cy} is 0.

APPENDIX 11**THE HEAT AND MASS TRANSFER ANALOGY**

Within the frame of the laminar boundary layer theory (boundary layer approximations) and taking into account the following approximations (Bird et al., 1960):

- a) - Constant physical properties
- b) - A small mass transfer rate at the interface
- c) - No chemical reactions in the fluid
- d) - No viscous dissipation in the fluid
- e) - No emission or absorption of radiant energy in the fluid
- f) - No pressure diffusion, thermal diffusion or forced diffusion at the interface

It can be shown theoretically (Bird et al., 1960; Incropera and DeWitt, 1985) that the dimensionless heat, mass and momentum conservation equations describing the state of the fluid within the boundary layer as well as the applicable boundary conditions (constant temperature, concentration and velocity at the wall) are similar¹. In such a case, the existence of the analogy between the transfer of heat and mass has a strong theoretical basis and the solution of equations yields classical expressions for the heat and mass transfer coefficient ratio (expression 4.24).

For a laminar flow, the high mass transfer rate effect on the boundary layers can theoretically be taken into account through use of the laminar boundary layer theory (Bird et al., 1960). Its practical result is a theoretical evaluation of the heat and mass transfer coefficient change due to the high mass transfer rate.

¹According to Incropera and DeWitt (1985), processes are said to be analogous if they are governed by dimensionless equations of the same form.

Although the flow within the test section is turbulent and the theoretical development (analogy of the transfer) has been derived for a laminar boundary layer, experimental observations (Hertjees and Ringens, 1956; Smolsky and Sergejev, 1962; Eckert and Drake, 1970; Bird et al., 1960) have already confirmed that the analogy between the transfer of heat and mass appears to exist in case of a turbulent flow. In such a case the boundary layer theory results can be used, as a first approximation, to account for the high mass transfer rate effect.

The use of I.R. heating superimposed on a laminar flow does not bring anything new as compared to the case of a laminar flow alone as long as (e) is true. With respect to the flow, the wall boundary condition is still one of a given surface temperature and not one of heat flux since I.R. heating is only a way to heat to a given T_s . As a result, the theoretical developments which lead to a statement of the analogy between the transfer of heat and mass as well as the boundary layer theory are still applicable in laminar flow-I.R. drying.

In turbulent flow-I.R. drying, the heat and mass transfer analogy and the laminar boundary layer theory should be applicable although no strong theoretical foundations exists to support this view (without I.R. heating the same was true).